

EPR Relaxation: Progress in Hardware and Analysis Methods

Peter Joseph Roberts, MPhys

**Thesis submitted to the University of Nottingham
for the degree of Doctor of Philosophy**

July 2014

Abstract

Dynamic nuclear polarization (DNP) is a technique for enhancing the sensitivity of nuclear magnetic resonance (NMR) experiments by increasing the polarization of the nuclear spins. DNP experiments are often characterized by the enhancement which is achieved, and the enhancement build-up rate. These parameters are strongly influenced by electronic and nuclear relaxation processes. The purpose of the work presented in this thesis was to develop hardware and analysis methods for studying relaxation in electron paramagnetic resonance (EPR) and NMR.

Two novel probes for combined NMR and longitudinally detected EPR experiments have been built. The first of these probes is designed for low temperature NMR, EPR and DNP experiments, with the main focus being relaxation studies in typical low-temperature DNP conditions. The second probe is designed for high temperature cryoporometry studies of lignin degradation

Relaxation data in magnetic resonance often exhibits multi-exponential decay. An algorithm for performing a Laplace inversion of multi-exponential relaxation data, and extracting distributions of time constants, is described. The algorithm, which is based on Tikhonov regularization, uses a uniform penalty and a zero-crossing penalty to stabilize the solution, but does not use a non-negativity constraint, so relaxation spectra with both positive and negative peaks can be produced.

Two experiments to study relaxation and other dynamic processes in samples containing organic radicals have been performed. The first of these was designed to study saturation, relaxation and spectral diffusion processes in EPR during continuous microwave irradiation. The second experiment measured relaxation of DNP-enhanced nuclear polarization, and revealed an offset dependence of the relaxation behaviour. Both experiments were performed using the low-temperature probe, and the data was analysed using the Laplace inversion algorithm.

Acknowledgements

I would like to express my gratitude to the following people, for making this project possible, and for making my time in Nottingham so enjoyable.

Josef Granwehr, for supervising this project, continued support and guidance with it, countless invaluable discussions, and extensive feedback on this thesis.

Alan Dorkes and Ian Thexton, for solutions to a wide variety of technical problems I found or created. I am especially grateful to Alan for his assistance with the probes we built: for help and ideas at the design stage, for solving or preventing various problems, and for machining all of the components.

Members of our research group, for helpful discussions, technical assistance, and being great people to work with, especially Anniek van der Drift, Alexander Karabanov, Ben McGeorge-Henderson, Daniel Wisniewski, Edward Breeds, Grzegorz Kwiatkowski, James Leggett, James Wilman, Rafal Panek, Sankeerth Hebbar, Sebastian Kemper, and Walter Köckenberger.

My friends at the Magnetic Resonance Centre, with whom I have shared many great experiences over the last four years, including games of football, basketball and volleyball, weekly film nights, and lunch-time attempts at the crossword. There are too many of you to mention individually.

My examiners, Anthony Horsewill and Gavin Morley, for feedback on this thesis, and the interesting discussions in my viva voce examination. Thanks also to Prof. Horsewill for feedback on my annual reports, and the very helpful annual progress interviews.

Will Place, for giving me a place to live, and for tolerating me as a particularly unsocial house-mate in the last few months of writing this thesis.

My speech therapist, Carolyn DesForges, for helping me to prepare for my talk at Euromar 2012 and my viva voce examination.

Devasuda Anblagan, for her support when I needed it, and patience when I didn't deserve it.

My family, for their love, support, generosity, and inspiration.

Contents

Abstract	iii
Acknowledgements	v
Contents	vii
List of Symbols, Abbreviations, and Physical Constants	xi
Introduction	xvii
1 Magnetic Resonance Theory	1
1.1 A spin in a magnetic field	1
1.2 Spin operators	3
1.3 An ensemble of spins	5
1.3.1 Density operator	6
1.3.2 Liouville-von Neumann equation	9
1.4 Hamiltonians	11
1.4.1 Zeeman interaction	11
1.4.2 Hyperfine interaction	13
1.4.3 Dipole-dipole interactions	15
1.4.4 Excitation Hamiltonians	17
1.5 Macroscopic magnetization	18
1.5.1 Polarization	18
1.5.2 Spin precession	21
1.5.3 Excitation	22
1.5.4 Relaxation	24
1.5.5 Bloch equations	25
1.6 Relaxation	26

1.6.1	Theoretical frameworks	27
1.6.2	Relaxation mechanisms in EPR	27
1.6.3	Relaxation studies	31
2	Dynamic Nuclear Polarization	37
2.1	Overhauser effect	39
2.2	Solid effect	40
2.2.1	Electron–nucleus spin system in the liquid state	41
2.2.2	Electron–nucleus spin system in the solid state	44
2.2.3	Dynamics of the solid effect	47
2.2.4	Summary	50
2.3	Cross effect	51
2.4	Thermal mixing	52
2.5	Spin diffusion	55
2.6	Simulating solid-state DNP	58
2.7	Polarizing agents	59
2.8	Discussion	62
3	NMR and EPR Detection	65
3.1	Introduction	65
3.2	Conventional EPR detection	66
3.2.1	Microwave field production and transmission	66
3.2.2	Resonator	67
3.2.3	Static magnetic field	68
3.2.4	Field modulation	68
3.2.5	Detection	68
3.3	Longitudinally detected EPR	69
3.3.1	Theory and simulations	70
3.3.2	LOD experiments	74
3.4	NMR detection	77
3.4.1	Spectrometer	78
3.4.2	Resonant circuits	78
3.4.3	Transmission lines	80
3.4.4	Coils	82
3.5	Quadrature detection	88
3.6	Instrumentation	91

3.6.1	Magnet	91
3.6.2	Microwave bridge	92
3.6.3	Probe	93
3.6.4	Timing control	93
3.6.5	Data acquisition	94
3.6.6	NMR spectrometer	94
3.6.7	Software	94
4	Novel Probes for Combined EPR and NMR Detection	97
4.1	A low temperature probe for NMR and LOD EPR	97
4.1.1	Introduction: multi-modal detection in magnetic resonance .	97
4.1.2	Objectives and Design Criteria	101
4.1.3	Construction	103
4.1.4	Performance	109
4.1.5	Applications	116
4.2	A combined NMR and EPR probe for cryoporometric studies of lignin degradation	116
4.2.1	Background: cryoporometry and lignin degradation	116
4.2.2	Objectives, design criteria, and modifications compared with low-temperature probe	118
4.2.3	Construction	120
4.2.4	Performance	123
4.2.5	Conclusions	125
5	Laplace Inversion of Relaxation Data	127
5.1	Introduction	127
5.2	Algorithm	128
5.2.1	Problem description	128
5.2.2	Data compression	129
5.2.3	Choice of kernel	132
5.2.4	Regularization	136
5.2.5	Parameter selection	140
5.2.6	Inversion procedure	142
5.2.7	Computation	143
5.2.8	Other considerations	144
5.3	Simulations	144

5.3.1	SNR	145
5.3.2	Zero-crossing penalty	146
5.3.3	Regularization parameters	146
5.4	Self-consistency test	147
5.5	Conclusions	149
6	EPR Transient Saturation	151
6.1	Introduction	151
6.2	Experimental details and data processing	154
6.3	Results and discussion	157
6.4	Conclusions	160
7	DNP Over Short Timecales	165
7.1	Introduction	165
7.2	Experimental details and data processing	166
7.3	Results and discussion	170
7.4	Conclusions	172
8	Conclusions and Outlook	175
8.1	Interpretation of EPR transient saturation data	176
8.2	Interpretation of DNP NMR data	177
8.3	Analysis of transient LOD EPR data	177
A	Spin matrices for the solid effect calculations	181
B	Energy levels of the electron Zeeman interaction	183
C	Illustration of an excitation Hamiltonian	185
	Bibliography	187

Symbols, Abbreviations, and Physical Constants

Symbols

\otimes	Kronecker product
*	convolution
$(\cdot)^{(2)}$	entry-wise square of a matrix
$\ \cdot\ $	Frobenius norm of a matrix
$H(\cdot)$	Heaviside step function
(\cdot)	time derivative of a matrix $\frac{d(\cdot)}{dt}$
$(\cdot)^T$	transpose of a matrix
$\tilde{(\cdot)}$	matrix compressed using SVD
$\tilde{\tilde{(\cdot)}}$	matrix compressed and decompressed using SVD
$\sigma(\cdot)$	standard deviation of a matrix
$\mathbf{a} \cdot \mathbf{b}$	scalar product of vectors \mathbf{a} and \mathbf{b} (equivalent to $\mathbf{a}^T \mathbf{b}$)
$\mathbf{1}_M$ or $\hat{1}_M$	$M \times M$ identity matrix or identity operator
$\hat{\Gamma}$	relaxation superoperator
δ	spectral linewidth
ϵ	relative polarization enhancement
ε_i	Boltzmann factor for spin i ($e^{-\hbar\omega_i/k_B T}$)
μ	magnetic moment
ν_{NMR}	NMR offset frequency
$\hat{\rho}$	density operator or density matrix
τ	saturation time constant
τ_c	correlation time
τ_{rise}	rise time of the LOD signal

Ω	frequency offset (frequency in the rotating frame)
ω_0	Larmor frequency
ω_e	electron Larmor frequency
ω_n	nuclear Larmor frequency
ω_1	amplitude of microwave or radio-frequency field in rad s ⁻¹
ω_{Ξ}	resonance frequency of the LOD circuit
ω_{mw}	frequency of microwave field
ω_{rf}	frequency of radio-frequency field
A	secular hyperfine interaction coefficient
A	hyperfine interaction matrix
B	magnetic field (magnetic induction)
B_0	amplitude of static magnetic field
B ₀	static magnetic field
B_1	amplitude of microwave or radio-frequency field in T
B ₁	oscillatory (microwave or radio-frequency) magnetic field
B_{\pm}	pseudo-secular hyperfine interaction coefficient
C	capacitance
D	electron-electron dipolar interaction coefficient
D	electron-electron dipolar interaction matrix
d	nucleus-nucleus dipolar interaction coefficient
d	nucleus-nucleus dipolar interaction matrix
f_{AM}	amplitude modulation frequency
g	electron g -value
g	electron g -matrix
\hat{H}	Hamiltonian (in angular frequency units)
$\hat{\mathcal{H}}$	Hamiltonian (in energy units)
I	nuclear spin quantum number
$\hat{\mathbf{I}}$	nuclear spin angular momentum
$\hat{I}_x, \hat{I}_y, \hat{I}_z$	x, y and z components of $\hat{\mathbf{I}}$
L	inductance
M	macroscopic magnetization
M ₀	thermal equilibrium macroscopic magnetization
M_{xy}	transverse magnetization
M_z	longitudinal magnetization
m_I	nuclear magnetic quantum number

m_S	electron magnetic quantum number
P	polarization
p	population of a quantum state
Q	quality factor
Q_{Ξ}	quality factor of the LOD circuit
R	resistance
R_1	longitudinal relaxation rate
R_2	transverse relaxation rate
S	electron spin quantum number ($S = \frac{1}{2}$)
$\hat{\mathbf{S}}$	electron spin angular momentum
$\hat{S}_x, \hat{S}_y, \hat{S}_z$	x, y and z components of $\hat{\mathbf{S}}$
T	temperature
T_1	longitudinal relaxation time
T_2	transverse relaxation time
T_{LOD}	duration of the LOD pulse sequence
T_m	phase-memory time
T_s	spin temperature
V	voltage
Z	partition function

Abbreviations

ADC	analogue-to-digital converter
AM	amplitude modulation <i>or</i> amplitude-modulated
a.u.	arbitrary units
BA	boundary artifact
cdc	compressed-decompressed
CE	cross effect
CP	cross-polarization
CPM probe	cryoporometry probe
CPMG	Carr-Purcell-Meiboom-Gill
CW	continuous wave
DAQ	analogue-digital/digital-analogue device (data acquisition device)
DC	direct current

DEER	double electron-electron resonance
DNP	dynamic nuclear polarization
DQ	double quantum
DRO	dielectric resonator oscillator
DTG	data timing generator
ELDOR	electron-electron double resonance
ENDOR	electron-nuclear double resonance
EPR	electron paramagnetic resonance
ESE	electron spin echo
FID	free induction decay
FPR	Fabry-Perot resonator
FT	Fourier transform
FWHM	full-width at half-maximum
GM	Gauss-Markov
hfi	hyperfine interaction
HR	horn-reflector (resonator)
ID	inner diameter
iid	independent and identically distributed
ILT	inverse Laplace transform
IR	inversion recovery
LOD	longitudinal (EPR) detection
LOD EPR	longitudinally detected EPR
LT probe	low temperature probe
MAS	magic angle spinning
MRI	magnetic resonance imaging
mw	microwave
NMR	nuclear magnetic resonance
NN	non-negativity
OD	outer diameter
OE	Overhauser effect
PAS	principal axis system
PCTFE	polychlorotrifluoroethylene
rf	radio-frequency
RTD	resistance temperature detector
SE	solid effect

SE	spin echo
SJ	sudden jump
SNR	signal-to-noise ratio
SQ	single quantum
SR	saturation recovery
STAMO	system of master oscillators
SV	singular value
SVD	singular value decomposition
TM	thermal mixing
UP	uniform penalty
VCO	voltage controlled oscillator
ZC	zero-crossing
ZQ	zero quantum

Physical Constants

Physical constants are the most up-to-date available, and are taken from the review by Mohr, Taylor and Newell [1], apart from the carbon-13 gyromagnetic ratio, which is taken from the book by Levitt [2].

γ_C	carbon-13 gyromagnetic ratio	6.7283×10^7	$\text{rad s}^{-1} \text{ T}^{-1}$
γ_e	electron gyromagnetic ratio $-g_e\mu_B/\hbar$	$-1.760\ 859\ 708(39) \times 10^{11}$	$\text{rad s}^{-1} \text{ T}^{-1}$
γ_p	proton gyromagnetic ratio $g_p\mu_N/\hbar$	$2.675\ 222\ 005(63) \times 10^8$	$\text{rad s}^{-1} \text{ T}^{-1}$
μ_0	vacuum permeability	$4\pi \times 10^{-7}$	$\text{T}^2 \text{ J}^{-1} \text{ m}^3$
μ_B	Bohr magneton $e\hbar/2m_e$	$9.274\ 009\ 68(20) \times 10^{-24}$	J T^{-1}
μ_N	nuclear magneton $e\hbar/2m_p$	$5.050\ 783\ 53(11) \times 10^{-27}$	J T^{-1}
e	elementary charge	$1.602\ 176\ 565(35) \times 10^{-19}$	C
g_e	free electron g -factor	2.002 319 304 361 53(53)	
g_p	proton g -factor	5.585 694 713(46)	
h	Planck constant	$6.626\ 069\ 57(29) \times 10^{-34}$	J s
\hbar	$\hbar = h/2\pi$	$1.054\ 571\ 726(47) \times 10^{-34}$	J s rad^{-1}
k_B	Boltzmann constant	$1.380\ 6488(13) \times 10^{-23}$	J K^{-1}
m_e	electron mass	$9.109\ 382\ 91(40) \times 10^{-31}$	kg

m_p proton mass $1.672\ 621\ 777(74) \times 10^{-27}$ kg

Introduction

Nuclear magnetic resonance (NMR) is a powerful and versatile tool which has applications in a diverse range of fields, including medicine, biomedical research, materials science, chemistry, quantum computing and the petroleum industry. It has the advantage of being non-invasive, meaning that systems can be studied in their natural state. One of the main challenges for NMR is its inherently low sensitivity, due to the extremely small thermal equilibrium polarizations of nuclei under many experimental conditions.

Several strategies exist for enhancing the sensitivity of NMR experiments, by increasing the polarization of nuclei. These strategies, which are often collectively known as hyperpolarization methods, include dynamic nuclear polarization (DNP) [3,4], spin-exchange optical pumping (SEOP) [5,6], parahydrogen induced polarization (PHIP) [7,8], and ‘brute-force’ polarization, utilizing low temperatures and high magnetic fields [9,10].

DNP encompasses a range of techniques in which electron polarization is used to enhance nuclear polarization by applying microwave radiation to a paramagnetically doped sample. Since its discovery in the 1950s [11,12], DNP has grown to become the major focus of many NMR research groups around the world. The major advancements in DNP are described briefly in Chapter 2, and in more detail in two recent review articles, which also describe some of the developments of the last few years [3,4].

DNP exploits the fact that electrons have much greater thermal equilibrium polarizations than nuclei. In a system containing both unpaired electrons and nuclei with non-zero spins, the nuclei and electrons are coupled via the hyperfine interaction, and this interaction makes it possible to use the higher polarization of the electron spins to enhance the nuclear spin polarization. In DNP, this polarization enhancement is achieved by applying microwave radiation to the system. DNP experiments are often characterized by two parameters, relative polarization

enhancement and enhancement build-up rate.

In NMR and a related phenomenon, electron paramagnetic resonance (EPR), a system can be perturbed by applying oscillating magnetic fields at or close to the resonance frequency of the nuclei or electrons. Following such a perturbation, the system returns to its thermal equilibrium state by a process known as relaxation. Relaxation is a complex process, and many different relaxation mechanisms exist. Relaxation processes are particularly important in DNP, and they can strongly influence enhancement and build-up rate.

The central theme of this thesis is the development of hardware and analysis methods to study relaxation in magnetic resonance, particularly EPR relaxation in samples commonly used for solid-state DNP.

The first part of this thesis introduces some of the main theoretical concepts which are a necessary precursor for the material presented in the rest of the thesis. Chapter 1 describes some of the fundamental theoretical concepts and equations describing NMR and EPR. It describes an ensemble of spins- $\frac{1}{2}$ in a magnetic field, including the density matrix, spin Hamiltonians, and the Louville-von Neumann equation. The bulk properties of an ensemble of spins are then considered: the macroscopic magnetization of a spin ensemble is discussed, and the Bloch equations are derived. Finally, some of the mechanisms causing relaxation are described, and methods of investigating relaxation are introduced.

Chapter 2 describes the polarization enhancement mechanisms in DNP. There are four distinct mechanisms, which are each described individually. The transfer of enhanced nuclear polarization through a sample by nuclear spin diffusion is then described. Some of the recent efforts at simulating solid-state DNP are reviewed, and some organic molecules used as polarizing agents in DNP are discussed.

EPR and NMR are conceptually very similar but, at a given magnetic field, they operate at very different frequencies. As such, EPR and NMR detection methods are very different. Chapter 3 describes detection methods in EPR, including both conventional (transverse) detection and longitudinal detection, and NMR. The instruments comprising the EPR and NMR spectrometer in our laboratory, used for the experiments presented in this thesis, are also described.

During the course of this PhD, two novel probes for combined NMR and EPR detection have been built. These are described in Chapter 4. The first of these probes is designed for low temperature NMR, EPR and DNP experiments, with the main focus being relaxation studies in samples commonly used for DNP. The

second probe is designed for combined NMR and EPR cryoporometry experiments, with the aim of studying lignin degradation. This probe is something of a diversion from the main theme of this thesis, but the probes are described together as they share many similarities.

Much of the data presented in this thesis, as well as a lot of relaxation data in the literature, exhibits multi-exponential decay. Chapter 5 describes an algorithm, based on Tikhonov regularization, for extracting distributions of time constants from multi-exponential relaxation data using an inverse Laplace transform. The algorithm does not use a non-negativity constraint, but uses a uniform penalty and a zero-crossing penalty to stabilize the solution.

The final two chapters describe experiments that have been performed to investigate relaxation behaviour in samples containing organic radicals. These experiments were performed using the low-temperature probe described in Chapter 4, and the data was analysed using the algorithm described in Chapter 5.

Chapter 6 describes an EPR experiment to investigate the behaviour of electron magnetization during mw irradiation, designed to study relaxation, saturation, and spectral diffusion processes. Using a sample of an organic radical with an inhomogeneously broadened EPR spectral line, the sample was irradiated with a fixed frequency microwave field, and the transient saturation of magnetization across the spectral line was recorded.

In low temperature DNP experiments, samples are typically polarized over time-scales of minutes to hours, and the enhancement process is often characterized by a single polarization build-up rate. Chapter 7 describes an experiment to investigate relaxation behaviour of DNP-enhanced nuclear polarization over much shorter time-scales and at different offset frequencies. Following DNP enhancement, NMR signal was recorded as it relaxed to thermal equilibrium. The relaxation data was inverted using the inverse Laplace transform algorithm, and the resulting relaxation spectrum revealed offset dependent multi-exponential relaxation behaviour.

Chapter 1

Magnetic Resonance Theory

This chapter outlines some of the fundamental theoretical concepts and equations describing nuclear magnetic resonance (NMR) and electron paramagnetic resonance (EPR), which are a necessary precursor for the rest of this thesis. The chapter begins with a description of a single spin- $\frac{1}{2}$ in a magnetic field, including the quantum mechanical operators associated with this spin. Following this, an ensemble of spins is described: the density matrix is introduced, and the Louville-von Neumann equation is derived. The overall spin Hamiltonian for an ensemble of electrons and spin- $\frac{1}{2}$ nuclei is then introduced, including the different Hamiltonians most relevant for this thesis. The concept of an ensemble of quantum mechanical spins leads naturally on to a consideration of the bulk properties of an ensemble of spins: the macroscopic magnetization vector \mathbf{M} is discussed, and the Bloch equations, which describe the motion of \mathbf{M} , are derived. Finally, relaxation is considered. Some of the mechanisms causing longitudinal and transverse relaxation are described, and methods of investigating relaxation and measuring relaxation rates are introduced.

1.1 A spin in a magnetic field

Elementary particles, such as electrons, and composite particles, such as nuclei, have a fundamental quantum mechanical property known as *spin angular momentum*. Electron spin angular momentum is denoted $\hbar\mathbf{S}$, while nuclear spin angular momentum is denoted $\hbar\mathbf{I}$.*

*Strictly speaking, $\hbar\mathbf{S}$ is the spin angular momentum and \mathbf{S} is a dimensionless quantity. However, it is often convenient, and conventional in NMR and EPR, to call \mathbf{S} the spin angular momentum.

Every particle with non-zero spin angular momentum has an associated magnetic moment \mathbf{p} . For a free electron this is given by

$$\mathbf{p}_S = -g_e \mu_B \mathbf{S}, \quad (1.1)$$

where g_e is the free electron g -factor, $\mu_B = e\hbar/2m_e$ is the Bohr magneton, e is the elementary charge, and m_e is the electron mass. This can also be written

$$\mathbf{p}_S = \gamma_e \hbar \mathbf{S}, \quad (1.2)$$

where $\gamma_e = -g_e \mu_B / \hbar$ is the electron gyromagnetic ratio. By analogy, the magnetic moment of a nucleus is given by

$$\mathbf{p}_I = \gamma_n \hbar \mathbf{I}, \quad (1.3)$$

where γ_n is the gyromagnetic ratio of the nucleus.

Consider a free electron or nucleus in a static magnetic field $\mathbf{B}_0 = (0, 0, B_0)$. Its magnetic moment is quantized: that is, it can only take discrete orientations with respect to \mathbf{B}_0 , each corresponding to a different quantum state with an associated energy E , given by

$$E_{m_i} = -\mathbf{p} \cdot \mathbf{B} = -m_i \gamma_i \hbar B_0, \quad (1.4)$$

where m_i is the magnetic quantum number associated with the z -component of the spin angular momentum, and the index $i = S, I$ labels the particle as an electron or a nucleus respectively. A single unpaired electron has a spin $S = \frac{1}{2}$, and m_S can take either of the values $m_S = \pm \frac{1}{2}$. For a nucleus with spin I , m_I can take any of the discrete set of values $m_I = -I, -I+1, \dots, +I$, where I is an integer or half integer. Two of the most commonly encountered nuclei in NMR, ^1H and ^{13}C , have a spin $I = \frac{1}{2}$, and therefore $m_I = \pm \frac{1}{2}$. ^{14}N , which is an important nucleus in certain radicals used for EPR, has a spin $I = 1$, and therefore $m_I = -1, 0, +1$.

The rest of this chapter describes some of the general concepts associated with spin- $\frac{1}{2}$ particles using electron spins as an example. Most of the theory can be equally well applied to spin- $\frac{1}{2}$ nuclei.

Since m_S can only take two discrete values $m_S = \pm \frac{1}{2}$, the energies of the two states are given by (eq (1.4)),

$$E_{\pm \frac{1}{2}} = \mp \frac{1}{2} \gamma_e \hbar B_0 = \pm \frac{1}{2} g_e \mu_B B_0, \quad (1.5)$$

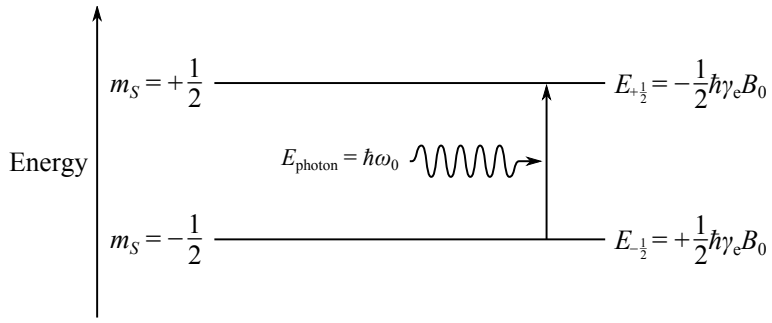


Figure 1.1: Absorption of a photon with energy $E_{\text{photon}} = \hbar\omega_0$ causes a transition from state $m = -\frac{1}{2}$ to state $m = +\frac{1}{2}$.

and the difference between the energy levels is

$$\Delta E = E_{+\frac{1}{2}} - E_{-\frac{1}{2}} = -\gamma_e \hbar B_0, \quad (1.6)$$

or, in angular frequency units,

$$\frac{\Delta E}{\hbar} = \omega_0 = -\gamma_e B_0. \quad (1.7)$$

Equation (1.7) is called the Larmor equation, and ω_0 is known as the Larmor frequency, or resonance frequency.

This splitting of energy states is called the Zeeman splitting. A transition between the $m_S = +\frac{1}{2}$ state and the $m_S = -\frac{1}{2}$ state is associated with the emission or absorption of a photon or a phonon with frequency ω_0 (see Figure 1.1).

1.2 Spin operators

In classical mechanics, spin angular momentum is represented by a vector, while in quantum mechanics it is represented by a vector operator. This section gives some definitions and properties of spin angular momentum operators which will be useful in the rest of this chapter.

For a single electron spin, the total spin angular momentum is denoted $\hat{\mathbf{S}}$, with x -, y -, and z -components \hat{S}_x , \hat{S}_y and \hat{S}_z . $\hat{\mathbf{S}}$ is given in terms of its components by

$$\hat{\mathbf{S}}^2 = \hat{S}_x^2 + \hat{S}_y^2 + \hat{S}_z^2, \quad (1.8)$$

and the components \hat{S}_i ($i = x, y, z$) are given by $\hat{S}_i = \frac{1}{2}\sigma_i$, where σ_i are the Pauli

matrices, so

$$\hat{S}_x = \frac{1}{2} \begin{pmatrix} 0 & 1 \\ 1 & 0 \end{pmatrix}, \quad (1.9a)$$

$$\hat{S}_y = \frac{1}{2} \begin{pmatrix} 0 & -i \\ i & 0 \end{pmatrix}, \quad (1.9b)$$

$$\hat{S}_z = \frac{1}{2} \begin{pmatrix} 1 & 0 \\ 0 & -1 \end{pmatrix}. \quad (1.9c)$$

The eigenvalues of $\hat{\mathbf{S}}^2$ are $S(S + 1)$, so

$$\hat{\mathbf{S}}^2 |\phi_{S,m_S}\rangle = S(S + 1) |\phi_{S,m_S}\rangle, \quad (1.10)$$

and the eigenvalues of \hat{S}_z are m_S , so

$$\hat{S}_z |\phi_{S,m_S}\rangle = m_S |\phi_{S,m_S}\rangle, \quad (1.11)$$

where S and m_S are the quantum numbers introduced in Section 1.1, and $|\phi_{S,m_S}\rangle$ are eigenvectors of $\hat{\mathbf{S}}^2$ and \hat{S}_z .

The operators \hat{S}_i ($i = x, y, z$), together with the identity operator $\hat{1} = \begin{pmatrix} 1 & 0 \\ 0 & 1 \end{pmatrix}$, form a complete basis in which a spin- $\frac{1}{2}$ can be described.

It can often be useful to use the raising and lowering operators \hat{S}_+ and \hat{S}_- instead of \hat{S}_x and \hat{S}_y . These are defined as

$$\hat{S}_+ = \hat{S}_x + i\hat{S}_y = \begin{pmatrix} 0 & 1 \\ 0 & 0 \end{pmatrix}, \quad (1.12)$$

$$\hat{S}_- = \hat{S}_x - i\hat{S}_y = \begin{pmatrix} 0 & 0 \\ 1 & 0 \end{pmatrix}. \quad (1.13)$$

To represent the quantum states of a spin- $\frac{1}{2}$ particle, it is convenient to use the orthonormal vectors $|\alpha\rangle = (1, 0)^T$ ('spin up', magnetic moment aligned parallel with external magnetic field) and $|\beta\rangle = (0, 1)^T$ ('spin down', magnetic moment aligned anti-parallel with external magnetic field). These are eigenvectors of the

operator \hat{S}_z , with

$$\hat{S}_z |\alpha\rangle = \frac{1}{2} |\alpha\rangle, \quad (1.14)$$

$$\hat{S}_z |\beta\rangle = -\frac{1}{2} |\beta\rangle. \quad (1.15)$$

For a spin system with more than one spin, the spin angular momentum matrices are constructed by taking Kronecker products of the relevant single-spin matrices \hat{S}_x , \hat{S}_y , \hat{S}_z and the identity matrix $\hat{1}$, and the basis vectors are formed by taking Kronecker products of the single-spin basis vectors $|\alpha\rangle$ and $|\beta\rangle$. For example, for a system comprising one electron coupled to one nucleus, the basis vectors are

$$|\alpha_e \alpha_n\rangle = |\alpha\rangle \otimes |\alpha\rangle = \begin{pmatrix} 1 & 0 & 0 & 0 \end{pmatrix}^T, \quad (1.16a)$$

$$|\alpha_e \beta_n\rangle = |\alpha\rangle \otimes |\beta\rangle = \begin{pmatrix} 0 & 1 & 0 & 0 \end{pmatrix}^T, \quad (1.16b)$$

$$|\beta_e \alpha_n\rangle = |\beta\rangle \otimes |\alpha\rangle = \begin{pmatrix} 0 & 0 & 1 & 0 \end{pmatrix}^T, \quad (1.16c)$$

$$|\beta_e \beta_n\rangle = |\beta\rangle \otimes |\beta\rangle = \begin{pmatrix} 0 & 0 & 0 & 1 \end{pmatrix}^T, \quad (1.16d)$$

and they represent the four possible states of the electron-nucleus spin system, with $|\alpha_e \alpha_n\rangle$ representing a state with both the electron and the nucleus in the state $|\alpha\rangle$, and so on. These basis vectors and the associated matrices will be particularly relevant for the description of dynamic nuclear polarization (DNP) in Chapter 2. A selection of the spin angular momentum matrices for a system comprising one electron and one nucleus are derived in Appendix A.

1.3 An ensemble of spins

Section 1.1 described a single spin in a magnetic field. The state of such a spin is completely indeterminate. However, the central limit theorem states that, even if the state of an individual particle is unknown, for an ensemble of such particles the average state can be known very accurately [13]. NMR is performed on very large ensembles of spins, and the results of NMR experiments are due to the action of these spin ensembles. In this section such an ensemble of spins is considered. The density operator, which contains all of the relevant statistical information of an spin ensemble, will be defined, and the equation of motion for the density operator

will be derived.

1.3.1 Density operator

The quantum state of an individual particle such as an electron can be represented by a wave-function, which describes the position, momentum, and spin state of the particle. Here we consider only spin states of particles, and the terms ‘quantum state’ and ‘eigenstate’ are used henceforth to describe spin states. The spin state of a particle can be represented by the spin state vector $|\psi\rangle$, which can be written as a linear combination of eigenvectors $|\phi_n\rangle$, each representing a different spin eigenstate of the system,

$$|\psi\rangle = \sum_{n=1}^N c_n |\phi_n\rangle, \quad (1.17)$$

where N is the number of spin eigenstates of the system, and the complex expansion coefficient $c_n = \langle\phi_n|\psi\rangle$ is the probability amplitude for state n . The Hermitian conjugate of $|\psi\rangle$ is given by

$$\langle\psi| = \sum_{n=1}^N c_n^* \langle\phi_n|, \quad (1.18)$$

where $c_n^* = \langle\psi|\phi_n\rangle$.

A property A that is measured in an experiment is represented by an operator \hat{A} . The expectation value of \hat{A} , which represents the outcome of the experiment, is given by

$$\begin{aligned} \langle\hat{A}\rangle &= \langle\psi|\hat{A}|\psi\rangle \\ &= \sum_{n=1}^N \sum_{m=1}^M c_m c_n^* \langle\phi_n|\hat{A}|\phi_m\rangle \\ &= \sum_{n=1}^N \sum_{m=1}^M \langle\phi_m|\psi\rangle \langle\psi|\phi_n\rangle \langle\phi_n|\hat{A}|\phi_m\rangle \\ &= \sum_{m=1}^M \langle\phi_m|\psi\rangle \langle\psi|\hat{A}|\phi_m\rangle \\ &= \text{Tr}(|\psi\rangle\langle\psi|\hat{A}). \end{aligned} \quad (1.19)$$

$|\psi\rangle\langle\psi|$ is called a *density operator*, in this case for a single spin. For a large ensemble of spins, it is common to use the ensemble average of properties of the

spin system, denoted by an overbar. The *ensemble average density operator* $\hat{\rho}$ is then given by

$$\hat{\rho} = \overline{|\psi\rangle\langle\psi|}. \quad (1.20)$$

$\hat{\rho}$ is usually just called the density operator, where the overbar is often omitted but the ensemble average is implied. $\hat{\rho}$ can be represented by a *density matrix*,* with elements ρ_{nm} given by

$$\rho_{nm} = \langle\phi_n|\hat{\rho}|\phi_m\rangle = \langle\phi_n|\psi\rangle\langle\psi|\phi_m\rangle = c_n c_m^*. \quad (1.21)$$

The expectation value of \hat{A} can then be written in terms of the density operator as

$$\langle\hat{A}\rangle = \text{Tr}(\hat{\rho}\hat{A}). \quad (1.22)$$

Example: a system with two quantum states

As an example, consider a system with two possible eigenstates represented by the eigenvectors $|\phi_1\rangle$ and $|\phi_2\rangle$, with

$$|\psi\rangle = c_1 |\phi_1\rangle + c_2 |\phi_2\rangle. \quad (1.23)$$

The expectation value of operator \hat{A} is

$$\begin{aligned} \langle\hat{A}\rangle &= \langle\psi|\hat{A}|\psi\rangle \\ &= c_1^* c_1 \langle\phi_1|\hat{A}|\phi_1\rangle + c_1^* c_2 \langle\phi_1|\hat{A}|\phi_2\rangle + c_2^* c_1 \langle\phi_2|\hat{A}|\phi_1\rangle + c_2^* c_2 \langle\phi_2|\hat{A}|\phi_2\rangle \\ &= \text{Tr} \left(\begin{pmatrix} c_1^* c_1 & c_2^* c_1 \\ c_1^* c_2 & c_2^* c_2 \end{pmatrix} \begin{pmatrix} A_{11} & A_{12} \\ A_{21} & A_{22} \end{pmatrix} \right) \\ &= \text{Tr}(\hat{\rho}\hat{A}) \end{aligned} \quad (1.24)$$

where $A_{nm} = \langle\phi_n|\hat{A}|\phi_m\rangle$ are the matrix elements of \hat{A} .

In this two-state system, the density operator $\hat{\rho}$ is given by the 2×2 matrix

$$\hat{\rho} = \begin{pmatrix} c_1^* c_1 & c_2^* c_1 \\ c_1^* c_2 & c_2^* c_2 \end{pmatrix}. \quad (1.25)$$

*The terms density operator and density matrix are often used interchangeably.

Populations and coherences

The probability amplitudes c_n can be written in terms of real amplitudes r_n and phases φ_n , so

$$c_n = r_n e^{i\varphi_n}. \quad (1.26)$$

Using this definition, the density matrix for the two-state system can be written

$$\hat{\rho} = \begin{pmatrix} r_1^2 & r_2 r_1 e^{i(\varphi_1 - \varphi_2)} \\ r_1 r_2 e^{i(\varphi_2 - \varphi_1)} & r_2^2 \end{pmatrix}. \quad (1.27)$$

The diagonal elements of $\hat{\rho}$ are $r_n^2 = |c_n|^2$, the populations of eigenstates $|\phi_n\rangle$. The off-diagonal elements of $\hat{\rho}$ are coherences between eigenstates $|\phi_n\rangle$ and $|\phi_m\rangle$ ($n \neq m$). This can be seen by noting that the off-diagonal elements of $\hat{\rho}$ depend on the phase difference $(\varphi_n - \varphi_m)$ between eigenstates $|\phi_n\rangle$ and $|\phi_m\rangle$. If there is a coherence between eigenstates $|\phi_n\rangle$ and $|\phi_m\rangle$, then the ensemble average of $(\varphi_n - \varphi_m)$ will have a definite value, so the off-diagonal elements will be non-zero, reflecting this coherence. On the other hand, if there is no coherence between eigenstates $|\phi_n\rangle$ and $|\phi_m\rangle$, then the phase difference $(\varphi_n - \varphi_m)$ will vary randomly across the system, and the off-diagonal elements will average to zero.

The density matrix or density operator contains all of the statistical information about the spin system, namely the populations of eigenstates and coherences between eigenstates. It does not contain information about individual spins, but does contain all of the information regarding the average quantities across an ensemble of spins. It can be said to completely describe the spin state of the spin system.

Density operator and magnetization

It is useful to relate the density matrix to the spin operators \hat{S}_x , \hat{S}_y , and \hat{S}_z defined in eqs (1.9). A density matrix $\hat{\rho} \propto \hat{S}_z = \frac{1}{2} \begin{pmatrix} 1 & 0 \\ 0 & -1 \end{pmatrix}$ represents z -magnetization. The diagonal elements are unequal, indicating a difference in populations of the two states, while the off-diagonal elements are zero, indicating no coherence between the states. On the other hand, a density matrix $\hat{\rho} \propto \hat{S}_x = \frac{1}{2} \begin{pmatrix} 0 & 1 \\ 1 & 0 \end{pmatrix}$ or $\hat{\rho} \propto \hat{S}_y = \frac{1}{2} \begin{pmatrix} 0 & -i \\ i & 0 \end{pmatrix}$ represents x - or y -magnetization respectively. In either case the diagonal elements are equal, indicating equal populations of the two states, while the off-diagonal elements are non-zero, indicating coherence between the states.

Thermal equilibrium density operator

For a system of spin- $\frac{1}{2}$ particles at thermal equilibrium, the populations of the two states are given by a Boltzmann distribution. The populations of states $m_S = \pm\frac{1}{2}$, denoted $p_{\pm\frac{1}{2}}$, are derived later in this chapter, and are given in eq (1.70). The thermal equilibrium density matrix is then given by

$$\begin{aligned}\rho^{\text{eq}} &= \begin{pmatrix} p_{-\frac{1}{2}} & 0 \\ 0 & p_{+\frac{1}{2}} \end{pmatrix} \\ &= \frac{1}{Z} \begin{pmatrix} \exp\left(+\frac{g_e\mu_B B_0}{2k_B T}\right) & 0 \\ 0 & \exp\left(-\frac{g_e\mu_B B_0}{2k_B T}\right) \end{pmatrix},\end{aligned}\quad (1.28)$$

where Z is the partition function of the system, defined in eq (1.69). In the high-temperature approximation ($\frac{g_e\mu_B B_0}{2k_B T} \ll 1$), eq (1.28) can be approximated to

$$\begin{aligned}\rho^{\text{eq}} &\approx \frac{1}{2} \begin{pmatrix} 1 + \frac{g_e\mu_B B_0}{2k_B T} & 0 \\ 0 & 1 - \frac{g_e\mu_B B_0}{2k_B T} \end{pmatrix} \\ &\approx \frac{1}{2} \left(\hat{1} - \left(\frac{g_e\mu_B B_0}{k_B T} \right) \hat{S}_z \right).\end{aligned}\quad (1.29)$$

The diagonal elements are non-zero and unequal, indicating non-zero z -magnetization, while the off-diagonal elements are zero, indicating no coherence between the states, and zero x - and y -magnetization.

1.3.2 Liouville-von Neumann equation

The evolution in time of the state of an individual particle is governed by its equation of motion, the time-dependent Schrödinger equation,

$$i\hbar |\dot{\psi}\rangle = \hat{\mathcal{H}} |\psi\rangle, \quad (1.30)$$

where $\hat{\mathcal{H}}$ is an operator called the Hamiltonian, and $|\dot{\psi}\rangle = \frac{d|\psi\rangle}{dt}$. The eigenvalues of the Hamiltonian are the energy levels of the system. Dividing both sides of eq (1.30) by $i\hbar$, and defining

$$\hat{H} = \frac{\hat{\mathcal{H}}}{\hbar}, \quad (1.31)$$

where \hat{H} is the Hamiltonian in units of angular frequency, eq (1.30) can now be written

$$\dot{|\psi\rangle} = -i\hat{H}|\psi\rangle. \quad (1.32)$$

For an ensemble of spins, we are interested in the time-evolution of the density matrix $|\psi\rangle\langle\psi|$. Differentiating $|\psi\rangle\langle\psi|$ with respect to time and substituting for $\dot{|\psi\rangle}$ and $\dot{\langle\psi|}$ using eq (1.32) and its Hermitian conjugate, we get

$$\begin{aligned} \frac{d}{dt}(|\psi\rangle\langle\psi|) &= |\dot{\psi}\rangle\langle\psi| + |\psi\rangle\langle\dot{\psi}| \\ &= -i\hat{H}|\psi\rangle\langle\psi| + i|\psi\rangle\langle\psi|\hat{H} \\ &= -i[\hat{H},|\psi\rangle\langle\psi|]. \end{aligned} \quad (1.33)$$

Equation (1.33) is linear in $|\psi\rangle\langle\psi|$, so therefore it holds for linear combinations of $|\psi\rangle\langle\psi|$, including an ensemble average, so we can write it in terms of $\hat{\rho}(t)$,

$$\frac{d}{dt}\hat{\rho}(t) = -i[\hat{H},\hat{\rho}(t)]. \quad (1.34)$$

Equation (1.34) is called the Liouville-von Neumann equation. It governs the evolution in time of the density matrix under the influence of a Hamiltonian \hat{H} . If the Hamiltonian is time-independent, the general solution to the Liouville-von Neumann equation is

$$\hat{\rho}(t) = \hat{U}(t)\hat{\rho}_0\hat{U}^\dagger(t) = e^{-i\hat{H}t}\hat{\rho}_0e^{i\hat{H}t}, \quad (1.35)$$

where $\hat{\rho}_0 = \hat{\rho}(0)$ is the density matrix at time $t = 0$, and $\hat{U}(t) = e^{-i\hat{H}t}$ is called a *propagator*.

Equation (1.34) was derived without considering relaxation, and it is only valid if relaxation can be neglected. If relaxation is considered, an extra term needs to be added, and the Liouville-von Neumann equation then becomes

$$\frac{d}{dt}\hat{\rho}(t) = -i[\hat{H},\hat{\rho}(t)] + \hat{\Gamma}(\hat{\rho}(t) - \rho^{\text{eq}}), \quad (1.36)$$

where $\hat{\Gamma}$ is the relaxation superoperator.

1.4 Hamiltonians

Hamiltonians govern the evolution in time of the density matrix. They are operators which contain information about interactions of spins with other spins and with the external magnetic field. The overall spin Hamiltonian \hat{H} is made up of several independent Hamiltonians, each describing a different property of the spin system. It can be expressed as

$$\hat{H} = \hat{H}_Z + \hat{H}_{\text{ZFS}} + \hat{H}_{\text{hf}} + \hat{H}_d + \hat{H}_{\text{NQ}} + \hat{H}_1 + \dots \quad (1.37)$$

where the Hamiltonians included in this equation represent the Zeeman interaction (\hat{H}_Z), zero-field splitting (\hat{H}_{ZFS}), hyperfine interaction (\hat{H}_{hf}), dipole-dipole interaction (\hat{H}_d), nuclear quadrupolar interaction (\hat{H}_{NQ}), and excitation (\hat{H}_1), respectively. Each of these Hamiltonians, aside from the zero-field splitting and nuclear quadrupolar interaction, will be described individually in this section. Other Hamiltonians describing other interactions may need to be included in certain situations. The overall spin Hamiltonian \hat{H} describes the different quantum states of the spin system: its eigenstates are these quantum states and the associated eigenvalues are the energy levels (in angular frequency units) of these states.

Hamiltonians are presented here in a very general form, for a system of N_e electrons (labelled a, b) and N_n nuclei (labelled m, n) in a static field \mathbf{B}_0 . There are some situations when the Hamiltonian can be simplified. For example, it is often the case that a radical concentration is low enough that coupling between electrons can be neglected and it is sufficient to consider just one electron ($N_e = 1$).

1.4.1 Zeeman interaction

The Zeeman interaction is the interaction between a spin and a static magnetic field. The nuclear and electron Zeeman interaction Hamiltonians are similar in principle, but are described separately. The nuclear Zeeman interaction is usually defined in terms of the gyromagnetic ratio of a nucleus, while the electron Zeeman interaction is usually defined in terms of the electron g -matrix.

Nuclear Zeeman interaction

The Hamiltonian for the interaction between nuclei and a static magnetic field \mathbf{B}_0 is given by

$$\hat{H}_{\text{NZ}} = - \sum_{m=1}^{N_n} \gamma_{n,m} \mathbf{B}_0^T \hat{\mathbf{I}}_m, \quad (1.38)$$

where $\gamma_{n,m}$ and $\hat{\mathbf{I}}_m$ are the gyromagnetic ratio and spin matrix for nucleus m , respectively. If $\mathbf{B}_0 = (0, 0, B_0)^T$ this simplifies to

$$\begin{aligned} \hat{H}_{\text{NZ}} &= -B_0 \sum_{m=1}^{N_n} \gamma_{n,m} \hat{I}_{z,m} \\ &= \sum_{m=1}^{N_n} \omega_{n,m} \hat{I}_{z,m}, \end{aligned} \quad (1.39)$$

where $\omega_{n,m}$ is the resonance frequency of nucleus m .

Electron Zeeman interaction

The Hamiltonian for the interaction between electrons and a static magnetic field \mathbf{B}_0 is given by

$$\hat{H}_{\text{EZ}} = \frac{\mu_B}{\hbar} \sum_{a=1}^{N_e} \mathbf{B}_0^T \mathbf{g}_a \hat{\mathbf{S}}_a, \quad (1.40)$$

where \mathbf{g}_a and $\hat{\mathbf{S}}_a$ are the g -matrix and spin matrix for electron a respectively. The free electron g -factor was introduced as a scalar g_e in Section 1.1. However, for most systems the g -factor is anisotropic, and is therefore represented as a 3×3 matrix \mathbf{g}_a rather than a scalar. \mathbf{g}_a can be expressed in its principal axis system (PAS) as

$$\mathbf{g}_a = \begin{pmatrix} g_x \\ & g_y \\ & & g_z \end{pmatrix}_a. \quad (1.41)$$

The energy levels of the electron Zeeman interaction are given by the eigenvalues, or expectation values, of \hat{H}_{EZ} ,

$$\langle \hat{H}_{\text{EZ}} \rangle = \frac{\mu_B B_0}{\hbar} \sum_{a=1}^{N_e} g_a m_{S_a}, \quad (1.42)$$

where $m_{S_a} = \pm \frac{1}{2}$, and g_a is an effective g -factor, given by

$$\begin{aligned} g_a &= (\mathbf{n}^T \mathbf{g} \mathbf{g}^T \mathbf{n})_a^{\frac{1}{2}} \\ &= (n_x^2 g_x^2 + n_y^2 g_y^2 + n_z^2 g_z^2)_a^{\frac{1}{2}}, \end{aligned} \quad (1.43)$$

where $\mathbf{n} = \frac{\mathbf{B}_0}{B_0} = (n_x, n_y, n_z)^T$ is a unit vector along \mathbf{B}_0 . The energy levels given in eq (1.42) are derived in Appendix B.

If g -anisotropy can be ignored, and if $\mathbf{B}_0 = (0, 0, B_0)^T$, then the electron Zeeman interaction simplifies to

$$\begin{aligned} \hat{H}_{EZ} &= -\frac{\mu_B B_0}{\hbar} \sum_{a=1}^{N_e} g_{e,a} \hat{S}_{z,a} \\ &= \sum_{a=1}^{N_e} \omega_{e,a} \hat{S}_{z,a}, \end{aligned} \quad (1.44)$$

where $\omega_{e,a}$ is the resonance frequency of electron a .

1.4.2 Hyperfine interaction

The interaction between a single electron (labelled a) and a single nucleus (labelled m), called the hyperfine interaction (hfi), is made up of contributions from two different mechanisms. The first of these, the *Fermi contact interaction*, is given by

$$\hat{H}_F = \frac{2}{3} \frac{\mu_0}{\hbar} g_a \mu_B g_m \mu_N |\psi(0)|^2 \hat{\mathbf{S}}_a \cdot \hat{\mathbf{I}}_m, \quad (1.45)$$

where $|\psi(0)|^2$ is the probability density of the electron at the nucleus [14].

The second contribution is a *dipole-dipole interaction*, given by

$$\hat{H}_{DD} = \frac{\mu_0}{4\pi\hbar} g_a \mu_B g_m \mu_N \left(\frac{\hat{\mathbf{S}}_a \cdot \hat{\mathbf{I}}_m}{r_{am}^3} - \frac{3(\hat{\mathbf{S}}_a \cdot \mathbf{r}_{am})(\hat{\mathbf{I}}_m \cdot \mathbf{r}_{am})}{r_{am}^5} \right) \quad (1.46)$$

where \mathbf{r}_{am} is the vector connecting the electron with the nucleus, and $r_{am} = |\mathbf{r}_{am}|$ [14].

The Hamiltonian for the hyperfine interaction is the sum of the Hamiltonians for the Fermi contact interaction \hat{H}_F and the electron-nuclear dipole-dipole interaction \hat{H}_{DD} , summed over all nuclei and electrons. For distant nuclei, the probability density of the electron at the nucleus is typically very small, so the

Fermi contact interaction can be neglected, and the hyperfine interaction is assumed to be a purely dipolar interaction. This approximation is assumed in the following description.

The hyperfine interaction Hamiltonian \hat{H}_{hf} can be concisely expressed using a hyperfine interaction matrix \mathbf{A}_{am} as

$$\hat{H}_{\text{hf}} = \sum_{a=1}^{N_e} \sum_{m=1}^{N_n} \hat{\mathbf{S}}_a^T \mathbf{A}_{am} \hat{\mathbf{I}}_m, \quad (1.47)$$

where

$$\mathbf{A}_{am} = \begin{pmatrix} A_{xx} & A_{xy} & A_{xz} \\ A_{yx} & A_{yy} & A_{yz} \\ A_{zx} & A_{zy} & A_{zz} \end{pmatrix}_{am}. \quad (1.48)$$

Expansion of the Hamiltonian results in nine terms for each electron-nucleus pair, given by $(\hat{S}_i A_{ij} \hat{I}_j)_{am}$, where $i, j = x, y, z$. At high magnetic fields, the electron Zeeman interaction is much larger than the other interactions, so only terms which commute with the electron Zeeman Hamiltonian must be retained. These are the terms containing \hat{S}_z , so eq (1.47) can be written

$$\hat{H}_{\text{hf}} = \sum_{a=1}^{N_e} \sum_{m=1}^{N_n} \left(\hat{S}_{z,a} A_{zz,am} \hat{I}_{z,m} + \hat{S}_{z,a} (A_{zx,am} \hat{I}_{x,m} + A_{zy,am} \hat{I}_{y,m}) \right). \quad (1.49)$$

The hyperfine Hamiltonian is often written in terms of raising and lowering operators (with a subscript \pm) rather than x and y components. Using this notation, \hat{H}_{hf} is written

$$\hat{H}_{\text{hf}} = \sum_{a=1}^{N_e} \sum_{m=1}^{N_n} \left(A_{am} \hat{S}_{z,a} \hat{I}_{z,m} + \frac{1}{2} (B_{+,am} \hat{S}_{z,a} \hat{I}_{+,m} + B_{-,am} \hat{S}_{z,a} \hat{I}_{-,m}) \right), \quad (1.50)$$

where A_{am} and $B_{\pm,am}$ are the secular and pseudo-secular hyperfine interaction constants respectively, and are given by

$$A_{am} = -\frac{\mu_0}{4\pi\hbar} \frac{g_a \mu_B g_m \mu_N}{r_{am}^3} (1 - 3 \cos^2 \theta_{am}), \quad (1.51)$$

$$B_{\pm,am} = \frac{3}{2} \frac{\mu_0}{4\pi\hbar} \frac{g_a \mu_B g_m \mu_N}{r_{am}^3} \sin \theta_{am} \cos \theta_{am} e^{\mp i\phi_{am}}, \quad (1.52)$$

where θ_{am} and ϕ_{am} are the polar and azimuthal angles of \mathbf{r}_{am} respectively [15, 16]. It is often more convenient to express the hyperfine interaction constants in terms

of gyromagnetic ratios, rather than g -factors. In this notation, the hyperfine interaction constants are

$$A_{am} = \frac{\mu_0 \hbar}{4\pi} \frac{\gamma_a \gamma_m}{r_{am}^3} (1 - 3 \cos^2 \theta_{am}), \quad (1.53)$$

$$B_{\pm,am} = -\frac{3}{2} \frac{\mu_0 \hbar}{4\pi} \frac{\gamma_a \gamma_m}{r_{am}^3} \sin \theta_{am} \cos \theta_{ame} e^{\mp i\phi_{am}}. \quad (1.54)$$

1.4.3 Dipole-dipole interactions

The dipole-dipole interactions between pairs of electrons and pairs of nuclei are in principle very similar. They are introduced separately in this section, however, because they are usually expressed differently. In EPR it is more common to express interactions in terms of g -factors, while in NMR interactions are usually expressed in terms of gyromagnetic ratios. These conventions are followed here

Electron dipole-dipole interaction

The Hamiltonian for the dipole-dipole interaction between electrons can be written as

$$\begin{aligned} \hat{H}_{ee} &= \sum_{a < b} \hat{\mathbf{S}}_a^T \mathbf{D}_{ab} \hat{\mathbf{S}}_b \\ &= \frac{\mu_0 \mu_B^2}{4\pi \hbar} \sum_{a < b} g_a g_b \left(\frac{\hat{\mathbf{S}}_a \cdot \hat{\mathbf{S}}_b}{r_{ab}^3} - \frac{3(\hat{\mathbf{S}}_a \cdot \mathbf{r}_{ab})(\hat{\mathbf{S}}_b \cdot \mathbf{r}_{ab})}{r_{ab}^5} \right), \end{aligned} \quad (1.55)$$

where \mathbf{D}_{ab} is the dipolar coupling matrix, $\hat{\mathbf{S}}_{a,b}$ and $g_{a,b}$ are the spin matrices and g -values of the two electrons respectively, \mathbf{r}_{ab} is the vector connecting electrons a and b , and $r_{ab} = |\mathbf{r}_{ab}|$.

In the high-field approximation, and if the anisotropy of the g -values is small enough to be neglected, the dipolar coupling matrix can be written

$$\mathbf{D}_{ab} = \frac{\mu_0 \mu_B^2 g_a g_b}{4\pi \hbar r_{ab}^3} \begin{pmatrix} 1 & & \\ & 1 & \\ & & -2 \end{pmatrix}, \quad (1.56)$$

and eq (1.55) can be written

$$\hat{H}_{ee} = \sum_{a < b} D_{ab} \left(\hat{\mathbf{S}}_a \cdot \hat{\mathbf{S}}_b - 3\hat{S}_{z,a}\hat{S}_{z,b} \right), \quad (1.57)$$

where

$$D_{ab} = \frac{\mu_0}{4\pi\hbar} \frac{\mu_B^2 g_a g_b}{r_{ab}^3} \quad (1.58)$$

is the dipolar interaction coefficient between the electron spins [14].

Nuclear dipole-dipole interaction

The Hamiltonian for the dipole-dipole interaction between nuclei is defined analogously to the electron dipolar interaction, and its Hamiltonian can be written

$$\begin{aligned} \hat{H}_{nn} &= \sum_{m < n} \hat{\mathbf{I}}_m^T \mathbf{d}_{mn} \hat{\mathbf{I}}_n \\ &= \frac{\mu_0 \hbar}{4\pi} \sum_{m < n} \gamma_m \gamma_n \left(\frac{\hat{\mathbf{I}}_m \cdot \hat{\mathbf{I}}_n}{r_{mn}^3} - \frac{3(\hat{\mathbf{I}}_m \cdot \mathbf{r}_{mn})(\hat{\mathbf{I}}_n \cdot \mathbf{r}_{mn})}{r_{mn}^5} \right) \end{aligned} \quad (1.59)$$

where \mathbf{d}_{mn} is the dipolar coupling matrix, $\hat{\mathbf{I}}_{m,n}$ and $\gamma_{m,n}$ are the spin matrices and gyromagnetic ratios of the two nuclei respectively, \mathbf{r}_{mn} is the vector connecting nuclei m and n , and $r_{nm} = |\mathbf{r}_{nm}|$.

In the high-field approximation, the non-secular part of the dipole-dipole Hamiltonian can usually be ignored, and the Hamiltonian is then given by

$$\hat{H}_{nn} = \sum_{m < n} d_{mn} \frac{1}{2} (3 \cos^2 \theta_{mn} - 1) \left(\hat{\mathbf{I}}_m \cdot \hat{\mathbf{I}}_n - 3\hat{I}_{z,m}\hat{I}_{z,n} \right), \quad (1.60)$$

where θ_{mn} is the angle between \mathbf{r}_{mn} and \mathbf{B}_0 , and

$$d_{mn} = \frac{\mu_0 \hbar}{4\pi} \frac{\gamma_m \gamma_n}{r_{mn}^3} \quad (1.61)$$

is the dipolar coupling coefficient [17]. In a heteronuclear spin system (m and n are not identical), weak coupling between the spins means that all terms involving $\hat{I}_{x,mn}$ and $\hat{I}_{y,mn}$ can be dropped, and the Hamiltonian simplifies further, [17]

$$\hat{H}_{nn} = \sum_{m < n} -d_{mn} (3 \cos^2 \theta_{mn} - 1) \hat{I}_{z,m}\hat{I}_{z,n}. \quad (1.62)$$

1.4.4 Excitation Hamiltonians

A spin ensemble can be manipulated by using a magnetic field $\mathbf{B}_1(t)$ oscillating at a frequency close to the Larmor frequency. For EPR this frequency is typically in the microwave (mw) region of the electromagnetic spectrum, while for NMR the frequency is typically in the radio-frequency (rf) region. This section describes the excitation Hamiltonian using the notation for an EPR system, with $\mathbf{B}_1(t)$ oscillating at a frequency ω_{mw} . An equivalent set of equations could be used to describe an rf excitation Hamiltonian for an NMR system.

The mw excitation Hamiltonian is given by

$$\hat{H}_{\text{mw}} = \frac{\mu_B}{\hbar} \sum_{a=1}^{N_e} \mathbf{B}_1^T(t) \mathbf{g}_a \hat{\mathbf{S}}_a, \quad (1.63)$$

where $\hat{\mathbf{S}}_a$ and \mathbf{g}_a are the spin matrix and g -matrix of an electron respectively, $\mathbf{B}_1(t) = 2(B_1 \cos(\omega_{\text{mw}}t + \phi), 0, 0)^T$ is arbitrarily defined to be along the x -axis without loss of generality, and ϕ is the phase of the oscillations.

It is often convenient to consider excitation by a mw field in a reference frame which rotates about the z -axis at a frequency ω_{mw} . In this frame, called the *rotating frame*, the time dependence of the mw field is removed, and its magnetic field can be written

$$\mathbf{B}_1^r = B_1 (\cos(\phi), \sin(\phi), 0)^T, \quad (1.64)$$

where the superscript r indicates the rotating frame. The concept of the rotating frame will be described in more detail in Section 1.5.3. If we choose a field with a phase $\phi = 0$, then \mathbf{B}_1^r simplifies to

$$\mathbf{B}_1^r = (B_1, 0, 0)^T. \quad (1.65)$$

If anisotropy of the g -value can be neglected, eq (1.63) can then be written

$$\hat{H}_{\text{mw}} = \sum_{a=1}^{N_e} \omega_{1,a} \hat{S}_{x,a}, \quad (1.66)$$

where $\omega_{1,a} = \frac{\mu_B B_1 g_a}{\hbar}$ is the *nutation frequency* of the microwave field, and is used to define its strength.

To illustrate the effect of a strong mw pulse on the density matrix, consider an ensemble of identical spins initially at thermal equilibrium. The initial density operator of such a system can be represented by \hat{S}_z . Neglecting all other Hamiltonians, which are assumed to act over much longer time-scales than the mw Hamiltonian,* it is straightforward to calculate the density matrix in the rotating frame as a function of time under the influence of the mw Hamiltonian, by using the solution to the Liouville-von Neumann equation, eq (1.35),

$$\begin{aligned}\hat{\rho}(t) &= e^{-i\hat{H}_{\text{mw}}t} \hat{S}_z e^{i\hat{H}_{\text{mw}}t} \\ &= \frac{1}{2} \begin{pmatrix} \cos(\omega_1 t) & i \sin(\omega_1 t) \\ -i \sin(\omega_1 t) & -\cos(\omega_1 t) \end{pmatrix} \\ &= \hat{S}_z \cos(\omega_1 t) - \hat{S}_y \sin(\omega_1 t).\end{aligned}\quad (1.67)$$

The full calculation of $\hat{\rho}(t)$ is given in Appendix C. The first term in eq (1.67), associated with the diagonal elements of $\hat{\rho}(t)$, shows that the mw field excites transitions between the states $|\alpha\rangle$ and $|\beta\rangle$, thereby changing the populations of these states. Likewise, the second term in eq (1.67), associated with the off-diagonal elements of $\hat{\rho}(t)$, shows that the mw field generates coherences between the states $|\alpha\rangle$ and $|\beta\rangle$ (see eq (1.27)).

1.5 Macroscopic magnetization

1.5.1 Polarization

An alternative to the quantum mechanical description of a spin system presented so far in this chapter is to consider the macroscopic properties of the spin ensemble. This can be a useful picture when visualizing relaxation or the effect of microwave and radio-frequency pulses.

To begin with we derive an expression for the thermal equilibrium polarization of a spin- $\frac{1}{2}$ ensemble. The normalized thermal equilibrium populations p of the

*The validity of this assumption must be confirmed individually for any particular Hamiltonian.

quantum states, labelled m_S , are given by a Boltzmann distribution,*

$$p_{m_S} = \frac{\exp\left(-\frac{E_{m_S}}{k_B T}\right)}{Z}, \quad (1.68)$$

where k_B is the Boltzmann constant, T is the temperature, and Z is the partition function of the system,

$$Z = \sum_{m_S} \exp\left(-\frac{E_{m_S}}{k_B T}\right). \quad (1.69)$$

For electrons, the energies of the $m_S = \pm \frac{1}{2}$ states are given by eq (1.5), so the normalized populations are

$$p_{\pm \frac{1}{2}} = \frac{1}{Z} \exp\left(\pm \frac{\gamma_e \hbar B_0}{2k_B T}\right) = \frac{1}{Z} \exp\left(\mp \frac{g_e \mu_B B_0}{2k_B T}\right). \quad (1.70)$$

For a two-state spin system, polarization is defined as the relative population difference between the lower energy state and the upper energy state. For electrons, the polarization P_e is defined

$$\begin{aligned} P_e &= p_{-\frac{1}{2}} - p_{+\frac{1}{2}} \\ &= \frac{\exp\left(-\frac{\gamma_e \hbar B_0}{2k_B T}\right) - \exp\left(+\frac{\gamma_e \hbar B_0}{2k_B T}\right)}{\exp\left(-\frac{\gamma_e \hbar B_0}{2k_B T}\right) + \exp\left(+\frac{\gamma_e \hbar B_0}{2k_B T}\right)} \\ &= \tanh\left(-\frac{\gamma_e \hbar B_0}{2k_B T}\right). \end{aligned} \quad (1.71)$$

P_e is positive since since γ_e is negative. For spin- $\frac{1}{2}$ nuclei, the polarization P_n is defined analogously,

$$P_n = \tanh\left(\frac{|\gamma_n| \hbar B_0}{2k_B T}\right). \quad (1.72)$$

Note that P_n is defined to be positive, irrespective of the sign of γ_n .

Thermal equilibrium polarizations for electrons, hydrogen nuclei and carbon-13 nuclei are plotted as a function of temperature and magnetic field in Figure 1.2. Thermal equilibrium polarizations for these spins under typical liquid-state NMR conditions and typical solid-state EPR and dynamic nuclear polarization (DNP) conditions are given in Table 1.1.

*Normalization $\implies \sum_{m_S} p_{m_S} = 1$.

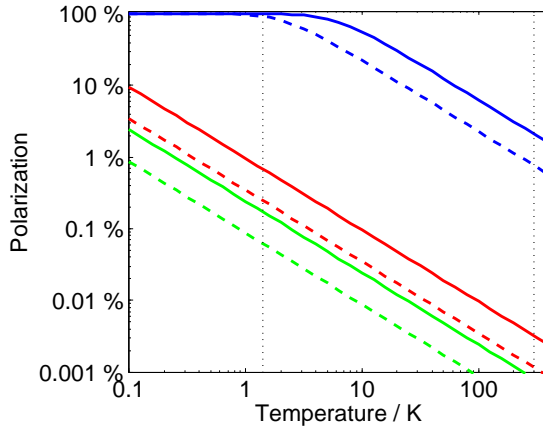


Figure 1.2: Polarizations of spin- $\frac{1}{2}$ systems as a function of temperature, with external magnetic fields $B_0 = 9.4$ T and $B_0 = 3.4$ T. Blue: electrons. Red: ^1H nuclei. Green: ^{13}C nuclei. Solid lines: $B_0 = 9.4$ T. Dashed lines: $B_0 = 3.4$ T. Dotted black lines indicate temperatures of 1.4 K and 300 K. Adapted from [16].

Another useful property of a spin ensemble is its magnetization \mathbf{M} , which can be defined as

$$\begin{aligned} \mathbf{M} &= \sum_{a=1}^{N_e} \mathbf{\mu}_{S,a} \\ &= N_e \bar{\mathbf{\mu}}_S, \end{aligned} \quad (1.73)$$

where $\mathbf{\mu}_S$ is the magnetic dipole moment of an electron, N_e is the number of electrons, and $\bar{\mathbf{\mu}}_S$ is the average magnetic dipole moment of the electrons in the ensemble. When a system is at thermal equilibrium, the magnetization is the thermal equilibrium magnetization,

$$\mathbf{M}_0 = (0, 0, M_0)^T, \quad (1.74)$$

	$B_0 = 9.4$ T, $T = 300$ K	$B_0 = 3.4$ T, $T = 1.4$ K
e	0.021	0.93
^1H	3.2×10^{-5}	2.5×10^{-3}
^{13}C	8.1×10^{-6}	6.2×10^{-4}

Table 1.1: Thermal equilibrium polarizations for electrons, hydrogen nuclei and carbon-13 nuclei under typical liquid-state NMR conditions ($B_0 = 9.4$ T, $T = 300$ K) and typical solid-state EPR and DNP conditions ($B_0 = 3.4$ T, $T = 1.4$ K). Adapted from [15].

where $M_0 = |\mathbf{M}_0|$.

In this section, the behaviour of the macroscopic magnetization \mathbf{M} in a magnetic field will be described. Since \mathbf{M} is proportional to the average magnetic dipole moment $\bar{\mathbf{p}}_S$, this is equivalent to considering the behaviour of a classical magnetic dipole moment.

1.5.2 Spin precession

A magnetic dipole moment $\bar{\mathbf{p}}_S$ in a magnetic field \mathbf{B}_0 experiences a torque,

$$\boldsymbol{\Gamma} = \bar{\mathbf{p}}_S \times \mathbf{B}_0. \quad (1.75)$$

Since the torque is equivalent to the rate of change of the dipole moment's angular momentum $\hbar\mathbf{S}$, we can write

$$\frac{d\hbar\mathbf{S}}{dt} = \bar{\mathbf{p}}_S \times \mathbf{B}_0 \quad (1.76)$$

Multiplying both sides by γ_e , substituting using eq (1.2), and noting that \mathbf{M} is proportional to $\bar{\mathbf{p}}_S$, we can write

$$\frac{d\mathbf{M}}{dt} = \gamma_e \mathbf{M} \times \mathbf{B}_0. \quad (1.77)$$

If the axes are defined, without loss of generality, such that $\mathbf{B}_0 = (0, 0, B_0)^T$, we can write the components of $\dot{\mathbf{M}}$ explicitly as

$$\dot{M}_x = \gamma_e B_0 M_y, \quad (1.78a)$$

$$\dot{M}_y = -\gamma_e B_0 M_x, \quad (1.78b)$$

$$\dot{M}_z = 0, \quad (1.78c)$$

where M_x , M_y and M_z are the cartesian components of \mathbf{M} . These equations describe the precession of \mathbf{M} around \mathbf{B}_0 . The solution to eqs (1.78) is

$$\mathbf{M} = \begin{pmatrix} M_{xy} \cos(\omega_0 t + \phi) \\ M_{xy} \sin(\omega_0 t + \phi) \\ M_z \end{pmatrix}, \quad (1.79)$$

where $M_{xy} = |M_x| = |M_y|$ is the transverse component of \mathbf{M} , and M_z , the longitudinal component of \mathbf{M} , is time independent. ω_0 and ϕ are the frequency and phase of the precession, with

$$\omega_0 = -\gamma_e B_0. \quad (1.80)$$

Comparing eq (1.80) with eq (1.7), it can be seen that the precession frequency ω_0 is equivalent to the Larmor frequency, or resonance frequency, defined in Section 1.1.

1.5.3 Excitation

As described in Section 1.4.4, a spin ensemble can be manipulated by using a magnetic field \mathbf{B}_1 oscillating at a frequency close to the Larmor frequency. \mathbf{B}_1 is often called the mw field in EPR or the rf field in NMR. The axes are defined, without loss of generality, such that \mathbf{B}_1 is along the x -direction. It is given by

$$\mathbf{B}_1 = 2(B_1 \cos(\omega_{\text{mw}}t + \phi), 0, 0)^T, \quad (1.81)$$

where $2B_1$, ω_{mw} and ϕ are the amplitude, frequency and phase of the field.* \mathbf{B}_1 can be decomposed into two counter-rotating fields,

$$\mathbf{B}_1^\pm = B_1 (\cos(\omega_{\text{mw}}t + \phi), \pm \sin(\omega_{\text{mw}}t + \phi), 0)^T. \quad (1.82)$$

\mathbf{B}_1^- rotates in the opposite sense to the electron spins and can be ignored, so only \mathbf{B}_1^+ , which rotates in the same sense as the electron spins, is retained.[†] To see the effect of \mathbf{B}_1^+ we convert to the rotating frame, introduced in Section 1.4.4, which rotates about the z -axis at a frequency ω_{mw} . In the rotating frame, the external oscillatory magnetic field is effectively static, and is given by

$$\mathbf{B}_1^r = B_1 (\cos(\phi), \sin(\phi), 0)^T, \quad (1.83)$$

*In this section, the notation for EPR is used, and we call the oscillating frequency ω_{mw} . This description holds for NMR with ω_{rf} instead of ω_{mw} .

[†]In NMR, the opposite can be true, depending on the sign of γ_n : for nuclei with positive values of γ_n , \mathbf{B}_1^- rotates in the same sense as the nuclear spins and \mathbf{B}_1^+ is ignored.

where the superscript r indicates the rotating frame. The oscillatory field can be combined with the static magnetic field to give an effective magnetic field,

$$\mathbf{B}_{\text{eff}}^{\text{r}} = \left(B_1 \cos(\phi), B_1 \sin(\phi), \frac{\Omega}{-\gamma_e} \right)^T, \quad (1.84)$$

where $\Omega = \omega_0 - \omega_{\text{mw}}$ is the frequency offset and $\frac{\Omega}{-\gamma_e}$ is the effective static field in the rotating frame. The magnetization precesses around $\mathbf{B}_{\text{eff}}^{\text{r}}$ at a frequency $\omega_{\text{eff}}^{\text{r}}$,

$$\omega_{\text{eff}}^{\text{r}} = -\gamma_e B_{\text{eff}}^{\text{r}} = (\omega_1^2 + \Omega^2)^{\frac{1}{2}}, \quad (1.85)$$

where $\omega_1 = -\gamma_e B_1$ is the *nutation frequency* of the oscillatory field.

If the oscillatory field is exactly on-resonance (that is, $\Omega = \omega_0 - \omega_{\text{mw}} = 0$), $\omega_{\text{eff}}^{\text{r}} = \omega_1$, and the magnetization precesses around \mathbf{B}_1^{r} . We can write this in terms of the magnetization vector in the rotating frame, \mathbf{M}^{r} , as

$$\frac{d\mathbf{M}^{\text{r}}}{dt} = \gamma_e \mathbf{M}^{\text{r}} \times \mathbf{B}_1^{\text{r}}, \quad (1.86)$$

and in terms of the components of \mathbf{M}^{r} as

$$\dot{M}_x^{\text{r}} = \omega_1 M_z^{\text{r}} \sin(\phi) \quad (1.87\text{a})$$

$$\dot{M}_y^{\text{r}} = -\omega_1 M_z^{\text{r}} \cos(\phi) \quad (1.87\text{b})$$

$$\dot{M}_z^{\text{r}} = \omega_1 (M_y^{\text{r}} \cos(\phi) - M_x^{\text{r}} \sin(\phi)). \quad (1.87\text{c})$$

To illustrate the effect of the mw field, consider a mw field oriented along the x^{r} -axis, that is $\mathbf{B}_1^{\text{r}} = (B_1, 0, 0)^T$, applied for a time $t = \frac{\pi}{2\omega_1}$ to a system initially at thermal equilibrium ($\mathbf{M}^{\text{r}}(t=0) = (0, 0, M_0)^T$). The solution to eqs 1.87 is then

$$\mathbf{M}^{\text{r}} = M_0 \begin{pmatrix} 0 \\ -\sin(\omega_1 t) \\ \cos(\omega_1 t) \end{pmatrix} = \begin{pmatrix} 0 \\ -M_0 \\ 0 \end{pmatrix}. \quad (1.88)$$

so the effect of the mw pulse is to rotate \mathbf{M}^{r} through $\frac{\pi}{2}$ radians around the x^{r} -axis. Such a mw pulse is called an ideal $(\frac{\pi}{2})_x$ or $(90^\circ)_x$ pulse—the $\frac{\pi}{2}$ indicates the nutation angle and the subscript $_x$ indicates nutation axis, or the phase, of the pulse [2].

Note the similarity of eqs (1.67) and (1.88), which describe the same process:

they represent a quantum mechanical and a classical description, respectively, of excitation by a mw field.

1.5.4 Relaxation

At thermal equilibrium, in a static magnetic field $\mathbf{B}_0 = (0, 0, B_0)$, the magnetization of the spin ensemble is given by $\mathbf{M}_0 = (0, 0, M_0)$. If the spin ensemble is taken away from thermal equilibrium, for example by a mw pulse, interactions between spins, and interactions with the environment, cause \mathbf{M} to return to \mathbf{M}_0 . This is called relaxation.

As an example, consider the situation immediately following an ideal 90°_x pulse: the magnetization is given by $\mathbf{M} = (0, -M_0, 0)^T$. The system can be pictured as an ensemble of spins precessing around \mathbf{B}_0 with some *phase coherence*, such that the sum of the transverse components of their magnetic moments is non-zero, and therefore the transverse magnetization is non-zero. From a quantum mechanical perspective, half of these spins are in the $m_S = -\frac{1}{2}$ state, and half are in the $m_S = +\frac{1}{2}$ state, so the total longitudinal magnetization is zero.

Local magnetic field differences cause spins to de-phase, leading to a decrease in the transverse magnetization. This is called *transverse relaxation* (also *spin-spin relaxation*). Spins also undergo transitions between the $m_S = -\frac{1}{2}$ state and the $m_S = +\frac{1}{2}$ state, exchanging energy with the lattice as they do so, and thereby cause M_z to return to its thermal equilibrium value M_0 . This is called *longitudinal relaxation* (also *spin-lattice relaxation*).

The effect of transverse and longitudinal relaxation on the magnetization can be expressed mathematically as

$$\frac{d\mathbf{M}}{dt} = -\mathbf{R}(\mathbf{M} - \mathbf{M}_0), \quad (1.89)$$

where

$$\mathbf{R} = \begin{pmatrix} R_2 & 0 & 0 \\ 0 & R_2 & 0 \\ 0 & 0 & R_1 \end{pmatrix} \quad (1.90)$$

is the relaxation matrix, with longitudinal and transverse relaxation rates R_1 and R_2 . The solution to this equation is straightforward,

$$M_{xy}(t) = M_{xy}(0)e^{-t/T_2}, \quad (1.91a)$$

$$M_z(t) = M_0 + (M_z(0) - M_0) e^{-t/T_1}, \quad (1.91b)$$

where $T_1 = R_1^{-1}$ and $T_2 = R_2^{-1}$ are the longitudinal and transverse relaxation times.

1.5.5 Bloch equations

Combining spin precession, relaxation and excitation, we can write the equation of motion of the magnetization \mathbf{M} as [18]

$$\frac{d\mathbf{M}}{dt} = \gamma_e \mathbf{M} \times (\mathbf{B}_0 + \mathbf{B}_1^-) - \mathbf{R}(\mathbf{M} - \mathbf{M}_0). \quad (1.92)$$

This set of coupled equations is known as the Bloch equations. In the rotating frame, eq (1.92) can be written [2]

$$\frac{d}{dt} \begin{pmatrix} M_x^r \\ M_y^r \\ M_z^r \end{pmatrix} = \begin{pmatrix} 0 & -\Omega & \omega_1 \sin(\phi) \\ \Omega & 0 & -\omega_1 \cos(\phi) \\ -\omega_1 \sin(\phi) & \omega_1 \cos(\phi) & 0 \end{pmatrix} \begin{pmatrix} M_x^r \\ M_y^r \\ M_z^r \end{pmatrix} + \begin{pmatrix} R_2 & 0 & 0 \\ 0 & R_2 & 0 \\ 0 & 0 & R_1 \end{pmatrix} \begin{pmatrix} M_x^r \\ M_y^r \\ M_z^r - M_0^r \end{pmatrix}. \quad (1.93)$$

The Bloch equations describe the motion of \mathbf{M} due to precession, relaxation and a mw or rf field. The concept of a macroscopic magnetization vector can be a very useful tool in many instances: this model can be a convenient way to visualize a spin system, and many experiments and processes can be understood using it. The Bloch equations are particularly applicable for spin systems exhibiting mono-exponential relaxation. Furthermore, the Bloch equations describe a system of isolated spins- $\frac{1}{2}$ completely.

However, the vector model and the Bloch equations also have some major drawbacks. They describe the bulk properties of the spin ensemble. The many complex interactions involving spins and magnetic fields are combined into a few parameters describing bulk properties of the spin ensemble, namely \mathbf{M} , ω_1 , Ω , R_1 , and R_2 . The model masks underlying physical processes and mechanisms, and details of single spins are hidden. Sometimes, if one process dominates over others, then one or more of the bulk parameters can be associated with a particular process or mechanism, but this is not always the case, and is often an oversimplification.

1.6 Relaxation

Relaxation is the process of a spin system returning from a non-equilibrium state to its thermal equilibrium state. The primary focus of this thesis is relaxation in EPR. However, much of the content of this thesis concerns both NMR and EPR, so this section attempts to describe relaxation in both of these fields. There are many mechanisms which cause relaxation: some of these are common to both NMR and EPR, while some of them are unique to one or the other. Similarly, some experiments to investigate relaxation are used in NMR and EPR, while some are only suitable for use in one of these fields.

Relaxation is usually divided into two categories: *longitudinal relaxation* is the recovery of longitudinal magnetization to its thermal equilibrium value, and *transverse relaxation* is the decay of transverse magnetization to its thermal equilibrium value (zero). In an ideal case, these processes are described by the Bloch equations (eq (1.92)), and the recoveries are exponential, with the well-defined time constants T_1 and T_2 which do not depend on experimental parameters. This is often the case in liquid-state NMR, but there are many systems where this is not the case, particularly solid-state EPR, which much of this thesis is concerned with.

In solid-state EPR, diffusion processes can cause changes in longitudinal and transverse magnetization, and they manifest themselves as relaxation processes. The effects of diffusion on magnetization differ between experiments, so different experiments can yield different apparent relaxation times. In studies of longitudinal relaxation, it is often possible to separate the effects of longitudinal relaxation and diffusion, and to quantify both processes and assign to them the time constants T_1 and T_D . This is generally not the case, however, in transverse relaxation studies. Instead, the empirical quantity T_m , known as the *phase-memory time*, is used to describe the decay of transverse magnetization.

This section begins with a brief summary of the theoretical frameworks in which relaxation can be described. Following this, some of the mechanisms causing relaxation in EPR are introduced. Finally, some methods for studying relaxation, and measuring relaxation time constants, are described.

1.6.1 Theoretical frameworks

Relaxation can be described in different ways, ranging from a fully quantum mechanical description to a fully classical description. Ernst et al. defined four frameworks, which are summarized here [17].

The most fundamental description is **quantum mechanical relaxation theory**, in which the spin system and surroundings are described quantum mechanically: the density matrix represents the spin system, and its evolution is described by the Liouville-von Neumann equation (Section 1.3).

In **semi-classical relaxation theory**, the spin system is also described by a density matrix, and its evolution by the Liouville-von Neumann equation. However, the interactions between the system and the surroundings are described classically as random fluctuating processes.

Longitudinal relaxation can be described using **transition probabilities** between different energy states, and relaxation rates can be calculated using perturbation theory. This approach is limited to longitudinal relaxation, because transverse relaxation does not involve transitions between energy states.

The least fundamental description uses the phenomenological **Bloch equations** (Section 1.5.5). These equations describe the relaxation of the macroscopic magnetization in terms of T_1 and T_2 , which can be either calculated using one of the previously mentioned frameworks, or measured experimentally.

1.6.2 Relaxation mechanisms in EPR

This section describes some of the main processes which cause longitudinal and transverse relaxation in magnetic resonance. The focus is on EPR, particularly solid-state EPR, since this is the main topic of this thesis. However, some of these processes are applicable to NMR and DNP as well. All of the mechanisms in this section are described in more detail in the review by Eaton and Eaton [19] and the book by Schweiger and Jeschke [14], which have been the main resources for this section.

This section is divided into three parts. Mechanisms causing longitudinal relaxation are described first, followed by mechanisms causing transverse relaxation. The third part covers diffusion processes, which can cause changes in both longitudinal and transverse relaxation.

Longitudinal relaxation

Longitudinal relaxation involves transitions between the different m_S states of a spin. The different quantum states have different energies, so this process involves an exchange of energy between the spin system and the surroundings, commonly referred to as the lattice. This energy transfer is mediated by lattice vibrations, which are associated with fluctuating magnetic fields. The energy quanta transmitting the energy are phonons.

In liquids, the magnetic field fluctuations are caused by thermal motion, which is mainly Brownian motion. The relaxation rate depends on the correlation time of the motion, τ_c . In the Redfield limit,* the longitudinal relaxation rate can be represented, in a classical framework, by [14]

$$\frac{1}{T_1} = \left(\frac{g\mu_B}{\hbar} \right)^2 \left(\overline{B_x^2} + \overline{B_y^2} \right) \frac{\tau_c}{1 + \omega_e^2 \tau_c^2}, \quad (1.94)$$

where $\overline{B_x^2}$ and $\overline{B_y^2}$ are the mean square amplitudes of the magnetic field fluctuations in the transverse direction.

In solid-state EPR, the most commonly considered processes are the direct process, Raman process, and Orbach process, which are illustrated in Figure 1.3 and summarized in the following paragraphs. They are described in more detail in [14, 19, 20]. Other longitudinal relaxation processes in solids include modulation of spin-orbit coupling, tunnelling, and fractal relaxation. These will not be discussed here, but are described in [19].

The simplest process is the **direct process**, in which a single phonon with a frequency equal to the electron Larmor frequency ω_e is emitted or absorbed (Figure 1.3a). In the high-field, high-temperature approximation, the relaxation rate as a function of temperature and magnetic field can be expressed as [14, 20]

$$T_1^{-1} \propto B_0^4 T.$$

The direct process can be the dominant longitudinal relaxation mechanism at high magnetic fields and low temperatures (below about 4 K) [14].

The **Raman process** involves two phonons: the spin system absorbs a phonon with frequency ω_{p1} , jumping to a virtual excited energy state, and emits a phonon

*The Redfield limit is the limit in which correlation times are very short, and is defined by the condition $\tau_c \ll (\delta\omega)^{-1}$, where $\delta\omega$ is the maximum frequency change caused by the motion.

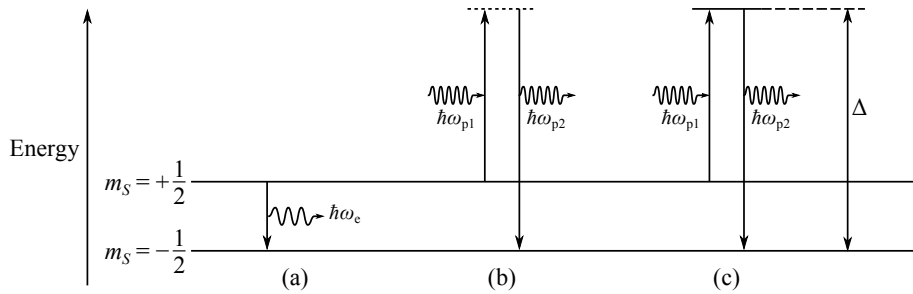


Figure 1.3: Longitudinal relaxation mechanisms in solid-state EPR. (a) Direct process: emission of a single phonon with frequency ω_e . (b) Raman process: absorption of a phonon with frequency ω_{p1} and emission of a phonon with frequency $\omega_{p2} = \omega_{p1} + \omega_e$. The dotted line represents a virtual energy state. (c) Orbach process: absorption and emission of phonon, in analogy with the Raman process. However, the solid line represents an actual energy state.

with frequency $\omega_{p2} = \omega_{p1} \pm \omega_e$, dropping into a ground state (Figure 1.3b). The scaling law with temperature for the Raman process is usually in the region [14,20]

$$T_1^{-1} \propto T^5 \quad \text{to} \quad T_1^{-1} \propto T^9.$$

Although two-phonon processes are generally less probable than single-phonon processes, there is usually a much greater density of phonons at a frequency ω_{p1} than at a frequency ω_e , so the Raman process is usually a more efficient relaxation mechanism than the direct process, particularly at higher temperatures.

A similar process to the Raman process is the **Orbach process**, which also involves two phonons, but in this case the excited energy state is an actual energy state, not a virtual one, at an energy Δ above the ground state (Figure 1.3c). The temperature dependence for the Orbach process is [14, 20]

$$T_1^{-1} \propto (e^{-\Delta/k_B T} - 1).$$

Transverse relaxation

Transverse magnetization is a consequence of phase coherence of precessing spins, so any process which reduces this coherence leads to transverse relaxation.

A spin flip associated with longitudinal relaxation also causes transverse relaxation, because it destroys the precession coherence of the flipped spin with respect to the other spins. A flip-flop process, in which two coupled spins simultaneously flip in opposite directions, thus conserving energy, destroys the coherence of both spins. This is called *spin-spin relaxation*. In the Redfield limit, the spin-spin

relaxation rate is [14]

$$\frac{1}{T_{2,ss}} = \left(\frac{g\mu_B}{\hbar} \right)^2 \overline{B_z^2} \tau_c, \quad (1.95)$$

where $\overline{B_z^2}$ is the mean square amplitude of the longitudinal magnetic field fluctuations. Ignoring other contributions to transverse relaxation, the transverse relaxation rate is then given by [14]

$$\frac{1}{T_2} = \frac{1}{T_{2,ss}} + \frac{1}{2T_1}. \quad (1.96)$$

Note that eqs (1.95) and (1.96) are only really relevant in liquid-state EPR. In solid-state EPR, the spin system is a virtually infinite network of coupled spins, the transverse relaxation is usually not mono-exponential, and the transverse relaxation rate is rarely a well-defined parameter. Instead, decay of transverse magnetization is characterized by the phase-memory time T_m [14, 20]. As well as spin-spin relaxation, other contributions to transverse relaxation include various diffusion processes, more rapidly relaxing coupled spins, librational motions, and methyl groups. Diffusion processes will be introduced briefly in the following section. They are described in more detail, along with all of the other processes mentioned, in [19].

Diffusion processes

In EPR, the bandwidth of the detected signal is often much smaller than the width of the spectrum, so any diffusion process which moves magnetization away from the detection frequency ω_{mw} is an apparent relaxation process [19]. Spins which are inside the excitation or detection window are called A spins, while other spins are called B spins. Processes which move spin magnetization across an EPR spectrum include instantaneous diffusion, spectral diffusion, cross-relaxation, and nuclear spin diffusion.

Instantaneous diffusion If a mw pulse flips a pair of dipolar-coupled A spins, then the local field at each spin is changed, and therefore the resonance frequency of each spin is also changed. The duration of the pulse is usually much less than the relaxation times, so the process is effectively instantaneous on the time-scale of the experiment.

Spectral diffusion Spectral diffusion is the change in EPR frequency of an individual spin. Relaxation of B spins can change the local field of A spins, and this change can move the resonance frequency of the A spins outside the detection window. Similarly, relaxation of A spins can move the resonance frequency of B spins *inside* the detection window.

Cross-relaxation (spectral spin diffusion) A flip-flop process, in which two coupled spins with different resonance frequencies flip in opposite directions, causes a transfer of magnetization between the spins. This is called cross-relaxation. Since cross-relaxation causes magnetization to diffuse in the spectral dimension, it is often called spectral spin diffusion. If the spins are an A spin and a B spin, this is an apparent relaxation process.

Nuclear spin diffusion Nuclear spin diffusion is the spatial transfer of magnetization through a sample by flip-flops of dipolar-coupled nuclei. The local field of an electron spin, and hence its resonance frequency, is dependent on the spin states of the nuclei dipolar-coupled to the electron. Therefore, nuclear spin diffusion is a source of de-phasing and can move the resonance frequency of A spins outside the detection window.

1.6.3 Relaxation studies

Many methods exist for studying longitudinal and transverse relaxation. If one wants to measure a particular parameter, for example the longitudinal relaxation time T_1 , then the method of choice depends on the physical properties of the system being studied and the hardware being used. A brief review of some of the most commonly used methods is presented here. Some of the methods are used in both EPR and NMR, while some are unique to one or other of these fields. Most of the methods described here are described in more detail in the book by Schweiger and Jeschke [14] and in Dr. Josef Granwehr's PhD thesis [20]. These methods and several others are described in the review by Eaton and Eaton [19].

Measurement of longitudinal relaxation times

Saturation recovery and inversion recovery One of the most commonly used methods of measuring the longitudinal relaxation time T_1 is an **inversion recovery** (IR) experiment. A preparation π pulse is applied to a spin system at

thermal equilibrium, inverting the magnetization \mathbf{M} , and the z -component of \mathbf{M} is measured as it returns to its thermal equilibrium value. The preparation pulse can be a hard (non-selective) pulse, which inverts spins at all frequencies, or a soft (selective) pulse, which only inverts spins in a particular frequency range. In NMR, both of these methods are usually possible. In EPR, however, IR with a hard pulse is restricted to certain samples, since the strength of the B_1 field (in frequency units) is often less than the width of the spectrum. In such cases the whole spectrum cannot be inverted with a single hard pulse. It is, in principle, possible to measure T_1 with a selective inversion, but such experiments are susceptible to spectral diffusion and cross-relaxation, so other methods for measuring T_1 are more commonly used [14].

A similar method to IR is a **saturation recovery** (SR) experiment. A saturation pulse is applied to a sample to completely destroy the longitudinal and transverse magnetization, and the z -component of \mathbf{M} is measured as it returns to its thermal equilibrium value. As with IR, the preparation pulse for SR in NMR can be non-selective or selective. In EPR, however, the limited strength of the B_1 field compared with the spectral width means it is often not possible to saturate the whole spectrum, so saturation pulses are usually selective. The saturation pulse should be applied for long enough to saturate all transitions at the mw frequency within the bandwidth of the pulse, and also all transitions that can exchange magnetization with this spectral region by diffusion processes on the time-scale of T_1 . This can usually be accomplished by applying a saturation pulse for longer than the detection period [14].

In both SR and IR, the z -component of \mathbf{M} is measured as it returns from its prepared state to its thermal equilibrium value, by applying a pulse after a delay time to convert some of the longitudinal magnetization into transverse magnetization and recording the free induction decay (FID) signal (FIDs are described in Section 3.5)*. This can be achieved by using either repetitions or a single scan. In the repetition method, a pulse with a relatively large flip angle (up to 90°) is applied, and the preparation-delay-record sequence is repeated with an increased delay time for each scan. To measure the recovery with a single scan, a series of pulses with a small flip angle is applied, with the pulses separated by a delay time T . If the repetition method is used in an IR experiment, a sufficiently long recycle

*For reasons discussed in Chapter 3, it is often not possible to record an FID in EPR, due to instrumental dead-time. Therefore, a spin echo is often recorded instead (spin echoes are described later in this section).

delay time, usually at least $5T_1$, must be included between each scan to allow the magnetization to recover to its thermal equilibrium value. For spin systems with long relaxation times, this can make repetition IR experiments unfeasibly long.

Stimulated echo A stimulated echo is generated by using the sequence $\pi/2 - \tau - \pi/2 - T - \pi/2 - \tau - \text{echo}$, where $\pi/2$ represents the pulse turn angle, and τ and T are delays. To measure T_1 , τ is fixed, and T is varied with successive repetitions. In the absence of diffusion processes, the amplitude of the echo signal would be expected to recover exponentially with T_1 . However, this is rarely the case: a stimulated echo is very susceptible to diffusion, so it is rarely a good way to measure T_1 . However, because the stimulated echo depends on diffusion processes, it can be used to investigate and quantify these processes by varying τ [14].

Echo saturation by fast repetition T_1 can be determined by measuring a series of primary spin echoes, each of which is produced by applying a $\frac{\pi}{2}$ pulse followed by a π pulse (spin echoes are described later in this section). If the delay between each spin echo sequence is long enough (greater than about $5T_1$), the amplitude of each spin echo will be constant. If, however, the repetition rate of the experiment is increased, such that M_z does not fully recover between each spin echo sequence, then the amplitude of successive spin echoes will be reduced, and T_1 can be determined.

Spectral hole-burning In EPR spectra, lines are often inhomogeneously broadened due to the orientation-dependent g -factor: they are effectively made up of a series of homogeneously broadened lines associated with separate spin packets. This makes it possible to selectively saturate a particular transition, thereby burning a hole in a line, and observe the effects of both longitudinal relaxation and spectral diffusion. A selective saturation pulse is used to burn a hole, and the amplitude and shape of the hole can be measured, after a mixing time, using a non-selective $\frac{\pi}{2}$ pulse and recording the FID signal, or using a spin echo sequence [21, 22]. As the mixing time is increased, the amplitude of the hole decreases due to longitudinal relaxation, while spectral diffusion causes the hole to broaden.

Measurement of transverse relaxation times

The FID signal (described in Section 3.5) caused by spins precessing in phase decays at a rate R_2^* as the spins de-phase. In the absence of diffusion, this de-phasing is caused by field inhomogeneities, and can be divided into two categories, reversible and irreversible de-phasing. Reversible de-phasing is caused by time-independent field inhomogeneities, due to either susceptibility differences in a sample or a static field which is not perfectly uniform. Irreversible de-phasing is caused by time-dependent field inhomogeneities, such as those caused by molecular motion. The decay rate can be expressed as the sum of two decay rates,

$$R_2^* = R_2 + R'_2 = \frac{1}{T_2} + \frac{1}{T'_2}, \quad (1.97)$$

where $R_2 = \frac{1}{T_2}$ and $R'_2 = \frac{1}{T'_2}$ are associated with irreversible and reversible de-phasing respectively. Since T'_2 depends on properties of the hardware and experimental set-up, T_2 is the relaxation time of interest.

Linewidth In some cases in NMR, T_2 can be measured from the linewidth $\Delta\nu$. The full-width at half-maximum of a Lorentzian broadened line is given by

$$\Delta\nu = \frac{1}{\pi T_2^*} = \frac{1}{\pi} \left(\frac{1}{T_2} + \frac{1}{T'_2} \right), \quad (1.98)$$

and if T'_2 is negligible, or can be measured from a reference line with a negligible contribution from $\frac{1}{T_2}$ to the linewidth, then T_2 can be easily measured [17].

Primary spin echo decay A commonly used method to measure T_2 is to produce a spin echo using two pulses, such as a $\frac{\pi}{2}$ pulse followed by a π pulse, with a delay T between the two pulses. During the delay following the $\frac{\pi}{2}$ pulse, the precessing spins de-phase at a rate R_2^* , because magnetic field differences cause some spins to precess faster than others. The π pulse inverts the spins about the pulse axis, thereby reversing the acquired phases of the spins. The de-phasing then becomes a re-phasing, and a pair of ‘back-to-back’ FIDs is produced, centred at a time T after the π pulse. This signal is called a spin echo. The π pulse re-focuses the reversible (T'_2) de-phasing, but not the irreversible (T_2) de-phasing, so in ideal

cases the amplitude E of the spin echo can be expressed

$$E(2T) \propto e^{-2T/T_2}. \quad (1.99)$$

Therefore, T_2 can, in principle, be measured by recording spin echoes at different delays times T [23].

In solid-state EPR, T_2 is often not a well-defined quantity because coupling between spins is so strong [20], and diffusion processes can contribute to decay of the echo signal [24]. The primary spin echo rarely decays mono-exponentially, as in eq (1.99), but can often instead be fitted with a stretched exponential: the amplitude E of the spin echo can be expressed

$$E(2T) \propto e^{-(2T/T_m)^\alpha}, \quad (1.100)$$

where the value of α depends on properties of the spin system and the experiment (usually $\frac{1}{2} \leq \alpha \leq 2$), and the *phase-memory time* T_m is an empirical time constant associated with the primary echo decay [24, 25]. Instantaneous diffusion can be a major cause of decay of the primary echo. Its effect can be reduced by reducing the mw power, and hence the turning angle, of the pulse [24].

Carr-Purcell-Meiboom-Gill (CPMG) If translational diffusion is not negligible, it can cause additional attenuation of the primary echo. In such cases eq (1.99) is an over-simplification and it is difficult to measure T_2 using a primary echo [17]. An alternative method, which is much less susceptible to diffusion, is to apply a series of refocusing π pulses following the initial $\frac{\pi}{2}$ pulse, and record the spin echoes produced in the intervals between the pulses. This method was designed by Carr and Purcell, who used the same phase for all of the pulses [26]. Problems arise with the Carr-Purcell method if the π pulses are not ideal, since this results in incomplete refocusing. Meiboom and Gill showed that non-ideal π pulses do not cause problems if the phase of the $\frac{\pi}{2}$ pulse is shifted by 90° with respect to the π pulses [27].

T_1 - T_2 correlation

In NMR studies of sedimentary rocks and other porous materials, measurements of the relaxation times T_1 and T_2 can be used to study molecular mechanisms of surface relaxation, and the ratio T_1/T_2 is often of particular interest [28]. The

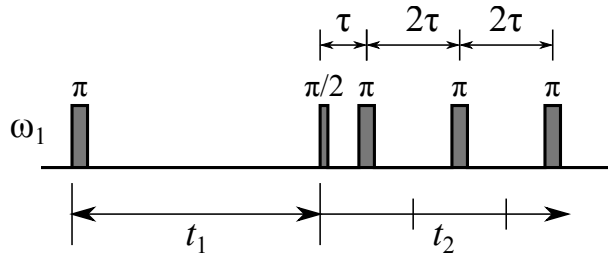


Figure 1.4: IR-CPMG pulse sequence for T_1 - T_2 correlation. Longitudinal magnetization recovers during t_1 , and transverse magnetization decays during t_2 . Adapted from [29].

relaxation times depend on the sizes of the pores, so usually a distribution of relaxation times is measured. Song et al. combined inversion recovery with a CPMG sequence to correlate measurements of T_1 and T_2 , in order to identify molecular species with distinct values of T_1/T_2 [29]. The pulse sequence is shown in Figure 1.4.

Phase-cycling

In many NMR and EPR experiments, including some of the experiments described in this section, imperfections in spectrometer hardware can cause spurious signals, meaning data can be misinterpreted if these artifacts are not identified or suppressed. Any experiment employing π or $\frac{\pi}{2}$ pulses is susceptible to such problems. Even if hardware or pulse sequence imperfections are negligible, a pulse sequence can still generate unwanted signals. For example, in a saturation recovery experiment, the saturation pulse can induce an FID which, for short recovery times, is recorded along with the signal. This can be removed by repeating the experiment with the phase of the saturation pulse reversed [14]. This is a specific example of a *phase-cycle*. More generally, phase-cycling is used to select particular *coherence transfer pathways*, and to enhance and suppress different EPR and NMR signals. Coherence transfer pathways and phase-cycling will not be discussed further here, but are described in detail in a series of educational papers [30].

Chapter 2

Dynamic Nuclear Polarization

One of the main challenges for high-resolution NMR spectroscopy and imaging is low sensitivity. This is because the thermal equilibrium polarizations of nuclei are extremely small under typical experimental conditions. For example, at $B_0 = 9.4$ T and $T = 300$ K, the thermal equilibrium polarizations of ^1H and ^{13}C are 3.2×10^{-5} and 8.1×10^{-6} respectively (see Table 1.1). Electrons have much greater thermal equilibrium polarizations than nuclei, and the thermal equilibrium polarizations of both nuclei and electrons increase as temperature is decreased, as was illustrated in Figure 1.2. In a system containing both unpaired electrons and nuclei with non-zero spins, the nuclei and electrons are coupled via the hyperfine interaction, and this interaction makes it possible to use the higher polarization of the electron spin system to enhance the nuclear spin polarization. This polarization enhancement can be achieved by applying microwave (mw) radiation to the system, as will be described in more detail in this chapter. This is known as dynamic nuclear polarization (DNP).

DNP was first proposed by Albert Overhauser in 1953 [11]. Shortly after this prediction, DNP was demonstrated by Carver and Slichter in metals [12] and liquids [31]. Following this pioneering work, DNP was soon demonstrated in solid state samples, and the solid effect (SE) [32–34], cross effect (CE) [35, 36], and thermal mixing (TM) [37, 38] mechanisms were identified.

The next major advancement in DNP was in the early 1990s, when Griffin and co-workers combined DNP with magic-angle spinning (MAS) NMR [39]. More recently, Golman and co-workers performed low temperature DNP followed by a rapid temperature and magnetic field jump, and acquisition of a liquid-state spectrum [40]. The temperature and field jump were achieved by dissolution of the

polarized sample using a hot solvent, and shuttling of the dissolved sample to a higher field magnet. This method, known as dissolution DNP, has opened up the possibility of *in vivo* imaging of hyperpolarized metabolites [41], and was later commercialized for NMR spectroscopy applications (HyperSense, Oxford Instruments, Abingdon, UK) and biomedical magnetic resonance imaging (MRI) (SpinLab, GE Healthcare, Chalfont St Giles, UK). MAS DNP NMR spectrometers are now also manufactured commercially (Avance III, Bruker BioSpin, Billerica, MA).

An extensive review of the major developments in DNP, as well as some recent advances, can be found, for example, in two recent review papers [3, 4].

In liquid-state DNP, the dominant mechanism is the Overhauser effect (OE). In solid-state DNP, three distinct enhancement mechanisms have been proposed. If the EPR linewidth δ is smaller than the nuclear Larmor frequency ω_n , the SE is usually the dominant mechanism, while if δ is greater than ω_n , the CE or TM usually dominates. For broad lines with $\delta > \omega_n$, the operative mechanism depends on the nature of the broadening and the behaviour of the line under mw irradiation: for samples with EPR lines which are inhomogeneously broadened by g -anisotropy, in which mw hole-burning is possible, the CE dominates, while for samples with homogeneous dipolar-broadened lines, for which mw radiation saturates the whole spectrum, TM is the dominant mechanism [42, 43].

The SE can be described in terms of a spin system with a single electron, in which mw radiation at frequencies $\omega_e \pm \omega_n$ transfers polarization from the electron to its surrounding nuclei, where ω_e and ω_n are the resonance frequencies of the electron and nuclei respectively. The CE involves two electrons, and polarization can be transferred from the electrons to their surrounding nuclei as long as the condition $|\omega_{e_1} - \omega_{e_2}| = \omega_n$ is fulfilled, where ω_{e_1} and ω_{e_2} are the resonance frequencies of the two electrons. Finally, TM involves many electron spins, and polarization transfer from electrons to nuclei is usually described thermodynamically.

The following sections describe these four DNP mechanisms. The OE, CE and TM are all described briefly, while the description of the SE is more detailed. The transfer of enhanced nuclear polarization through a sample by nuclear spin diffusion is then described, and some of the recent efforts at simulating solid-state DNP are reviewed. Finally, some organic molecules used as polarizing agents in DNP are described at the end of this chapter.

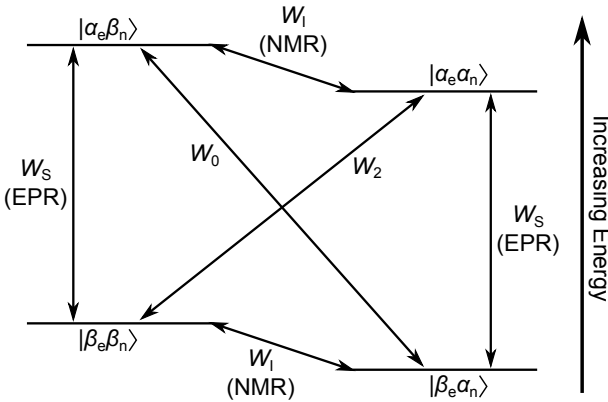


Figure 2.1: Energy level diagram of a liquid-state electron-nucleus (e-n) system. The six possible transitions are shown: four single-quantum (SQ) NMR and EPR transitions, indicated by W_1 and W_S respectively, and the forbidden double quantum (DQ) and zero quantum (ZQ) transitions, indicated by W_2 and W_0 .

2.1 Overhauser effect

As stated above, the OE is the dominant polarization transfer mechanism in liquid-state DNP. The spin system comprises one electron spin coupled to one nuclear spin, as illustrated by the energy level diagram in Figure 2.1. Microwave radiation is applied at the EPR transition frequencies to saturate the W_S transitions and equalize the populations of $|\alpha_e\beta_n\rangle$ and $|\beta_e\beta_n\rangle$, and the populations of $|\alpha_e\alpha_n\rangle$ and $|\beta_e\alpha_n\rangle$. When the mw radiation is switched off, the system relaxes according to the transition probabilities W_S (electron relaxation), W_1 (nuclear relaxation), and W_0 and W_2 (cross relaxation). The cross relaxation is the source of nuclear polarization enhancement. A mathematical treatment of OE nuclear polarization build-up involves a system of coupled rate equations known as the Solomon equations [44], which can be solved to give a theoretical enhancement factor. The full derivation will not be presented here; only selected results will be given.

The enhancement factor ϵ , defined as the relative increase in nuclear polarization, can be expressed as [45]

$$\epsilon = \frac{P_n - P_n^{eq}}{P_n^{eq}} = \xi f s \frac{\gamma_e}{\gamma_n} \quad (2.1)$$

where P_n and P_n^{eq} are the enhanced nuclear polarization and thermal equilibrium polarization respectively, ξ is called the coupling factor, f is called the leakage factor, and s is called the saturation factor. ξ , f , s and $\frac{\gamma_e}{\gamma_n}$ will be described in the following text.

The coupling factor ξ is given by

$$\xi = \frac{W_2 - W_0}{W_0 + W_2 + 2W_I}. \quad (2.2)$$

ξ can take any value in the range $-1 \leq \xi \leq 0.5$, with the value depending on the nature of the coupling: $\xi = -1$ for dipolar coupling, and $\xi = 0.5$ for scalar coupling.

The leakage factor f is a measure of the amount of ‘leakage’ of the nuclear polarization due to processes not associated with the electron spin. It is given by

$$f = \frac{W_0 + W_2 + 2W_I}{W_0 + W_2 + 2W_I + W^0} = 1 - \frac{T_{1,n}^{+S}}{T_{1,n}^{-S}}, \quad (2.3)$$

where $W^0 = (T_{1,n}^{-S})^{-1}$ and $(T_{1,n}^{+S})^{-1}$ are the nuclear relaxation rates in the absence and presence of electron spins respectively.

The saturation factor s indicates how effectively the mw field saturates the electron transitions. It is given by

$$s = \frac{\omega_1^2 T_{1S} T_{2S}}{1 + \omega_1^2 T_{1S} T_{2S}}, \quad (2.4)$$

where ω_1 is the mw field amplitude in the rotating frame, and T_{1S} and T_{2S} are the longitudinal and transverse electron relaxation times respectively.

Finally, $\frac{\gamma_e}{\gamma_n}$ is the ratio of electron and nuclear gyromagnetic ratios. With optimal conditions, the maximum possible enhancement by the OE, given by eq (2.1) with $\xi = -1$, $f = 1$, and $s = 1$, is approximately 660 for hydrogen and 2600 for carbon-13.

2.2 Solid effect

The SE is the simplest solid-state DNP mechanism. The spin system for the SE consists of one electron spin and one nuclear spin, coupled by the hyperfine interaction. This section is divided into three main parts. First, the electron-nucleus system is described with a simplified Hamiltonian applicable to the *liquid* state: energy levels and populations are derived, and it is demonstrated that the transitions necessary for the SE cannot take place in the liquid state. The spin system is then described with the full, solid-state, Hamiltonian, and it is demonstrated that

the required transitions can take place in the solid state. Finally, dynamics of the SE are described, and it is shown that the mw-driven transitions and relaxation processes can lead to polarization enhancement. Parts of this section closely follow the approaches in a publication by Hovav et al. [46] and a lecture by Dr. Walter Köckenberger [16].

2.2.1 Electron–nucleus spin system in the liquid state

Hamiltonian

The Hamiltonian for a spin system comprising one electron spin coupled to one nuclear spin is given by

$$\hat{H} = \hat{H}_{EZ} + \hat{H}_{NZ} + \hat{H}_{hf}, \quad (2.5)$$

where the three terms represent the electron Zeeman interaction, the nuclear Zeeman interaction, and the hyperfine interaction respectively. Using the simplified Zeeman Hamiltonians given in eqs (1.44) and (1.39), for single spins, and the hyperfine Hamiltonian given in eq (1.50), for a single pair of spins, eq (2.5) can be written as

$$\hat{H} = \omega_e \hat{S}_z + \omega_n \hat{I}_z + A \hat{S}_z \hat{I}_z + \frac{1}{2} \left(B_+ \hat{S}_z \hat{I}_+ + B_- \hat{S}_z \hat{I}_- \right), \quad (2.6)$$

where A and B_{\pm} are the secular and pseudo-secular hyperfine interaction constants given in eqs (1.51) and (1.52) respectively.

In the liquid state, molecules are able to move and rotate. If molecular motion is fast enough, the anisotropic part of the hyperfine interaction averages to zero and can be ignored, so eq (2.6) can be written

$$\begin{aligned} \hat{H} &= \omega_e \hat{S}_z + \omega_n \hat{I}_z + A \hat{S}_z \hat{I}_z \\ &= \begin{pmatrix} +\frac{\omega_e}{2} + \frac{\omega_n}{2} + \frac{A}{4} & 0 & 0 & 0 \\ 0 & +\frac{\omega_e}{2} - \frac{\omega_n}{2} - \frac{A}{4} & 0 & 0 \\ 0 & 0 & -\frac{\omega_e}{2} + \frac{\omega_n}{2} - \frac{A}{4} & 0 \\ 0 & 0 & 0 & -\frac{\omega_e}{2} - \frac{\omega_n}{2} + \frac{A}{4} \end{pmatrix}. \end{aligned} \quad (2.7)$$

The Hamiltonian is diagonal, and the diagonal elements are the energy levels of the pure product states $|\alpha_e \alpha_n\rangle$, $|\alpha_e \beta_n\rangle$, $|\beta_e \alpha_n\rangle$ and $|\beta_e \beta_n\rangle$, where each individual spin can be represented by its state $|\alpha\rangle$ or $|\beta\rangle$. The energy level diagram for this

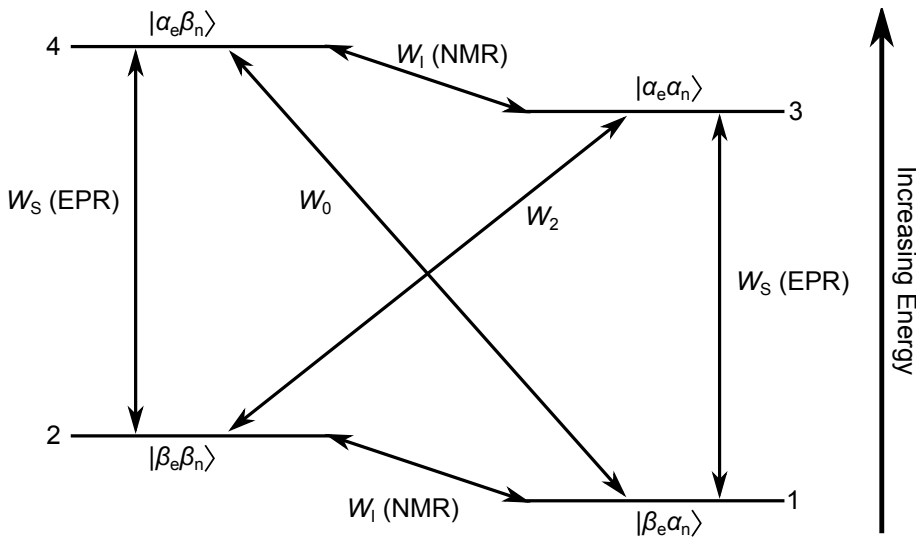


Figure 2.2: Energy level diagram of an electron-nucleus (e-n) system (ignoring the pseudo-secular part of the hyperfine interaction), where each possible quantum state is a pure product state of the single-spin states $|\alpha\rangle$ and $|\beta\rangle$. The six possible transitions are shown: four single-quantum (SQ) NMR and EPR transitions, indicated by W_1 and W_S respectively, and the forbidden double quantum (DQ) and zero quantum (ZQ) transitions, indicated by W_2 and W_0 .

system is shown in Figure 2.2.

Polarization

The normalized thermal equilibrium populations p_i^{eq} of the four states in the electron-nucleus (e-n) system, labelled $i = 1, 2, 3, 4$ as shown in Figure 2.2, can be calculated using eq (1.68),

$$p_1^{\text{eq}} = p_2^{\text{eq}} = \frac{1}{2} \frac{1}{1 + \varepsilon_e}, \quad (2.8)$$

$$p_3^{\text{eq}} = p_4^{\text{eq}} = \frac{1}{2} \frac{\varepsilon_e}{1 + \varepsilon_e}, \quad (2.9)$$

where $\varepsilon_e = e^{-\hbar\omega_e/k_B T}$ is the electron Boltzmann factor, and the nuclear Boltzmann factor is ignored to simplify expressions. The nuclear and electron polarizations P_n and P_e are defined as

$$P_n = \frac{1}{2} ((p_1 - p_2) + (p_3 - p_4)), \quad (2.10)$$

$$P_e = \frac{1}{2} ((p_1 - p_3) + (p_2 - p_4)), \quad (2.11)$$

where p_i ($i = 1, 2, 3, 4$) are the relative populations of the four states. Therefore, the thermal equilibrium nuclear and electron polarizations are

$$P_n^{eq} = \frac{1}{2} ((p_1^{eq} - p_2^{eq}) + (p_3^{eq} - p_4^{eq})) \approx 0, \quad (2.12)$$

$$P_e^{eq} = \frac{1}{2} ((p_1^{eq} - p_3^{eq}) + (p_2^{eq} - p_4^{eq})) = \frac{1}{2} \frac{1 - \varepsilon_e}{1 + \varepsilon_e}. \quad (2.13)$$

As stated previously, DNP increases the nuclear polarization P_n by using the coupling between the electron and nuclear spins. The theoretical maximum nuclear polarization attainable by DNP is $P_n^{\max} = P_e^{eq}$.

Microwave radiation

The Hamiltonian of the mw field (assumed, without loss of generality, to be along the x -axis) was given by eq (1.66). For a single spin, it can be written

$$\hat{H}_{mw} = \omega_1 \hat{S}_x = \begin{pmatrix} 0 & 0 & \frac{\omega_1}{2} & 0 \\ 0 & 0 & 0 & \frac{\omega_1}{2} \\ \frac{\omega_1}{2} & 0 & 0 & 0 \\ 0 & \frac{\omega_1}{2} & 0 & 0 \end{pmatrix}, \quad (2.14)$$

where ω_1 is the nutation frequency induced by the mw radiation. Each matrix element represents the probability amplitude of generating transitions between particular quantum states. This can be seen more clearly if \hat{H}_{mw} is expressed in tabular form, together with the basis vectors:

	$ \alpha_e\alpha_n\rangle$	$ \alpha_e\beta_n\rangle$	$ \beta_e\alpha_n\rangle$	$ \beta_e\beta_n\rangle$
$\langle\alpha_e\alpha_n $	0	0	$\frac{\omega_1}{2}$	0
$\langle\alpha_e\beta_n $	0	0	0	$\frac{\omega_1}{2}$
$\langle\beta_e\alpha_n $	$\frac{\omega_1}{2}$	0	0	0
$\langle\beta_e\beta_n $	0	$\frac{\omega_1}{2}$	0	0

In this representation of the mw Hamiltonian, it can be seen that each matrix element ‘connects’ two quantum states, the two states with which it is aligned. The matrix element represents the probability amplitude of generating transitions between these two states. In this case, the mw field can generate transitions between states $|\alpha_e\alpha_n\rangle$ and $|\beta_e\alpha_n\rangle$, and between states $|\alpha_e\beta_n\rangle$ and $|\beta_e\beta_n\rangle$, with a probability proportional to $(\frac{\omega_1}{2})^2$. These transitions correspond to a single flip of the electron

spin, as illustrated in Figure 2.2. However, as will be seen later, the relevant mw transitions for the solid effect are the ‘zero-quantum’ (ZQ) ($|\alpha_e\beta_n\rangle \longleftrightarrow |\beta_e\alpha_n\rangle$) and ‘double-quantum’ (DQ) ($|\alpha_e\alpha_n\rangle \longleftrightarrow |\beta_e\beta_n\rangle$) transitions, in which both spins flip simultaneously. In the spin system considered so far, the matrix elements joining states $|\alpha_e\beta_n\rangle$ and $|\beta_e\alpha_n\rangle$, and states $|\alpha_e\alpha_n\rangle$ and $|\beta_e\beta_n\rangle$, are all zero, so the ZQ and DQ transitions are ‘forbidden’.

2.2.2 Electron–nucleus spin system in the solid state

We now consider a solid-state spin system, in which the assumptions that led to the removal of the pseudo-secular part of the hyperfine interaction are no longer valid. Molecular motion and rotation are more restricted, so anisotropic terms in the Hamiltonian do not average out. Therefore, the pseudo-secular part of the hyperfine interaction must be included, and the Hamiltonian is given by eq (2.6).

For the calculations that follow in this section, an alternative notation to that used in eq (2.6) is used for the pseudo-secular part of the hyperfine Hamiltonian. Note that the pseudo-secular part of the hyperfine Hamiltonian, which is written in terms of \hat{I}_+ and \hat{I}_- as

$$\hat{H}_{\text{hfi:ps}}^{(\pm)} = \frac{1}{2} (B_+ \hat{S}_z \hat{I}_+ + B_- \hat{S}_z \hat{I}_-), \quad (2.15)$$

can instead be written in terms of \hat{I}_x and \hat{I}_y as

$$\hat{H}_{\text{hfi:ps}}^{(xy)} = B_x \hat{S}_z \hat{I}_x + B_y \hat{S}_z \hat{I}_y, \quad (2.16)$$

where $B_x = \frac{1}{2}(B_+ + B_-)$, $B_y = \frac{1}{2i}(B_+ - B_-)$, $\hat{I}_x = \frac{1}{2}(\hat{I}_+ + \hat{I}_-)$, and $\hat{I}_y = \frac{1}{2i}(\hat{I}_+ - \hat{I}_-)$. To simplify the calculations, $\hat{H}_{\text{hfi:ps}}^{(xy)}$ is substituted for $\hat{H}_{\text{hfi:ps}}^{(\pm)}$ in eq (2.6), and the second term in $\hat{H}_{\text{hfi:ps}}^{(xy)}$ is ignored in the following description. Furthermore, the notation $C = B_x$ is used; this is the notation used in reference [16]. The Hamiltonian is then written

$$\hat{H} = \omega_e \hat{S}_z + \omega_n \hat{I}_z + A \hat{S}_z \hat{I}_z + C \hat{S}_z \hat{I}_x \quad (2.17)$$

$$= \begin{pmatrix} +\frac{\omega_e}{2} + \frac{\omega_n}{2} + \frac{A}{4} & +\frac{C}{4} & 0 & 0 \\ +\frac{C}{4} & +\frac{\omega_e}{2} - \frac{\omega_n}{2} - \frac{A}{4} & 0 & 0 \\ 0 & 0 & -\frac{\omega_e}{2} + \frac{\omega_n}{2} - \frac{A}{4} & -\frac{C}{4} \\ 0 & 0 & -\frac{C}{4} & -\frac{\omega_e}{2} - \frac{\omega_n}{2} + \frac{A}{4} \end{pmatrix}. \quad (2.18)$$

The Hamiltonian is no longer diagonal in this basis. In order to calculate the energy levels of the states we need to find the eigenvalues of the Hamiltonian, which can be achieved by diagonalizing it. The Hamiltonian diagonalization and subsequent calculations, the results of which are shown here, were performed using the Matlab Symbolic Math Toolbox (MuPAD 5.4.0 (R2010a), SciFace Software GmbH & Co. KG, Paderborn, Germany).

The normalized eigenvectors of the Hamiltonian are

$$|\lambda_3\rangle = |\alpha_e\alpha_n^*\rangle = c_\alpha |\alpha_e\alpha_n\rangle - s_\alpha |\alpha_e\beta_n\rangle, \quad (2.19a)$$

$$|\lambda_4\rangle = |\alpha_e\beta_n^*\rangle = c_\alpha |\alpha_e\beta_n\rangle + s_\alpha |\alpha_e\alpha_n\rangle, \quad (2.19b)$$

$$|\lambda_1\rangle = |\beta_e\alpha_n^*\rangle = c_\beta |\beta_e\alpha_n\rangle + s_\beta |\beta_e\beta_n\rangle, \quad (2.19c)$$

$$|\lambda_2\rangle = |\beta_e\beta_n^*\rangle = c_\beta |\beta_e\beta_n\rangle - s_\beta |\beta_e\alpha_n\rangle, \quad (2.19d)$$

where $c_{\alpha,\beta} = \cos\left(\frac{\eta_{\alpha,\beta}}{2}\right)$, $s_{\alpha,\beta} = \sin\left(\frac{\eta_{\alpha,\beta}}{2}\right)$, and $\eta_{\alpha,\beta} = \arctan\left(\frac{-C}{2\omega_n \pm A}\right)$. (Note that, in the limit of weak coupling, $s_{\alpha,\beta} \approx -\frac{C}{4\omega_n}$ and $c_{\alpha,\beta} \approx 1 - \frac{1}{2}\left(\frac{C}{4\omega_n}\right)^2 \approx 1$.) The numbering of the eigenvectors reflects the ordering of the energy levels, with $|\lambda_1\rangle$ representing the lowest energy state and $|\lambda_4\rangle$ the highest. The eigenvectors are ‘mixtures’ of the pure product states in eqs (1.16): the off-diagonal matrix elements associated with the pseudo-secular part of the hyperfine interaction have caused a mixing of quantum states and energy levels, and this is represented by the asterisk in eqs (2.19). The energy level diagram for this system is shown in Figure 2.3.

The eigenvectors can be arranged into the matrix D ,

$$D = (|\lambda_3\rangle, |\lambda_4\rangle, |\lambda_1\rangle, |\lambda_2\rangle) = \begin{pmatrix} c_\alpha & s_\alpha & 0 & 0 \\ -s_\alpha & c_\alpha & 0 & 0 \\ 0 & 0 & c_\beta & -s_\beta \\ 0 & 0 & s_\beta & c_\beta \end{pmatrix}, \quad (2.20)$$

and D can be used to diagonalize \hat{H} ,

$$\hat{H}^\Lambda = D^{-1}\hat{H}D = \begin{pmatrix} E_3 & 0 & 0 & 0 \\ 0 & E_4 & 0 & 0 \\ 0 & 0 & E_1 & 0 \\ 0 & 0 & 0 & E_2 \end{pmatrix}, \quad (2.21)$$

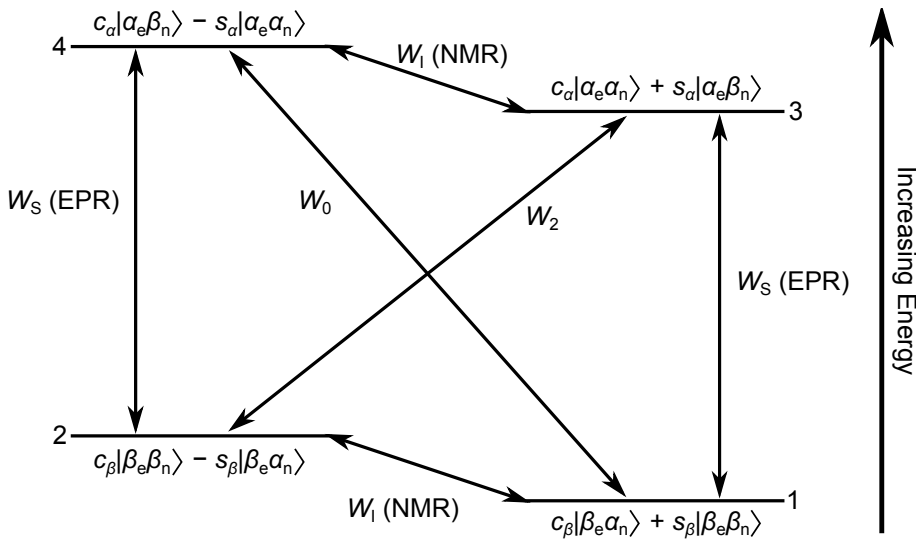


Figure 2.3: Energy level diagram of an e-n system in the solid state, where each possible quantum state is a mixture of the pure product states in Figure 2.2. The six possible transitions are shown: four SQ NMR and EPR transitions, indicated by W_1 and W_S respectively, and the DQ and ZQ transitions, indicated by W_2 and W_0 . The DQ and ZQ transitions are forbidden in the liquid state, but are weakly allowed in the solid state due to the mixing of quantum states caused by the off-diagonal matrix elements associated with the pseudo-secular part of the hyperfine interaction.

where the diagonal elements of \hat{H}^Λ represent the energy levels $E_{1,2,3,4}$,

$$E_{1,2} = -\frac{\omega_e}{2} \mp a_\beta, \quad (2.22)$$

$$E_{3,4} = +\frac{\omega_e}{2} \mp a_\alpha, \quad (2.23)$$

where $a_{\alpha,\beta} = \sqrt{\left(\frac{\omega_n}{2} \pm \frac{A}{4}\right)^2 + \left(\frac{C}{4}\right)^2}$.

\hat{H}^Λ is the Hamiltonian in its eigenbasis, the eigenvectors of \hat{H} . We now consider the effect of mw radiation: the mw Hamiltonian \hat{H}_{mw} , given by eq (2.14), must be transformed into the eigenbasis of \hat{H} using the diagonalization matrix D ,

$$\hat{H}_{\text{mw}}^\Lambda = D^{-1} \hat{H}_{\text{mw}} D = \frac{\omega_1}{2} \begin{pmatrix} 0 & 0 & f_1 & -f_2 \\ 0 & 0 & f_2 & f_1 \\ f_1 & f_2 & 0 & 0 \\ -f_2 & f_1 & 0 & 0 \end{pmatrix}, \quad (2.24)$$

where

$$f_1 = \cos\left(\frac{\eta_\alpha}{2} + \frac{\eta_\beta}{2}\right) = c_\alpha c_\beta - s_\alpha s_\beta \approx 1, \quad (2.25)$$

$$f_2 = \sin\left(\frac{\eta_\alpha}{2} + \frac{\eta_\beta}{2}\right) = s_\alpha c_\beta + c_\alpha s_\beta \approx 2s_{\alpha,\beta} \approx -\frac{C}{2\omega_n}. \quad (2.26)$$

Therefore, \hat{H}_{mw}^Λ can be written more simply as

$$\hat{H}_{mw}^\Lambda \approx \frac{\omega_1}{2} \begin{pmatrix} 0 & 0 & 1 & -2s \\ 0 & 0 & 2s & 1 \\ 1 & 2s & 0 & 0 \\ -2s & 1 & 0 & 0 \end{pmatrix}, \quad (2.27)$$

where

$$s = -\frac{C}{4\omega_n}. \quad (2.28)$$

Comparing \hat{H}_{mw}^Λ with \hat{H}_{mw} (eq (2.14)), it can be seen that \hat{H}_{mw}^Λ can generate the same SQ transitions as \hat{H}_{mw} , with a similar probability. However, in contrast to eq (2.14), the matrix elements ‘linking’ states $|\lambda_1\rangle$ and $|\lambda_4\rangle$, and states $|\lambda_2\rangle$ and $|\lambda_3\rangle$, which were zero in \hat{H}_{mw} , now have values $\pm s\omega_1$. This shows that the mw radiation can generate the previously forbidden ZQ ($|\lambda_1\rangle \longleftrightarrow |\lambda_4\rangle$) and DQ ($|\lambda_2\rangle \longleftrightarrow |\lambda_3\rangle$) transitions, with a probability proportional to $\left(\frac{C}{4\omega_n}\omega_1\right)^2$.

2.2.3 Dynamics of the solid effect

As described in the previous section, the pseudo-secular part of the hyperfine interaction, represented by the term $C\hat{S}_z\hat{I}_x$ in the Hamiltonian, causes a mixing of quantum states that allows the mw radiation to generate the previously forbidden ZQ ($|\lambda_1\rangle \longleftrightarrow |\lambda_4\rangle$) and DQ ($|\lambda_2\rangle \longleftrightarrow |\lambda_3\rangle$) transitions, with a probability proportional to $\left(\frac{C}{4\omega_n}\omega_1\right)^2$.

This section describes how ZQ or DQ transitions, combined with relaxation processes, can lead to an enhancement of the nuclear polarization via the SE, with the cases when the mw radiation is at the DQ frequency and the ZQ frequency considered separately. This section closely follows the description presented by Hovav et al. [46].

DQ radiation

Consider an e-n system, as described in the previous sections, initially at thermal equilibrium, as illustrated in Figure 2.4a. If the system is perturbed from its

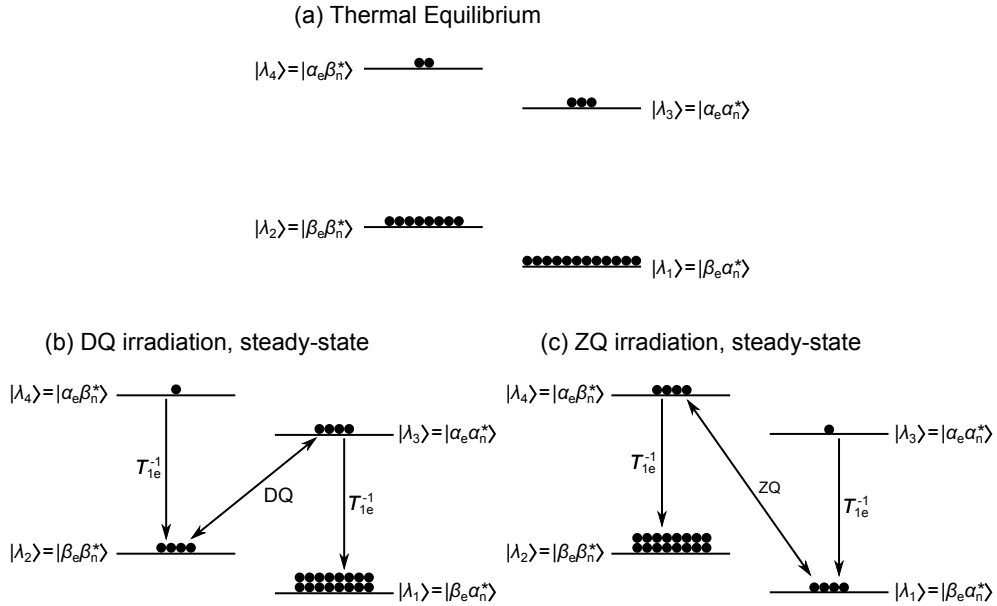


Figure 2.4: Energy level diagram of an e-n system in the solid state, showing relative populations (not to scale). (a) System at thermal equilibrium, with populations determined by a Boltzmann distribution. (b) and (c) System in a steady-state configuration (mw radiation applied for much longer than $T_{1,e}$) during mw radiation at the (b) DQ and (c) ZQ frequency, with the saturation condition fulfilled. Only the relevant transitions are shown, assuming $T_{1,e}^{-1}$ is much faster than all of the other relaxation processes. (b) Populations of states $|\alpha_e\alpha_n^*\rangle$ and $|\beta_e\beta_n^*\rangle$ are equal, while relative populations of states $|\alpha_e\beta_n^*\rangle$ and $|\beta_e\alpha_n^*\rangle$, and states $|\alpha_e\alpha_n^*\rangle$ and $|\beta_e\alpha_n^*\rangle$, are determined by Boltzmann statistics. This results in steady-state polarizations $P_n^{ss} = P_e^{ss} = P_e^{eq}$. (c) Populations of states $|\beta_e\alpha_n^*\rangle$ and $|\alpha_e\beta_n^*\rangle$ are equal, while relative populations of states $|\alpha_e\beta_n^*\rangle$ and $|\beta_e\beta_n^*\rangle$, and states $|\alpha_e\alpha_n^*\rangle$ and $|\beta_e\alpha_n^*\rangle$, are determined by Boltzmann statistics. This results in steady-state polarizations $P_n^{ss} = -P_e^{ss} = -P_e^{eq}$.

equilibrium configuration by, for example, mw radiation at one of the transition frequencies, relaxation processes act to restore the system to its equilibrium configuration. We first consider mw radiation at the DQ transition frequency ω_{DQ} . The relevant relaxation rates for this system are $T_{1,DQ}^{-1} = T_{1,23}^{-1}$, $T_{2,DQ}^{-1}$, $T_{1,e}^{-1}$, $T_{1,n}^{-1}$ and $T_{1,ZQ}^{-1} = T_{1,14}^{-1}$ [46]. To illustrate polarization enhancement by the SE, we begin by considering a simplified e-n system, in which the longitudinal electron relaxation ($T_{1,e}^{-1}$) is assumed to be much faster than the other relaxation processes, and all of the other relaxation processes are ignored. This is not necessarily a realistic assumption, but it is convenient because it illustrates the DQ SE in a relatively uncomplicated way.

Microwave radiation at the DQ transition frequency ω_{DQ} drives transitions between states $|\lambda_2\rangle$ and $|\lambda_3\rangle$. Because $p_2^{eq} > p_3^{eq}$, the mw radiation increases p_3 and decreases p_2 . Assuming the saturation condition $s^2\omega_1^2 \gg T_{1,DQ}^{-1}T_{2,DQ}^{-1}$ is

fulfilled, continued mw radiation will result in equilibration of the populations of states $|\lambda_2\rangle$ and $|\lambda_3\rangle$,

$$p_2^{\text{ss}} = p_3^{\text{ss}}, \quad (2.29)$$

where the superscript ss indicates that these are steady-state populations.

The mw radiation creates a non-Boltzmann distribution across the four energy states. However, longitudinal electron relaxation causes spins to relax from $|\lambda_3\rangle$ to $|\lambda_1\rangle$, and from $|\lambda_4\rangle$ to $|\lambda_2\rangle$. This acts to restore the Boltzmann distribution across the transitions $|\lambda_1\rangle \longleftrightarrow |\lambda_3\rangle$ and $|\lambda_2\rangle \longleftrightarrow |\lambda_4\rangle$. For times much longer than $T_{1,e}$, these Boltzmann distributions are restored,

$$\frac{p_3^{\text{ss}}}{p_1^{\text{ss}}} = \frac{p_4^{\text{ss}}}{p_2^{\text{ss}}} = \varepsilon_e = e^{-\hbar\omega_e/k_B T}. \quad (2.30)$$

The net result of the transitions induced by mw radiation and by longitudinal electron relaxation is an increase in p_2 with respect to p_1 , and an increase in p_4 with respect to p_3 . In other words, the nuclear polarization P_n is enhanced (see eq (2.10)). Using eqs (2.29) and (2.30), it is straightforward to show that the steady-state nuclear polarization is

$$\begin{aligned} P_n^{\text{ss}} &= \frac{1}{2} ((p_1^{\text{ss}} - p_2^{\text{ss}}) + (p_3^{\text{ss}} - p_4^{\text{ss}})) \\ &= \frac{1}{2} \frac{1 - \varepsilon_e}{1 + \varepsilon_e} \\ &= P_e^{\text{eq}}. \end{aligned} \quad (2.31)$$

This is illustrated in Figure 2.4b.

In this simplified model, we only considered mw radiation and longitudinal electron relaxation. When the other relaxation processes, with relaxation rates $T_{1,\text{DQ}}^{-1} = T_{1,23}^{-1}$, $T_{2,\text{DQ}}^{-1}$, $T_{1,\text{ZQ}}^{-1}$, and $T_{1,n}^{-1}$, are considered, the steady-state population difference between states $|\lambda_2\rangle$ and $|\lambda_3\rangle$ becomes more complicated than eq (2.29). It can be shown that, according to the steady-state Bloch equations, mw radiation at the DQ frequency applied for a time much longer than $T_{1,\text{DQ}}$ results in a steady-state population difference,

$$p_2^{\text{ss}} - p_3^{\text{ss}} = \frac{1 + (\Delta\omega_{\text{DQ}} T_{2,\text{DQ}})^2}{1 + (\Delta\omega_{\text{DQ}} T_{2,\text{DQ}})^2 + s^2 \omega_1^2 T_{1,\text{DQ}} T_{2,\text{DQ}}} (p_2^{\text{eq}} - p_3^{\text{eq}}), \quad (2.32)$$

where $\Delta\omega_{\text{DQ}} = \omega_{\text{DQ}} - \omega_{\text{mw}}$ and $\omega_{\text{DQ}} = \omega_e + \omega_n$ [46]. It is straightforward to see that, when the saturation condition $s^2\omega_1^2 \gg T_{1,\text{DQ}}^{-1}T_{2,\text{DQ}}^{-1}$ is fulfilled, and $\Delta\omega_{\text{DQ}} = 0$, the DQ radiation results in a population difference $p_2^{\text{ss}} - p_3^{\text{ss}} = 0$, and eq (2.32) reduces to eq (2.29).

ZQ radiation

The first part of this section demonstrated how continuous mw radiation at the DQ frequency creates a new steady-state configuration of populations, resulting in an increase in the polarization of the nuclear spins. Application of continuous mw radiation at the ZQ frequency also creates a new steady-state configuration of populations, with an increased nuclear spin polarization. The polarization enhancement mechanism for the ZQ SE is similar to the mechanism for the DQ SE described previously, and will be summarized briefly here.

Microwave radiation at the ZQ frequency drives transitions between states $|\lambda_1\rangle$ and $|\lambda_4\rangle$, and a steady-state population difference $p_1^{\text{ss}} - p_4^{\text{ss}}$, analogous to eq (2.32), can be derived. Under ideal saturating conditions, populations p_1 and p_4 equilibrate, while longitudinal electron relaxation restores the Boltzmann distributions across the transitions $|\lambda_1\rangle \longleftrightarrow |\lambda_3\rangle$ and $|\lambda_2\rangle \longleftrightarrow |\lambda_4\rangle$. For continuous mw radiation, the steady-state nuclear polarization (for times much longer than $T_{1,e}$) is then given by

$$P_n^{\text{ss}} = -\frac{1}{2} \frac{1 - \varepsilon_e}{1 + \varepsilon_e} = -P_e^{\text{eq}}. \quad (2.33)$$

This is illustrated in Figure 2.4c. Note that the enhanced polarizations for the DQ SE and the ZQ SE, in eqs (2.31) and (2.33) respectively, have the same magnitude but opposite sign.

2.2.4 Summary

This section has demonstrated that, for an e-n spin system, continuous mw radiation at the DQ or ZQ frequency can enhance the nuclear polarization. Steady-state nuclear polarizations were calculated for the simplified situations described, with the assumptions of sufficient mw power to saturate the respective transitions, and negligible relaxation rates compared with $T_{1,e}^{-1}$: it was shown that radiation at the DQ frequency and ZQ frequency results in positive and negative enhanced nuclear polarizations respectively, with the magnitudes of each enhanced polarization

equal to the thermal equilibrium electron polarization.

When only the effects of mw radiation and longitudinal electron relaxation are considered, and all other relaxation processes are disregarded, the steady-state polarization enhancement is relatively simple. This enhancement becomes more complex when other relaxation processes are included. Furthermore, the dynamic (time-dependent) polarization build-up can be particularly complex because of the many different processes involved. Polarization enhancement as a function of time often exhibits exponential behaviour, and is often fitted by a single exponential [40]. However, fitting such data with a single component can sometimes be an oversimplification, and may mask the true nature of the enhancement. It is conceivable that dynamic polarization enhancement can show multi-exponential behaviour, or even broad distributions of relaxation times, because of the many different processes involved, and that the time constants exhibited in the polarization build-up can be attributed to particular relaxation processes. This is discussed in more detail at the end of this chapter.

2.3 Cross effect

In a spin system consisting of two electron spins, with different resonance frequencies, coupled to one nuclear spin, the CE can be an effective solid-state DNP mechanism. Such a situation can arise in a radical with an inhomogeneously broadened EPR line, since an inhomogeneously broadened EPR line is made up of a series of homogeneously broadened spectral lines associated with electrons with different resonance frequencies. This is illustrated in Figure 2.5a, which shows an inhomogeneously broadened EPR line, and two of the homogeneously broadened spectral lines, with frequencies ω_{e1} and ω_{e2} , contributing to this line. The energy level diagram for a spin system comprising a nuclear spin coupled to two electrons with resonance frequencies ω_{e1} and ω_{e2} is shown in Figure 2.5b.

Polarization can be transferred from the electrons to the nucleus via the CE if the condition $|\omega_{e1} - \omega_{e2}| = \omega_n$ is satisfied. In Figure 2.5b, this corresponds to the energies of the states $|\beta\alpha\beta\rangle$ and $|\alpha\beta\alpha\rangle$ being equal. Calculations for CE DNP enhancement are given in references [47, 48], along with the results of simulations of polarization build-up.

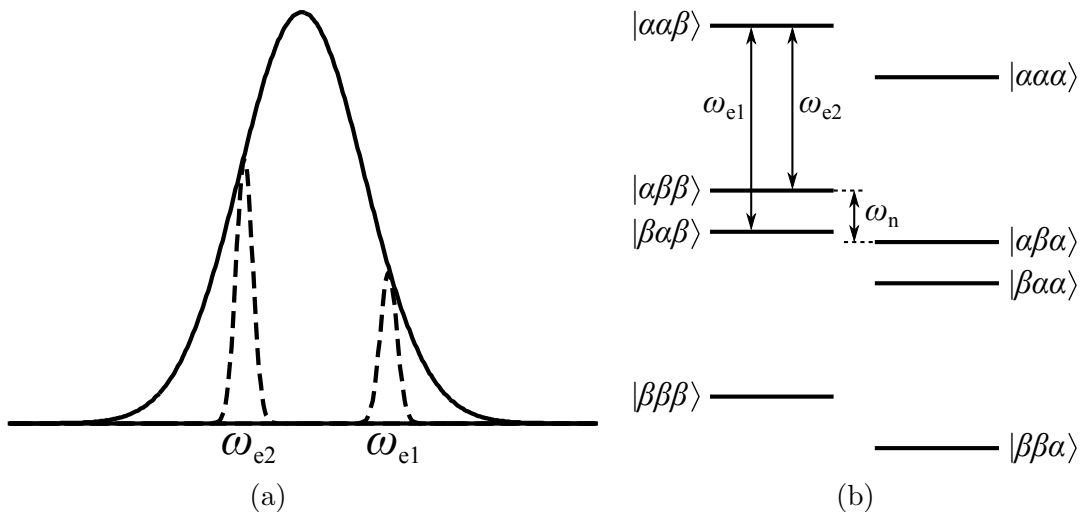


Figure 2.5: Illustration of the requirements for the CE. (a) An inhomogeneously broadened EPR spectral line (solid line), and two of the homogeneously broadened lines (dashed lines) at frequencies ω_{e1} and ω_{e2} contributing to this spectral line. (b) Energy level diagram for a system of two electrons and a nucleus, with frequencies ω_{e1} , ω_{e2} , and ω_n , respectively. The three states in each Dirac ket refer to electron 1, electron 2, and the nucleus, respectively. The CE matching condition, $|\omega_{e1} - \omega_{e2}| = \omega_n$, is equivalent to the energies of states $|\beta\alpha\beta\rangle$ and $|\alpha\beta\alpha\rangle$ being equal.

2.4 Thermal mixing

Before thermal mixing is described, it is useful to briefly introduce the concept of spin temperature. For a system of spins at thermal equilibrium, the populations of the quantum states are determined by a temperature-dependent Boltzmann distribution defined in eq (1.68). Conversely, when such a system is taken away from thermal equilibrium, it is often possible to define an effective ‘spin temperature’ of the system through the population distribution,

$$p_i = \frac{1}{Z} \exp\left(-\frac{E_i}{k_B T_s}\right), \quad (2.34)$$

where E_i and p_i are the energy and population of a state labelled i , Z is the partition function, and T_s is the spin temperature. Spin temperature is illustrated by some extreme examples of population distributions in Figure 2.6. Figure 2.6a corresponds to a system at thermal equilibrium, with T_s equal to the thermal equilibrium temperature T^{eq} . Figure 2.6b shows an inverted population distribution, with $T_s = -T^{\text{eq}}$. In Figure 2.6c the populations of all states are equal, and thus $T_s = \infty$. Finally, Figure 2.6d shows the population distribution at $T_s = 0$, with all spins in the lowest energy state. Figures 2.6b and 2.6c correspond to the situations

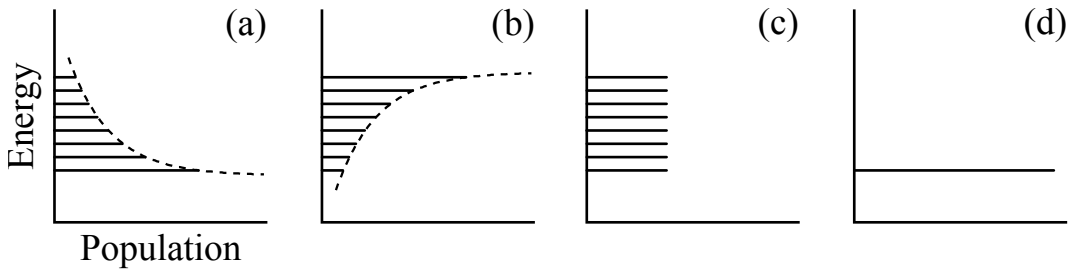


Figure 2.6: An illustration of spin temperature for a system of eight quantum states i with equally spaced energy levels. Solid lines represent quantum states, with the vertical position of the lines representing energy and the lengths of the lines representing relative populations p_i . Spin temperature T_s is defined by the population distribution $p_i = \frac{1}{Z} \exp\left(-\frac{E_i}{k_B T_s}\right)$, where E_i is the energy of state i and Z is the partition function. (a) Thermal equilibrium: $T_s = T^{\text{eq}}$, where T^{eq} is the thermal equilibrium temperature. (b) $T_s = -T^{\text{eq}}$. (c) $T_s = \infty$. (d) $T_s = 0$.

immediately following an ideal 180° pulse and 90° pulse respectively.

For a system of isolated electrons or spin- $\frac{1}{2}$ nuclei, the polarization P is expressed in terms of the spin temperature as

$$P = \tanh\left(\frac{|\gamma| \hbar B_0}{2k_B T_s}\right), \quad (2.35)$$

where γ is the gyromagnetic ratio of the spins. Clearly, an increase in the polarization of nuclear spins corresponds to a reduction in the nuclear spin temperature, or a ‘cooling’ of the nuclear spin system.

Thermal mixing is the dominant solid-state DNP mechanism when the EPR spectral line has a linewidth greater than the nuclear Larmor frequency, and mw radiation can saturate the whole spectrum rather than burn a spectral hole.

Microwave radiation at a frequency close to, but slightly off-resonance from, the electron resonance frequency saturates a transition at that frequency. Cross-relaxation then proceeds via flip-flop processes, spreading the saturation through the spectral line, and a new steady-state is established in the electron spin system. For flip-flops involving two electron spins with Larmor frequencies which differ by the nuclear Larmor frequency (in other words, spins which satisfy $|\omega_{e1} - \omega_{e2}| = \omega_n$ (see Figure 2.5)), nuclear spins can also change sign in energy-conserving three-spin processes. Thereby, the nuclear spin order is enhanced, and the polarization is increased [49].

This process can also be described thermodynamically, as follows. The system is divided into three subsystems: an electron Zeeman bath (EZB), a nuclear Zee-

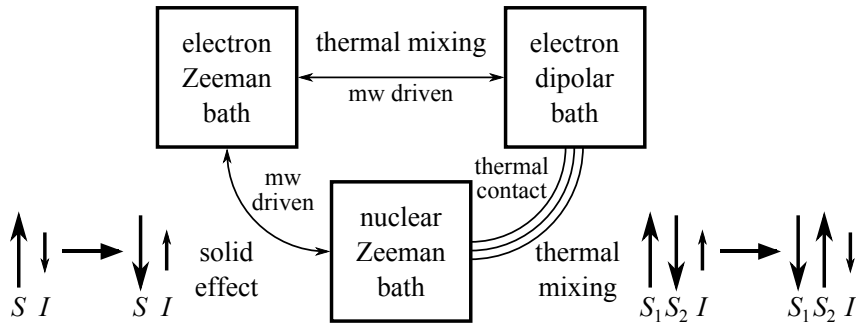


Figure 2.7: An illustration of the thermodynamic description of thermal mixing. As described in the text, off-resonance mw radiation cools the electron dipolar bath (EDB). Three-spin exchange process, each involving two electron spins S_1 and S_2 and a nuclear spin I , then cool the nuclear Zeeman bath (NZB), due to the thermal contact between the EDB and the NZB. The solid effect is also illustrated. Thermodynamically, the solid effect corresponds to a cooling of the NZB directly by the electron Zeeman bath. Diagram adapted from [50].

man bath (NZB), and an electron dipolar bath (EDB), as shown in Figure 2.7 [50]. Each of these ‘spin baths’ has a spin temperature associated with it. The mw radiation has two roles: it reduces the spin temperature of, or ‘cools’, the EDB, and it thermally connects the electron system with the nuclear spins [38]. The EDB, which has been cooled by the mw radiation, then cools the NZB, therefore increasing the nuclear polarization.

In the high-temperature limit, the density matrix can be linearly expanded, and the evolution of the spin system can be described quantitatively by a system of rate equations formulated by Provotorov [38]. At low temperatures, however, when the high-temperature approximation is no longer valid, the density matrix cannot be linearly expanded, and the spin temperature concept needs to be modified. Borghini proposed a spin temperature model for TM DNP at low temperatures, which also accounts for inhomogeneously broadened EPR spectra [38, 51]. Recently, Hovav et al. have performed simulations of low temperature TM DNP with spin systems comprising seven electrons and one nucleus. Although these systems were too small to accurately represent physical spin systems in which TM would take place, they were sufficiently large to demonstrate the existence of well-defined spin temperatures and the presence of TM [52].

2.5 Spin diffusion

When describing samples containing paramagnetic centres, such as a solution containing a DNP polarizing agent, a distinction is often made between core nuclei and bulk nuclei. Although there is no precise, consistently applied definition of these two types of nuclei, it is generally accepted that nuclei close to the unpaired electron, which have a significantly shifted resonance frequency due to the electron spin, are core nuclei, while nuclei further from the unpaired electron are bulk nuclei. These two groups of nuclei are separated by a so-called diffusion barrier [53, 54]. This is illustrated in Figure 2.8.

The bulk nuclei, whose Larmor frequencies are not significantly shifted by the electron, are the nuclei which are ‘observed’ in an NMR experiment. Conversely, core nuclei would be expected to have a broad distribution of frequencies, and may be too few in number to be observed. Therefore, it is important to understand the mechanisms which transfer enhanced polarization to bulk nuclei, since it is these nuclei which contribute to the NMR signal.

Transport of enhanced polarization through a system of nuclear spins is mediated by nuclear spin diffusion. This involves energy-conserving ‘flip-flop’ interactions, in which a pair of neighbouring nuclear spins simultaneously flip in opposite directions.

Several possible bulk polarization pathways have been described [55, 56]. One possibility is that polarization enhancement of bulk spins is a two-step process,

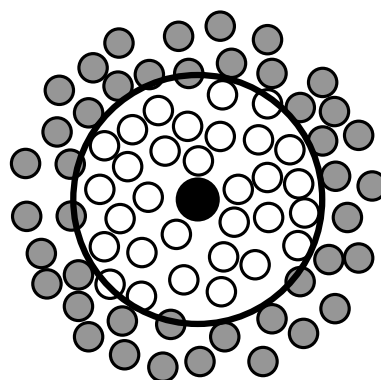


Figure 2.8: An illustration of core nuclei, bulk nuclei, and the diffusion barrier. Core nuclei (white circles) close to the electron spin (solid black circle) are distinguished from bulk nuclei (grey circles) far from the electron spin. These two groups of nuclei are separated by the diffusion barrier (large black circle). This illustration is not representative of the shape of the diffusion barrier or the number of nuclear spins inside it. Diagram adapted from [55].

involving polarization of core nuclei, followed by nuclear spin diffusion across the diffusion barrier. In this case, the spin diffusion across the diffusion barrier would be the slower of the two processes, thereby determining the overall rate of polarization build-up. Note that, in this proposed pathway, it may be necessary to consider a third step—enhanced polarization transfer away from the diffusion barrier by relatively fast spin diffusion between bulk spins—in addition to the two steps mentioned.

Another possible mechanism is that bulk spins are polarized directly, and enhanced polarization spreads through the sample by spin diffusion between bulk spins. In this case, core spins are also polarized, but do not transfer their enhanced polarization to the bulk spins. Instead, they relax, and act as a ‘polarization sink’.

A third possibility is that the diffusion barrier can be ignored altogether, and nearby spins can be treated as bulk spins. In this model, all nuclei are polarized by the electron, and spin diffusion is fast among all spins whose polarization is enhanced.

Smith et al. compared these three possible models, and presented data consistent with the second model, suggesting that bulk spins are polarized directly, and core spins act as a polarization sink. They also noted that this model predicts that polarization of core spins is a faster process than polarization of bulk spins, and that core polarization enhancement increases the effective electron relaxation rate [55].

Hovav et al. performed simulations of SE DNP and spin diffusion, considering a linear chain of spins consisting of an electron hyperfine-coupled to a core nucleus, which is in turn dipolar-coupled to a chain of up to eight bulk nuclei which are not directly coupled to the electron [56]. They concluded that the polarization enhancement of core spins and spin diffusion processes should not be treated independently, but instead that polarization enhancement of bulk spins should be considered as ‘DNP-assisted spin diffusion’. They also noted that spin diffusion in DNP depends on a large number of parameters, whose contributions to DNP enhancement must be carefully analysed.

Köckenberger and co-workers have performed simulations of DNP enhancement with up to 25^3 spins [57]. Van der Drift presented elegant illustrations of some of these simulations, two of which are reproduced in Figures 2.9 and 2.10. For these simulations, the spin system consisted of an electron at the centre of a system of 1330 nuclei arranged in an $11 \times 11 \times 11$ cubic lattice. To demonstrate the

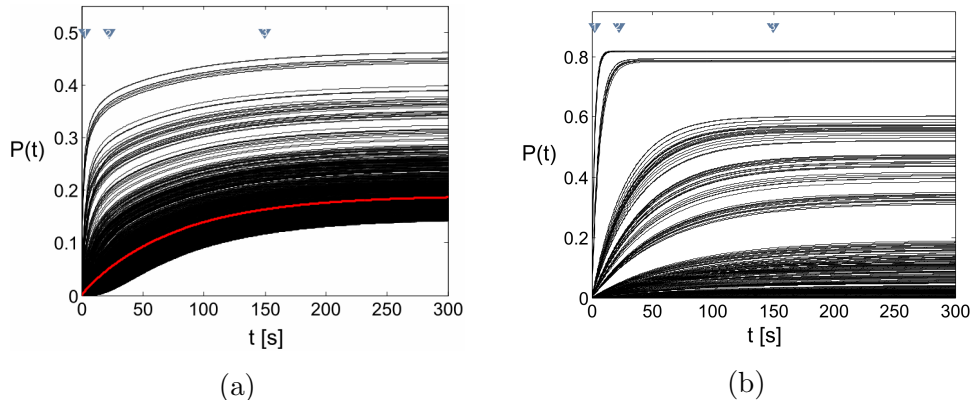


Figure 2.9: Polarization build-up for simulations of the SE in a system of one electron and 1330 nuclei. (a) Simulation performed with all relevant spin interactions included. Red line shows average polarization build-up of ‘observable’ nuclei (defined as those nuclei with a hyperfine interaction constant of less than 500 Hz). (b) Simulation performed with nuclear dipolar interaction set to zero. Reproduced with permission from Anniek van der Drift [15].

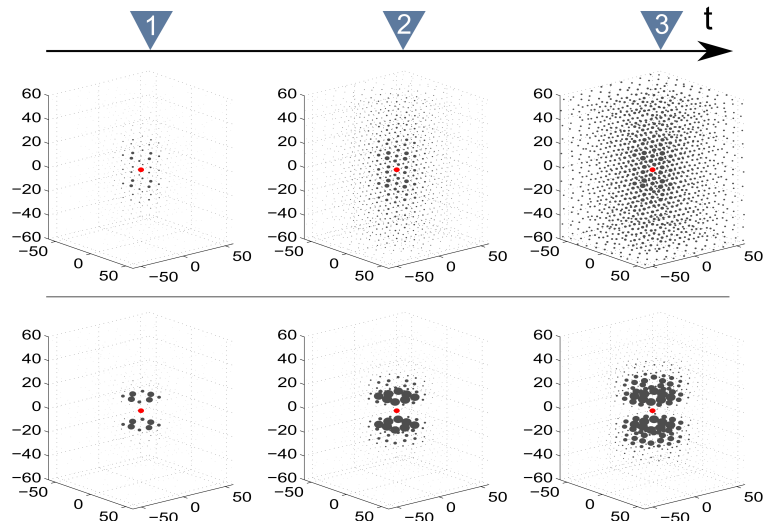


Figure 2.10: Spatial distribution of polarization build-up for simulations of the SE in a system of one electron and 1330 nuclei, at the three different time points indicated by the inverted triangles numbered 1, 2 and 3 in Figure 2.9. Red dot is electron, black dots are nuclei, with the size of the dots indicating relative polarization. All axis units are in Å. Top row: simulation performed with all relevant spin interactions included. Bottom row: simulation performed with nuclear dipolar interaction set to zero. Reproduced with permission from Anniek van der Drift [15].

effect of spin diffusion, simulations were performed twice, once with and once without nuclear dipolar interactions [15]. When nuclear dipolar interactions were neglected (Figure 2.9b and bottom row of Figure 2.10), a small proportion of nuclei were polarized very strongly, while others were polarized much more weakly. Conversely, when nuclear dipolar interactions were included ((Figure 2.9a and top row of Figure 2.10)), enhanced polarization spread out more evenly through a greater number of nuclei. This suggests that spin diffusion is a crucial factor in transferring enhanced polarization through a system of nuclear spins. Note that, in both cases, there was a broad distribution of polarization build-up rates.

Finally, it is worth mentioning briefly that Ramanathan and co-workers have studied and compared the diffusion of dipolar order and Zeeman order, and found that dipolar spin diffusion is significantly faster than Zeeman spin diffusion [58,59]. Ramanathan has also described spin diffusion, and the importance of the diffusion barrier, in detail in a recent review article [60].

2.6 Simulating solid-state DNP

As described in the previous sections, there are three distinct enhancement mechanisms in solid-state DNP: the solid effect, cross effect, and thermal mixing. Another mechanism, nuclear spin diffusion, is responsible for the transfer of enhanced nuclear polarization through a sample. A current area of interest is an extension of our theoretical understanding of these mechanisms, and in particular an improvement of simulations used to describe DNP experiments [49,55,61–64]. This section is a brief review of some of the recent efforts at simulating solid-state DNP.

Karabanov et al. have developed simulations of DNP spin systems using Krylov-Bogolyubov averaging to confine the state space to the zero quantum coherence subspace. The space is truncated at a low spin order, and only certain relaxation terms are retained when the relaxation superoperator is derived [48,62]. Using this method, the dimensions of simulations in Liouville space can be dramatically reduced, and a spin system comprising up to 25^3 spins can currently be simulated [57].

Hovav et al. have presented numerical calculations of polarization enhancement ε involving SE, CE, and TM. Their approach, using the density operator formalism, is based on diagonalization of the static spin Hamiltonian and evaluation of effective mw amplitudes and relaxation rates. They discussed the dependence of

ε on spin interaction and relaxation parameters, as well as on mw power and frequency [46, 47, 52]. For organic radicals with broad EPR lines, they showed that off-resonant electrons, which are not actively involved in DNP enhancement, do influence on-resonant electrons and hence the DNP enhancement [61].

Griffin and co-workers used a different approach to simulating DNP, neglecting relaxation, and described the evolution of the density operator in SE and CE DNP as the transfer of electron Zeeman order to nuclear Zeeman order, with the aim of evaluating the time-dependent growth of the DNP enhancement [65]. They also compared different models of polarization transfer, and discussed the role of nuclear spin diffusion in the enhancement process, as described in Section 2.5 [55].

Sezer et al. used molecular dynamics simulations to calculate liquid-state DNP enhancement profiles in a two-spin system, using semi-classical relaxation theory to analyze the electron saturation [63].

Finally, Thurber and Tycko calculated theoretical CE enhancements in MAS DNP, and looked at the dependence of ε on various parameters, including MAS frequency, mw field strength and hyperfine and electron-electron coupling strengths [64].

2.7 Polarizing agents

Polarization enhancement using DNP requires the presence of an unpaired electron. In solid and liquid state DNP, organic molecules with one or more unpaired electron, known as polarizing agents, are often used. Two particularly important properties of polarizing agents are the width of the EPR spectral line and the nature of the broadening, as these factors can determine the operative DNP mechanisms in solid state DNP. As described in the introduction to this chapter, if the EPR linewidth δ is smaller than ω_n , the SE is usually the dominant mechanism, while if δ is greater than ω_n , the CE dominates for samples with inhomogeneously broadened EPR lines, in which hole-burning is possible, while TM dominates for samples with homogeneously broadened lines, for which mw radiation saturates the whole spectrum [42, 43].

Many polarizing agents used in DNP are derived from 2,2,6,6-tetramethylpiperidine-1-oxyl (TEMPO), a small organic molecule with a stable nitroxyl radical, shown in Figure 2.11a. TEMPO itself can be used as a polarizing agent, but derivatives of TEMPO with increased solubility are more commonly used. Ex-

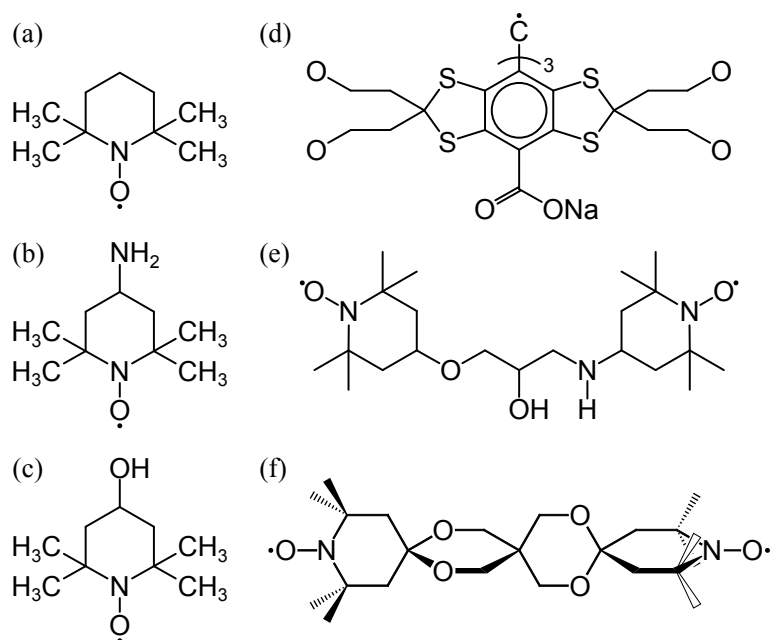


Figure 2.11: Some polarizing agents commonly used in DNP. (a) TEMPO. (b) 4-Amino-TEMPO. (c) 4-Hydroxy-TEMPO (TEMPOL). (d) Ox063 trityl. (e) TOTAPOL. (f) bTbk.

amples include 4-Amino-TEMPO (Figure 2.11b) and 4-Hydroxy-TEMPO, also known as TEMPOL (Figure 2.11c).

The principal g -values of TEMPO are $g_{xx} = 2.0094$, $g_{yy} = 2.0061$, and $g_{zz} = 2.0021$ [66], and its EPR spectral line has an inhomogeneous width of approximately 600 MHz at $B_0 = 3.4$ T. This is significantly greater than the Larmor frequencies of hydrogen (145 MHz) and carbon-13 (36 MHz), so the CE and TM would be expected to be the dominant mechanisms in solid-state DNP using TEMPO and its derivatives.

Another radical commonly used in DNP is tris{8-carboxyl-2,2,6,6-tetra[2-(1-hydroxyethyl)]-benzo(1,2-d:4,5d')bis(1,3) dithiole-4-yl} methyl sodium salt (Ox063 trityl), shown in Figure 2.11d. The principal g -values of trityl are approximately isotropic ($g_{xx} = 2.0034$, $g_{yy} = 2.0031$, and $g_{zz} = 2.0027$ [42]), so trityl has a much narrower EPR spectral linewidth than TEMPO. At $B_0 = 3.4$ T, $\delta \sim 30$ MHz, which is significantly smaller than the Larmor frequency of hydrogen, and slightly smaller than that of carbon-13. Therefore, the SE tends to dominate in solid-state DNP when trityl is used as a polarizing agent.

Other molecules which can be used for DNP include 1,3-bisdiphenylene-2-phenylallyl (BDPA) [39,67,68] and 2,2-diphenyl-1-picrylhydrazyl (DPPH) [67,69]. BDPA is similar to trityl, in that the unpaired electron is centred on a carbon

atom. However, use of BDPA and DPPH for DNP is not widespread because both suffer from poor solubility in conventional DNP solvents.

Griffin and co-workers have demonstrated DNP enhancement using a variety of different biradicals, which are formed by tethering two TEMPO derivatives. Such molecules constrain the distance between the two unpaired electrons, so these molecules can be used to optimize the efficiency of CE DNP, since the dipolar interaction between the electrons depends on their separation. In their first example, the TEMPO molecules were tethered with a variable-length flexible* poly(ethylene glycol) chain [70]. A new biradical, 1-(TEMPO-4-oxy)-3-(TEMPO-4-amino)propan-2-ol (TOTAPOL) [71], shown in Figure 2.11e, was later introduced and shown to have unpaired electrons with a stronger dipolar coupling. The efficiency of the CE can be further increased by constraining the relative orientations of the TEMPO rings, since this determines the relative orientations of the *g*-matrices of the two unpaired electrons, and hence influences the frequency difference. This was demonstrated with rigid biradicals, including bis-TEMPO-bisketal (bTbk) [72], shown in Figure 2.11f, and bis-TEMPO-bis-thioketal-tetra-tetrahydropyran (bTbtk-py) [73]. bTbk and bTbtk-py share an important similarity in that the TEMPO rings are orthogonal in both molecules. However, the use of bTbk for DNP is restricted since it has a low solubility in conventional DNP solvents.

Under certain conditions, mixtures of radicals can increase the efficiency of DNP, as has been demonstrated with mixtures of trityl and 4-Hydroxy-TEMPO. At $B_0 = 5$ T, the maxima of the trityl and TEMPO EPR spectra are separated by approximately 225 MHz, which is close to the hydrogen Larmor frequency of 211 MHz. Therefore, the CE condition $|\omega_{e_1} - \omega_{e_2}| = \omega_n$ can be satisfied by a higher fraction of electrons than in a sample in which a TEMPO derivative is the sole polarizing agent [42].

Finally, paramagnetic transition metal ion complexes can also be used as polarizing agents in DNP. For example, the use of Mn^{2+} and Gd^{3+} complexes has recently been demonstrated [74, 75].

*In this context, the term ‘flexible’ is used to describe the fact that the carbon-carbon bonds can rotate, so the relative orientations of the TEMPO rings are not constrained.

2.8 Discussion

This chapter has introduced the main mechanisms for polarization enhancement in liquid-state and solid-state DNP.

When DNP experiments are performed, the enhancement process is often characterized by two main parameters: relative nuclear polarization enhancement ϵ , defined in eq (2.1), and polarization build-up rate, often expressed as the build-up time constant τ_{buildup} which fits the equation,

$$P_n(t) = P_n^{\max} \left(1 - e^{-t/\tau_{\text{buildup}}}\right), \quad (2.36)$$

where $P_n(t)$ and P_n^{\max} are the time dependent nuclear polarization and maximum achievable nuclear polarization, respectively. This can be a satisfactory approach if the data exhibits mono-exponential behaviour, or if one is only interested in measuring the overall polarization enhancement time. However, if multi-exponential experimental data is to be compared with simulations or theoretical models, it can be necessary to analyse such data more closely. If multi-exponential data is fitted with a mono-exponential function, such as eq (2.36), this fit can hide the underlying behaviour.

For the simplest solid-state DNP enhancement mechanism, SE DNP without spin diffusion, the polarization enhancement depends on at least two processes, mw driven transitions and electron longitudinal relaxation, as shown in Figure 2.4. Therefore, it is conceivable that polarization enhancement in this case could exhibit bi-exponential behaviour, or even multi-exponential behaviour with more than two time constants or a distribution of time constants. When the operative mechanism is the CE or TM, and when spin diffusion is considered, many more spins and processes are involved in the polarization enhancement, so it is possible that polarization enhancement could exhibit multi-exponential behaviour with many time constants, because of the many different processes involved. Under certain conditions, more than one mechanism can be responsible for polarization transfer, and this complicates the build-up further still [76]. Furthermore, anisotropy of interaction strengths and g -values can cause time constants to be orientation dependent. In a glassy sample, this can lead to broad distributions of time constants. Multi-exponential polarization build-up has been demonstrated in simulations of SE DNP [15], but it is something that is not yet fully understood.

The solid-state DNP mechanisms depend on many parameters. These can

be broadly grouped into two categories (with some overlap): purely experimental parameters (magnetic field, mw frequency, mw power, temperature, sample, concentration, solvent, and extent of deuteration); and intrinsic properties of the sample, which in turn depend on experimental parameters (electron and nuclear relaxation times, hyperfine and dipolar interaction strengths, diffusion rates (spectral, instantaneous, and spin), and cross-relaxation rates).

If DNP experiments are to be optimized, it is important to understand how experimental parameters affect the DNP mechanisms. Simulations of DNP can be used to better understand the DNP mechanisms and the effect that these parameters have on the enhancement mechanisms, and hence they can be used as a tool to improve experimental methods [50]. Therefore, it is important to know the intrinsic parameters accurately if these simulations are to accurately represent realistic experimental conditions.

The two challenges described in this discussion, the ‘multi-exponentiality’ of polarization enhancement, and the dependence of polarization enhancement on a significant number of parameters and processes, are the motivations for a large amount of the work presented in this thesis. In Chapter 4, a probe that was built to measure DNP processes and parameters using both NMR and EPR detection is described. This probe has been used for two main sets of experiments, which are described in subsequent chapters: Chapter 6 describes experiments investigating the behaviour of electron magnetization during mw irradiation, designed to study dynamic processes including spectral diffusion and saturation, and Chapter 7 describes measurements of relaxation of DNP-enhanced nuclear polarization over short time-scales and at different offset frequencies. In Chapter 5, an inverse Laplace transform algorithm for extracting distributions of time constants from multi-exponential data is described. This algorithm was used to analyse the data in Chapters 6 and 7.

Chapter 3

NMR and EPR Detection

3.1 Introduction

In both NMR and EPR experiments, an ensemble of spins is placed in a static magnetic field \mathbf{B}_0 , and an oscillating magnetic field \mathbf{B}_1 , at or near the resonance frequency of the spins, is applied (see Section 1.1). \mathbf{B}_1 perturbs the spins from thermal equilibrium, and the spins produce oscillating fields in response, which can be detected as an NMR or EPR signal. Although these basic principles of NMR and EPR experiments are very similar, in practice the implementation is very different. Electrons have a much larger gyromagnetic ratio than nuclei, and consequently a much larger resonance frequency at a given magnetic field (see Table 3.1). The vast difference in NMR and EPR detection frequencies means that different experimental apparatus must be used. In NMR, radio-frequency (rf) electrical signals are created by an rf synthesizer, amplified, and transmitted to a coil of wire which is part of a resonant circuit, and within which sits the sample. The amplifier and coil are connected by a coaxial cable. Conversely, EPR uses microwave (mw) fields, which are generated by a mw oscillator, amplified, and transmitted through a wave-guide to the sample, which sits inside a mw resonator.

spin	gyromagnetic ratio γ (rad s ⁻¹ T ⁻¹)	$\omega_0/2\pi$ at $B_0 = 3.4$ T
electron	-1.7609×10^{11}	95.285 GHz
hydrogen-1	2.6752×10^8	144.76 MHz
carbon-13	6.7283×10^7	36.409 MHz

Table 3.1: Gyromagnetic ratios of electrons, hydrogen-1 and carbon-13, and resonance frequencies at 3.4 T [1, 2].

This chapter describes various aspects of NMR and EPR detection. Section 3.2 is a description of conventional (transverse) EPR detection, and Section 3.3 introduces an alternative EPR detection method, known as longitudinal detection (LOD). The majority of EPR experiments conducted during this PhD used longitudinal detection, so only a very brief outline of the basic principles of conventional EPR detection is given in this chapter, while LOD is described in more detail. Section 3.4 describes the main components of an NMR system: transmission lines, resonant circuits, and coils. Section 3.5 describes quadrature detection in the context of a simple NMR experiment. Finally, the instruments comprising the EPR and NMR spectrometer used in our laboratory are described in Section 3.6.

3.2 Conventional EPR detection

In conventional EPR, a sample sits in a resonator in a magnetic field \mathbf{B}_0 , a microwave field with a fixed frequency is applied to the sample, and EPR signal is detected at the same fixed frequency. EPR experiments can be divided into two categories: continuous wave (CW) and pulsed. In a typical CW EPR experiment, mw radiation is applied continuously, B_0 (the amplitude of \mathbf{B}_0) is swept, and the reflected mw power is measured as a function of B_0 . In pulsed EPR, a short mw pulse, with a large bandwidth compared with CW mw radiation, is applied to the sample and the response of the sample to the pulse is recorded.

A schematic diagram of an EPR spectrometer is shown in Figure 3.1. The main elements of an EPR detection system are described in the following sections.

3.2.1 Microwave field production and transmission

In our set-up, the microwave field is generated by either a dielectric resonator oscillator (DRO), with a fixed output frequency of 94.899 GHz, or a voltage controlled oscillator (VCO), with a tunable output frequency of 94.92 ± 0.34 GHz. The mw bridge has three output channels: two pulse channels and a continuous wave channel. The oscillators are collectively known as the system of master oscillators (STAMO).

The mw field passes through a DC controlled attenuator, and is transmitted to the sample by a wave-guide. As can be seen in Figure 3.1, the same wave-guide is used to transmit both the mw field and the EPR signal. A circulator is used to

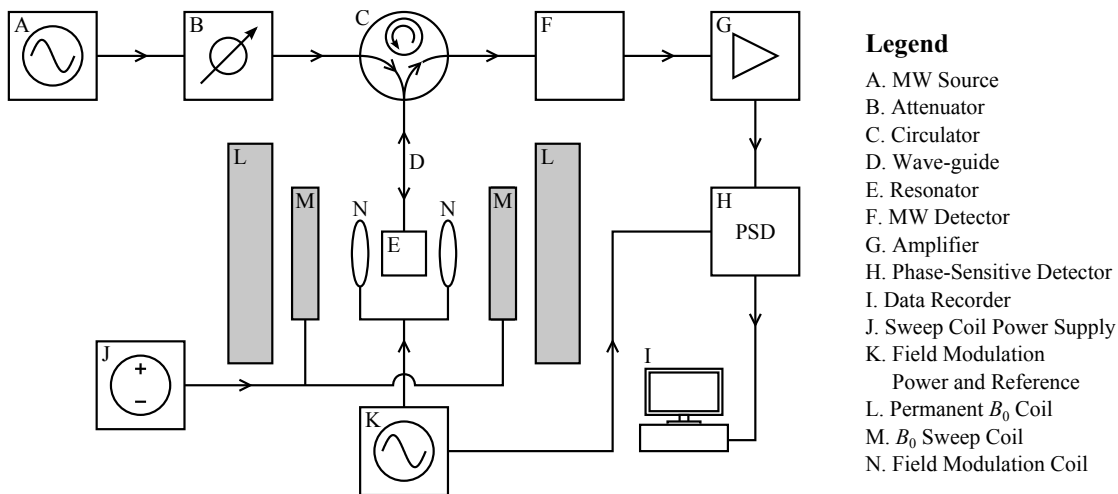


Figure 3.1: Schematic diagram of an EPR spectrometer. Adapted from [77].

direct the mw field from the source to the sample, and the EPR signal from the sample to the detector.

3.2.2 Resonator

The sample sits inside a resonator, which, at W-band frequencies and above, is usually an optical resonant cavity, but other types of resonator can also be used [78]. An optical resonant cavity is an enclosure with electrically conductive interior surfaces and an iris through which radiation enters. Reflection of waves from the surfaces leads to interference: for radiation with a wavelength λ which satisfies $a = n\frac{\lambda}{2}$, where a is a cavity dimension and n is an integer, constructive interference occurs and standing waves are formed. For all other wavelengths, destructive interference occurs. Thereby, the amplitude of the radiation may be dramatically increased at certain positions within the cavity for radiation with $\lambda = \frac{a}{2n}$. The frequency of radiation with $\lambda = \frac{a}{2}$ is known as the *fundamental resonance frequency* of the cavity.

In CW EPR, the resonator is tuned to the frequency of the mw source and coupled to the wave-guide, such that all energy incident on the resonator at this frequency is completely absorbed. When the resonance condition is satisfied, that is when the electron Larmor frequency $\omega_e = \frac{g_e \mu_B}{\hbar} B_0$ matches the frequency of the mw radiation ω_{mw} , additional absorption by the sample occurs, the resonator becomes de-tuned, and mw power is reflected by the resonator [79].

In pulsed EPR, a short mw pulse, or series of such pulses, is applied to the sample and the response of the sample to the pulse(s) is recorded. Due to the

finite length τ_p of a pulse, spins in a larger frequency range can be excited than with CW EPR, since the excitation bandwidth of a pulse is approximately τ_p^{-1} . EPR signal cannot be recorded during or immediately after the pulse, because pulsed EPR uses higher power radiation than CW EPR, and the reflected power can damage the receiver. In addition, the dissipation of energy by the resonator, known as ring-down, can obscure the EPR signal and even damage the receiver, so there is a ‘dead-time’ before any signal can be recorded.

3.2.3 Static magnetic field

In our set-up, two independent superconducting coils are used to produce the static magnetic field \mathbf{B}_0 . The first of these produces a persistent field of 3.39 T. The second coil is a sweep coil, capable of producing a field which can be swept through the range ± 0.1 T. For a typical CW EPR experiment, the frequency of the mw field is fixed, and the amplitude of the magnetic field, B_0 , is swept, with the EPR signal being recorded as a function of B_0 .

3.2.4 Field modulation

CW EPR detection with a static magnetic field can suffer from large noise contributions, or slow drifts of the signal. Improvements in the SNR can be made by applying a small oscillatory magnetic field, known as the *modulation field*, and detecting the EPR signal at this frequency. The modulation field is oriented along the direction of the static field, and is usually produced using a pair of coils either side of the resonator. It can be expressed as $B_M \sin(\omega_M t)$, where B_M is the amplitude of the field, and the modulation frequency $\frac{\omega_M}{2\pi}$ is typically about 100 kHz. A consequence of the modulation field is that the recorded signal is proportional to the first derivative of the EPR absorption lineshape, as illustrated in Figure 3.2.

3.2.5 Detection

EPR signal is transmitted from the resonator to the receiver, where it is combined with a reference signal in a quadrature detector, resulting in two signal components with a phase difference of 90°. Quadrature detection, and the reasons for using it, are described in Section 3.5 in the context of NMR detection. For CW EPR, the signal is then amplified at the frequency of the field modulation ω_M and recorded using a phase-sensitive detector.

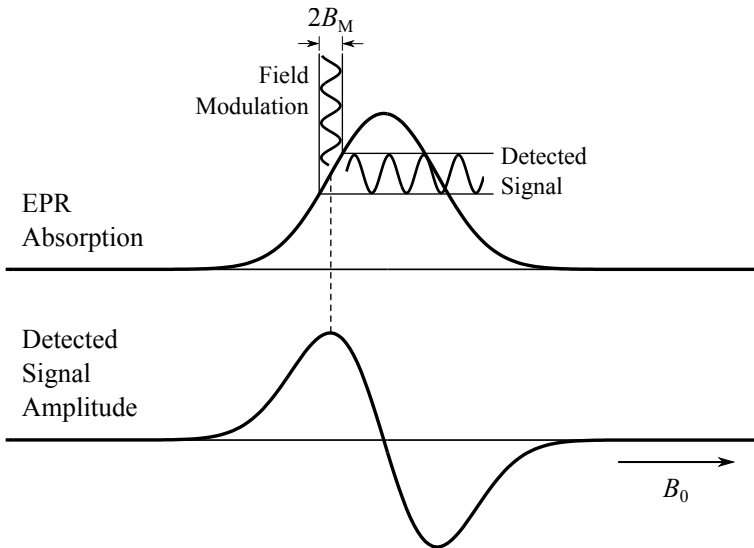


Figure 3.2: Effect of the modulation field. A low amplitude field $B_M \sin(\omega_M t)$ is added to the static field, where B_M is the amplitude of the field, and the modulation frequency $\frac{\omega_M}{2\pi} \sim 100$ kHz. The detected signal, also oscillating at a frequency $\frac{\omega_M}{2\pi}$, has an amplitude proportional to the first derivative of the EPR absorption lineshape. Adapted from Weil et al. [78].

3.3 Longitudinally detected EPR

An alternative method for EPR signal measurement is longitudinal detection (LOD), in which changes in the z -component of the electron magnetization, M_z , are detected using a coil with its axis aligned parallel with the B_0 field. LOD has several advantages compared with transverse detection. It is possible to detect signals during high-power mw irradiation [80], there is no experimental dead-time, it is more robust, and it is in principle possible to measure faster longitudinal relaxation processes than can be measured with conventional EPR. It is also not necessary to place the sample in a mw resonator, meaning that experiments utilizing multiple excitation frequencies can be performed, and larger samples can be used. This makes it easier to perform LOD EPR, DNP and NMR experiments with a single probe. Finally, it can be performed with an unstabilized mw source [81], and it is cheaper to set up.

This section provides a brief overview of LOD: the detection circuit is described and the equation for the detected voltage is derived using a simple harmonic oscillator (SHO) model. This description is based on the approach presented in reference [20].

3.3.1 Theory and simulations

In LOD, changes in the z -component of the electron magnetization, M_z , are detected. These changes can be caused by a microwave field at the Larmor frequency, longitudinal relaxation, or interactions with neighbouring spins. They induce changes in a detection coil according to Faraday's law of induction,

$$\oint \mathbf{E} \cdot d\mathbf{l} = - \iint_S \frac{\partial \mathbf{B}}{\partial t} \cdot d\mathbf{A}, \quad (3.1)$$

where \mathbf{E} is the electric field induced in an infinitesimal length $d\mathbf{l}$ of the wire forming the coil, $\frac{\partial \mathbf{B}}{\partial t}$ is the time-differential of the magnetic field and is proportional to the time-differential of the electron magnetization $\frac{\partial \mathbf{M}}{\partial t}$, S is the surface bounded by one loop of the coil, and $d\mathbf{A}$ is an infinitesimal vector element of the surface S . Since $d\mathbf{A}$ is aligned with the z -axis, the axis of the external magnetic field, only changes in the z -component of the electron magnetization, M_z , are detected.

The left-hand-side of eq (3.1) is equal to the voltage induced in one turn of the coil, so the voltage induced in the whole coil is given by

$$V_{\text{ind}} \propto -nA \frac{dM_z}{dt}, \quad (3.2)$$

where n is the number of turns in the coil and A is the cross-sectional area of the coil.

At thermal equilibrium, $\frac{dM_z}{dt} = 0$, so no voltage is induced in the coil. Changes in M_z can be induced by a microwave field B_1 , which can be continuous or comprise a series of pulses, and by relaxation and other dynamic processes. An example of a pulse-detect sequence for an LOD experiment is shown in Figure 3.3. In this sequence, the microwave field is amplitude-modulated by a square-wave, giving a 'pulse train' comprising a series of 'OFF' and 'ON' periods. During the ON periods, the spins precess around B_1 in the rotating frame, as described in Section 1.5.3, causing an oscillation or, in the case of saturation, a decrease in M_z . During the OFF periods, M_z increases as it relaxes towards thermal equilibrium. Therefore, the periodic switching of B_1 causes changes in M_z , which in turn induce a voltage V_{ind} in the detection coil.

The LOD coil forms part of a detection circuit, shown in Figure 3.4(a), which also includes a resistor and a capacitor. The input voltage is the voltage induced in the coil [82], and the measured voltage is the voltage across the capacitor.

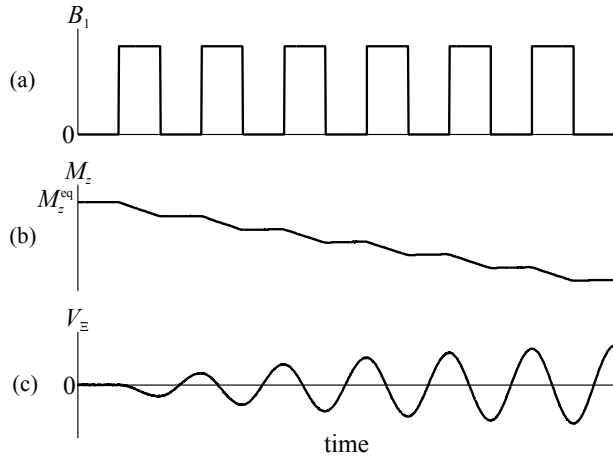


Figure 3.3: An example of an LOD EPR pulse-detect sequence. (a) amplitude of microwave field B_1 as a function of time. B_1 (frequency $\omega_{\text{mw}} = \omega_e \sim \text{GHz}$) is amplitude-modulated by a square wave (frequency $\omega_\Xi \sim \text{kHz}$), giving a ‘pulse train’, which cause changes in M_z . (b) M_z , which decreases when mw field is on, and increases due to longitudinal relaxation when mw field is off. (c) V_Ξ , detected voltage induced by changes in M_z . The nature of V_Ξ as a function of time will be described later in this section.

In our set-up, the coil has 1000 turns arranged over many layers. For multi-turn and multi-layer coils such as this, it is often an over-simplification to regard the coil as a discrete inductor with a voltage source across it. The coil may act as a system of inductors and capacitors, and a larger voltage may be induced in the inner layers of the coil, compared with the outer layers which can be shielded by the inner layers. However, in the following description, the coil and input voltage are modelled by a discrete inductor, with inductance L , and a voltage source V_{in} in series with the inductor. The model circuit, shown in Figure 3.4(b), will be used to calculate the response of the circuit to an input voltage. The circuit can be described by the equation of motion of a driven and damped harmonic oscillator [20], as explained below.

Using Kirchhoff’s voltage law, the voltage source V_{in} is equal to the sum of the voltages across the other three circuit components,

$$V_L + V_R + V_C = V_{\text{in}}, \quad (3.3a)$$

$$L \frac{dI}{dt} + IR + V_\Xi = V_{\text{in}}, \quad (3.3b)$$

where V_L , V_R and V_C are the voltages across the inductor, resistor and capacitor, respectively, I is the current through the circuit, L is the inductance of the coil, R is the resistance of the resistor, and $V_\Xi = V_C$ is the detected voltage.

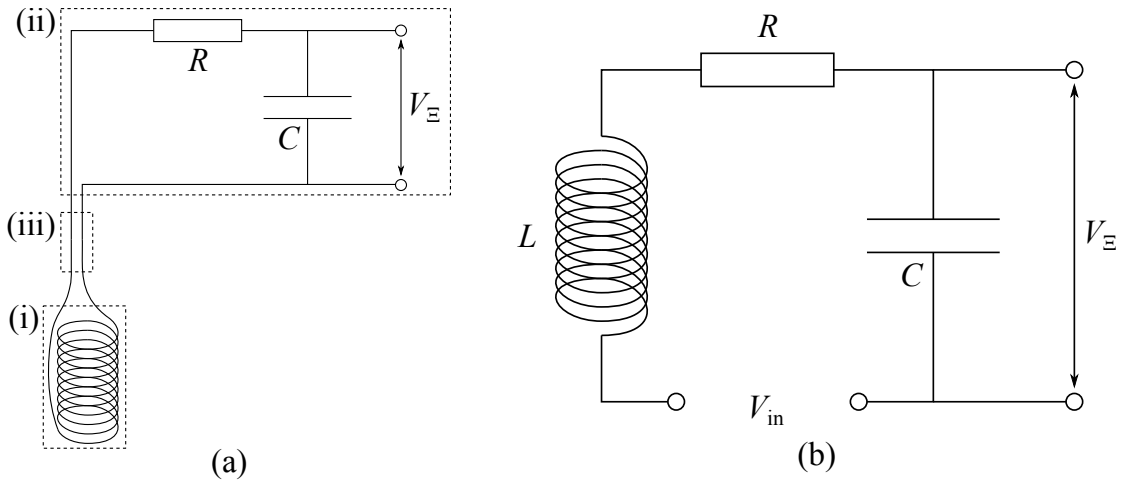


Figure 3.4: (a) LOD primary detection circuit, showing (i) the detection coil (wound on probe-head), (ii) the rest of the primary detection circuit, comprising a resistor and a capacitor, contained in an aluminium box above the probe, and (iii) the connection between the coil and the rest of primary detection circuit, consisting of a twisted pair of copper wires (lower part) and a coaxial cable (upper part). (b) Model circuit. Coil and input voltage are modelled by a discrete inductor and a voltage source V_{in} in series with the inductor. Capacitance and inductance of co-axial cable have been ignored. Resistance R_{coil} of coil has also been ignored (appropriate for low temperature experiments, where $R_{\text{coil}} \ll R$).

This equation can be written

$$\frac{1}{\omega_{\Xi}^2} \frac{d^2 V_{\Xi}}{dt^2} + \frac{1}{Q_{\Xi} \omega_{\Xi}} \frac{dV_{\Xi}}{dt} + V_{\Xi} = V_{\text{in}}, \quad (3.4)$$

where

$$\omega_{\Xi} = \frac{1}{\sqrt{LC}} \quad (3.5)$$

is the resonance frequency of the detection circuit,

$$Q_{\Xi} = \frac{1}{R} \sqrt{\frac{L}{C}} \quad (3.6)$$

is the quality factor of the detection circuit, and C is the capacitance of the capacitor.

To simulate the response of the circuit, eq (3.4) was solved numerically, with an input voltage $V_{\text{in}} = -V_0 \sin(\omega_{\Xi} t)$, using the Matlab Symbolic Math Toolbox (MuPAD 5.4.0 (R2010a), SciFace Software GmbH & Co. KG, Paderborn, Ger-

parameter	value
R	10 Ω
C	470 nF
L	5.6 mH
ω_{Ξ}	19.5×10^3 rad s $^{-1}$
$f_{\Xi} = \omega_{\Xi}/(2\pi)$	3.1 kHz
Q_{Ξ}	10.9

Table 3.2: Parameters for the detection circuit shown in Figure 3.4, at a probe-head temperature of 1.5 K. R , C , ω_{Ξ} and f_{Ξ} are measured values, and L and Q_{Ξ} were calculated using eq (3.5) and (3.6) respectively.

many). Note that this is not a realistic experimental input voltage. However, for a periodic pulse train with an amplitude modulation frequency ω_{Ξ} , such as that shown in Figure 3.3a, M_z , the input voltage, and the detected voltage have oscillatory components at a frequency ω_{Ξ} , as can be seen in Figures 3.3b and 3.3c. This is the resonance frequency of the detection circuit, so the circuit responds most strongly to a signal component at this frequency.

The parameters used for the simulation are taken from our set-up and are shown in Table 3.2. The resulting expression for the voltage across the capacitor (the detected voltage) is

$$V_{\Xi} = Q_{\Xi} V_0 (\cos(\omega_{\Xi} t) - \alpha_{\Xi} \cos(\omega_r t) e^{-t/\tau_{\text{rise}}}), \quad (3.7)$$

where ω_r , τ_{rise} , and α_{Ξ} are defined as follows,

$$\omega_r = \omega_{\Xi}/\alpha_{\Xi}, \quad (3.8a)$$

$$\tau_{\text{rise}} = \frac{2Q_{\Xi}}{\omega_{\Xi}} = \frac{2L}{R} = 1.12 \text{ ms}, \quad (3.8b)$$

$$\alpha_{\Xi} = \frac{1}{\sqrt{1 - \left(\frac{1}{2Q_{\Xi}}\right)^2}} = 1.001. \quad (3.8c)$$

V_{Ξ} can be expressed more concisely by noting that $\alpha_{\Xi} \approx 1$, so eq (3.7) can be approximated to

$$V_{\Xi} \approx Q_{\Xi} V_0 \cos(\omega_{\Xi} t) (1 - e^{-t/\tau_{\text{rise}}}). \quad (3.9)$$

Equation (3.9) shows that V_{Ξ} oscillates at a frequency close to ω_{Ξ} and has an

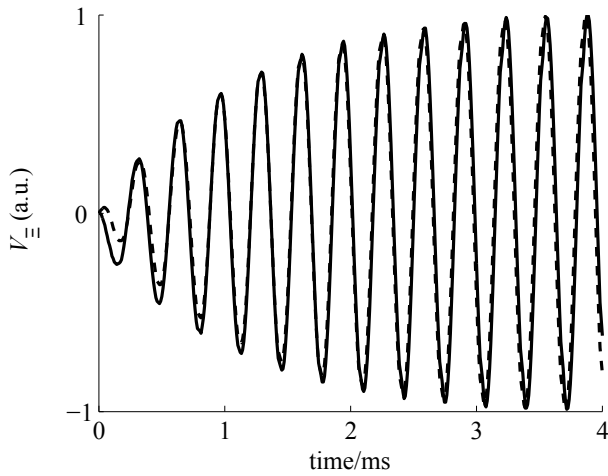


Figure 3.5: Detected voltage V_{Ξ} . Solid line: typical experimental trace of V_{Ξ} , detected during mw irradiation amplitude-modulated by a square wave with frequency $f_{AM} = 3.1$ kHz and 50 % duty-cycle. Dashed line: theoretical trace of V_{Ξ} , simulated with an input voltage $V_{in} = -V_0 \sin(\omega_{\Xi} t)$ with $\frac{\omega_{\Xi}}{2\pi} = 3.1$ kHz, calculated using eq (3.9).

exponentially recovering envelope. It can be characterized by three parameters: Q_{Ξ} , the quality factor of the circuit; V_0 , the amplitude of the input voltage; and ω_{Ξ} , the resonance frequency of the circuit, and frequency of the input and output oscillations.

The output voltage $V_{\Xi,\text{sim}}(t)$ given by eq (3.9) is plotted for $0 \leq t \leq 4$ ms in Figure 3.5. For comparison, an experimentally measured output voltage $V_{\Xi,\text{exp}}(t)$, detected during mw irradiation amplitude-modulated by a square wave with a modulation frequency ω_{Ξ} , is also plotted, and the two traces have been rescaled. The two traces are qualitatively similar, showing that the response of the actual circuit to changes in M_z caused by an amplitude-modulated mw field is not too dissimilar to the simulated response of the model circuit to a sinusoidal input voltage, despite the approximative nature of the input voltage.

3.3.2 LOD experiments

EPR longitudinal detection methods can be roughly divided into two categories: continuous wave (CW) and pulsed. In CW LOD EPR experiments, signal is recorded continuously, often during and after continuous or amplitude-modulated mw radiation, and the spin system does not relax to thermal equilibrium between taking data points. Conversely, in pulsed LOD EPR experiments, signal is recorded during or after a mw pulse or pulse train, and a recycle delay is included

between the recording of successive data points.

An example of a pulse sequence and detected signal was shown in Figure 3.3: the pulse-train causes a periodic change in M_z , which induces a periodic voltage in the detection coil, and a periodic voltage V_{Ξ} in the detection circuit which can be amplified and recorded.

This detection method can be used, for example, to record a spectrum as a function of magnetic field B_0 or mw frequency ω_{mw} . The steady-state amplitude, $V_{s,0}$, of the detected voltage, V_{Ξ} , is proportional to the amplitude of $\frac{dM_z}{dt}$. Therefore, assuming each on-resonance spin makes an equal contribution to $\frac{dM_z}{dt}$, $V_{s,0}$ is proportional to the number of on-resonance spins. On-resonance spins are spins with a resonance frequency equal to ω_{mw} at the field B_0 . $V_{s,0}$ can be approximately measured by taking the Fourier transform of $V_{\Xi}(t)$ and recording the amplitude of the peak at ω_{Ξ} . To acquire a spectrum, either of the parameters ω_{mw} or B_0 is kept constant, while the other is increased in steps, with a pulse-detect sequence applied at each step.

For a pulse-train such as that shown in Figure 3.3, the three main parameters are the amplitude modulation (AM) frequency f_{AM} , duration T_{LOD} , and duty cycle of the pulse-train, all of which influence the SNR of the acquired data, as described in the following paragraphs.

AM frequency The optimal AM frequency for a given detection circuit is typically the resonance frequency f_{Ξ} of the circuit. The optimal AM frequency for a given experiment is more difficult to attain, and depends on the mw field strength, relaxation times, and line-widths, as well as properties of the detection circuit, so SNR can be optimized by adjusting both f_{Ξ} and f_{AM} . For a more thorough description of the effect of relaxation times and mw field strength, readers are directed to references [20, 81].

Duration Increasing T_{LOD} increases the amount of data recorded, so can increase the SNR of the data, but also has a significant drawback. M_z decreases during the mw pulses, and relaxes towards its thermal equilibrium value $M_{z,0}$ during the intervals between pulses. However, M_z does not fully recover unless $T_1 \ll f_{\text{AM}}^{-1}$, so the net effect is that M_z is gradually reduced during the pulse-train. The physical quantity of interest is the value of M_z at the beginning of the pulse-train, before M_z is perturbed by the mw pulses. If the Fourier transform

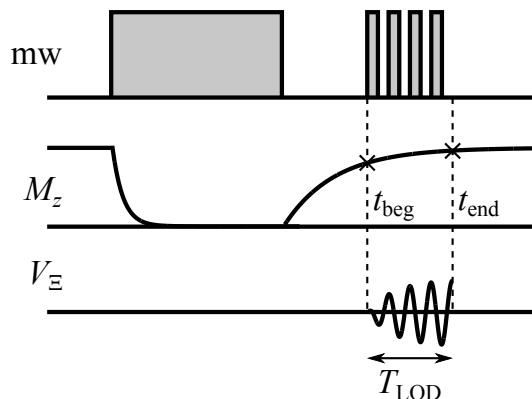


Figure 3.6: An LOD saturation recovery experiment to measure T_1 , illustrating the problem of a detection pulse sequence with a non-negligible duration. A constant mw field is applied for long enough to saturate M_z . Following this, the mw field is switched off and $M_z(t)$ relaxes, during which time $M_z(t)$ can be measured using a train of mw pulses. $M_z(t)$ is sampled between times t_{beg} and t_{end} , so measurements are smoothed in the time domain, and the resolution of the time axis is limited to approximately the duration of the pulse sequence T_{LOD} .

method is used to measure a single value of $V_{s,0}$ from $V_E(t)$ recorded during a long pulse-train, then $V_{s,0}$ may not be proportional to the unperturbed value of M_z . If the behaviour of M_z during the pulse-train is not fully understood, it can be difficult to reliably calculate the value of M_z at the beginning of the pulse train.

In relaxation studies, long detection pulse trains present an additional problem. An example is a saturation-recovery experiment, such as that shown in Figure 3.6: a constant microwave field is applied for long enough so that M_z is completely destroyed, or at least reaches a steady state. Following this, the mw field is switched off and M_z relaxes towards $M_{z,0}$, during which time $M_z(t)$ can be measured using a pulse train. Ideally $M_z(t)$ would be measured in an infinitesimal time interval but, due to the finite length of the pulse train, $M_z(t)$ is sampled between times t_{beg} and t_{end} , the beginning and end of the pulse train. Therefore, measurements are smoothed in the time domain, and the resolution of the time axis is limited to approximately the duration of the pulse train, T_{LOD} . This is not a problem as long as T_{LOD} is much less than any of the relaxation times being measured, but should be taken into consideration if this is not the case. Maximum temporal resolution can be achieved with a single, short detection pulse.

To optimize the duration of the pulse sequence for any given experiment, a compromise must be made between a longer T_{LOD} which increases SNR, and a shorter T_{LOD} which improves temporal resolution.

Duty cycle The duty cycle, usually expressed as a percentage, is the fraction of time that the mw field is on for during the pulse sequence. The effect of the duty cycle on SNR depends on relaxation times and the mw field strength. It will not be discussed in detail here. However, it is worth pointing out that the gradual depletion of M_z during the pulse sequence can be reduced if the duty cycle is lowered.

For fast longitudinal relaxation, when T_1 is of a similar magnitude to, or shorter than, T_{LOD} , the saturation recovery experiment shown in Figure 3.6 is not usually a suitable method to measure T_1 . An alternative detection method is to measure the relaxation transiently, without using a pulse-train to perturb M_z . Using this method, the LOD signal induced by the relaxing magnetization is used to calculate $\frac{dM_z}{dt}$, which can be integrated to give M_z . Analysis methods for fast relaxation data acquired using this technique are discussed in Chapter 8.

3.4 NMR detection

The basic principles of NMR detection are very similar to those of transverse EPR detection. In NMR, a sample is placed in a static magnetic field, rf radiation is transmitted from an amplifier to the sample, and the response of the spin system is recorded by a coil in a resonant circuit and transmitted back to a receiver. A basic schematic diagram of an NMR system is shown in Figure 3.7. The system consists of two main elements, a probe and spectrometer, which are connected by a cable. The spectrometer has two main purposes: it synthesizes and amplifies the rf radiation, and it digitizes and records the received signal. The probe houses a resonant circuit, containing an NMR coil, which sits at the end of a transmission line.

This section presents an overview of NMR detection, with the primary focus being NMR probes. The three main components of NMR probes, namely resonant circuits, transmission lines, and NMR coils, will be discussed separately. Other parts of the NMR system, including the amplifier and receiver, will not be discussed in detail. Lecture notes by Dr. Andy Howes [83] and the books by Horowitz and Hill [84], Levitt [2], and Slichter [85] have been the main resources for this section, and parts of this section closely follow the approaches presented in these documents.

A very brief overview of an NMR spectrometer will be followed by descriptions

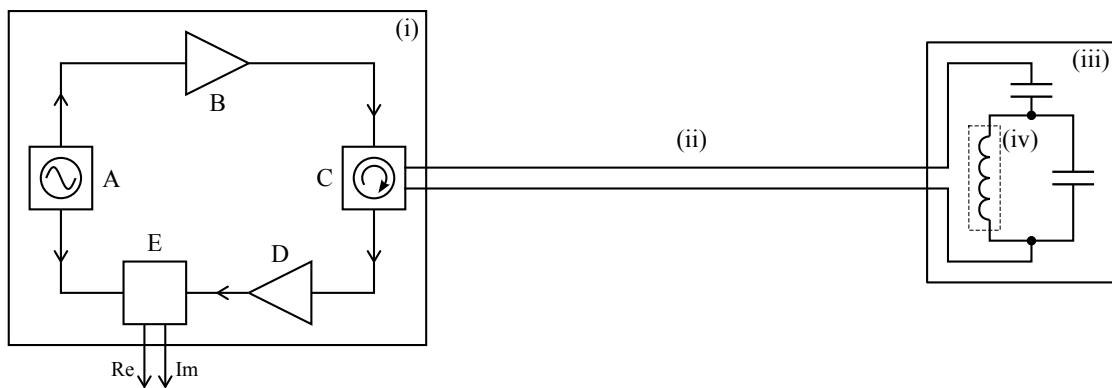


Figure 3.7: Schematic diagram of an NMR probe and spectrometer. (i) NMR spectrometer, including its main components: A. synthesizer; B. amplifier; C. duplexer; D. signal amplifier; E. receiver. (ii) Transmission line. (iii) Probe, containing a resonant circuit. (iv) NMR coil.

of the three main components of NMR probes: resonant circuits, transmission lines, and NMR coils.

3.4.1 Spectrometer

A schematic diagram of an NMR spectrometer, showing its main components, is shown in Figure 3.7. The basic functions of such a spectrometer are as follows. An rf waveform is generated by a synthesizer, amplified, and transmitted to the probe-head. The NMR signal from the probe-head is then transmitted to the spectrometer, where it is amplified and transmitted to a receiver. At the receiver, the signal is mixed with a waveform from the synthesizer, and two signals, referred to as the real and imaginary parts of the signal, are digitized and recorded. This is known as quadrature detection, and is described in more detail in Section 3.5. Note that the transmission line carries both the synthesized rf waveform and the NMR signal. A unit called a duplexer is used to direct the synthesized rf waveform to the probe, and the NMR signal to the signal amplifier.

3.4.2 Resonant circuits

The resonant circuit, which sits at the end of the probe, typically consists, in its most basic form, of a coil of wire and a capacitor. Such a circuit is shown in Figure 3.8a. The coil has an inductance L and often a non-negligible internal resistance, which is represented by a resistance r in series with the coil. The capacitor has a capacitance C .

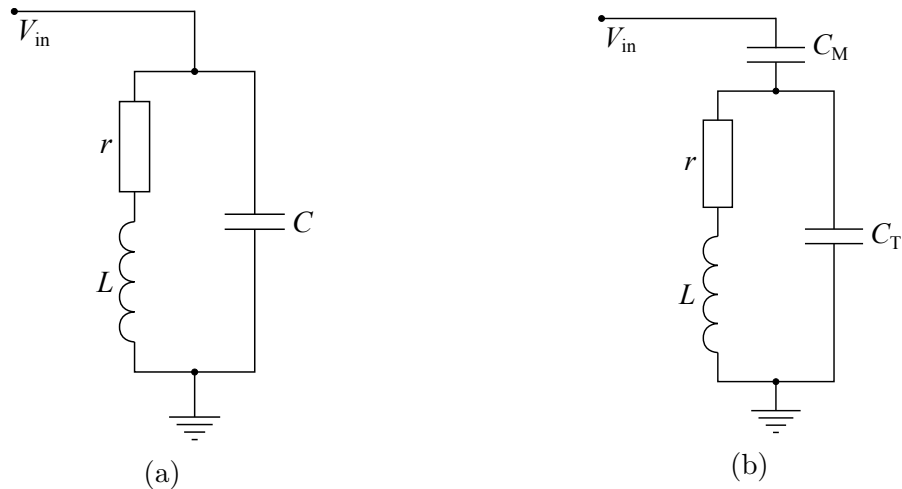


Figure 3.8: (a) A simple resonant circuit, consisting of an inductor L and a capacitor C . The internal resistance r of the inductor is represented by a series resistor. (b) A resonant circuit as shown in (a), with a second capacitor added. The two capacitors are labelled C_T (tuning capacitor) and C_M (matching capacitor).

Consider applying an alternating rf voltage $V_{\text{in}} = V_0 e^{i(\omega t + \phi)}$ to the circuit between arbitrary times t_1 and t_2 . In the coil, this voltage generates a magnetic field, which transfers rf energy to the sample. The energy transferred to the sub-circuit containing the inductor, capacitor and resistor in this time is given by [84]

$$E = \int_{t_1}^{t_2} V_{LCr}(t) I_{LCr}(t) dt, \quad (3.10)$$

where $V_{LCr}(t)$ and $I_{LCr}(t)$ are the voltage across and current through the sub-circuit, respectively, and are both complex. They are related by $V_{LCr}(t) = Z_{LCr}I_{LCr}(t)$, where Z_{LCr} is the impedance of the sub-circuit, and is given by

$$Z_{LCr} = \frac{r}{(1 - \omega^2 LC)^2 + (\omega r C)^2} + i \frac{\omega L (1 - \omega^2 LC - r^2 \frac{C}{L})}{(1 - \omega^2 LC)^2 + (\omega r C)^2} \\ \approx \frac{r}{(1 - \omega^2 LC)^2 + (\omega r C)^2} + i \frac{\omega L (1 - \omega^2 LC)}{(1 - \omega^2 LC)^2 + (\omega r C)^2}. \quad (3.11)$$

The approximation holds as long as $r^2 \frac{C}{L} \ll 1$.^{*} One of the objectives in NMR probe and coil design is to maximize the energy transferred to the NMR coil. Since the voltage and current vary sinusoidally, the energy transferred is maximized when they are in phase, so the energy transferred is maximized when Z_{LCr} is purely

^{*}Typically $C \sim \text{pF}$, $L \sim \mu\text{H}$, and $r < 1 \Omega$, so $r^2 \frac{C}{L} \lesssim 10^{-6}$.

real, which is when

$$\Im \{Z_{LCr}\} = \frac{\omega L (1 - \omega^2 LC)}{(1 - \omega^2 LC)^2 + (\omega r C)^2} = 0, \quad (3.12)$$

or when $\omega = (LC)^{-\frac{1}{2}}$. So $\omega_{LCr} = (LC)^{-\frac{1}{2}}$ is the frequency at which the energy transferred to the NMR coil L is maximized, and is called the resonance frequency of the circuit.

The resonance frequency of the circuit can be adjusted, or *tuned*, by changing the capacitance C . For reasons which will be explained later, it can be necessary to set the impedance of the resonant circuit to a particular value. This can be done by adding a capacitor in series with the other circuit components, as shown in Figure 3.8b. We label the new *matching* capacitor C_M , and the existing *tuning* capacitor C_T . It can be shown that the resonance frequency of the circuit in Figure 3.8b is given by [83]

$$\omega_{LCrC} = (L(C_T + C_M))^{-\frac{1}{2}}, \quad (3.13)$$

and the impedance is given by

$$Z_{LCrC} = \frac{\omega^2 L^2}{r} \left(1 + \frac{C_M}{C_T}\right)^{-2}, \quad (3.14)$$

so both the resonance frequency ω_{LCrC} and impedance Z_{LCrC} can be adjusted by adjusting the capacitances C_T and C_M . This process is called *tuning and matching*. The importance of matching will be discussed in the context of transmission lines in the following section.

3.4.3 Transmission lines

The resonant circuit described in the previous section is usually connected to the amplifier and receiver of the spectrometer by a transmission line (a coaxial cable). A schematic diagram of the spectrometer, cable and circuit is shown in Figure 3.9. The cable has a characteristic impedance Z_0 , and the load at the end of the cable (the resonant circuit) has an impedance Z_L . The impedance of the cable is chosen to be equal to the impedance of the amplifier and receiver (50Ω).^{*} The impedance of the load can be adjusted by changing the capacitances

^{*}There are many standard nominal impedances used for cables and equipment, the most common being 50Ω , 75Ω and 600Ω . All of the equipment used in the course of this PhD project has an impedance of 50Ω .

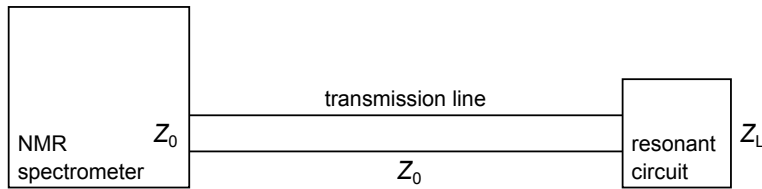


Figure 3.9: A schematic diagram of a transmission line, with impedance Z_0 , connecting the NMR spectrometer with impedance Z_0 to a load with impedance Z_L . In this case the load is the resonant circuit shown in Figure 3.8b.

C_T and C_M of the capacitors in the resonant circuit. When an electromagnetic wave is transmitted from the spectrometer to the probe, the two impedances Z_0 and Z_L determine how much of the incident energy is transmitted to the resonant circuit, and how much is reflected back up the cable. A derivation of the equations governing electromagnetic waves in transmission lines will not be included here; only a few relevant results will be given. It can be shown that the reflection coefficient K , which is the ratio between the reflected and incident voltages at the load, is given by

$$K = \frac{Z_L - Z_0}{Z_L + Z_0}. \quad (3.15)$$

If $Z_L = Z_0$, then $K = 0$, so all of the energy incident on the resonant circuit is transmitted to the circuit. In this case we say that the resonant circuit is *matched* to the impedance of the spectrometer. If the circuit is not correctly matched to the spectrometer, that is $Z_L \neq Z_0$, then $K \neq 0$, and some of the power incident on the circuit is reflected back up the cable to the spectrometer. This is problematic for two reasons: first, not all of the incident energy is transmitted to the circuit, meaning the probe will be less efficient than if it were properly matched; second, more seriously, the energy reflected back up the cable can damage the receiver in the spectrometer.

Note that Z_L can of course have an imaginary as well as a real part. A successfully matched circuit should have

$$\Re(Z_L) = 50 \Omega \quad (3.16)$$

$$\Im(Z_L) = 0 \Omega. \quad (3.17)$$

If the impedance of the circuit approaches the extremely mis-matched cases of $Z_L = \infty$ or 0 (corresponding to an open or a short cable respectively), K approaches ± 1 , so all of the energy is reflected back up the cable to the spectrometer.

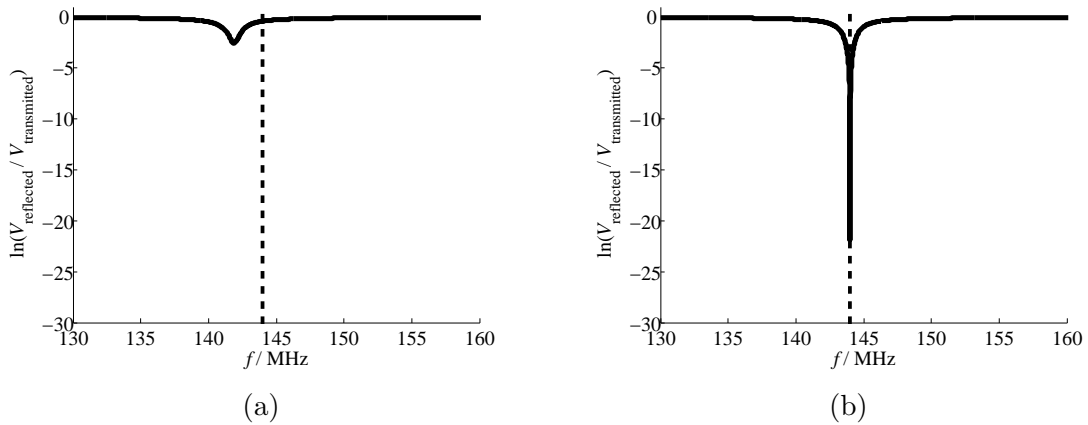


Figure 3.10: Frequency responses of (a) a poorly tuned and matched probe, and (b) a correctly tuned and matched probe. The desired tuning frequency of 144 MHz is indicated by the dashed line.

Figure 3.10 shows how the magnitude of the voltage reflected from a probe varies with frequency for a poorly tuned and matched and a correctly tuned and matched probe. Note that, in the correctly tuned and matched case, very little voltage is reflected back up the cable at the resonance frequency of 144 MHz: nearly all of the energy is transmitted to the circuit at this frequency. In both cases, at very high and very low frequencies, nearly all of the voltage is reflected back to the spectrometer.

3.4.4 Coils

The NMR coil is part of the resonant circuit in an NMR probe. Its two main purposes are to transmit the rf field to the sample, which sits inside the coil (excitation), and to measure the NMR signal produced by the sample (detection). This section introduces some concepts about coils used for NMR excitation and detection. It begins with a brief description of excitation and detection, and the relationship between these, known as the *principle of reciprocity*. It then describes how an NMR coil can be characterized by measuring certain properties of the coil. Finally, the Biot-Savart law is introduced and two specific types of NMR coil, a solenoid and a saddle coil, are discussed.

Excitation and detection

The coil in an NMR probe typically has two purposes: excitation and detection. When used for excitation, the purpose of the coil is to produce an oscillatory

magnetic field \mathbf{B}_1 to transfer energy to the sample inside the coil. The resonance frequency of the oscillatory field is chosen by tuning the circuit as described in Section 3.4.2, and is chosen to be equal to, or close to, the Larmor frequency of the spins in the sample. This is the frequency at which the coil transmits the most energy. The frequencies used in NMR are typically in the radio-frequency (rf) range, so \mathbf{B}_1 is often referred to as the *rf field*, and the coil is often called the *rf coil*. \mathbf{B}_1 is produced in the coil when an alternating current is passed through the coil.

The second purpose of the rf coil is to detect a signal produced by the sample. This signal can be thought of as being produced in the following way. The macroscopic magnetization vector of the spins in the sample, \mathbf{M} , precesses around the static field, \mathbf{B}_0 , and has an oscillating component in the sensitive direction of the rf coil.* This oscillating component has an associated oscillatory magnetic field, which induces an oscillating voltage in the coil according to Faraday's law of induction (eq (3.1)). The left-hand-side of eq (3.1) is equal to the voltage induced in one turn of the coil. If we assume that the coil is only sensitive to magnetic field changes in one direction, defined arbitrarily as the x -direction, the voltage induced in the whole coil is given by

$$V_{\text{ind}} \propto -nA \frac{dM_x}{dt}, \quad (3.18)$$

where n is the number of turns in the coil, A is the cross-sectional area of the coil, and M_x is the x -component of \mathbf{M} . An rf coil detects a signal most strongly at the resonance frequency of its circuit.

Principle of reciprocity

The principle of reciprocity relates the excitation and detection properties of an NMR coil. It states that the sensitivity of a coil is proportional to the magnetic field it produces when a current is applied to it. If a direct current were applied to an NMR coil it would produce a magnetic field $\mathbf{B}_1(\mathbf{r})$ at a position \mathbf{r} , which could in principle be measured. The voltage V_{ind} induced in the coil by a precessing

*The *sensitive direction* of the coil is the direction of the magnetic field produced when a current is passed through the coil, as described later in this section.

magnetic moment \mathbf{M} at position \mathbf{r} is then given by [86, 87]

$$V_{\text{ind}} \propto -\frac{d}{dt} (\mathbf{B}_1(\mathbf{r}) \cdot \mathbf{M}). \quad (3.19)$$

Characterization of NMR coils

NMR coils are typically characterized by two properties: the strength of the rf field produced by the coil at a given input power level, and the homogeneity of the field.

The strength of the rf field is usually described by a property called the nutation frequency. In Section 1.5.3 it was shown that, when an oscillatory field \mathbf{B}_1 is applied to a system of spins, on-resonance spins precess around this field in the rotating frame at a frequency $\omega_1 = -\gamma B_1$. ω_1 , typically stated in Hz, is the nutation frequency. An equivalent property to characterize the strength of the rf field is the duration of a pulse required to flip spins by 90° : given by $t_{90} = \frac{\pi/2}{\omega_1}$, this is called the 90-time.

The homogeneity of the rf field produced by a coil describes the variation in the strength and direction of the field \mathbf{B}_1 across the sample inside the coil. An ideal rf coil would produce a field that is completely uniform inside the coil, but in practice this is not the case, and both the magnitude and direction of the field are position-dependent [88]. During an rf pulse, this causes spins at different positions in the sample to experience different nutation frequencies and directions, so the spins become de-phased during the rf pulse.

When designing rf coils for NMR experiments, two primary objectives are maximization of ω_1 and minimization of inhomogeneities in \mathbf{B}_1 . A higher nutation frequency means that rf pulses can be shorter, so a larger bandwidth can be excited by a given rf pulse,* and relaxation of spins has a smaller effect during the pulse. Greater field homogeneity means de-phasing of spins is reduced, and hence the SNR of experiments is increased.

The rf field strength can be measured by recording a *nutation curve*, which also demonstrates the inhomogeneity of an rf field. An example of a nutation curve, and the pulse sequence used to acquire it, is shown in Figure 3.11. Figure 3.11b shows the amplitude of the free induction decay (FID) as the duration of the pulse is increased at fixed power level. The amplitude of the FID after a 450° pulse is smaller than after a 90° pulse, which is a direct consequence of the inhomogeneity

*Pulse length T and bandwidth $\Delta\nu$ are related by $\Delta\nu \sim \frac{1}{T}$.

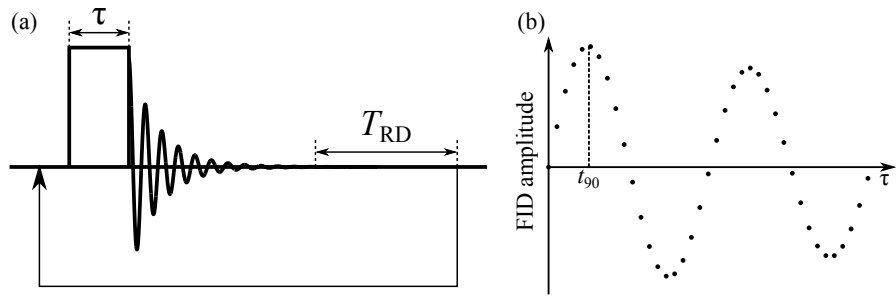


Figure 3.11: Acquisition of a nutation curve. (a) Pulse sequence. A pulse of duration τ is applied and the FID is recorded. After a recycle delay time ($T_{RD} > 5T_1$), the pulse-FID sequence is repeated with a pulse of the same power level, but an increased duration τ , and so on. (b) Nutation curve. FID amplitude is plotted against pulse duration τ for two complete cycles, and the 90-time t_{90} is indicated. Inhomogeneity of B_1 is exaggerated to demonstrate its effect: FID amplitude is smaller after a 450° pulse than after a 90° pulse.

of the rf field.

Calculation of field strength: the Biot-Savart law

An rf coil produces a magnetic field when an electric current is present in the coil, according to the Biot-Savart law. In this section the Biot-Savart law is briefly described. It is then used to derive the magnetic field produced by two specific types of NMR coil, a solenoid and a saddle coil.

Consider a small element $d\mathbf{l}$ of a wire carrying a current I , as shown in Figure 3.12. The magnetic field produced by the element $d\mathbf{l}$ at a position \mathbf{r} is given by the Biot-Savart law,

$$d\mathbf{B}(d\mathbf{l}, \mathbf{r}) = \frac{\mu_0 I}{4\pi} \frac{d\mathbf{l} \times \mathbf{r}}{r^3}, \quad (3.20)$$

where $r = |\mathbf{r}|$. The total magnetic field produced by a length of wire can be calculated by integrating equation (3.20) along the length of the wire,

$$\mathbf{B}(\mathbf{r}) = \int \frac{\mu_0 I}{4\pi} \frac{d\mathbf{l} \times \mathbf{r}}{r^3}. \quad (3.21)$$

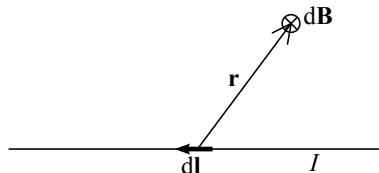


Figure 3.12: The Biot-Savart law. An electric current I in an element of wire $d\mathbf{l}$ produces a magnetic field $d\mathbf{B}$ at position \mathbf{r} , given by eq (3.20).

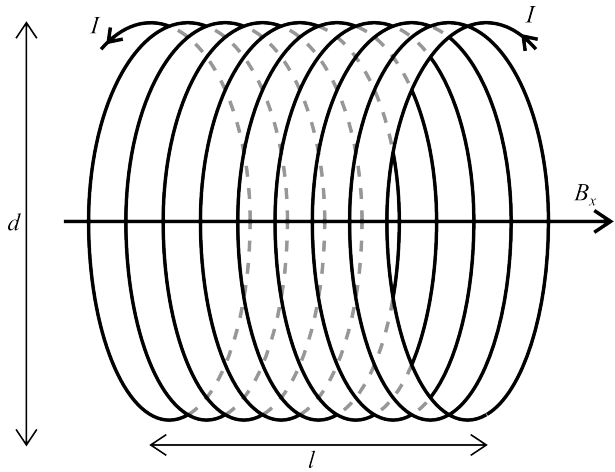


Figure 3.13: A solenoid of length l and diameter d with n loops carrying a current I

The Biot-Savart law can be used to calculate the magnetic field produced by an electric current in any arbitrary shape of coil. In the following sections the results of using eq (3.21) to calculate the magnetic field produced by a current in two types of coil, a solenoid and a saddle coil, will be shown.

Magnetic field produced by a solenoid

Consider a solenoid of length l and diameter d with n turns carrying a current I (see Figure 3.13). To a good approximation, the magnetic field \mathbf{B}_1 inside such a solenoid is aligned along the axis of the solenoid (in this case the x -axis). The symmetry of the coil means that the y and z components can be ignored, and it can be shown using equation (3.21) that the x component is given by [86]

$$B_{1(x)} = \frac{\mu_0 I n}{(d^2 + l^2)^{1/2}}. \quad (3.22)$$

$B_{1(x)}$ is proportional to the number of turns n in the coil and the current through the coil I . In the limiting case $l \gg d$, $B_{1(x)} \approx \frac{\mu_0 I n}{l}$, and $B_{1(x)}$ is proportional to $\frac{n}{l}$, the number of turns per unit length.

Magnetic field produced by a saddle coil

Consider a saddle coil of length (or height) l and diameter d with one pair of loops with angular width φ carrying a current I (see Figure 3.14). The magnetic field \mathbf{B}_1 produced by such a saddle coil can be broken down into two parts, that produced by the arcs at the ends of the coil ($\mathbf{B}_{1(\text{arcs})}$), and that produced by the vertical

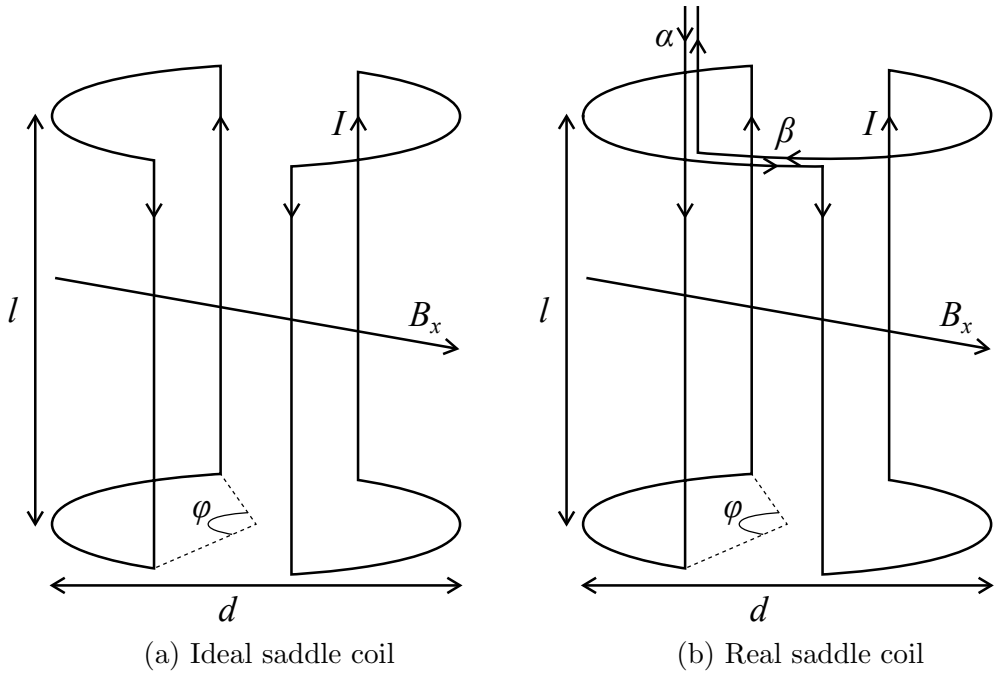


Figure 3.14: A saddle coil of length l and diameter d with one pair of loops with angular width φ carrying a current I . (a) shows an ‘ideal’ saddle coil containing two isolated loops. In practice the loops need to be connected as shown in (b). The currents in the extra lengths of wire needed for the connections (α and β) are approximately equal and opposite, so the magnetic fields produced by them approximately cancel, and the ‘real’ saddle coil in (b) produces a nearly identical magnetic field to that produced by the ‘ideal’ saddle coil in (a).

wires parallel to the axis of the coil ($\mathbf{B}_{1(\text{verticals})}$). For convenience, we consider the magnetic field \mathbf{B}_1 at the centre of the coil. At this point, the symmetry of the coil means that any contributions to the y and z components of \mathbf{B}_1 exactly cancel, and the field is aligned along the x -axis. It can be shown using equation (3.21) that the two contributions to $B_{1(x)}$ at the centre of the coil are [86]

$$B_{1(\text{verticals})(x)} = 4 \sin\left(\frac{\varphi}{2}\right) \frac{\mu_0 I}{\pi} \frac{l}{d(d^2 + l^2)^{1/2}}, \quad (3.23)$$

and

$$B_{1(\text{arcs})(x)} = 4 \sin\left(\frac{\varphi}{2}\right) \frac{\mu_0 I}{\pi} \frac{dl}{(d^2 + l^2)^{3/2}}. \quad (3.24)$$

The total field is then,

$$B_{1(x)} = B_{1(\text{verticals})(x)} + B_{1(\text{arcs})(x)} = 4 \sin\left(\frac{\varphi}{2}\right) \frac{\mu_0 I}{\pi} \left(\frac{l}{d(d^2 + l^2)^{1/2}} + \frac{dl}{(d^2 + l^2)^{3/2}} \right). \quad (3.25)$$

Clearly the strength of the magnetic field \mathbf{B}_1 produced by a saddle coil depends on the angular width φ of the arcs of the coil. The homogeneity of the field also depends on φ . \mathbf{B}_1 is most homogeneous when the arcs have an angular width of $\varphi = 120^\circ$ and the ratio of height to diameter $l/d = 2$ [88, 89]. In this case, the field at the centre of the coil is given by

$$B_{1(x)} = \frac{24}{5} \sqrt{\frac{3}{5}} \frac{\mu_0 I}{\pi d}. \quad (3.26)$$

3.5 Quadrature detection

The previous sections on NMR and transverse EPR detection have introduced some of the key elements of NMR and EPR spectrometers. This section describes a simple NMR experiment to illustrate quadrature detection. The equations and derivations in this section can also be applied to transverse detection with pulsed EPR. In the simplest NMR experiment, a 90° pulse is applied to a sample at thermal equilibrium, which rotates the magnetization vector \mathbf{M} onto the transverse plane. Following the 90° pulse, \mathbf{M} precesses around the static field \mathbf{B}_0 at a frequency ω_0 while the transverse component of \mathbf{M} decays at a rate R_2^* (Section 1.5.5). The precessing magnetization \mathbf{M} induces a voltage in a detection coil proportional to the rate of the change of the x -component of \mathbf{M} (eq (3.18)), which is then transmitted to the receiver and digitized using an analogue-to-digital converter (ADC). The detected signal is known as the free induction decay (FID). The voltage $V_S(t)$ induced in the coil is given by*

$$V_S(t) = V_{S0} \cos(\omega_0 t + \phi) e^{-R_2^* t}, \quad (3.27)$$

where ϕ and V_{S0} are the phase and initial amplitude of the detected voltage. For NMR, $\frac{\omega_0}{2\pi}$ is usually hundreds of MHz, while EPR is often performed at frequencies of tens of GHz. Modern NMR spectrometers are capable of digitizing signals at these frequencies directly, but for older spectrometers, such signals are too fast for the ADC. For such NMR spectrometers, and also for typical EPR spectrometers, the signal must be converted to a lower frequency before it is digitized. This is

Typically the induced voltage will be a linear sum of components with different values of ω_0 and R_2^ . However, we can consider just one of these components without loss of generality.

accomplished by mixing $V_S(t)$ with a reference signal $V_R(t)$, given by

$$V_R(t) = V_{R0} \cos(\omega_R t + \theta), \quad (3.28)$$

where ω_R , θ and V_{R0} are the frequency, phase and amplitude of the reference signal. $V_S(t)$ and $V_R(t)$ are multiplied together, and the resulting voltage V_{out} is given by*

$$V_{\text{out}}(t) = V_0 (\cos[(\omega_0 - \omega_R)t + \phi - \theta] + \cos[(\omega_0 + \omega_R)t + \phi + \theta]) e^{-R_2^* t}, \quad (3.29)$$

where the constants have been absorbed into V_0 , the initial amplitude of V_{out} . The second cosine term in $V_{\text{out}}(t)$ is filtered out by a low-pass filter, and the remaining voltage $V'_{\text{out}}(t) = V_0 \cos[(\omega_0 - \omega_R)t + \phi - \theta] e^{-R_2^* t}$ is digitized.

Note that ϕ is not known absolutely, and therefore the sign of $(\omega_0 - \omega_R)$ cannot be determined from a single recording of $V_{\text{out}}(t)$. This ambiguity can be resolved by recording two signals: $V'_{\text{out}(1)}(t)$ is recorded with $\theta = \theta_1$ and $V'_{\text{out}(2)}(t)$ is recorded with $\theta = \theta_1 + \pi/2$. We label these two signals as ‘real’ and ‘imaginary’ respectively:

$$V_{\text{real}}(t) = V'_{\text{out}(1)}(t) = V_0 \cos[(\omega_0 - \omega_R)t + \phi - \theta_1] e^{-R_2^* t} \quad (3.30)$$

$$\begin{aligned} V_{\text{imag}}(t) &= V'_{\text{out}(2)}(t) = V_0 \cos[(\omega_0 - \omega_R)t + \phi - \theta_1 - \pi/2] e^{-R_2^* t} \\ &= V_0 \sin[(\omega_0 - \omega_R)t + \phi - \theta_1] e^{-R_2^* t}. \end{aligned} \quad (3.31)$$

These can be combined into a more concise complex signal:

$$\begin{aligned} V(t) &= V_{\text{real}}(t) + iV_{\text{imag}}(t) \\ &= V_0 \exp(i\Omega_0 t) \exp(-R_2^* t), \end{aligned} \quad (3.32)$$

where $\Omega_0 = \omega_0 - \omega_R$ is the offset frequency, and the phase of the signal $(\phi - \theta_1)$ is assumed to be zero.[†] This method of detecting two signals with a 90° phase shift after multiplication by a reference signal is known as quadrature detection. It is routinely used in NMR spectrometers to record NMR signal with an unambiguous frequency.

The offset frequency of the signal Ω_0 can be found by performing a Fourier

*Using the product-to-sum identity $\cos(\varphi_1) \cos(\varphi_2) = \frac{1}{2} (\cos(\varphi_1 - \varphi_2) + \cos(\varphi_1 + \varphi_2))$.

[†]The phase can be assumed to be zero without loss of generality, since the phase of the signal is usually adjusted after the experiment.

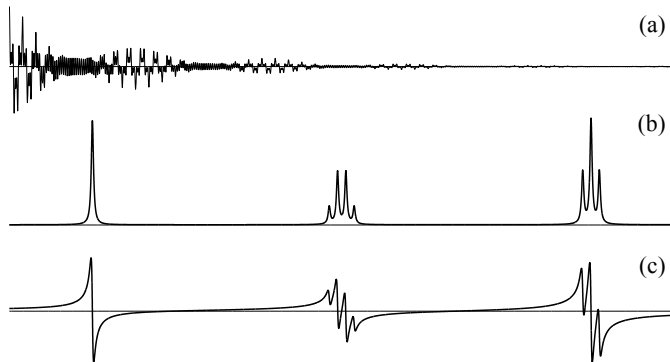


Figure 3.15: A simulated FID and spectrum for an NMR sample with three distinct spin species: (a) the real part of the FID; (b) and (c) the real and imaginary parts of the spectrum $S(\Omega)$, showing peaks at three distinct frequencies and the splitting of peaks due to J -coupling.

transform of $V(t)$, producing a spectrum $S(\Omega)$ given by

$$\begin{aligned}
 S(\Omega) &= \int_{-\infty}^{+\infty} V(t) e^{-i\Omega t} dt \\
 &= V_0 \frac{1}{R_2^* + i(\Omega - \Omega_0)} \\
 &= V_0 \frac{R_2^* - i(\Omega - \Omega_0)}{(R_2^*)^2 + (\Omega - \Omega_0)^2}.
 \end{aligned} \tag{3.33}$$

The spectrum is a Lorentz distribution. The real part has a maximum at $\Omega = \Omega_0$ and a full-width at half-maximum (FWHM) of $2R_2^*$. If more than one spin species is present, $V(t)$ and $S(\Omega)$ are simply summed over all spin species. As an illustration, Figure 3.15 shows a simulated FID and spectrum for an NMR sample with three distinct spin species: (a) shows the FID and (b) and (c) show the real and imaginary parts of the spectrum.

One technical consideration in pulsed EPR and NMR experiments is the delay between an rf or mw pulse and the recording of the FID. Following the pulse, the resonant circuit or resonant cavity dissipates energy—this is the so-called ‘ring-down’ of the resonator—which can obscure the detected signal and even damage the receiver, so there is a ‘dead-time’ before any signal can be recorded. In NMR, the dead-time can usually be much shorter than the duration of the FID, so little information is lost. In EPR, however, the dead-time is often close to, or even longer than, the duration of the FID, making it difficult or impossible to use the FID to acquire data. For this reason, it is common in EPR to record a spin-echo, rather than the primary FID.

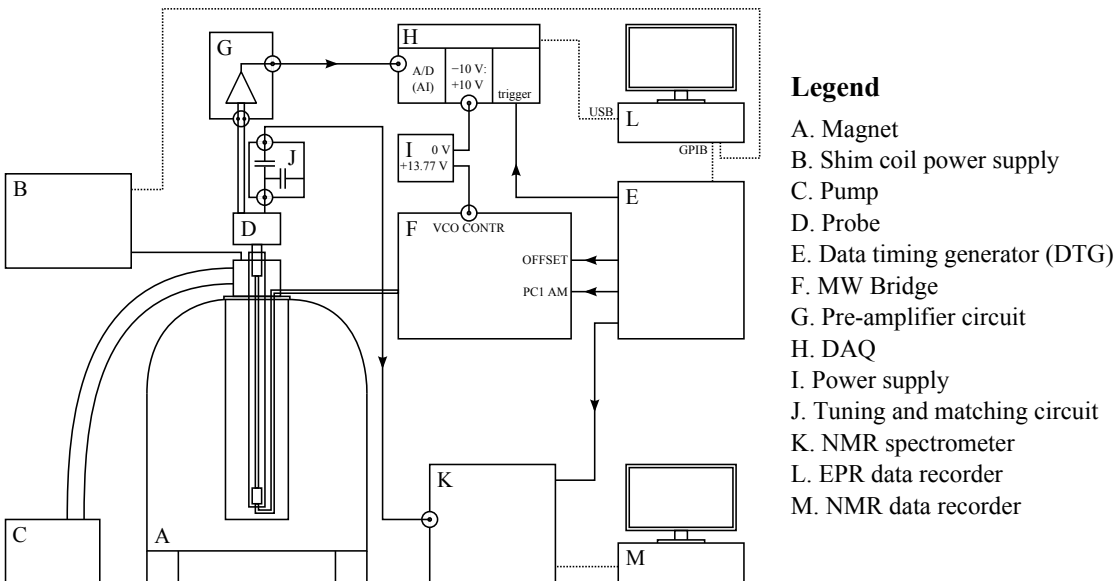


Figure 3.16: Experimental set-up for NMR and LOD EPR experiments, as described in the main text.

3.6 Instrumentation

The experimental set-up used for NMR and LOD EPR in our laboratory, shown schematically in Figure 3.16, is a modified version of a system described elsewhere [43, 81]. It can be divided into seven sections, described separately here: magnet and sample environment control, microwave bridge, probe, timing control, data acquisition, NMR spectrometer, and software.

3.6.1 Magnet

The magnet is a 3.39 T superconducting cold bore magnet (Oxford Instruments, Abingdon, UK). It contains a superconducting sweep coil capable of producing a field which can be swept through the range ± 0.1 T. The sweep coil power supply (ISS10, Oxford Instruments, ibid.) is controlled from within the LabVIEW program used to control the experiments. Liquid helium can be transferred from the magnet dewar into the bore through a needle valve controlled by a stepper motor (26M048B-2U, McLennan Servo Supplies, Ash Vale, UK). Temperatures below the helium boiling point can be reached by pumping on the helium bath with a rotary vane pump (Trivac D 65 B HE3, Oerlikon Leybold Vacuum, Cologne, Germany): a temperature of about 1.35 K can be maintained for several hours, and a temperature of 1.5 K can be maintained indefinitely. The bore also con-

tains an electric heating coil, and can be warmed to 300 K for high-temperature experiments. The stepper motor for the needle valve and the current in the heating coil are controlled by a console (Intelligent Temperature Controller ITC503, Oxford Instruments, *ibid.*). The helium flow rate and coil current can be adjusted manually, or a desired temperature can be chosen on the ITC, and either or both of the flow rate and coil current can be adjusted automatically. The magnet is connected to a gas helium supply, so the bore can be pressurized with helium for sample exchange.

3.6.2 Microwave bridge

The mw field is generated using a Krymov microwave bridge [90]. The bridge has two oscillators: a dielectric resonator oscillator (DRO) with a fixed frequency of 7.30 GHz, and a voltage controlled oscillator (VCO) with a tunable frequency centred at 7.30 GHz. The frequency of the mw field is up-converted by a factor of 13 by a frequency multiplier, giving a frequency of 94.9 GHz for the fixed frequency source, and a frequency of 94.92 ± 0.34 GHz for the tunable source. Switching between the DRO and VCO is performed using a TTL signal at the input **OFFSET**, and the frequency can be tuned by applying a voltage of between 0 V and 23.77 V to the input **VCO CONTR**, corresponding to a realizable output frequency range of 94.58 GHz to 95.23 GHz. The oscillators are collectively known as the system of master oscillators (STAMO). The bridge has three output channels: two pulse channels and a continuous wave channel. The mw field passes through a DC controlled attenuator and is transmitted to the sample using the wave-guide in the external part of a Krymov probe [90].

When the conventional EPR probe is used (not shown in Figure 3.16), the bridge is also used for detection: mw radiation from the probe is transmitted to the receiver in the bridge. The receiver uses two 7.3 GHz reference signals which it receives from the STAMO. The first of these, after being up-converted by a factor of 12 to 87.6 GHz, is used as a reference signal in a mixer. The EPR signal from the sample also enters the mixer, where it is converted to a 7.3 GHz signal. This signal then enters the quadrature detector together with the second reference signal from the STAMO, where it is divided and combined with the reference signal, resulting in two signal components with a phase difference of 90°.

3.6.3 Probe

Three different probes are used to detect NMR and EPR signals. The probe pictured in Figure 3.16 is a home-built probe used for low temperature NMR and LOD EPR. A second home-built probe, similar in design to this probe, is also used for NMR and LOD EPR. It is used in a very similar set-up to that depicted in Figure 3.16, but is primarily designed for high temperature experiments. These two probes are described in Chapter 4.

Finally, a Krymov EPR and electron-nuclear double resonance (ENDOR) probe [90] is used for conventional EPR detection. This probe consists of two parts: the wave-guide is fixed to the outer part of the probe, while the inner part contains the resonator and field modulation coils.

The wave-guide has a rectangular cross-section of $5.2 \times 2.6 \text{ mm}^2$ for most of its length, with two short curved sections with a cross-section of $2.4 \times 1.2 \text{ mm}^2$. The upper curved section is a 90° bend to connect the wave-guide to the mw bridge, while the lower curved section is a 180° bend below the resonator, so that radiation enters the resonator from underneath. The resonator is a cylindrical gold and silver plated TE₀₁₁ cavity of total length 13.4 mm and inner diameter 4.2 mm. The cavity can be tuned by adjusting its length using a silver and gold plated plunger. A similar plunger at the opposite end of the cavity serves as a sample holder. The cavity has an iris of diameter 1.1 mm and sixteen 0.15 mm slits, 0.25 mm apart, to allow penetration of the modulation field and rf field (for ENDOR experiments).

Both of the home-built probes are designed to be inserted into the external part of the Krymov probe. This facilitates easy probe insertion and removal, and means that the Krymov wave-guide can be used for transmission of the microwave power.

3.6.4 Timing control

LOD EPR and conventional pulsed EPR experiments are controlled by a data timing generator (DTG 5078, Tektronix, Beaverton, OR) and an analogue-digital/digital-analogue device (USB-6259 DAQ, National Instruments, Austin, TX). The DTG triggers detection on the DAQ, and also controls the majority of the switches on the mw bridge. For example, the mw field can be switched on and off by changing the voltage applied to the input PC1 AM ('Pulse Channel 1 Amplitude

Modulation') on the mw bridge. The switching of the field amplitude takes less than 25 ns. A detection pulse sequence commonly used for low temperature pulsed LOD experiments comprises an amplitude-modulation of the mw field by a square-wave with frequency $f_{AM} = 3.1$ kHz and 50 % duty-cycle. The voltage to the input VCO CONTR to select the VCO frequency of the bridge is supplied by the DAQ. To synchronize EPR and NMR experiments, the NMR spectrometer can also be triggered by the DTG.

3.6.5 Data acquisition

Three different instruments are used for acquiring EPR data, depending on the experiment. For conventional pulsed EPR experiments, a digital phosphor oscilloscope (DPO) (TDS 7154, Tektronix, Beaverton, OR) is used for detection, while for conventional CW EPR experiments, a lock-in amplifier (SR830, Stanford Research Systems, Sunnyvale, CA) is used.

For LOD EPR experiments, either the DAQ or the DPO is used for detection, depending on the desired detection frequency. The DAQ can record data at a maximum sampling rate of 1 MHz, while the DPO has a maximum sampling rate of 20 GHz and a detection bandwidth of 1.5 GHz. For experiments not requiring detection frequencies above 1 MHz, such as studies of relaxation processes that are significantly longer than 1 μ s, the DAQ is preferred, because it has a lower noise figure. This was the most common detection method used for the experiments presented in this thesis, and is the arrangement depicted in Figure 3.16. For experiments requiring fast detection frequencies, including fast relaxation studies, it is necessary to use the DPO for detection.

3.6.6 NMR spectrometer

NMR experiments were performed using the broadband channel of a Bruker Avance 400 console (Bruker BioSpin, Billerica, MA). The spectrometer is connected to the probe by a coaxial cable, and experiments are controlled using Xwin-NMR (Version 3.2, Bruker BioSpin, ibid.).

3.6.7 Software

Experiments are controlled using a home-written LabVIEW program (Version 7.1, National Instruments, Austin, TX). This software controls the DTG, DAQ,

and sweep coil, and is also used to transfer data from the DAQ or DPO to the computer.

Chapter 4

Novel Probes for Combined EPR and NMR Detection

This chapter describes two probes that have been built for combined EPR and NMR detection. The first of these probes is designed for low temperature NMR, EPR and DNP experiments, while the second probe is designed for combined NMR and EPR cryoporometry, with the aim of studying lignin degradation. Although the two probes have different applications, they share many similarities.

The two probes are described separately in Sections 4.1 and 4.2. Each of the probes is described in terms of: (i) background and motivation, (ii) objectives and design criteria, (iii) construction, and (iv) performance.

4.1 A low temperature probe for NMR and LOD EPR

4.1.1 Introduction: multi-modal detection in magnetic resonance

Dynamic nuclear polarization (DNP), a method for increasing the polarization of nuclear spins, and thereby enhancing the signal in NMR and MRI experiments, was introduced in Chapter 2. In solid-state DNP, three enhancement mechanisms have been proposed. A current area of interest is an extension of our theoretical understanding of these mechanisms, and in particular an improvement of simulations to describe and optimize DNP experiments [49, 55, 61–64].

A better understanding of the underlying processes requires careful experimental characterization of the corresponding time constants. Many of the parameters and processes can be directly measured and studied using either an EPR system or an NMR system. However, since EPR and NMR are usually performed under different conditions, it can be hard to compare experimental data robustly. Ideally, all of the relevant EPR and NMR experiments would be performed in the same probe, under DNP conditions. However, state-of-the-art EPR and NMR hardware are typically not compatible: conventional EPR usually requires a mw cavity with a high quality factor (Q), which is small at static magnetic fields above 1 T, and completely closed, aside from an iris for mw coupling. An NMR coil inside such a cavity, along with openings in the cavity for connections to the coil, can disturb the mode and therefore reduce the Q . In addition, sample volumes used in EPR are too small for NMR experiments. Therefore, compromises must be made if EPR and NMR detection are to be incorporated into the same DNP system. The compromise chosen depends on the properties and processes which are to be studied. In some cases, high mw power at the sample is not essential, so a large mw cavity with a low Q can be used [91], giving more space for a larger sample and NMR coil, allowing higher performance NMR detection. Alternatively, the low quality factor (Q) can sometimes be partially compensated for by using a higher power microwave source. In contrast, there may be cases where the NMR circuit is just required for monitoring relative enhancement, and high performance NMR detection is not necessary. In such cases, a small sample can be used, to allow for better mw and EPR performance.

The following paragraphs contain a summary of some of the probes and spectrometers that have been built to study DNP, EPR and NMR in a DNP-like system. It is not an exhaustive review, but does illustrate some of the examples that have been reported. Some of the approaches described in the literature are illustrated in Figure 4.1.

An arrangement commonly used in DNP probes is an open resonant structure, such as a Fabry-Perot resonator (FPR) or a horn-reflector (HR) structure, with the NMR coil placed inside the resonator (Figure 4.1a). Open resonators such as these typically have much lower quality factors than resonant cavities, such as cylindrical cavities, commonly used in EPR. Singel et al. used an FPR for EPR and DNP, with a solenoid placed inside the resonator for NMR excitation and detection, and demonstrated DNP enhancement of both ^1H and ^{13}C at a

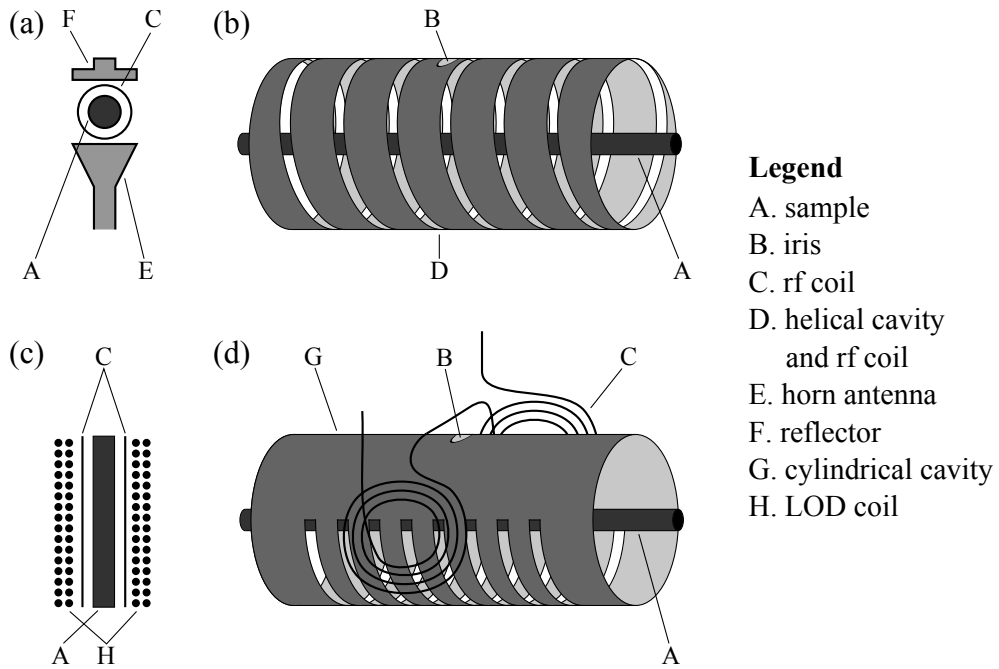


Figure 4.1: Some detection systems for NMR, EPR and DNP, as described in the text. (a) A helical cavity which acts as both a mw resonator and an rf coil (adapted from [92, 93]). (b) An open horn-reflector structure, with an rf coil (solenoid or Helmholtz coils) between the mw components. (c) A cylindrical cavity with an rf coil outside the cavity. Slits are cut in the cavity wall to allow penetration of the rf field (adapted from [90, 94]). (d) A saddle coil for NMR and a solenoid for longitudinal EPR detection (our arrangement).

magnetic field of 1.4 T [95]. Wind et al. used a similar approach on two probes, also demonstrating DNP enhancement of both ^1H and ^{13}C at 1.4 T. The NMR coil was placed inside an oversize cylindrical cavity in their first probe, and inside an HR structure in their second probe, which was also designed for DNP with cross-polarization (CP) and magic angle spinning (MAS) [96].

More recently, groups at MIT, Radboud University Nijmegen, and the Weizmann Institute of Science have built probes for higher field DNP, EPR, and NMR. Cho et al. built two low-temperature DNP probes for use at 2.35 T: the first used a solenoid for ^1H NMR inside an HR structure (Figure 4.1a), and the second used a double-tuned solenoid for ^1H and ^{13}C NMR inside a double-horn structure [97]. Kentgens and co-workers used a resonance structure based on a non-radiative dielectric resonator, for liquid-state DNP at 3.4 T in small volume (~ 10 nl) samples. NMR signal was measured using a U-shaped coil with a single loop inside the resonator. The simplicity of the NMR coil was deemed an acceptable sacrifice since its only purpose was to monitor relative polarization enhancement [98, 99].

Feintuch et al. have built a spectrometer designed to study solid-state DNP spin dynamics, also at 3.4 T. They used an HR structure for EPR excitation and detection and DNP enhancement, and Helmholtz coils between the horn and reflector for NMR detection (Figure 4.1a) [100].

One method of accommodating both an NMR coil and a mw resonant cavity is to modify a cylindrical cavity so that it also serves as a radio-frequency (rf) coil (Figure 4.1b). This method was demonstrated by Weis et al. at 5 T, who used a helical structure based on a cylindrical TE₀₁₁ cavity, which was used as a doubly-tuned rf coil for solid-state ¹³C-detected ¹H DNP and liquid-state ²H electron-nuclear double resonance (ENDOR) [92]. Denysenkov et al. also used this method: they constructed a doubly-tuned helical structure for liquid-state ¹H DNP at 9.2 T [93].

Granwehr et al. built a probe to study EPR processes in a set-up designed for dissolution DNP at 3.4 T. A non-resonant sample holder was used, and EPR signal was measured using longitudinal detection (LOD) (Figure 4.1c) [81]. LOD EPR, which was described in Section 3.3, can be advantageous because it is possible to detect signals during high-power mw irradiation, and it is, in principle, possible to measure faster relaxation processes than can be measured with conventional EPR [101]. In addition, since no mw resonator was used, experiments utilizing a broad range of excitation frequencies could be performed. Using this LOD EPR system, Granwehr and Köckenberger studied relaxation and other dynamic processes under low temperature DNP conditions, using electron-electron double resonance (ELDOR), transient saturation, and saturation recovery [43]. ELDOR has also been used to study EPR processes using a single-mode resonator and rapid magnetic field jumps [102, 103], and, more recently, with a dual-mode resonator at fixed magnetic field [104].

Another approach for tuning probes to both EPR and NMR frequencies is to place the sample inside a resonant cavity, with the rf coil outside the cavity (Figure 4.1d). Because of the skin effect, slits are usually cut into the cavity to allow penetration of the rf field. This has been implemented on probes designed for ENDOR, for example by Bennati et al. at an EPR frequency of 140 GHz [94], and by Gromov et al. at 95 GHz [90].

Smith and co-workers have built a spectrometer for CW EPR, ENDOR, and DNP, with a high power mw source. Non-resonant sample holders and high volumes samples are used, and the absence of a mw resonator is compensated for by

the high mw power available [105, 106].

We have built a probe, described in detail in the following sections, for investigating EPR, NMR and DNP processes and parameters in a low-temperature solid-state DNP environment. We use an LOD coil for EPR detection and as a non-resonant mw shield, and two rf saddle coils (Figure 4.1c): one is part of a tuned circuit for NMR excitation and detection, and the other is a broadband coil for rf irradiation of the sample for ENDOR experiments. The main objectives and design criteria are described in Section 4.1.2, the construction of the probe is described in Section 4.1.3, and Section 4.1.4 describes the performance of the probe

4.1.2 Objectives and Design Criteria

As stated above, the purpose of the probe is to study EPR, NMR and DNP processes, and measure relevant parameters, in a solid-state DNP environment. The magnet and spectrometer system, which is described in Section 3.6, is based on a system which was designed for dissolution DNP. The existing hardware consists of the following: a 3.39 T superconducting magnet, with a sweep coil capable of producing a field in the range ± 0.1 T, and a variable temperature bore designed for low temperatures but capable of sustaining temperatures in the range $\sim 1.3\text{--}300$ K; a CW and pulsed EPR spectrometer, the main component of which is a Krymov mw bridge with a mw frequency of 94.92 ± 0.34 GHz [90]; and a two-part Krymov EPR and ENDOR probe, with the wave-guide fixed to the outer part of the probe, and the resonator and field modulation coils on the inner part [90].

One of the fundamental decisions when designing a probe for NMR, EPR and DNP is choosing how to accommodate both NMR and EPR excitation and detection. As described above, an ideal EPR system is incompatible with an ideal NMR system, so compromises must be made. We used an approach that, to our knowledge, has not been previously implemented: we used a high volume (~ 300 μl) sample holder, two rf saddle coils (one for NMR excitation and detection, the other for broadband rf irradiation), and a solenoid for LOD EPR. This system has a notable drawback: the large volume of the sample holder means that the mw field over the sample volume has a relatively low amplitude and high inhomogeneity [105]. However, it has several advantages. Since the sample holder is not a resonant mw structure, the amplitude of the microwave field inside the sample is uniform across a broad range of frequencies, so experiments utilizing multiple

mw excitation frequencies can be performed. In addition, longitudinal signal can be detected during high-power mw irradiation.

The main criteria for the design of the probe are as follows:

High performance NMR detection The main goals when designing an NMR detection circuit are maximization of rf field amplitude and homogeneity. Ideally, the tuned NMR coil would be tuned and matched locally, but this can be difficult in low temperature probes. The design of the NMR coil and circuit is discussed in detail in Section 4.1.3.

Maximization of mw field amplitude and homogeneity The absence of a resonator means that the mw field will necessarily have a relatively low amplitude, and may be inhomogeneous across the sample. However, it is still important to maximize the amplitude and homogeneity of the mw field within these limitations, by optimizing the mw field transmission and containment.

Sensitive longitudinal EPR detection The signal-to-noise ratio (SNR) of LOD is typically much lower than that of conventional EPR detection [107]. One of the crucial properties of the probe is the SNR of the LOD circuit. Note that the SNR of LOD is dependent on sample- and temperature-dependent quantities such as relaxation times and thermal noise, so the coil, as well as the rest of the detection circuit, would ideally be optimized across a range of temperatures.

Minimization of coupling between coils The probe is designed to be used with three independent coils: two rf coils for NMR and a solenoid for LOD EPR. The coils are oriented orthogonally with respect to each other to minimize coupling between them, but it is still possible that coupling exists between the coils with this arrangement. In addition, there are other circuit components in close proximity to one another (including capacitors for the NMR tuned circuit, and wires for the three coils), and it is possible that these components couple to each other capacitively or inductively.

Coupling between coils and circuits can reduce the performance of the circuits. For example, when an rf pulse is applied to an NMR circuit, the desired result is that as much power as possible is transferred to the sample inside the coil, and not to other coils to which the coil and circuit are coupled. Any power which is not transferred to the sample is wasted, and performance is reduced. In addition,

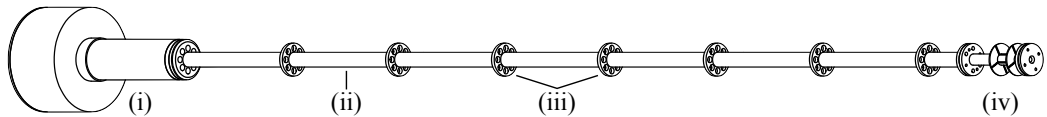


Figure 4.2: Scale diagram of low-temperature probe, not showing cables, coils, and other circuit components. (i) Stainless steel and brass enclosure. (ii) Stainless steel shaft. (iii) Brass baffles. (iv) Probe head assembly. Drawing produced with Autodesk Inventor Professional 2013, Educational Version (Autodesk Inc., San Rafael, CA).

power applied to one coil and transferred to another coil can damage amplifiers attached to the second coil. For these reasons, it is necessary to reduce any coupling between coils and circuits as much as possible.

Sustainable low temperature and pressure The probe is intended for use at temperatures as low as ~ 1 K. As the top of the probe sits outside the magnet at room temperature, the probe should be capable of maintaining significant temperature gradients.

Temperatures below the boiling point of helium are achieved by allowing helium to flow from the magnet cryostat into the (low pressure) magnet bore. It is imperative that air does not leak into and contaminate the bore of the magnet, so the probe needs to be well sealed and able to maintain low pressures. Therefore, connections between probe components should be sealed, and the number of these connections should be kept to a minimum.

4.1.3 Construction

The probe can be described in terms of three sub-units: probe body, EPR excitation and detection, and NMR excitation and detection. These are described separately in the following sections.

Probe body

The probe is shown in Figure 4.2. The main probe body consists of a hollow stainless steel shaft, with inner and outer diameters of 10.6 mm and 12.7 mm respectively. It can be used to route cables and wires from the coils at the bottom of the probe to the connectors at the top, shielding them from cables outside the shaft. An enclosure made of part stainless steel and part brass sits at the top of the shaft. The top of the enclosure is a removable brass plate, which is sealed

with an o-ring. The enclosure at the top of the probe houses the connectors at the ends of the coaxial cables. The brass plate at the top of the enclosure supports five hermetically sealed bulkhead female-female coaxial connectors: three type N (R161753000, Radiall, Paris, France), and 2 SMA (R125753001, Radiall, *ibid.*). The type N and SMA connectors have leakage rates of 10^{-6} bar cm³ s⁻¹ and 10^{-5} bar cm³ s⁻¹ respectively. One of the SMA connectors, which is used for the LOD circuit, is electrically isolated from the brass plate using polyimide film tape (Electrical Tape 92, 3M, Saint Paul, MN).

Brass baffles are placed along the length of the probe shaft. The probe is cooled by cold helium gas or liquid, which enters the magnet bore through a needle valve at the bottom of the bore, and is pumped out of the top of the bore. The brass baffles prevent a laminar flow of helium gas to the top of the bore, thereby allowing more efficient heat exchange between the helium and the probe. The baffles also provide mechanical stability for the probe and the cables, and grounding for the cables.

The probe is designed to be inserted into the external part of a Krymov probe [90]. This design allows it to be easily removed from the magnet for sample exchange. An o-ring is used to seal the connection between the probe and the outer part of the Krymov probe.

The probe-head is shown in Figure 4.3. It is manufactured from PCTFE* (polychlorotrifluoroethylene, supplied by Elder Engineering, Herts, UK), which has similar properties to PTFE: it does not contain hydrogen, so is suitable for ¹H NMR, has a low thermal expansion coefficient, high chemical resistance, and very low moisture absorption, and can withstand repeated cooling to liquid helium temperatures and heating to room temperature. The main reason that PCTFE was chosen over PTFE is that PCTFE is harder and has a higher tensile strength [108]. This means that the small parts (including small alignment pegs and thin plates for coil forming) are less fragile.

The probe-head was designed to form and support three independent coils. It has plates and grooves to shape two orthogonal saddle coils, and the plates also act as limiters for a solenoid. The wires forming the saddle coils can sit inside the grooves, providing a smooth surface on which to wind the solenoid.

The sample holder, also manufactured from PCTFE, is shown in Figure 4.4. It

*Note that PCTFE is more commonly known by one of its trade names: Kel-F, Diaflon, or Aclon.

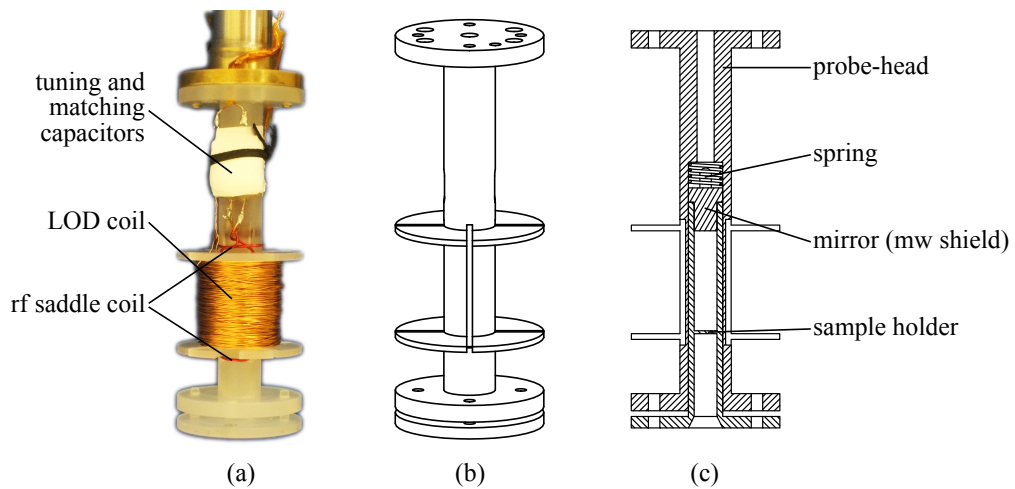


Figure 4.3: Probe-head assembly for the low-temperature probe. (a) Photograph of assembled probe-head, with coils and other circuit components connected. (b) Scale diagram of assembled probe-head, not showing coils and other circuit components. (c) Cross-section through assembled probe-head, showing probe-head, sample holder, copper mw mirror, and spring, not showing coils and other circuit components. Drawings produced with Autodesk Inventor Professional 2010, Educational Version (Autodesk Inc., San Rafael, CA).

was originally made as a single piece, shown in Figure 4.4a, which was optimal for easy insertion and removal. However, because of the material and manufacturing costs, it was only practical to have one such sample holder made. This meant that samples had to be transferred to separate containers for storage, which is not ideal because a small amount of sample can be lost with each transfer, and sample exchange is much slower. An updated version of the sample holder, shown in Figure 4.4b, consists of two separate pieces: a cylindrical sample cup and a top-hat shaped plug, similar to the design used by Granwehr et al. [81]. This design has the advantage that many more sample cups could be made, and they are only slightly more difficult to remove from the probe-head. The second version of the sample cup also has a larger inner diameter. The original and modified sample cups have respective inner diameters of 4 mm and 5 mm, and both have an outer diameter of 6 mm and a height of 17.5 mm, so samples of up to 220 μl and 340 μl could be used, respectively. The plug is secured in place by a steel screw, and a copper spring above the sample cup ensures that the sample sits immediately above the microwave antenna.

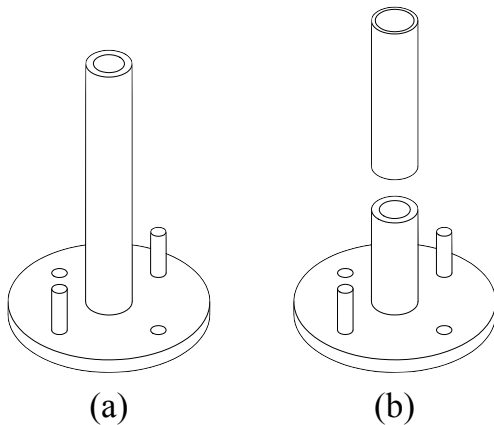


Figure 4.4: Sample holders for the low-temperature probe. (a) Original single-piece design. (b) Modified design, consisting of two pieces. Drawings produced with Autodesk Inventor Professional 2013, Educational Version (Autodesk Inc., San Rafael, CA).

EPR excitation and detection

For transmission of the microwave field to the sample, we decided to use the wave-guide in the external part of the Krymov probe [90], rather than design and build a new wave-guide. The Krymov wave-guide has a 180° bend at the bottom of the probe, and microwave radiation enters the sample from underneath. The sample sits directly above the microwave antenna, and any upwards movement of the sample due to thermal contraction of the probe is compensated for by a copper spring above the sample cup. The sample does not sit inside a resonator, but copper shielding is used to contain the mw field: the LOD coil around the sample and a copper ‘mirror’ on top of the sample cup shield the sample in the radial and axial directions respectively.

The LOD coil is a solenoid (1000 turns, height 18 mm, inner diameter 9 mm, outer diameter 18 mm) made of enamelled copper wire (diameter 0.2 mm), with its axis parallel to \mathbf{B}_0 . The coil is connected using a twisted pair of copper wires and a coaxial cable to a home-built pre-amplifier/filter circuit [81] which sits at the top of the probe. A simplified diagram of the pre-amplifier/filter circuit is shown in Figure 4.5. The EPR signal is amplified by 60 dB (corresponding to a voltage gain of 1000) using an audio pre-amplifier (SSM2019, Analog Devices, Norwood, MA). The pre-amplifier is equipped at its output with a high-pass and a low-pass filter, both of them passive RC designs, with cut-off frequencies of 129 Hz and 145 kHz respectively. The pre-amplifier has a very high input impedance, so its load on the detection circuit (Figure 3.4) can be neglected. The LOD coil and

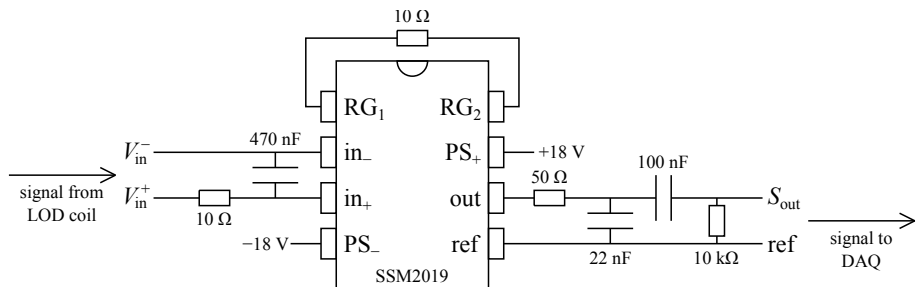


Figure 4.5: LOD EPR signal pre-amplifier/filter circuit. V_{in}^+ and V_{in}^- are the voltages from the LOD coil, and the capacitor and resistor at the inputs to the pre-amplifier are the components R and C in the detection circuit shown in Figure 3.4. The resistance between RG_1 and RG_2 determines the gain: $10\ \Omega$ corresponds to a voltage gain of 1000, or an amplification of 60 dB. PS_+ and PS_- are the power supply inputs. The output signal at outputs out and ref passes through a low-pass and a high-pass filter before it is digitized.

pre-amplifier/filter circuit are electrically isolated from the probe body. The signal is digitized using an external analogue-digital/digital-analogue device (USB-6259 DAQ, National Instruments, Austin, TX).

NMR excitation and detection

The probe-head was designed to include two saddle coils for NMR. The first of the saddle coils (1 pair of turns, height 20 mm, diameter 7 mm, angular width of loops 90°) is used for 1H NMR excitation and detection. It forms part of a resonant circuit tuned to the 1H frequency at 3.39 T of 144 MHz (shown in Figure 4.6c). The second saddle coil (1 pair of turns, height 6 mm, diameter 7 mm, angular width of loops 90°) is designed for broadband excitation. It is oriented orthogonally with respect to the first saddle coil to minimize coupling between the coils. The loops of both coils have angular widths of 90° , which makes it easier to mount two orthogonal coils, and it was thought that this would reduce the coupling between the coils. However, an obvious drawback of this angular width, compared with an angular width of 120° , is that the B_1 field is less homogeneous.

One of the challenges in low-temperature NMR probe design is the location of the tuning and matching capacitors. Tuning and matching at the probe-head with fixed capacitors is usually unsuitable because thermal contraction of the components causes the resonance frequency and impedance of the resonant circuit to change when the probe is cooled [97]. Three alternative arrangements of the tuning and matching circuit are shown in Figure 4.6: (a) variable capacitors for tuning and matching are located in the probe-head, and can be adjusted using rods

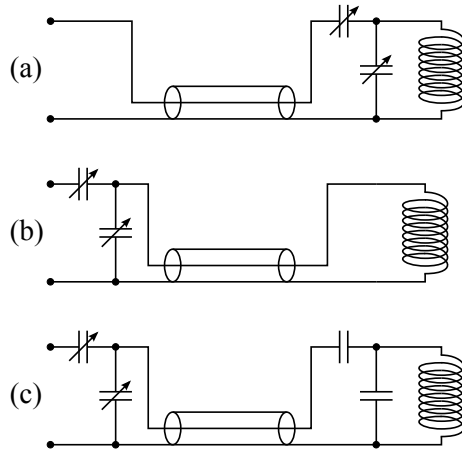


Figure 4.6: Three arrangements for a tuning and matching circuit in a low temperature probe. (a) Variable capacitors are located in the probe-head, and can be adjusted using rods which extend to the top of the probe [97]; (b) variable capacitors are located at the far end of the probe, where they can be easily adjusted by hand [109]; (c) fixed capacitors for coarse tuning and matching are located in the probe-head, and variable capacitors for fine tuning and matching are located at the far end of the probe. The cylinder represents a transmission line.

which extend to the top of the probe [97]; (b) variable capacitors for tuning and matching are located at the top of the probe at the end of a transmission line, where they can be easily adjusted by hand [109]; (c) fixed capacitors for coarse tuning and matching are located in the probe-head, and variable capacitors for fine tuning and matching are located at the top of the probe at the end of a transmission line, where they can be easily adjusted by hand [110]. Local tuning and matching (Figure 4.6a) offers the best performance in terms of both B_1 amplitude and SNR of NMR signal [111]. However, a disadvantage of this arrangement is that variable capacitors can seize up if not thoroughly cleaned [97], and low-temperature, non-magnetic variable capacitors are generally expensive, bulky, and have limited lifetimes. In addition, the tuning rods can add an extra heat load to the probe-head, and the connection at the top of the probe can be a source of air leakage into the evacuated probe. Remote tuning and matching (Figure 4.6b) removes all of the problems associated with local tuning and matching, usually at the expense of performance: the coaxial cable forms a part of the resonant circuit, and energy is dissipated in the cable as well as in the coil. Local coarse tuning and remote fine tuning (Figure 4.6c) offers something of a compromise: the performance reduction can be minimized if the fixed-tuned circuit is tuned to within $\sim 2\%$ of the operating frequency [110], and the difficulties associated with local tuning and matching are removed. The main drawback of this method is that coarse tuning and matching

with fixed capacitors can be difficult and tedious.

We decided to use option (c): local coarse tuning and remote fine tuning. The capacitances necessary to coarsely tune and match the circuit were found using variable capacitors and an LCR meter. Measuring the values of the variable capacitors was difficult and unreliable because the capacitances were small ($\sim 5\text{--}10\text{ pF}$), and of similar magnitude to the capacitance of the pair of wires used to connect the capacitors to the LCR meter, so this method became something of a trial-and-error process of using different fixed capacitors until a suitable arrangement was found. Fine-tuning outside the magnet was done using variable air capacitors (5601, Johanson Manufacturing Corporation, Boonton, NJ) enclosed in an aluminium box at the top of the probe.

The large, rapid temperature changes that the probe-head undergoes can cause capacitors to break due to thermal contraction and expansion, but it was found that ceramic multilayer fixed capacitors (Johanson Technology, Camarillo, CA) coated in epoxy resin (Araldite, Huntsman Corporation, The Woodlands, TX) were able to withstand repeated cycles of cooling to liquid helium temperatures and heating to room temperature. The epoxy resin coating also prevented arcing in the helium atmosphere.

The NMR tuned circuit and broadband NMR coil are connected to the top of the probe with semi-rigid cables (UT-141B-SS, Micro-Coax, Pottstown, PA) with a length of 1 m, chosen for their high electrical conductivity and low thermal conductivity. They have a beryllium copper inner conductor (diameter 0.912 mm), PTFE dielectric (diameter 2.98 mm), and a stainless steel outer conductor (diameter 3.58 mm). The semi-rigid cables and the NMR circuit and coil were connected using enamelled copper wire and ‘snap-on’ MMCX connectors (plug: 73034, Pomona Electronics, Everett, WA; jack: 37-06-TGG, Multicomp, Premier Farnell UK Limited, Leeds, UK), chosen because there was not sufficient space for more commonly used screw connectors such as SMA. It was found that the MMCX connectors withstood repeated cycles of cooling to cryogenic temperatures and heating to ambient temperature without performance degradation.

4.1.4 Performance

The performance of the probe is discussed in the following paragraphs, with reference to the objectives and design criteria described in Section 4.1.2.

Environment

Pressure For reference, when using both the inner and outer parts of the Krymov probe [90], a pressure of 8×10^{-4} mbar (8×10^{-2} Pa) was reached and sustained when the pump outlet was open. When the presently described probe was used with the outer part of the Krymov probe, the pressure was slightly higher, usually in the range $1\text{--}2 \times 10^{-3}$ mbar (0.1–0.2 Pa). This indicates a small, but non-negligible, leakage, from either the two SMA bulkhead connectors or one of the two o-rings (between the probe and the outer part of the Krymov probe, or between the brass plate and the brass enclosure).

Temperature The magnet bore temperature is controlled by a needle valve which allows liquid helium to flow from the magnet cryostat into the bore, and an electric heating coil. Both of these can be adjusted manually or automatically. It was generally found that a stable temperature could be maintained with a fixed helium flow, chosen manually, and the heating coil adjusted automatically by the temperature controller. Temperature control is described in more detail in Section 3.6.1.

The lowest temperature reached with the probe inserted into the magnet bore was approximately 1.25 K. However, this temperature was not sustainable for more than a few seconds. A temperature of about 1.35 K could be sustained for several hours, and a temperature of 1.5 K could be sustained indefinitely. The duration of the cooling process, in which the magnet bore is cooled from its steady-state temperature of about 120 K to a temperature of 1.5 K and allowed to stabilize at this temperature, typically takes about 2–3 hours.

The temperature sensor is at the edge of the magnet bore, at the same height as the sample, but a few centimetres laterally from the sample. This arrangement is adequate if there are no significant radial temperature gradients in the bore, but is not ideal if there are substantial radial temperature gradients. Temperature gradients are difficult to measure and predict with only one dedicated temperature sensor, so under certain conditions there can be some uncertainty in the sample temperature.

Liquid helium-4 undergoes a phase transition to a superfluid state at a temperature $T_\lambda \approx 2.17$ K [112]. For bore temperatures below T_λ , a film of superfluid helium is formed which reaches both the sample and the temperature sensor, and ensures a uniform temperature. Hence, for experiments performed at temperatures

below T_λ , the accuracy of the temperature measurements is adequate. Alternatively, temperature gradients can be reduced by immersing the sample and sensor in liquid helium.

For temperatures above the boiling point of helium, temperature gradients can be significant. This is not a problem for experiments for which the temperature is not critical. However, the interpretation of some experimental data requires the temperature to be known accurately, so if any such experiments are to be performed at higher temperatures, the temperature measurement system would need to be improved. The temperature sensor can, in principle, be calibrated by measuring the sample temperature using known properties of the sample. NMR chemical shifts can be used to calibrate higher temperatures, but are not suitable for temperatures in the region of 1.5 K, for which this probe is designed. Longitudinal relaxation time measurements are another possibility for temperature calibration. A more robust method would be to place a temperature sensor or sensors in the probe-head, as close to the sample as possible.

This probe was primarily designed for experiments at temperatures below 4 K. Furthermore, many of the experiments performed with this probe do not critically depend on temperature. However, it is important that the sample temperature is *stable* throughout an experiment, even if the temperature is not known exactly. At temperatures below about 10 K, the sample temperature stability can be monitored by repeated measurements of the thermal equilibrium signal.

Microwave field amplitude and homogeneity

The mw field amplitude cannot be measured using the standard nutation curve method commonly used to characterize NMR coils, described in Section 3.4.4: the mw field amplitude is too small, and relaxation processes too fast, to measure the flip angle of a given pulse. The mw field amplitude at very low temperatures can instead be estimated using the method described by Granwehr and Köckenberger [43], which is outlined here.

Following continuous mw irradiation at a mw frequency ω_e , for long enough for the system to reach a steady state, the ratio of saturated to unsaturated magnetization can be approximated as

$$\frac{n_s(\omega_e)}{n_0(\omega_e)} = \frac{1}{1 + \pi\omega_1^2 T_1 f(\omega_e)}, \quad (4.1)$$

where $n_s(\omega_e)$ is the steady-state population difference of the energy levels of the saturated electron spin transition after continuous mw irradiation, $n_0(\omega_e)$ is the equivalent population difference at thermal equilibrium, ω_1 is the nutation frequency of the mw field, T_1 is the longitudinal relaxation time, and $f(\omega_e)$ is the normalized line shape factor ($\int f(\omega_e)d\omega_e = 1$). This expression holds for homogeneously broadened lines, as well as spectra that behave like homogeneously broadened lines during continuous mw irradiation.

The amplitude of the mw field ω_1 can be estimated using pump-probe ELDOR measurements. It can be shown that ω_1 is approximately

$$\omega_1 \approx \sqrt{\left(\frac{\sum_k s(\omega_{\text{off}}^p, \omega_k^d)}{\sum_k s(\omega_{\text{on}}^p, \omega_k^d)} - 1 \right) / \pi T_1 f(\omega_{\text{on}})}, \quad (4.2)$$

where ω_{off}^p and ω_{on}^p are pump frequencies far off-resonance and on-resonance respectively, ω_k^d are detection frequencies, $s(\omega^p, \omega^d)$ is the detected signal at a frequency ω^d after saturating mw irradiation at a frequency ω^p , and $\sum_k s(\omega_{\text{off}}^p, \omega_k^d)$ and $\sum_k s(\omega_{\text{on}}^p, \omega_k^d)$ are obtained by summing all of the data points in the spectrum [43]. Finally, $f(\omega_{\text{on}})$ can be determined using

$$f(\omega_{\text{on}}) = \frac{s(\omega_{\text{off}}^s, \omega_{\text{on}}^d)}{\sum_k s(\omega_{\text{off}}^s, \omega_k^d)}. \quad (4.3)$$

ω_1 was estimated using this method using a 100 μl sample of 50 mM 4-Amino-TEMPO in 1:1 water/glycerol at $B_0 = 3.384$ T. At this field, the complete frequency-swept 4-Amino-TEMPO spectrum could be spanned, so it is straightforward to measure the two summations in eq (4.2). ω_{on} was chosen to be 94.899 GHz, the output frequency of the DRO. The ratio of the off-resonant saturation summation to the on-resonant summation is approximately 2.5, and $f(\omega_{\text{on}}) \approx 2.3 \times 10^{-9}$. The longitudinal relaxation could be fitted with a bi-exponential function, with a dominant relaxation component $T_1^a = 76$ ms and a much weaker component $T_1^b = 21$ ms. Using T_1^a , the approximate amplitude of the mw field is $\omega_1/2\pi \approx 8.1$ kHz, which is similar to the value of 6.5 kHz reported by Granwehr and Köckenberger [43].

The absence of a mw resonator means that the mw field may have a relatively high inhomogeneity across the sample. Therefore, the measured value should be thought of as an effective amplitude [106]. This should be taken into account where

possible when considering experimental data. We plan to perform simulations of the mw field in the sample holder to quantify the inhomogeneity.

EPR detection

The properties of the LOD coil were studied through a range of temperatures from 294 K to 1.35 K. It was found that the resonance frequency of the detection circuit was slightly dependent on the bore temperature, with a higher resonance frequency at higher temperatures. The capacitor in the circuit sits outside the magnet bore, so this change is most likely due to a temperature-dependence of the inductance of the LOD coil, or some temperature-dependent stray capacitance. In the range of temperatures of interest for this probe ($\lesssim 20$ K) the resonance frequency of the detection circuit changed very little.

The quality factor Q of the detection circuit changes significantly with temperature, due to the change in resistance of the LOD coil. At 294 K, the resistance of the LOD coil is approximately 20Ω , and Q is approximately 3. At liquid helium temperatures, the resistance is zero, and Q is approximately 11. The significant increase of Q and decrease of coil resistance show that a considerably improved noise figure can be achieved at low temperatures with a low-frequency detection approach such as LOD.

NMR detection

To assess the performance of the tuned NMR coil, initial NMR experiments were carried out using a 200 μl sample of 1:1 water/glycerol at 300 K. To begin with, these tests were performed in the absence of the broadband coil and the LOD coil. A nutation curve, shown in Figure 4.7, was acquired by varying the pulse length at constant B_1 amplitude. The coil had a 90-time of 15 μs with an input power of 30 W. In the second cycle, the signal amplitude reaches 88 % of the maximum amplitude in the first cycle, demonstrating a good B_1 field homogeneity. Note that the baseline is not flat: there is a background signal which consists of a broad, low-amplitude peak. This needs to be accounted for in solid-state experiments.

Following these experiments, the broadband coil and LOD coil were installed and the tuned coil was tested again. The presence of the two new coils significantly changed the properties of the tuned circuit (both resonance frequency and impedance), making it much more difficult to tune and match. Presumably this was for three reasons: coupling between the two NMR saddle coils, distortion of

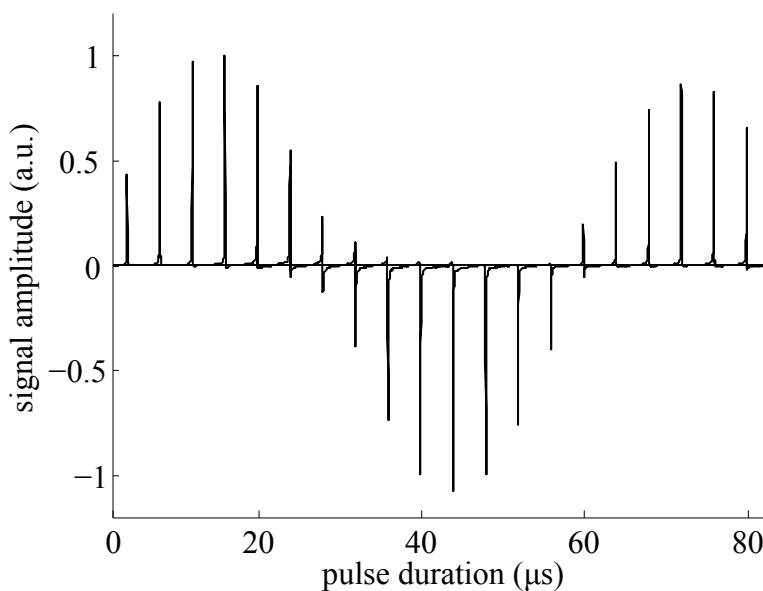


Figure 4.7: Nutation curve for the tuned NMR saddle coil using 200 μl 1:1 water/glycerol at 300 K. Peaks are spectra produced by a Fourier transform of the FID following an rf pulse with an input power of 30 W. B_1 duration was increased in steps of 4 μs . 90-time was measured from the curve as 15 μs .

the B_1 field of the tuned coil by the LOD coil, and capacitive coupling between the tuned NMR coil and the LOD coil. The tuning procedure described in section 4.1.3 (local coarse tuning and remote fine tuning) was followed again with the new arrangement. However, with this arrangement it became extremely difficult to adequately tune and match the circuit with fixed capacitors for coarse tuning. For this reason, a new approach was taken: we decided to design and build low temperature, non-magnetic variable capacitors for local coarse tuning and matching of the NMR coil, rather than using fixed capacitors.

Each home-built capacitor consisted of two concentric cylinders of flexible copper-coated polyester laminate (Mega Electronics, Cambridge, UK). Some of the copper coating was removed from a rectangle of the laminate, so that a smaller rectangle of copper remained. Two of these rectangles were then wrapped around the shaft of the probe-head to form two cylinders, with the copper surfaces forming the two plates of the capacitor, as shown in Figure 4.8. The inner cylinder was fixed in place, while the other cylinder was free to rotate and move up and down, thereby changing the overlapping area between the copper surfaces, and hence the capacitance. It was found that the maximum capacitance of these home-built capacitors was lower than predicted, so it was necessary to add a fixed capacitor in parallel with one of the capacitors to increase the capacitance to a suitable range

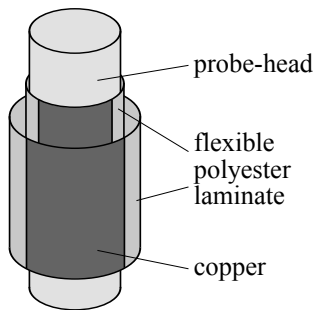


Figure 4.8: Schematic diagram of the home-built variable capacitors on the shaft of the probe-head. As described in the text, the capacitors comprise two concentric cylinders of flexible polyester laminate, partly coated in copper. The inner cylinder is fixed, while the outer cylinder can be rotated and moved up and down to change the capacitance. Diagram is not to scale.

of values.

With the new capacitors for local coarse tuning and matching, together with the variable capacitors outside the probe for remote fine tuning and matching, the NMR circuit was tuned and matched, and the performance of the NMR coil was assessed by acquiring a nutation curve, as described previously. The nutation curve is shown in Figure 4.9. The coil had a 90-time of approximately 32 μ s with an input power of 30 W. In the second cycle, the signal amplitude reaches 70 % of

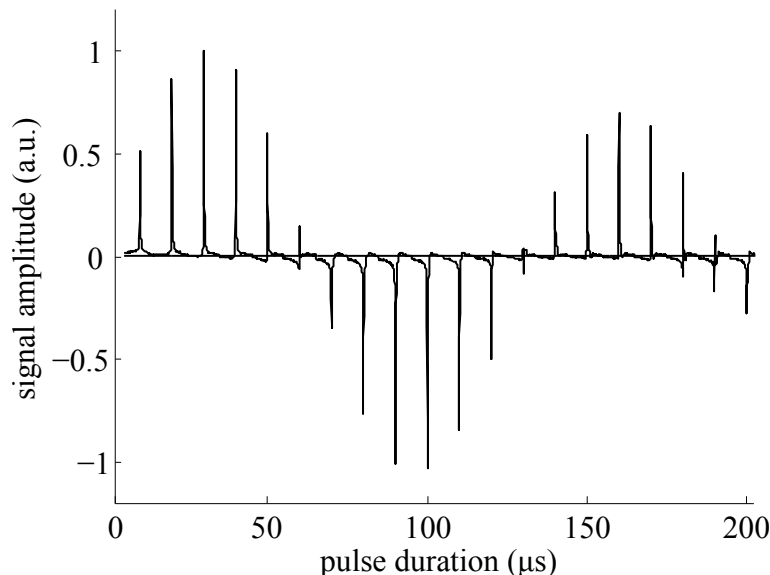


Figure 4.9: Nutation curve for the tuned NMR saddle coil, in the presence of the broadband rf coil and the LOD coil, using 200 μ l 1:1 water/glycerol at 300 K. Peaks are spectra produced by a Fourier transform of the FID following an rf pulse with an input power of 30 W. B_1 duration was increased in steps of 10 μ s. 90-time was measured from the curve as approximately 32 μ s.

the maximum amplitude in the first cycle, showing that the B_1 field homogeneity is lower in this arrangement compared with the previous arrangement. Note that the broad, low-amplitude background signal is still present.

4.1.5 Applications

The probe described in this section was built to study NMR, EPR and DNP processes, and measure DNP-relevant parameters, in samples and experimental conditions commonly used for low-temperature solid-state DNP.

Two main sets of experiments have been performed with this probe, and are presented in this thesis. The first set of experiments studied electron polarization at multiple mw frequencies in a spectral line during continuous mw radiation. The purpose of these experiments was to provide information on dynamic processes, including cross relaxation and spectral diffusion, which are operational during DNP experiments and may influence the DNP enhancement. The second set of experiments measured DNP enhancement over short timescales at a range of NMR offset frequencies. The purpose of these experiments was to investigate the multi-exponential behaviour of polarization build-up in the initial stages of DNP, and to attempt to distinguish build-up rates associated with core nuclei and bulk nuclei. These two sets of experiments are presented in Chapters 6 and 7 respectively.

4.2 A combined NMR and EPR probe for cryoporometric studies of lignin degradation

The second part of this chapter is a slight deviation from the main theme of this thesis. It describes the design, manufacture and testing of a probe for combined NMR and EPR cryoporometric studies of lignin degradation. It is included here because the probe itself shares many similarities with the probe described in the first part of this chapter.

4.2.1 Background: cryoporometry and lignin degradation

Lignin, a substance found in wood and other plant systems, is one of the most abundant natural organic polymers [113]. It is a by-product of paper manufacture, generated in large quantities at pulp and paper refineries, and a principal

component of lignocellulosic biomass. It is currently treated as a waste product by the paper and lignocelulose industries, and is burned as a low-grade fuel to supply energy. However, its molecular structure suggests that it could be utilized as a source of aromatic compounds and other valuable chemicals, as an alternative to and future replacement for petroleum. It is not yet used in this way because controlled lignin depolymerization is challenging and not well understood. Depolymerization of lignin, and its importance, are described in more detail in two recent review articles [114, 115].

Degradation of lignin by the enzyme laccase requires the presence of organic radicals that act as mediators, and both enzyme and mediator must permeate into the lignin for efficient degradation. Previous research has focused on the depolymerization chemical reactions, and the processes involving the movement of laccase and mediators into the lignin have been largely ignored. These processes, which may be an important factor in the rate of lignin depolymerization, were the focus of the project described in this section.

In studies of porous materials, such as lignin, the distribution of pore sizes is important. Furthermore, in the case of lignin degradation, the distribution of fluids inside the pores is of particular interest. The distribution of pore sizes for solvent-filled pores can be measured using NMR cryoporometry, which exploits temperature dependent properties of solvents in pores. The melting temperature of a crystallized solvent in a pore depends on the size of the pore, according to the Gibbs-Thomson equation,

$$\Delta T_m = T_m^\infty - T_m(a) = \frac{4\sigma_{sl}T_m^\infty}{a\Delta H_f\rho_s}, \quad (4.4)$$

where $T_m(a)$ is the melting temperature of a crystal of diameter a , T_m^∞ is the bulk melting temperature of the solid, σ_{sl} is the surface energy at the solid-liquid interface, ΔH_f is the bulk enthalpy of fusion, and ρ_s is the density of the solid [116]. For a particular solvent, the melting temperature depression ΔT_m can be written as a simple function of the crystal diameter,

$$\Delta T_m = T_m^\infty - T_m(a) = \frac{k}{a}, \quad (4.5)$$

where k is a property of the solvent [117].

Liquid-state and solid-state NMR spectra have very different properties, so NMR is an ideal technique to measure the melting point of a solvent confined in an

opaque porous material. To illustrate a basic cryoporometry experiment, consider a solvent-filled porous medium close to the melting temperature of the solvent: the transverse relaxation time T_2^s of the solid solvent is typically much shorter than that of the liquid solvent, so a spin-echo pulse sequence, with an appropriate inter-pulse delay time (longer than $5T_2^s$), produces a spin echo signal which is entirely due to the liquid solvent and, therefore, has an amplitude proportional to the volume of liquid in the medium. Spin echo experiments performed at a range of temperatures provide the melting point distribution of the solvent, from which the pore size distribution can be obtained. Note that hysteresis is observed in freeze-melt cryoporometry experiments, with different transition temperatures obtained in the two parts of the freeze-melt cycle [118]. The lower transition temperature upon freezing can often be attributed to supercooling, so melting curves are generally used. The principles and applications of NMR cryoporometry are described in more detail in two recent review articles [119, 120].

Returning to the subject of lignin degradation, it is hypothesized that lignin initially contains small pores that allow the mediator and, to a lesser extent, the enzyme to permeate, and that these pores grow, in number or in size, as the lignin degrades. The purpose of the project described in this section was to simultaneously characterize the distribution of a solvent, the paramagnetic copper-containing enzyme, and the organic radical mediator in a lignin sample as it degrades, using combined NMR and EPR cryoporometry. This section describes the design, manufacture and testing of the probe built for this purpose.

4.2.2 Objectives, design criteria, and modifications compared with low-temperature probe

The design for the presently described cryoporometry (CPM) probe was based on the previously described low-temperature (LT) probe. Although the intended applications of the two probes are very different, the probes themselves are quite similar. Like the LT probe, the CPM probe is designed to be inserted into the external part of the Krymov probe [90]. The CPM probe and probe-head are similar to the LT probe and probe-head: they have a similar design and many of the same features.

Many of the objectives and design criteria for the CPM probe are the same as those for the LT probe: high performance NMR detection (maximization of rf

field amplitude and homogeneity), maximization of mw field amplitude and homogeneity, optimization of EPR LOD sensitivity, minimization of coupling between coils and other circuit components, and the ability to sustain low pressures.

The main differences between the CPM probe and the LT probe are that the CPM probe is intended for use at higher temperatures, and precise temperature control and accurate temperature measurement are critical. In addition, the CPM probe only has two coils, a solenoid for LOD and a saddle coil for NMR, and the LOD coil will be used at higher detection frequencies than the LOD coil in the LT probe.

The design and construction of the LT probe were described in detail in Section 4.1. Because certain features of the CPM probe are so similar to features of the LT probe, detailed descriptions of these features will not be repeated. Instead, references will be made to the descriptions in the previous section, and similarities and differences will be emphasized.

Improved temperature control and modified probe-head One of the drawbacks of the LT probe was the uncertainty in the temperature measurement: the probe did not contain any temperature sensors, so only the sensor at the edge of the magnet bore, which is a few centimetres from the sample, was used. Because of possible temperature gradients in the bore, this arrangement is insufficient to accurately measure the temperature of the sample for temperatures above the boiling point of helium. In addition, the LT probe did not contain any heaters, and heating the sample with only the heating coil at the edge of the magnet bore can be inefficient and slow, particularly is heating to ambient temperature if required.

For the CPM probe, we decided to modify the probe-head to allow for more accurate temperature measurement and control. The general shape and features of the probe-head are the same, but the height was increased to allow more space for temperature sensors and heaters. The extra space also makes it easier to mount and adjust the home-built variable capacitors.

Optimized NMR coil The LT probe has two orthogonal rf saddle coils with angular widths of 90°. The CPM probe has only one saddle coil, which reduces the constraints on the coil. Therefore, an angular width of 120° was used instead of 90°, giving a more homogeneous B_1 field. In addition, the distance between the NMR coil and the LOD coil was increased, to reduce capacitive coupling and

improve B_1 homogeneity.

The fact that the CPM probe has only two coils in total, rather than three, should mean that there are fewer problems associated with coupling between coils and associated circuit components.

4.2.3 Construction

Probe body

The body of the CPM probe is very similar to that of the LT probe: the main probe body consists of a stainless steel shaft, with brass baffles placed along the length of the probe shaft for the reasons described earlier (mechanical stability, grounding, and restriction of helium flow). Like the LT probe, the CPM probe is designed to be inserted into the external part of a Krymov probe [90]. In place of the brass enclosure at the top of the LT probe is a larger stainless steel enclosure, to allow more space for the cables and connectors. An insulating plate made of epoxy glass fabric laminate (Grade 10G/40, Tufnol Composites Limited, Birmingham, UK) is used instead of the brass plate on the LT probe, to electrically isolate the connectors. This plate supports four hermetically sealed bulkhead female-female type N connectors (R161753000, Radiall, Paris, France) and one circular bulkhead 12-pin connector (DBEU 1031 A012-130, Fischer Connectors, Saint-Prex, Switzerland). The type N and Fischer connectors have leakage rates of 10^{-6} bar cm³ s⁻¹ and 10^{-8} bar cm³ s⁻¹ respectively.

The probe-head for the CPM probe, shown in Figure 4.10, is very similar to that for the LT probe: it was manufactured from PCTFE (polychlorotrifluoroethylene, supplied by Elder Engineering, Herts, UK), and the general shape and features of the probe-head are the same.

The sample holder is identical to the sample holder used for the LT probe, described in Section 4.1.3 and shown in Figure 4.4b. It is manufactured from PCTFE, and consists of two separate pieces: a cylindrical sample cup and a top-hat shaped plug.

The NMR and EPR detection circuits in the probe-head are connected to the connectors at the top of the probe using semi-rigid cables, which are split into two parts to make them easier to remove from the probe. The two parts of the cable are made of the same materials, but have different diameters. The longer, lower part of the cables (UT-141C-TP, Micro-Coax, Pottstown, PA) have a silver-plated

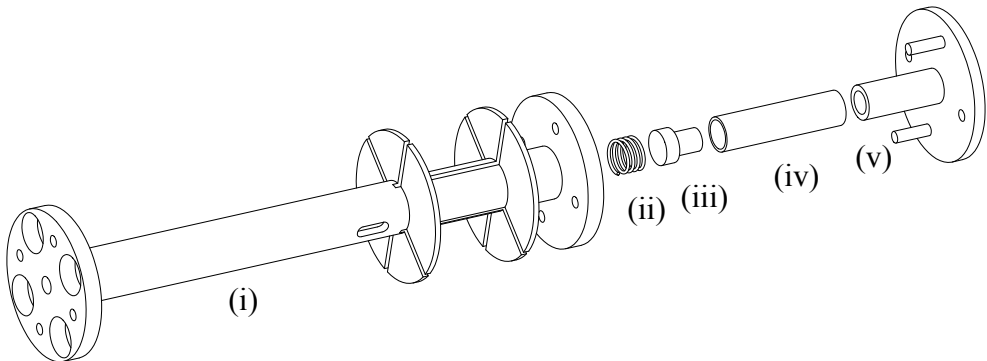


Figure 4.10: Exploded view drawing of the probe-head assembly for the CPM probe. (i) Probe-head. (ii) Spring. (iii) Copper mw mirror. (iv) Sample holder. (v) ‘Top-hat’ plug for sample holder. Coils and other components not shown. Drawings produced with Autodesk Inventor Professional 2013, Educational Version (Autodesk Inc., San Rafael, CA).

copper inner conductor (diameter 0.92 mm), PTFE dielectric (diameter 2.98 mm), and a tin-plated copper outer conductor (diameter 3.58 mm). The respective dimensions of the shorter, upper part of the cables (UT-085C-TP, Micro-Coax, *ibid.*) are 0.51 mm, 1.68 mm, and 2.20 mm. The two parts of each cable were connected using MCX connectors (plug: 73014, Pomona Electronics, Everett, WA; jack: 252131, Amphenol Connex, Moorpark, CA).

In the LT probe, MMCX connectors were used to connect the coils and capacitors in the probe-head to the semi-rigid cables. These ‘snap-on’ connectors are adequate but not ideal, as they are quite fragile. The lower part of the CPM probe was modified to allow space for SMA connectors (plug: 1-1478903-0, TE Connectivity (Greenpar), Schaffhausen, Switzerland; jack: 142-0701-201, Emerson Network Power Connectivity Solutions (Johnson Components), Bannockburn, IL), and to make attachment and detachment of the probe-head more robust.

EPR excitation and detection

The mw field is transmitted to the sample in the same way as it is on the LT probe, using the wave-guide in the external part of the Krymov probe [90]. Copper shielding is again used to contain the mw field: the LOD coil around the sample and a copper ‘mirror’ on top of the sample cup shield the sample in the radial and axial directions respectively. The LOD coil is a single-layer solenoid (30 turns, height 18 mm, inner diameter 9 mm) made of enamelled copper wire (diameter 0.5 mm), with its axis parallel to \mathbf{B}_0 . The coil is connected using

one of the two-part semi-rigid cables, described previously, to a voltage amplifier (HVA-200M-40-F, Laser Components, Olching, Germany) which sits at the top of the probe. The signal is amplified by 40 dB, and digitized using an external analogue-digital/digital-analogue device (USB-6259 DAQ, National Instruments, Austin, TX) for detection frequencies up to about 250 kHz, and a digital phosphor oscilloscope (TDS 7154, Tektronix, Beaverton, OR) for detection frequencies up to about 10 MHz.

NMR excitation and detection

The probe-head supports one saddle coil for ^1H NMR excitation and detection (1 pair of turns, height 20 mm, diameter 7 mm, angular width of loops 120°). It forms part of a resonant circuit tuned to the ^1H frequency at 3.39 T of 144 MHz. The NMR circuit is tuned and matched using the same method as for the LT probe, described in Sections 4.1.3 and 4.1.4 and illustrated in Figure 4.6c: it is coarsely tuned and matched locally with home-built variable capacitors (shown in Figure 4.8), and finely tuned and matched remotely using variable air capacitors (5601, Johanson Manufacturing Corporation, Boonton, NJ) enclosed in an aluminium box at the top of the probe. The NMR coil and local tuning circuit are connected to the top of the probe with one of the two-part semi-rigid cables described previously.

Temperature control

To improve the efficiency and speed of heating the probe to ambient temperature, a home-built resistive heating element was included on the probe-head, in addition to the existing heating coil at the edge of the magnet bore. The heater was formed of loops of enamelled copper wire (diameter 0.1 mm) secured between two layers of copper tape, and wrapped around the LOD coil. The loops of wire were perpendicular to the LOD coil, to minimize coupling between the coil and the loops.

To improve the accuracy of temperature measurements, two temperature sensors were placed in the probe-head. The first of these, a Pt100 resistance temperature detector (RTD) (HEL-705-T-0-12-00, Honeywell, Morristown, NJ) was situated inside the probe-head, immediately above the copper mw mirror. This position was chosen to give the most accurate sample temperature measurement possible with the geometry of the probe-head: the RTD was in good thermal contact with the copper mirror, which was in close proximity to the sample. The

second temperature sensor, also a Pt100 RTD (P0k1.232.2I.B.1000-3, Innovative Sensor Technology AG, Ebnat-Kappel, Switzerland), was used to measure the temperature of the heating element: it was situated adjacent to the outer layer of copper tape which formed part of the heating element.

4.2.4 Performance

Environment

Pressure When using the CPM probe with the outer part of the Krymov probe [90], a pressure of 4×10^{-3} mbar (0.4 Pa) was reached and sustained when the pump outlet was open. For comparison, pressures of 8×10^{-4} mbar (8×10^{-2} Pa) and $1-2 \times 10^{-3}$ mbar (0.1–0.2 Pa) were sustained with the inner part of the Krymov probe and the LT probe respectively. This indicates a small, but non-negligible, leakage from one or more of the bulkhead connectors, or from one of the two o-rings (between the probe and the outer part of the Krymov probe, or between the stainless steel enclosure and the insulating plate). However, this probe is designed for experiments at temperatures above about 250 K, and the magnet bore is not evacuated during experiments, so the seal was considered adequate.

Temperature The sample temperature sensor was tested using the freezing point of water as a reference temperature. At a sample temperature of about 273 K, found by observing the transition of the NMR spectrum from a solid-state to a liquid-state spectrum as the water melted, the temperature sensor measured a value of approximately 271 K. The reasons for this difference are illustrated in Figure 4.11. There is a vertical temperature gradient in the bore, from ~ 273 K at the sample to ~ 100 K where the bore is in thermal contact with the nitrogen cryostat. Furthermore, the wires, which connect the temperature sensor to the top of the magnet bore, are in thermal contact with the colder regions of the bore. These wires conduct heat and, therefore, transmit heat away from the sensor. These two factors cause the sensor to measure a temperature about 2 K lower than the sample temperature. So far, this has only been tested at the freezing point of water.

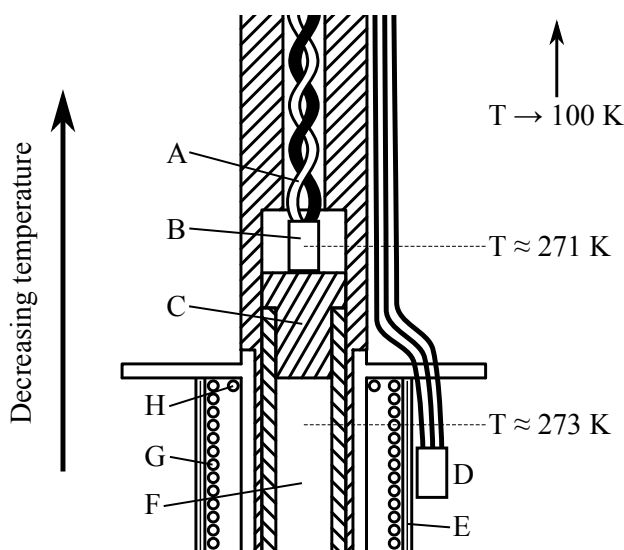


Figure 4.11: Cross-section through assembled probe-head, illustrating temperature control and monitoring components, and vertical temperature gradient at a sample temperature of 273 K. A. Wires for sample temperature sensor. B. Sample temperature sensor. C. Microwave mirror. D. Heating element temperature sensor. E. Home-built heating element. F. Sample. G. LOD EPR solenoid. H. NMR saddle coil.

NMR detection

To assess the performance of the NMR coil, initial NMR experiments were carried out using a 100 μl sample of ethanol at 300 K. A nutation curve was acquired by varying the pulse length at constant B_1 amplitude, and is shown in Figure 4.12: the coil had a 90-time of 24 μs with a transmit power attenuation of 4 dB (30 W). In the second cycle, the signal amplitude reaches approximately 85 % of the maximum amplitude in the first cycle, demonstrating a reasonable B_1 field homogeneity.

EPR detection

The LOD system was designed to operate at detection frequencies in the region of 10 MHz, while the LOD voltage amplifier had a bandwidth of 200 MHz. The LOD system was tested at ambient temperature and detection frequencies up to 10 MHz. Under these conditions, it was found that the SNR was too low to detect any LOD EPR signal.

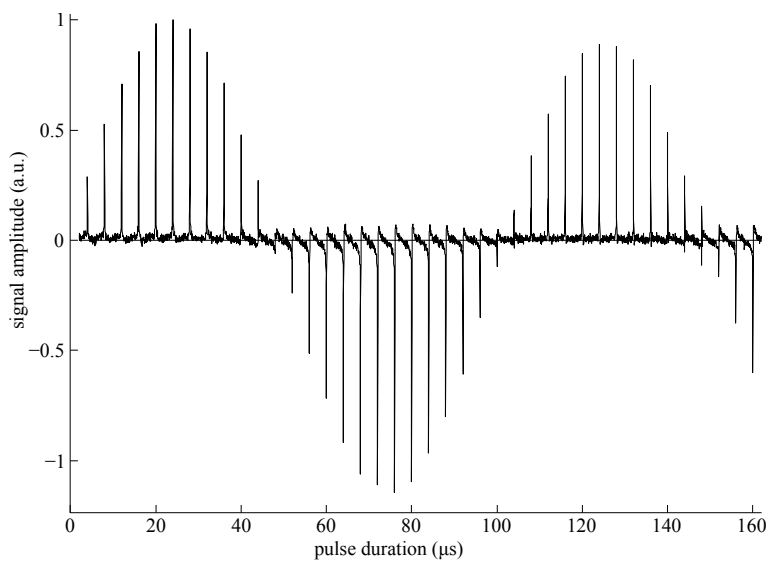


Figure 4.12: Nutation curve for tuned NMR saddle coil using 100 μl ethanol at 300 K. Peaks are spectra produced by a Fourier transform of the FID following an rf pulse with an input power of 30 W B_1 duration was increased in steps of 4 μs . 90-time was measured from the curve as 24 μs .

4.2.5 Conclusions

Two limitations of this probe were the SNR of the LOD EPR system, and the temperature control.

Temperature control was the lesser of these two problems. It would, in principle, be possible to calibrate the sample temperature sensor by measuring the offset of the measurement through a range of temperatures. This could be done by observing the solid–liquid transition of the NMR spectra of different substances with a range of known freezing temperatures. For example, the freezing temperatures of mixtures of ethanol and water in different ratios are well known, so they could be used for such a purpose [121].

However, although such a temperature sensor calibration may be possible in principle, in practice it is likely to be difficult, as the temperature gradients were not constant, and depended on the duration of the heating. Temperature measurements could be made more accurate by using a smaller temperatures sensor, and thinner wires to connect the sensor to the top of the magnet bore. The wires could also be made longer, and wound around the probe to give a greater length of wire through a given temperature gradient. The sensor could also be placed closer to the sample, by drilling a hole in the copper mirror and placing the sensor inside the mirror.

The limiting factor for the probe was the low SNR of the LOD EPR system, which prevented the recording of any useful EPR data. However, the experiments proposed in this chapter should still be feasible if the EPR LOD system is modified to operate at a lower detection frequency: a solenoid with more turns could be used, in combination with a lower frequency pre-amplifier, such as the SSM2019 pre-amplifier used for LOD EPR with the LT probe. The SSM2019 has a minimum noise figure of $1.0 \text{ nV}/\sqrt{\text{Hz}}$, which is significantly lower than the minimum noise figure of $4.5 \text{ nV}/\sqrt{\text{Hz}}$ for the higher frequency pre-amplifier used for the CPM probe. The SSM2019 has a bandwidth of 200 kHz for a voltage gain of 1000 (an amplification of 60 dB), so it would be possible to use detection frequencies as high as this value using this pre-amplifier. LOD EPR has been previously demonstrated at frequencies in this region: examples from the literature include frequencies of 100 kHz and 80 kHz at X-band [122, 123] and frequencies ranging from 70 kHz to 1 MHz at a magnetic field of $\sim 10 \text{ mT}$ [124, 125].

Chapter 5

Laplace Inversion of Relaxation Data

5.1 Introduction

Much of the data presented in this thesis exhibits multi-exponential decay. Many methods exist for fitting a function to multi-exponential relaxation data such as this and extracting the time constants. Where there is sufficient prior knowledge of the pattern of the distribution, least-squares fitting is a suitable tool [126]. For example, published EPR relaxation data has been fitted with exponential functions with either several individual components or distributions of relaxation times [127, 128]. However, such information is often not available *a priori*, so techniques for finding the distribution which do not require prior knowledge about the shape of the distribution can often return more reliable results. Inversions such as these are ill-conditioned: noisy data can be represented by many different time constant distributions, and a direct inversion is very susceptible to noise. If it is assumed that the underlying distribution is smooth, regularization can be used to obtain a robust and physically meaningful result. A commonly used method is Tikhonov regularization, which is often used with a non-negativity (NN) constraint to prevent oscillations in the solution. A NN constraint forces the spectrum to be positive everywhere, and hence it is assumed that all of the relaxation components have the same sign. However, such a constraint is not always justified, for example in magnetic resonance systems where magnetic exchange or cross-relaxation occur.

An algorithm based on Tikhonov regularization for performing an inverse Laplace transform (ILT) of multi-exponential relaxation data without a NN con-

straint is presented in this chapter. The algorithm uses the uniform penalty and a zero-crossing penalty to stabilize the solution and prevent unphysical oscillations in the spectrum [129]. In principle the algorithm can be used on data with an arbitrary number of dimensions. It is demonstrated here on synthetic 1-dimensional data, and is used to analyse 2- and 3-dimensional data elsewhere in this thesis. The algorithm was presented in detail in a recent publication [130].

For data of which the nature of the relaxation (for example, exponential or Gaussian) is known or assumed, this algorithm can be used as a stand-alone procedure. However, there are often cases when it is difficult to classify data as such, and for these cases we have proposed a two-step procedure to analyse the data: the nature of the relaxation is determined in the first step, and the second step is the fitting algorithm.

5.2 Algorithm

5.2.1 Problem description

Consider an R -dimensional NMR data set $S \in \mathbb{R}^{N_1 \times N_2 \times \dots \times N_R}$ with $N = \prod_{r=1}^R N_r$ data points measured at discrete sampling times t_1, \dots, t_R . The data can be expressed as

$$S(t_1, \dots, t_R) = \int_0^\infty \dots \int_0^\infty \mathcal{K}_1(t_1, \tau_1) \dots \mathcal{K}_R(t_R, \tau_R) \mathcal{G}(\tau_1, \dots, \tau_R) d\tau_1 \dots d\tau_R + E(t_1, \dots, t_R), \quad (5.1)$$

where $\mathcal{G}(\tau_1, \dots, \tau_R)$ is the probability density of spins with parameters τ_r ($r = 1, \dots, R$), and is called the spectrum; $\mathcal{K}_r(t_r, \tau_r)$ are continuous functions which relate experimental parameters t_r to spectral parameters τ_r , and are called the kernels; and $E(t_1, \dots, t_R)$ is the experimental noise. For example, for data decaying exponentially along dimension r , a suitable kernel is $\mathcal{K}_r = e^{-t_r/\tau_r}$. If a dimension is not inverted, an identity matrix can be used for the kernel. If the signal and spectrum vary smoothly along the non-inverted dimension, the SNR is improved compared with inversions of individual data subsets [131].

The noise is usually assumed to be additive, independent and identically distributed (iid) Gaussian white noise with zero mean. In the following algorithm, data is scaled by the inverse of the standard deviation of the noise, so that the

noise has a variance equal to one.

The data set S would often be acquired to measure the parameters τ_r , which are contained in the spectrum \mathcal{G} . The objective of the ILT algorithm is to estimate the spectrum \mathcal{G} from the data S .

The first step is to represent eq (5.1) in matrix form. The spectrum \mathcal{G} and Kernels \mathcal{K}_r are discretized: $\mathcal{G} \rightarrow \mathbf{G} \in \mathbb{R}^{M_1 \times M_2 \times \dots \times M_R}$ with $M = \prod_{r=1}^R M_r$ points; $\mathcal{K}_r \rightarrow \mathbf{K}_r \in \mathbb{R}^{N_r \times M_r}$. The signal and noise, expressed as matrices \mathbf{S} and \mathbf{E} , are then vectorized along with the spectrum: $\mathbf{S} \rightarrow \mathbf{s} \in \mathbb{R}^{N \times 1}$; $\mathbf{G} \rightarrow \mathbf{g} \in \mathbb{R}^{M \times 1}$; $\mathbf{E} \rightarrow \mathbf{e} \in \mathbb{R}^{N \times 1}$. Finally, the kernels \mathbf{K}_r are combined into a single matrix using

$$\mathbf{K} = \mathbf{K}_R \otimes \mathbf{K}_{R-1} \otimes \dots \otimes \mathbf{K}_1. \quad (5.2)$$

Equation (5.1) can now be written

$$\mathbf{s} = \mathbf{K}\mathbf{g} + \mathbf{e}, \quad (5.3)$$

so the objective is now to estimate the vectorized spectrum \mathbf{g} from the discretized data \mathbf{s} , and the spectrum can then be reshaped to give \mathbf{G} .

5.2.2 Data compression

Solving eq (5.3) with the full data set and kernels can be very CPU and memory intensive, making it impractical on most computers. For example, for the 2-dimensional experiments presented in Chapter 6, a typical data set consisted of about 20×50 data points, and spectra with about 100×100 points were calculated, giving a typical kernel size of $10^3 \times 10^4$ points. However, by taking advantage of the smoothness of the data, data can be compressed and a solution on a standard desktop computer can be enabled, as will be demonstrated here.

The size of the data matrix and the kernels can be reduced using a singular value decomposition of the kernels: kernel \mathbf{K}_r can be decomposed into [29, 132]

$$\mathbf{K}_r = \mathbf{U}_r \boldsymbol{\Sigma}_r \mathbf{V}_r^T, \quad (5.4)$$

where $\mathbf{U}_r \in \mathbb{R}^{N_r \times N_r}$ and $\mathbf{V}_r \in \mathbb{R}^{M_r \times M_r}$ are unitary matrices, and $\boldsymbol{\Sigma}_r \in \mathbb{R}^{N_r \times M_r}$ is a rectangular matrix which is zero everywhere, except for along the diagonal which contains the singular values (SVs) in decreasing order. SVs of smooth kernels typically decay quickly to zero, so the kernels can be compressed by choosing a

sub-matrix $\tilde{\Sigma}_r$ of Σ_r corresponding to the n_r largest SVs, and similar sub-matrices $\tilde{\mathbf{U}}_r$, and $\tilde{\mathbf{V}}_r$ of \mathbf{U}_r and \mathbf{V}_r :

$$\tilde{\mathbf{U}}_r = \mathbf{U}_r [1, \dots, N_r; 1, \dots, n_r], \quad (5.5)$$

$$\tilde{\Sigma}_r = \Sigma_r [1, \dots, n_r; 1, \dots, n_r], \quad (5.6)$$

$$\tilde{\mathbf{V}}_r = \mathbf{V}_r [1, \dots, M_r; 1, \dots, n_r]. \quad (5.7)$$

The sub-matrices can now be used to compress the kernels and the data: compressed kernels $\tilde{\mathbf{K}}_r \in \mathbb{R}^{n_r \times M_r}$ are given by

$$\tilde{\mathbf{K}}_r = \tilde{\Sigma}_r \tilde{\mathbf{V}}_r^T. \quad (5.8)$$

The data \mathbf{S} is compressed along each dimension r sequentially using the matrices $\tilde{\mathbf{U}}_r$. First, the dimensions of \mathbf{S} are cyclically permuted so that r is the first dimension, then \mathbf{S} is reshaped into a 2-dimensional matrix $\mathbf{S}_{\langle r \rangle} \in \mathbb{R}^{N_r \times (\prod_{p \neq r} N_p)}$, with r the first dimension, and the remaining dimensions combined into the second dimension of $\mathbf{S}_{\langle r \rangle}$. The matrix $\mathbf{S}_{\langle r \rangle}$ is then compressed using

$$\tilde{\mathbf{S}}_{\langle r \rangle} = \tilde{\mathbf{U}}_r^T \mathbf{S}_{\langle r \rangle}. \quad (5.9)$$

The reshaping of the data can then be undone and a matrix with data compressed along dimension r is obtained. The reshape–compress–reshape cycle is repeated for each dimension until the fully compressed matrix $\tilde{\mathbf{S}} \in \mathbb{R}^{n_1 \times n_2 \times \dots \times n_R}$ is obtained.

For synthetic data, where the noise matrix is available directly, the noise can be compressed using the same procedure as for data compression: the noise matrix \mathbf{E} is compressed along each dimension r using

$$\tilde{\mathbf{E}}_{\langle r \rangle} = \tilde{\mathbf{U}}_r^T \mathbf{E}_{\langle r \rangle}. \quad (5.10)$$

If the noise is iid, the noise compression does not change the noise statistics: the compressed noise has the same mean and variance as the original noise [132].

The data and noise can be compressed and decompressed along each dimension r using:

$$\tilde{\tilde{\mathbf{S}}}_{\langle r \rangle} = \tilde{\mathbf{U}}_r \tilde{\mathbf{U}}_r^T \mathbf{S}_{\langle r \rangle}, \quad (5.11)$$

$$\tilde{\tilde{\mathbf{E}}}_{\langle r \rangle} = \tilde{\mathbf{U}}_r \tilde{\mathbf{U}}_r^T \mathbf{E}_{\langle r \rangle}. \quad (5.12)$$

The compression-decompression process does not return the original data, since $\tilde{\mathbf{U}}_r \tilde{\mathbf{U}}_r^T \neq \mathbf{1}$. However, if a suitable number of SVs is used for data compression and decompression, the compressed-decompressed (cdc) data should accurately represent the data. Furthermore, the residuals between the original data and the cdc data should be equivalent to noise, with the same mean and variance as the original noise. Note that the cdc data is not free from noise, but high-frequency noise not compatible with the kernels is removed by the data compression, in a similar manner to a low-pass filter.

For optimal data compression, an appropriate number of SVs, n_r , must be determined. n_r is chosen such that only the SVs with a contribution larger than the random noise level are retained, so the optimum number of SVs, \check{n}_r , is the minimum value of n_r which satisfies

$$\frac{(\Sigma_r)_1}{(\Sigma_r)_{n_r}} \geq \frac{\max(\mathbf{S})}{\sigma(\mathbf{E})}, \quad (5.13)$$

where $\max(\mathbf{S})$ and $\sigma(\mathbf{E})$ are the maximum value of \mathbf{S} and the standard deviation of \mathbf{E} respectively. If too few SVs are retained ($n_r < \check{n}_r$), the data is over-compressed, and the compressed data does not accurately represent the data. On the other hand, if too many SVs are retained ($n_r > \check{n}_r$), the compressed data and kernels are larger than necessary, and the compressed data will be too noisy at small values of t_r , meaning the algorithm may over-fit this part of the compressed data. This is illustrated in Figure 5.1.

\check{n}_r can also be found by comparing the noise with the residuals between the data \mathbf{S} and the cdc data $\tilde{\mathbf{S}}$. Using this method, the optimum number of SVs, \check{n}_r , is the minimum value of n_r which satisfies

$$\sigma(\tilde{\mathbf{S}} - \mathbf{S}) \leq \sigma(\mathbf{E}). \quad (5.14)$$

Once the data, kernels and noise have been compressed, the vectorization process described previously can be applied to the compressed matrices, and eq (5.3) can be rewritten as

$$\tilde{\mathbf{s}} = \tilde{\mathbf{K}}\mathbf{g} + \tilde{\mathbf{e}}, \quad (5.15)$$

where $\tilde{\mathbf{K}} = \tilde{\mathbf{K}}_R \otimes \tilde{\mathbf{K}}_{R-1} \otimes \cdots \otimes \tilde{\mathbf{K}}_1 \in \mathbb{R}^{n \times M}$, $\tilde{\mathbf{s}} \in \mathbb{R}^{n \times 1}$ and $\tilde{\mathbf{e}} \in \mathbb{R}^{n \times 1}$ are obtained by vectorizing $\tilde{\mathbf{S}}$ and $\tilde{\mathbf{E}}$, and $n = \prod_{r=1}^R n_r$ is the total number of points in the compressed data.

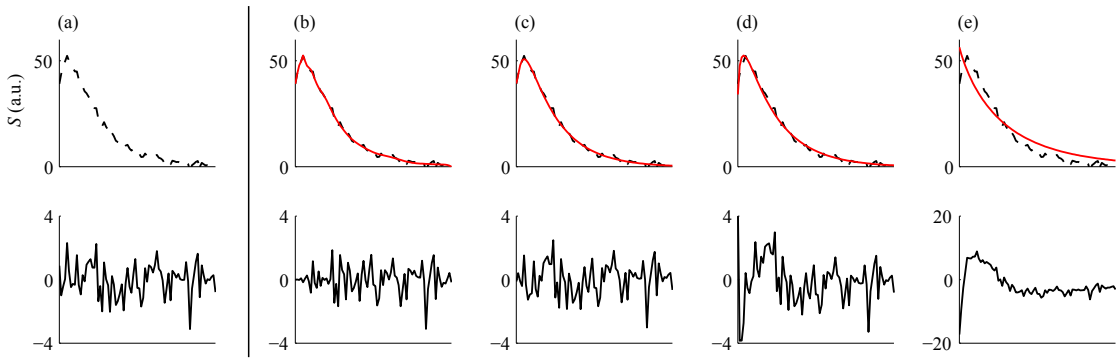


Figure 5.1: Effect of number of SVs, n_r , on cdc data. (a) synthetic 1-dimensional data with 81 points (upper panel) and noise with unity variance (lower panel). (b)–(e) upper panels show synthetic data compressed and decompressed with different values of n_r (solid red trace) and original synthetic data for comparison (dashed black trace); lower panels show residuals between original data and cdc data. (b) $n_r = 20$, $\sigma = 0.84$, (c) $n_r = 5$, $\sigma = 0.99$, (d) $n_r = 3$, $\sigma = 1.4$, (e) $n_r = 1$, $\sigma = 4.3$, where σ is the standard deviation of the residuals.

Data compression can be advantageous for two reasons. First, the reduction in matrix sizes reduces the computational memory requirements, meaning larger spectra can be calculated, or spectra can be calculated faster. Second, the singular vectors (the columns of \mathbf{U}_r and \mathbf{V}_r) associated with the smallest singular values contribute most heavily to the spectrum. These are the singular vectors which are removed in the data compression. If they were not removed, noise in the data would be amplified by the small singular values upon inversion of the data [133].

5.2.3 Choice of kernel

The data compression process relies on a suitable kernel being chosen. If an unsuitable kernel is used, it is still possible to compress the data, with the cdc data accurately reflecting the raw data, and the algorithm may still fit the data with acceptable residuals. However, in such a case, the fitted spectrum usually shows significant oscillations, and may consist of many narrow peaks which do not accurately represent physical processes or parameters.

There are many cases when a particular kernel can be assumed. Exponential kernels are often used because relaxation data in EPR [50] and NMR [134] and polarization build-up in DNP [40] can usually be described by exponential functions. However, other decay functions have also been observed in EPR relaxation data, including Gaussian decay [135, 136], ‘stretched exponential’ decay [24, 127, 137], and products of exponential and Gaussian decay, resulting in Voigt-broadened

spectral lines [138, 139].

Romanelli and Kevan derived equations for echo signal decay in two- and three-pulse echo EPR experiments using the Gauss-Markov (GM) and sudden jump (SJ) models [25]. The form of the decay depends strongly on the correlation time τ_c and the model used to describe the decay. In extreme cases, the two-pulse echo signal decay can be expressed as a simple function of inter-pulse time τ_e . For the case $\frac{\tau_e}{\tau_c} \gg 1$, the signal decay can be expressed as

$$S(2\tau_e) = e^{-a\sqrt{\tau_e\tau_c}}, \quad (5.16)$$

if either the GM or SJ model is used, where a is a value which depends on properties of the spin system. For $\frac{\tau_e}{\tau_c} \ll 1$, the signal decay can be expressed as

$$S(2\tau_e) = e^{-a\sqrt{4\tau_e^3/3\tau_c}}, \quad (5.17)$$

if the GM model is used, and as

$$S(2\tau_e) = e^{-a\sqrt{\pi}\tau_e^2/\tau_c}, \quad (5.18)$$

if the SJ model is used.

In each of eqs (5.16) to (5.18), the echo decay as a function of τ_e has the form of a ‘stretched exponential’. That is, the inter-pulse time appears in the exponent as τ_e^α , where the value of the ‘stretch parameter’ α depends on the case considered, and on whether the GM model or the SJ model is used to explain the decay.

In the presently described algorithm, such data would be represented by a kernel $e^{-(t/\tau)^\alpha}$ in eq (5.1). For experimental data, if it is known that the data is a stretched exponential decay, and the stretch parameter is known, the corresponding kernel can be used in the algorithm. For data with an unknown kernel, a method for algorithmically choosing an appropriate kernel is proposed in the following. We assume that the kernel is a stretched exponential $e^{-(t/\tau)^\alpha}$ with an unknown stretch parameter α . The data is then compressed using SVD of a range of kernels with different values of α , and the minimum number of SVs needed to adequately represent the data, \check{n}_r , is found for each kernel. An unsuitable kernel requires more SVs than a suitable kernel to compress and decompress the data without losing information, so a suitable kernel can be found by minimizing \check{n}_r with respect to α . This is illustrated in Figure 5.2 for synthetic data exhibiting

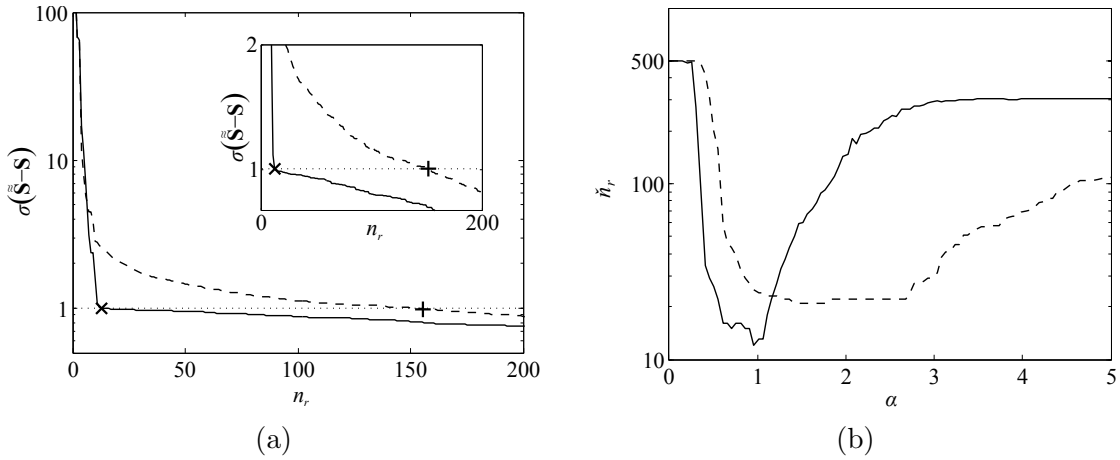


Figure 5.2: (a) Standard deviation σ of residuals between data $(\tilde{\mathbf{S}})$ synthesized with an exponential kernel and cdc data $(\tilde{\tilde{\mathbf{S}}})$, compressed and decompressed with two different kernels and different values of n_r . Solid line: data were compressed and decompressed with an exponential kernel. Dashed line: data were compressed and decompressed with a Gaussian kernel. Dotted line represents $\sigma = 1$. The inset highlights the points at which n_r crosses the $\sigma = 1$ line. \check{n}_r is marked with a \times for the exponential kernel ($\check{n}_r = 13$) and with a + for the Gaussian kernel ($\check{n}_r = 154$). (b) \check{n}_r for data synthesized with an exponential kernel (solid line) and a Gaussian kernel (dashed line), and compressed and decompressed with a stretched exponential kernel $e^{-(t/\tau)^\alpha}$.

both exponential and Gaussian decay.

Figure 5.2a shows $\sigma(\tilde{\mathbf{S}} - \mathbf{S})$ as a function of the number of SVs, n_r , for synthetic exponential data compressed and decompressed with both exponential and Gaussian kernels. In both cases the spectrum in Figure 5.8 was used to create the data with an exponential kernel. For each case, the optimum number of SVs, \check{n}_r , as defined by eq (5.14), can be clearly seen from the plot, with \check{n}_r greater for the Gaussian data compression than for the exponential data compression. Figure 5.2b shows \check{n}_r for data sets created with exponential and Gaussian kernels and compressed and decompressed with stretched exponential kernels $e^{-(t/\tau)^\alpha}$ ($0 \leq \alpha \leq 5$). \check{n}_r have minima close to $\alpha = 1$ and $\alpha = 2$, respectively, as expected.

It is interesting to note that, in Figure 5.2b, $\check{n}_r(\alpha)$ has a minimum at a significantly lower value of \check{n}_r for the exponential data ($\check{n}_r = 12$) than it does for the Gaussian data ($\check{n}_r = 21$), even though the same spectrum was used to calculate both data sets, and they have the same SNR. This suggests that data compression with SVD is more successful with exponential data than it is with Gaussian data. It is possible to rationalize this by considering the contrasting properties of Gaussian and exponential decay. Figure 5.3 shows an exponential function and a Gaussian function with the same time constant. The exponential curve initially

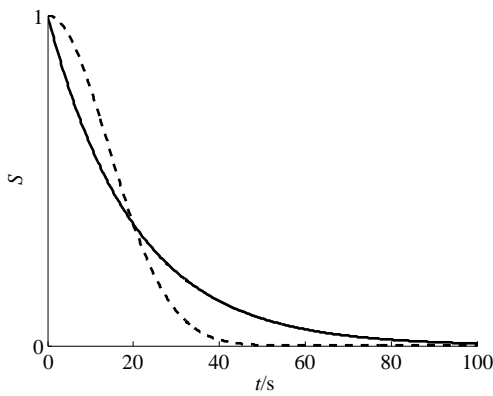


Figure 5.3: Exponential and Gaussian decay with a time constant $\tau = 20$ s. Solid line: exponential decay, $S = \exp(-t/\tau)$. Dashed line: Gaussian decay, $S = \exp(-(t/\tau)^2)$.

decreases more quickly, with the gradient decreasing with increasing time, while the Gaussian curve decreases more slowly at first, before decreasing quickly towards zero. The Gaussian curve has a gradient very close to zero for very small values of t , and for values of t greater than about 2.5τ . Therefore, it is more ‘difficult’ to represent decay at small and large values of t with a Gaussian kernel than it is with an exponential kernel, and this is a possible reason why the Gaussian data compression requires more singular values than the exponential data compression.

Limitations

There are certain cases for which this method for determining an appropriate kernel may not be suitable. For example, consider data exhibiting a superposition of exponential and Gaussian components. The above method only returns one value of the stretch parameter α for a given data set, so it would not be possible to identify and separate the exponential and Gaussian components using this method.

For exponential data with distributions of mono-exponential decay components, it may be possible in some cases to empirically fit the data with a stretched exponential. In such cases, the above method may return a stretch parameter not equal to one, even though the underlying data is exponential. Therefore, this method should be used carefully if kernels are to be determined reliably, and the method may need to be improved to distinguish between empirical fits and underlying behaviour. Note that exponential data with distributions of components, that can be empirically fitted with stretched exponential functions, are distinct

from genuine stretched exponential data, such as that represented by eqs. (5.16) to (5.18).

If it is not possible to reliably determine a kernel using this method, and if there is no fundamental reason to believe that a particular kernel should be used, an exponential kernel is generally used as a ‘default’ kernel.

5.2.4 Regularization

Using eq (5.15), a naive approach to finding the spectrum \mathbf{g} would be to solve

$$\hat{\mathbf{g}} = \arg \min_{\mathbf{g}} \left\{ \left\| \tilde{\mathbf{K}}\mathbf{g} - \tilde{\mathbf{s}} \right\|^2 \right\}, \quad (5.19)$$

where $\|\cdot\|$ represents the Frobenius norm of a matrix.* However, eq (5.15) is ill-conditioned: there is not a unique spectrum \mathbf{g} which produces a data matrix $\tilde{\mathbf{s}}$, and the results of a direct inversion are very susceptible to noise in the data. Therefore, a direct inversion using eq (5.19) will not give a stable solution. Instead, a regularization term is added to the inversion equation to stabilize the inversion, and it is re-written

$$\begin{aligned} \hat{\mathbf{g}} &= \arg \min_{\mathbf{g}} \left\{ \left\| \tilde{\mathbf{K}}\mathbf{g} - \tilde{\mathbf{s}} \right\|^2 + \lambda^2 \|\Lambda\mathbf{g}\|^2 \right\} \\ &= \arg \min_{\mathbf{g}} \left\{ \mathbf{g}^T \tilde{\mathbf{K}}^T \tilde{\mathbf{K}}\mathbf{g} - 2\tilde{\mathbf{s}}^T \tilde{\mathbf{K}}\mathbf{g} + \tilde{\mathbf{s}}^T \tilde{\mathbf{s}} + \lambda^2 \mathbf{g}^T \Lambda^T \Lambda \mathbf{g} \right\}, \end{aligned} \quad (5.20)$$

where $\Lambda \in \mathbb{R}^{M \times M}$ is the regularization matrix and λ is a global scaling factor.

In NMR applications, a common choice for the regularization matrix is the identity matrix $\mathbf{1}_M$ in combination with a non-negativity (NN) constraint. NN cannot always be justified, for example in situations when different processes cause signal to both increase and decrease during acquisition. However, using $\Lambda = \mathbf{1}_M$ without a NN constraint rarely leads to reliable, meaningful spectra when using exponential kernels. The algorithm presented here is based on the uniform-penalty (UP) regularization proposed by Borgia et al. [129, 140], and no NN constraint is used. The UP regularization was designed to produce spectra with both narrow and wide peaks, but it also reduces the need for a NN constraint. However, it is still possible to produce spectra with unphysical undershoots in the vicinity of

* $\|\mathbf{A}\| = \sqrt{\sum_{i=1}^m \sum_{j=1}^n |a_{ij}|^2} = \sqrt{\text{Tr}(\mathbf{A}\mathbf{A}^\dagger)}$, where a_{ij} are the elements of $m \times n$ matrix \mathbf{A} . Henceforth, *norm* refers to *Frobenius norm*.

narrow peaks. This problem can be reduced by using a zero-crossing (ZC) penalty, weighted with the slope. The ZC penalty does not preclude zero-crossing, but it makes it more expensive, thereby making unphysical undershoots more unlikely.

The regularization term $\Lambda^T \Lambda$ in eq (5.20) is given by

$$\begin{aligned} \Lambda^T \Lambda = & \left(\sum_{r=1}^R \mathbf{C}_r \mathbf{L}_{2,r} \right)^T \left(\sum_{r=1}^R \mathbf{C}_r \mathbf{L}_{2,r} \right) + \left(\sum_{r=1}^R \mathbf{D}_r \mathbf{L}_{1,r} \right)^T \left(\sum_{r=1}^R \mathbf{D}_r \mathbf{L}_{1,r} \right) \\ & + \left(\sum_{r=1}^R \mathbf{A}_r \right)^T \left(\sum_{r=1}^R \mathbf{A}_r \right), \end{aligned} \quad (5.21)$$

where the three terms are a uniform penalty (UP), a zero-crossing (ZC) penalty and a boundary artifact (BA) penalty, respectively, and each dimension r has a separate contribution to the regularization. $\mathbf{L}_1 \in \mathbb{R}^{M \times M}$ and $\mathbf{L}_2 \in \mathbb{R}^{M \times M}$ are the first and second derivative operators, corresponding to slope and curvature, respectively [141]. $\mathbf{C} \in \mathbb{R}^{M \times M}$, $\mathbf{D} \in \mathbb{R}^{M \times M}$ and $\mathbf{A} \in \mathbb{R}^{M \times M}$ are the coefficient matrices for the three penalty terms.

Uniform penalty

The regularization term $\lambda^2 \Lambda^T \Lambda$ in equation (5.20) determines the smoothness of the spectrum \mathbf{g} : a larger regularization will mean more smoothing is applied, and the resulting spectrum will have broader peaks, while a smaller regularization means less smoothing and narrower peaks. An appropriate degree of regularization is essential in order to perform a reliable inversion, as too much regularization can cause nearby narrow peaks to merge into one broad peak, while too little regularization can break up a long tail or a broad peak into several separate peaks.

For a spectrum containing both narrow and broad peaks, or a narrow peak with a broad tail, a constant regularization may lead to either or both of these problems. This problem can be overcome by choosing a regularization matrix Λ which varies across the spectrum, such that the smoothing *penalty* is approximately constant [129]. Using this technique, called uniform-penalty (UP) smoothing, it is possible to produce spectra with both narrow and broad peaks, without broadening or merging nearby narrow peaks or splitting broad peaks.

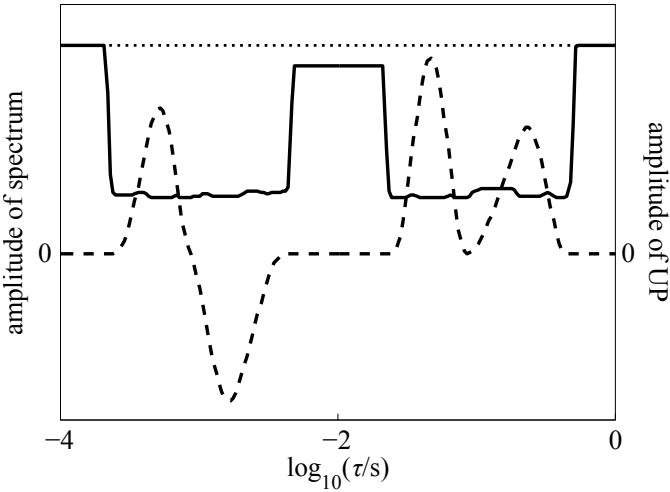


Figure 5.4: Uniform Penalty. Dashed line is a synthetic 1-dimensional spectrum with four peaks. Solid line is the UP. Dotted line is the upper limit of the UP, given by $(\alpha_{0,r}\Delta_r^5)^{-\frac{1}{2}}$.

The coefficient matrix for the UP regularization is

$$\begin{aligned} (\mathbf{C}_r)_{k,l} = & \delta_{kl} \left(\alpha_{c,r}\Delta_r^{-1} \max \left\{ \left((\mathbf{L}_{2,r}\mathbf{g})^{(2)} \right)_j \right\}_{j=k-\eta_2, \dots, k+\eta_2} \right. \\ & + \left. \alpha_{p,r}\Delta_r \max \left\{ \left((\mathbf{L}_{1^*,r}\mathbf{g})^{(2)} \right)_j \right\}_{j=k-\eta_1, \dots, k+\eta_1} + \alpha_{0,r}\Delta_r^5 \right)^{-\frac{1}{2}}, \end{aligned} \quad (5.22)$$

where Δ_r is the spacing between adjacent points in dimension r of the spectrum, $(2\eta_{1,2} + 1)$ is the number of neighbouring points over which the maximum is determined, $\alpha_{0,r}$, $\alpha_{c,r}$, and $\alpha_{p,r}$ are adjustable compliance parameters, and $(\cdot)^{(2)}$ represents the entry-wise square of a matrix or vector. $\alpha_{c,r}$ is a curvature parameter, and is the main term to ensure a uniform penalty. $\alpha_{p,r}$ is a slope regularization parameter: it prevents broad peaks in the spectrum from being broken up into several narrow peaks, and also prevents unphysical straight segments. $\alpha_{0,r}$ is a compliance floor, which should be large enough to seed curvature development, but not so large that it causes under-smoothing. The optimal values of $\alpha_{c,r}$ and $\alpha_{p,r}$ depend on the signal-to-noise ratio (SNR) of the data, while the choice of $\alpha_{0,r}$ is less dependent on the data. Selection of compliance parameters will be discussed later. $\eta_{1,2}$ were chosen to be either 1 or 2, meaning maxima were taken over three or five points to increase stability

The UP is illustrated in Figure 5.4. It has an approximately constant value where the gradient and curvature are significant, and approaches an upper limit,

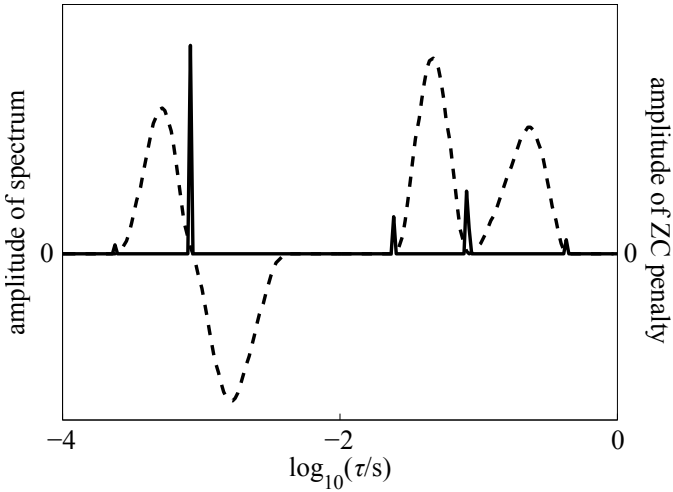


Figure 5.5: Zero-Crossing Penalty. Dashed line is a synthetic 1-dimensional spectrum with four peaks. Solid line is the ZC penalty.

determined by the compliance floor, where the gradient and curvature approach zero.

Zero-crossing penalty

As stated previously, the algorithm presented here does not use a NN constraint. The UP significantly reduces unphysical zero-crossing, but undershooting at the edges of sharp peaks can still occur. To prevent such unphysical zero-crossing, a ZC penalty, weighted with the gradient, is applied [130]. The coefficient matrix for the ZC penalty is

$$(\mathbf{D}_r)_{k,l} = \frac{\delta_{kl} \max \left\{ \left(\left(\frac{1}{2} \mathbf{L}_{1-,r} \text{sign}(\mathbf{g}) \right)^{(2)} + \left(\frac{1}{2} \mathbf{L}_{1+,r} \text{sign}(\mathbf{g}) \right)^{(2)} \right)_j \right\}_{j=k-\eta_D, \dots, k+\eta_D}}{\sqrt{\alpha_{d,r} \Delta_r^3 + \alpha_{D,r} \Delta_r^{-1} \left((\mathbf{L}_{1*,r} \mathbf{g})^{(2)} \right)_k}}, \quad (5.23)$$

where $\alpha_{d,r}$ and $\alpha_{D,r}$ are the weighting and upper limit for the ZC penalty respectively, and $\mathbf{L}_{1\pm,r}$ are the first upper and lower subdiagonals of $\mathbf{L}_{1,r}$. The ZC penalty is illustrated in Figure 5.5. It is non-zero and weighted by the slope wherever the spectrum crosses the horizontal axis, and zero everywhere else.

Boundary artifacts

For a successful, reliable inversion, upper and lower limits $\tau_{r,\min}$ and $\tau_{r,\max}$ of the spectral axes should be chosen to be significantly beyond any features in the

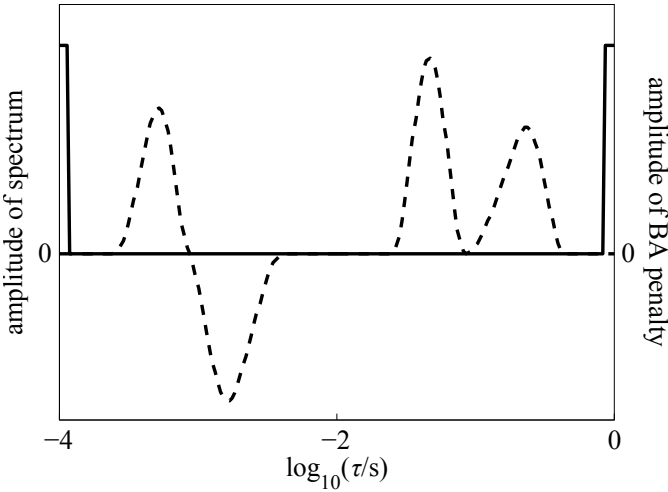


Figure 5.6: Boundary Artifact Penalty. Dashed line is a synthetic 1-dimensional spectrum with four peaks. Solid line is the BA Penalty.

spectrum. However, even when this is the case, boundary artifacts can still appear. For example, a baseline offset in the data may be represented by a peak in the spectrum close to $\tau_{r,\max}$. Such boundary artifacts can be prevented by applying a penalty to the amplitude of points at the edges of the spectrum. The coefficient matrix for the BA penalty is

$$(\mathbf{A}_r)_{k,l} = \frac{(\mathbf{H}_r)_{k,l}}{\sqrt{\alpha_{a,r}\Delta_r + \alpha_{A,r}\Delta_r^{-1}(\mathbf{g}^{(2)})_k}}, \quad (5.24)$$

where $\alpha_{a,r}$ and $\alpha_{A,r}$ are the weighting and upper limit for the BA penalty respectively, and \mathbf{H}_r is given by

$$\mathbf{H}_r = \mathbf{1}_{M_R} \otimes \mathbf{1}_{M_{R-1}} \otimes \dots \otimes \mathbf{1}_{M_{r+1}} \otimes \mathbf{H}_{0,r} \otimes \mathbf{1}_{M_{r-1}} \otimes \dots \otimes \mathbf{1}_{M_1}, \quad (5.25)$$

with

$$(\mathbf{H}_{0,r})_{k,l} = (H(h_{0,r} - k) + H(h_{0,r} - M_r + k))\delta_{k,l}, \quad (5.26)$$

where $H(\cdot)$ is the Heaviside step function, and $h_{0,r}$ defines the width of the BA penalty. The BA penalty is illustrated in Figure 5.6. It is non-zero near the edges of the spectrum, and zero everywhere else.

5.2.5 Parameter selection

The regularization matrix Λ depends on many adjustable parameters, namely $\alpha_{c,r}$, $\alpha_{p,r}$ and $\alpha_{0,r}$ for the UP; $\alpha_{d,r}$ and $\alpha_{D,r}$ for the ZC penalty; and $\alpha_{a,r}$ and $\alpha_{A,r}$ for

the BA penalty. In addition, Λ is scaled by the global scaling factor λ , which is also adjustable. Since the main term in the regularization is the UP, $\alpha_{c,r}$, $\alpha_{p,r}$ and $\alpha_{0,r}$ are the most critical parameters. In the following, a procedure for choosing $\alpha_{c,r}$ and $\alpha_{p,r}$ is described, followed by a discussion of methods for choosing λ . The exact values of the other compliance parameters, for the ZC and BA penalty, are not critical. For example, it was shown in reference [130] that $\alpha_{0,r}$ and $\alpha_{d,r}$ have very little effect on the spectrum. Compliance parameters are set prior to the iterative fitting of the spectrum, and remain constant throughout the iterations.

Uniform penalty

The most important parameter in the UP is the curvature parameter, $\alpha_{c,r}$. To determine $\alpha_{c,r}$ we first note that, for a successful inversion, the norm of the regularization should be similar in magnitude to the norm of the residuals,

$$\lambda^2 \|\Lambda \mathbf{g}\|^2 = \|\tilde{\mathbf{K}}\mathbf{g} - \tilde{\mathbf{s}}\|^2. \quad (5.27)$$

Since the data are re-scaled such that the noise has a variance of one, and the residuals are statistically equivalent to the noise, the right hand side of this equation is equal to the number of data points n in the compressed data. The left hand side can be estimated by ignoring the ZC penalty and BA penalty, since the UP dominates the norm of $\Lambda \mathbf{g}$. Therefore, only the first (UP) term from eq (5.21) is included, and eq (5.27) can be re-written

$$\lambda^2 \mathbf{g}^T \left(\sum_{r=1}^R \mathbf{C}_r \mathbf{L}_{2,r} \right)^T \left(\sum_{r=1}^R \mathbf{C}_r \mathbf{L}_{2,r} \right) \mathbf{g} = n. \quad (5.28)$$

Substituting in for \mathbf{C}_r using eq (5.22), with the approximation $\alpha_{p,r} = \alpha_{0,r} = 0$, and simplifying, we get

$$\frac{\lambda^2 R \Delta_r M}{\alpha_{c,r}} \approx n, \quad (5.29)$$

where it has been assumed that each dimension r contributes an equal amount to the regularization. Finally, setting λ to a default value of 1, we are left with

$$\alpha_{c,r} \sim \frac{R \Delta_r M}{n}, \quad (5.30)$$

so $\alpha_{c,r}$ can be easily estimated from pre-determined quantities.

The choice of $\alpha_{p,r}$ is less critical than that of $\alpha_{c,r}$. We chose to use a fixed ratio of $\alpha_{p,r}$ to $\alpha_{c,r}$ [140]; $\alpha_{p,r} = 5\alpha_{c,r}$ worked well in tests of this algorithm. $\alpha_{0,r}$ is even less critical than $\alpha_{p,r}$: it is only important in parts of the spectrum with little or no signal, where it dominates. In most applications of this algorithm, $\alpha_{0,r} = 10^{-4}$ was used.

Equation (5.30) generally provides a good ‘initial guess’ for $\alpha_{c,r}$ but some adjustment is often required. Most significantly, when the full regularization matrix is included, equality (5.27) is no longer satisfied. To overcome this problem, the initial guesses of $\alpha_{c,r}$ and $\alpha_{p,r}$ are used to calculate a ‘first version’ of the spectrum \mathbf{g}_1 . $\alpha_{c,r}$ and $\alpha_{p,r}$ are then all scaled by $\frac{\|\Lambda_{UP}\mathbf{g}_1\|}{\|\tilde{\mathbf{K}}\mathbf{g}_1 - \tilde{\mathbf{s}}\|}$, where Λ_{UP} is the UP contribution to Λ , and the spectrum is re-calculated. If necessary this process can be repeated until convergence, but usually only one or two repetitions are sufficient.

Global scaling factor

By default, the global scaling factor λ is set to 1, so that the equality in eq (5.27) is satisfied with the chosen value of $\alpha_{c,r}$ and $\Lambda = \Lambda_{UP}$. However, with the inclusion in Λ of the ZC and BA penalty terms, equality (5.27) may no longer be satisfied, and λ can be re-scaled to correct for this.

There are several methods for choosing an optimal value for λ [141]. We usually used the S-curve method [142], in which spectra were calculated for different values of λ , and the norm of the residuals between the fit and the data, $\|\tilde{\mathbf{K}}\mathbf{g} - \tilde{\mathbf{s}}\|$, is plotted as a function of λ on a log-log plot. The optimal value λ_0 is chosen at the heel of the curve, at the end of the plateau before $\|\tilde{\mathbf{K}}\mathbf{g} - \tilde{\mathbf{s}}\|$ rapidly increases. This point is typically slightly below the norm of the noise in the data. For a consistent choice that does not depend on the user, λ_0 can be taken as the point where the norm of the residuals is equal to the norm of the noise.

5.2.6 Inversion procedure

The inversion equation, eq (5.20), is solved iteratively, and a spectrum $\hat{\mathbf{g}}_i$ is calculated for each iteration i . For the first iteration, coefficient matrices \mathbf{C}_r , \mathbf{D}_r , and \mathbf{A}_r are calculated using a null vector in place of \mathbf{g} . For each subsequent iteration i , \mathbf{C}_r , \mathbf{D}_r , and \mathbf{A}_r are calculated using $\hat{\mathbf{g}}_{i-1}$, the spectrum calculated in the previous iteration.

The inversion procedure continues until the fit converges. Convergence is

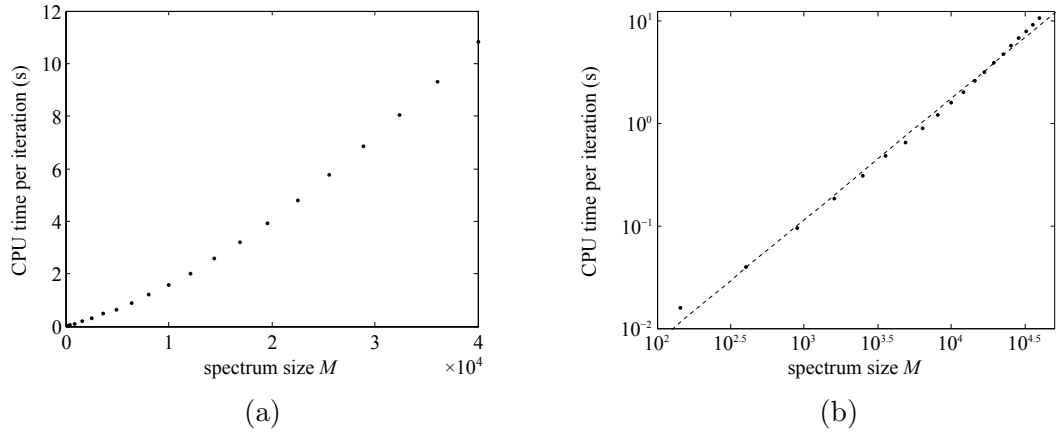


Figure 5.7: CPU time per iteration for calculations of 2-dimensional spectra of different sizes. (a) Linear plot. (b) Logarithmic plot of the same data. The dashed line is the linear least square fit, corresponding to the relationship: $\text{CPU time} \propto M^{1.2}$.

achieved when the spectrum does not change significantly in subsequent iterations, that is when $\|\hat{\mathbf{g}}_i - \hat{\mathbf{g}}_{i-1}\|$ is less than a priorly chosen value. If convergence is not achieved, the fit is generally terminated after 100 iterations, since the spectrum does not usually change substantially in subsequent iterations.

5.2.7 Computation

To asses the computational costs and limitations of the algorithm, it was tested using the synthesized 2-dimensional spectrum used for the simulations in [130]. Calculations were performed using Matlab (R2010b, The Mathworks, Natick, MA) on a desktop computer with a 3.1 GHz Intel Core i3-2100 CPU and 4 GB of RAM (2.94 GB usable) running Windows 7 Enterprise (32-bit).

A data matrix with 64×64 points was inverted, and 12 singular values were used in the data compression along each dimension. Inversions were performed with different spectrum sizes, and the CPU time per iteration was measured for each inversion. A maximum spectrum size M of about $M \approx 200 \times 200$ elements could be calculated. CPU time per algorithm iteration is plotted as a function of M on a linear scale in Figure 5.7a and on a logarithmic scale in Figure 5.7b. The relationship between CPU time and M is approximately a power law, with CPU time roughly proportional to $M^{1.2}$. However, the power law is not exact, as can be seen in the logarithmic plot, and the relationship between CPU time and M depends on the CPU and the linear algebra library used.

5.2.8 Other considerations

As stated in Section 5.2.1, noise is usually assumed to be additive, iid Gaussian white noise, and the signal is scaled by the inverse of the standard deviation of the noise, to give noise with unity variance. If the noise is not iid, for example noise with a multiplicative contribution, this can be accounted for by scaling the signal and kernels by the inverse of the noise variance [140].

The original equation to be solved, eq (5.1), assumes that all relaxation components eventually decay to zero. This is not always the case. For example, saturation recovery and inversion recovery data decay to non-zero baselines. If data such as this is used in the inversion without modification, the algorithm may interpret the baseline as a relaxation component with a very long time constant, and hence fit a peak in the spectrum representing this component. Therefore, if possible, baselines are subtracted at the beginning of the inversion, to avoid artifacts such as this. If baseline subtraction is not possible, a relaxation component with a very long time constant can be fitted, and the integral of the peak can be interpreted as a baseline, or an additional data point can be added to the spectrum to account for the baseline [140].

5.3 Simulations

The performance of the algorithm was demonstrated on synthetic 1D data with a kernel $\mathcal{K}(t, \tau) = \exp(-t/\tau)$. A spectrum consisting of one negative and three positive lines with Gaussian shape in log-space was chosen, as shown in Figure 5.8. A data vector of 500 logarithmically spaced points was calculated and Gaussian white noise with unit variance was added. An inversion was then performed and a spectrum with 200 logarithmically spaced points was fitted. Simulations with SNRs of 1000 (Figure 5.8a) and 100 (Figure 5.8b) were performed with standard parameters as described in [130]. The effect of removing the ZC penalty was demonstrated using the data with an SNR of 1000 (Figure 5.8c), and the effect of using a ZC penalty that is too high was demonstrated on the same data (Figure 5.8d). SNR was defined as

$$\text{SNR} = \frac{\max(\mathbf{S})}{\sigma(\mathbf{E})}, \quad (5.31)$$

where $\max(\mathbf{S})$ and $\sigma(\mathbf{E})$ are the maximum value of \mathbf{S} and the standard deviation of \mathbf{E} respectively.

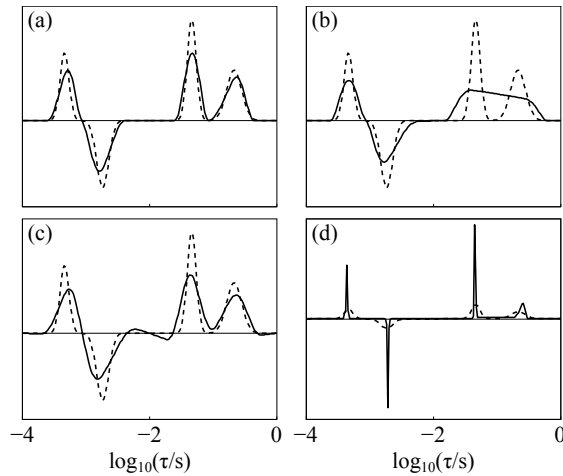


Figure 5.8: Inversion of synthetic 1D data, showing the effect of SNR and the ZC penalty. The solid line represents the respective fitted spectrum and the dashed line represents the exact spectrum. (a) SNR of 1000 with ZC penalty. (b) SNR of 100 with ZC penalty. (c) SNR of 1000 without ZC penalty. (d) SNR of 1000 with very high ZC penalty.

5.3.1 SNR

With an SNR of 1000, the spectrum is accurately reproduced, including the positions, signs and integrals of all four peaks. The peaks are noticeably broadened, particularly the narrower peaks. There are no spurious features in the spectrum. With an SNR of 100, the two peaks at small values of τ are accurately reproduced, but significantly broadened; the two peaks at larger values of τ are not resolved, but the position, sign and integral of the broad peak in the spectrum reflect the peaks in the exact spectrum. The broadening at lower SNR values and associated uncertainty in peak identification are consequences of the regularization: as described in Section 5.2.5, the regularization parameters λ and $\alpha_{c,r}$ are chosen so that the norm of the regularization is equal to the norm of the noise (eq (5.27)), so a lower SNR means a larger regularization is required and the spectrum has broader peaks. In other words, the algorithm produces lines with widths that are consistent with the SNR of the data.

Song et al. investigated resolution as a function of SNR quantitatively, and showed that the resolution $\Delta\kappa$ of a 1-dimensional spectrum can be expressed as

$$\begin{aligned}\Delta\kappa &\sim \frac{\kappa_2 - \kappa_1}{n} \\ &\sim \frac{\kappa_2 - \kappa_1}{a \ln (\text{SNR})},\end{aligned}\tag{5.32}$$

where κ_2 and κ_1 are the upper and lower limits of $\log_{10}(\tau)$, respectively, n is the

number of singular values retained, and $a = 1.2$ was obtained empirically [133].

The line broadening as a result of noise represents uncertainty: if data can be fitted equally well with different distributions of narrow and broad peaks, the broadest distribution that is consistent with the SNR of the data should be chosen. This does not exclude the possibility of a more detailed true spectrum, it simply states that the data does not support the more detailed distribution with statistical confidence.

5.3.2 Zero-crossing penalty

The effect of the ZC penalty can clearly be seen by comparing Figures 5.8a, 5.8c and 5.8d. Without the ZC penalty (Figure 5.8c), there is significant undershooting and overshooting close to the centre of the spectrum, and smaller undershoots close to the edges of the spectrum. With the ZC penalty (Figure 5.8a), this undershooting and overshooting is almost completely removed. When the ZC penalty is too high (Figure 5.8d), it dominates the regularization and causes significant under-regularization. The result is a spectrum with very narrow peaks, which are in the correct locations in the spectrum and have the correct sign, but are much narrower than the peaks in the original spectrum, and suggest a far higher resolution than can be justified by the SNR of the data.

5.3.3 Regularization parameters

For most of the compliance parameters $\alpha_{i,r}$ ($i = 0, p, c, d, D, a, A$), the exact value is not critical. Reference [130] showed the effect on the spectrum and the regularization of changing several of the compliance parameters. Even the main term, $\alpha_{c,r}$, could be changed by an order of magnitude above or below its default value without significantly affecting most of the main features of the spectrum and the overall shape of the regularization. However, the global scaling factor, λ , is critical, and a value too high or too low can lead to significant over- or under-regularization. To demonstrate this, Figure 5.9 shows the effect of changing λ by an order of magnitude above and below its default value: spectra are shown on the left and residuals between the original transient data and the fitted transient data are shown on the right.

When λ is too large, the spectrum is over-regularized: the peak at the smallest value of τ is slightly over-broadened, while the two peaks at larger values of

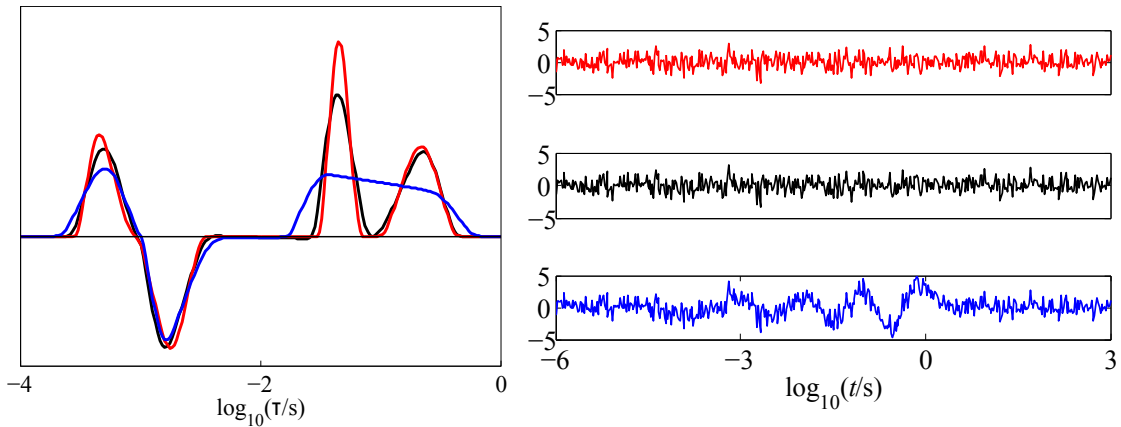


Figure 5.9: Spectra obtained by varying the global scaling factor λ . λ was set a factor of 10 above (blue) and below (red) its default value λ_0 (black). The left plot shows the three spectra, and the right plot shows the residuals between the original transient data and the fitted transient data for each value of λ . The standard deviation of the residuals was 1.00 for $\lambda = \lambda_0$, 1.51 for $\lambda = 10\lambda_0$, and 0.99 for $\lambda = 0.1\lambda_0$.

τ are significantly over-broadened and cannot be resolved. The effect of over-regularization can also be seen by looking at the residuals between the original transient data and the fitted transient data. The residuals for the over-regularized spectrum show a significant trend and have a standard deviation of 1.51, in contrast to the residuals with the default value of λ , which are indistinguishable from noise and have a standard deviation of 1.00.

When λ is too small, the fitted spectrum is under-regularized, with slightly narrowed peaks. However, the effects of under-regularization are not as noticeable as the effects of over-regularization in this example. The residuals are almost identical to the residuals with the default value of λ , and have a standard deviation that is only very slightly smaller.

It should be emphasized that the broadening caused by over-regularization is different to the broadening caused by noise (Figure 5.8). The noise broadening represents uncertainty, and does not lead to an increase of the standard deviation of the residuals, while the over-regularization broadening is due to incorrectly chosen parameters, and leads to a degraded quality of the fit.

5.4 Self-consistency test

To test the robustness of a fit, a self-consistency test can be performed. This is demonstrated with the synthetic data set with an SNR of 1000. The fitted

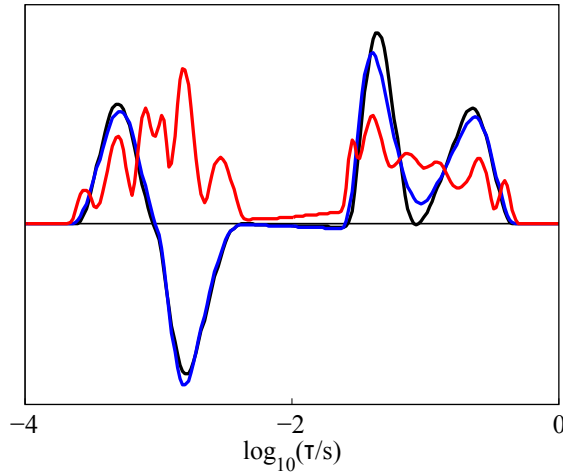


Figure 5.10: Self-consistency test: results of refitting a spectrum ten times with different random noise vectors. Black trace shows original fitted spectrum $\hat{\mathbf{g}}$, blue trace shows mean of the refitted spectra ($\langle \mathbf{g}_{\text{refit}} \rangle$), and red trace shows standard deviation of refitted spectra at each point (σ_{refit}) multiplied by a factor of 10.

spectrum $\hat{\mathbf{g}}$ was used to calculate a fitted data set \mathbf{s}' , to which ten different noise vectors \mathbf{e}_i with unit variance were added. Each data set $\mathbf{s}' + \mathbf{e}_i$ was then inverted with identical fitting parameters to give ten refitted spectra $\hat{\mathbf{g}}_i$, which were used to calculate a mean $\langle \mathbf{g}_{\text{refit}} \rangle$ and standard deviation σ_{refit} for each point in the spectrum. The results of the self-consistency test are shown in Figure 5.10. σ_{refit} is, qualitatively, approximately proportional to the signal amplitude: it is close to zero at positions in the spectrum where the signal is close to zero, and much larger at positions where there is significant signal in the spectrum.

The results of the self-consistency test can be used to qualitatively justify the use of the UP regularization, by comparing these results with the probabilistic regularization method used by Krakauer et al. [143]. They used the inverse of a covariance matrix as a regularization matrix, with a regularization of the form

$$\lambda^2 (\mathbf{g} - \mathbf{g}_0)^T \mathbf{C}_{\mathbf{g}_0}^{-1} (\mathbf{g} - \mathbf{g}_0), \quad (5.33)$$

where \mathbf{g}_0 is a prior estimate to the spectrum, and $\mathbf{C}_{\mathbf{g}_0}$ is a covariance matrix which represents uncertainty about \mathbf{g}_0 . $\mathbf{C}_{\mathbf{g}_0}$ is analogous to $\sigma_{\text{refit}}^{(2)}$,^{*} the variance of the refitted spectra, which also represents uncertainty. This regularization has a similar form to the regularization used in our approach, which is given by

$$\lambda^2 \mathbf{g}^T \boldsymbol{\Lambda}^T \boldsymbol{\Lambda} \mathbf{g}. \quad (5.34)$$

^{*} $\sigma_{\text{refit}}^{(2)}$ is the entry-wise square of σ_{refit} .

The Krakauer regularization penalizes deviations of the solution \mathbf{g} from \mathbf{g}_0 , whereas our regularization penalizes the amplitude of the spectrum, which is the same as setting $\mathbf{g}_0 = \mathbf{0}$ in eq (5.33), where $\mathbf{0}$ is a null vector. The UP regularization used in our approach is otherwise very similar to the probabilistic regularization used by Krakauer et al., with the regularization matrix $\Lambda^T \Lambda$ used in place of the inverse of the covariance matrix, $\mathbf{C}_{\mathbf{g}_0}^{-1}$.

For the UP method and Krakauer's probabilistic method to be compatible, $\Lambda^T \Lambda$ should be equivalent to $\mathbf{C}_{\mathbf{g}_0}^{-1}$. The UP regularization matrix, $\Lambda^T \Lambda$, is, by definition, roughly inversely proportional to the signal, as shown in Figure 5.4. $\sigma_{\text{refit}}^{(2)}$, which represents the uncertainty of the spectrum, is roughly proportional to the signal. Therefore, the UP regularization and the Krakauer regularization are essentially equivalent, if $\sigma_{\text{refit}}^{(2)}$ is identified with $\mathbf{C}_{\mathbf{g}_0}$. The main difference is that the covariance matrix (the inverse of the regularization matrix) is chosen as an input in the Krakauer method, whereas it is updated iteratively in each iteration of the inversion in the UP method.

5.5 Conclusions

This chapter has presented a one- or two-step procedure to analyse relaxation data, using Tikhonov regularization to fit a relaxation spectrum with an arbitrary number of dimensions. The algorithm does not use a non-negativity constraint, but a zero-crossing penalty is applied to prevent unphysical undershooting. In the one-step process, a pre-determined relaxation kernel is used to fit a spectrum to the data. If, on the other hand, the relaxation kernel is not known, the two-step process is used: the relaxation kernel is determined in the first step by minimizing the number of singular values needed to represent the data, and the second step is the fitting routine.

Chapter 6

EPR Transient Saturation

6.1 Introduction

Many physical processes give rise to multi-exponential relaxation data, often with many discrete components or smooth distributions of components [144]. Examples include EPR relaxation and transient saturation data, and solid-state dynamic nuclear polarization (DNP) enhancement. As described in Chapter 2, there are three distinct enhancement mechanisms in solid-state DNP. A current area of interest is an extension of our theoretical understanding of these mechanisms, and in particular an improvement of simulations used to describe DNP experiments [49, 55, 61–64]. In their simplest form, these DNP experiments involve a resonant or near-resonant irradiation of electron spins with an oscillating magnetic field on time-scales that are long compared with all of the relaxation time constants that involve a transition of the electron spins. Therefore, a new equilibrium of the spin system is established during such an experiment. The DNP mechanisms depend on many factors, including nuclear and electron spin relaxation and electron spectral diffusion, particularly for radicals with inhomogeneously broadened EPR lines. Therefore, a better understanding of these processes and experimental characterization of the corresponding time constants is essential for a complete understanding of DNP enhancement.

There is a large body of work on EPR relaxation, spectral diffusion, and magnetization transfer. Relaxation processes, and experimental methods for studying relaxation, have been discussed in detail in some relatively recent reviews [19, 145], and a large amount of existing relaxation data has been compiled and presented [19, 146]. Many different mechanisms contribute to longitudinal and transverse re-

laxation, and several theoretical models to interpret experimental data have been proposed [19, 145]. Some of the electron spin relaxation mechanisms are temperature dependent, so the dominant mechanism can often be determined by variable temperature experiments [147–149].

Among the models used to describe spectral diffusion are the Gauss-Markov model [150], stochastic model [151], and the uncorrelated sudden jump model [152, 153]. Romanelli and Kevan presented a detailed theoretical framework for both the Gauss-Markov and sudden jump models [25, 154]. Portis presented microscopic and macroscopic models to describe spectral diffusion in terms of the electron dipole-dipole interaction [155]. Suter and Ernst discussed spectral diffusion in NMR in terms of energy exchange with a dipolar reservoir [156, 157]. Spectral diffusion has also been studied using electron spin echo (ESE) techniques [135, 158, 159], and selective hole-burning [21, 22].

Electron-electron double resonance (ELDOR) can be used to investigate magnetization transfer through the EPR spectrum. ELDOR has been used to study EPR processes using a single-mode resonator and rapid magnetic field jumps [102, 103, 160, 161], and, more recently, with a dual-mode resonator, with frequencies separated by up to 350 MHz, at fixed magnetic field [104].

Most experiments on EPR relaxation have used short microwave (mw) pulses to manipulate the spin system, and have detected EPR signals using conventional (transverse) detection. However, we use samples which are also suitable for complementary DNP and NMR experiments, and are therefore too large to be contained in a mw resonator at W band frequencies, so the mw field is too small to apply a $\frac{\pi}{2}$ pulse in a time shorter than the phase-memory time T_m . Instead, we used longitudinal detection (LOD) to detect signal, and performed transient saturation, which includes the effects of T_1 and T_m , and saturation recovery experiments. The absence of a mw resonator also means that a broad range of mw frequencies across the whole EPR spectrum could be used for excitation and detection [43].

Granwehr and Köckenberger recorded transient saturation, saturation recovery, and pump-probe ELDOR data using LOD under typical DNP conditions ($B_0 = 3.4$ T, $T = 1.5$ K) using samples of TEMPO and Ox063 trityl [43]. These experiments could be used to investigate relaxation and spectral diffusion. A selection of the transient saturation and saturation recovery data for a 20 mM TEMPO sample are displayed in Figure 6.1. Saturation recovery data close to the centre

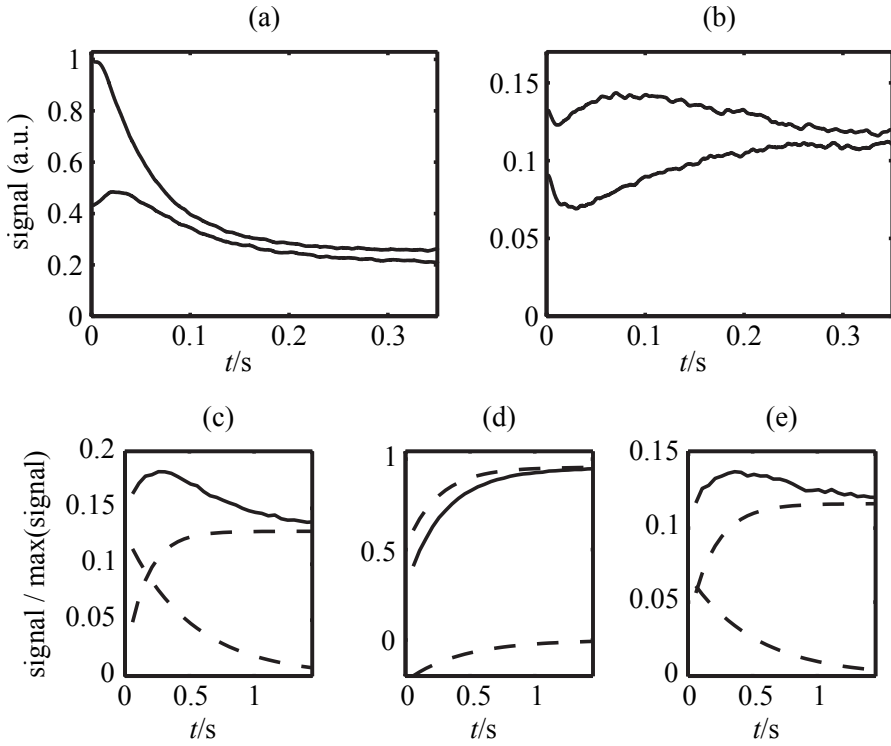


Figure 6.1: Transient saturation and saturation recovery LOD EPR data recorded at different mw frequencies (ω_{mw}) across the EPR spectrum using a 20 mM sample of TEMPO at $B_0 = 3.4$ T, $T = 1.5$ K. Upper panel: transient saturation data recorded with ω_{mw} close to the centre (a) and close to the edges (b) of the EPR spectrum. Lower panel: saturation recovery data recorded with ω_{mw} close to the centre (d) and close to the edges (c,e) of the EPR spectrum. Solid lines are experimental data, dashed lines are components of bi-exponentially fitted data. Reproduced with permission from Josef Granwehr [43].

of the spectrum (Figure 6.1d) could be fitted with mono-exponential functions, but the residuals between the fitted and experimental data showed systematic errors. These could be removed by fitting the data with bi-exponential functions. Saturation recovery data at the edges of the spectrum (Figures 6.1c and 6.1e) showed an increase in signal followed by a decrease, and could also be fitted with bi-exponential functions. At the position in the spectrum with maximum signal, saturation recovery data fitted using a mono-exponential function revealed a phenomenological longitudinal relaxation time $T_1 \approx 0.31$ s. This chapter presents an extension to these experiments, including transient saturation experiments with a fixed pump frequency and variable probe frequency.

Much of the data presented here and elsewhere exhibits multi-exponential decay. Eaton and Eaton have fitted EPR relaxation data with exponential functions with either several individual components or distributions of relaxation times

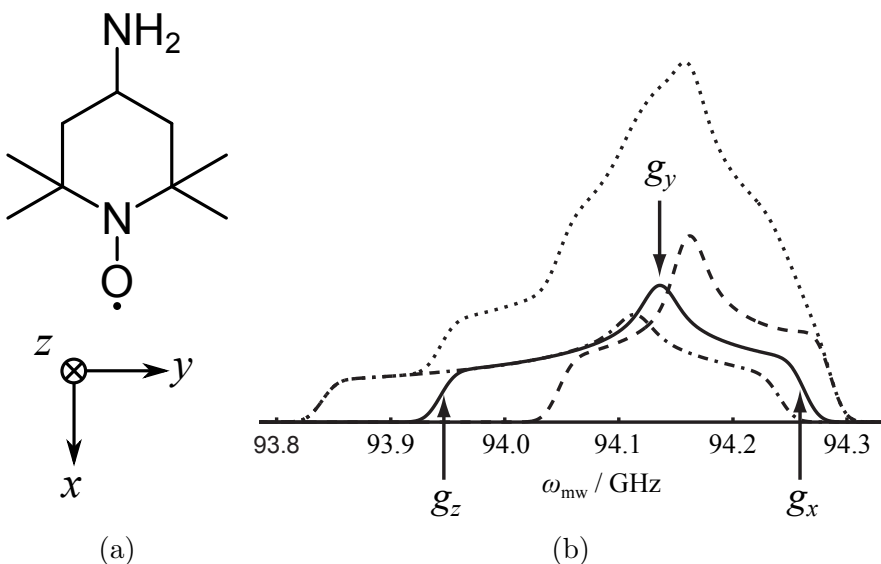


Figure 6.2: (a) Molecular structure and g -matrix principal axis system of 4-Amino-TEMPO radical. (b) Simulated W-band EPR spectrum of 4-Amino-TEMPO, showing the ^{14}N hyperfine components of the spectrum [166]. Only components corresponding to transitions with $\Delta m_I = 0$ are shown: dash-dotted, solid and dashed lines correspond to $m_I = -1$, $m_I = 0$, and $m_I = 1$, respectively; dotted line corresponds to the sum of the three components. For $m_I = 0$, the frequencies of the signal with the x -, y -, and z -axes of the molecule aligned with the external magnetic field are indicated by arrows. Reproduced with permission from Josef Granwehr [43].

[127, 137, 162], with the multi-exponential fit calculated using Provencher's algorithm [128], and the distributions calculated using either a Levenberg-Marquardt algorithm or a uniform-penalty algorithm [129, 140]. In this chapter, it is shown how the inversion algorithm described in Chapter 5 can be used to analyse experimental transient saturation data. The inversion is ill-conditioned, so Tikhonov regularization, which has been widely used in EPR to calculate distance distributions from double electron-electron resonance (DEER) data [163–165], is used to stabilize the solution. After the experiment is described, this algorithm is used to calculate 2-dimensional relaxation spectra from the transient saturation data.

6.2 Experimental details and data processing

Experiments were performed at 3.381 T using a 20 mM sample of 4-Amino-2,2,6,6-tetramethylpiperidine-1-oxyl (4-Amino-TEMPO; Sigma-Aldrich Co Ltd, Dorset, UK) in 1:1 water/glycerol at a temperature of 1.5 K. The molecular structure and simulated LOD EPR spectrum of 4-Amino-TEMPO are shown in Figure 6.2.

EPR signal was measured using a home-built LOD system based on a Krymov

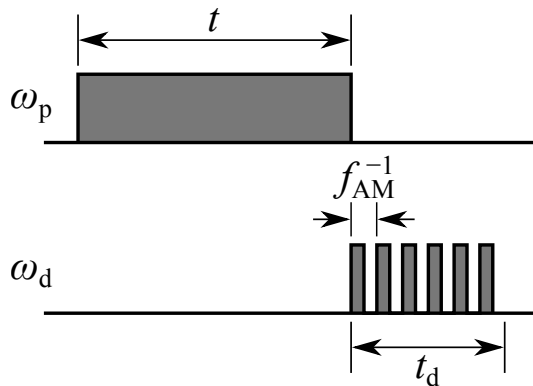


Figure 6.3: Pulse sequence used for irradiation and detection: microwave pump pulse (frequency ω_p) was switched on for a time t , and electron magnetization remaining after t was measured using LOD. Detection pulse train comprised a microwave field (frequency ω_d) amplitude-modulated by a square-wave with 50 % duty cycle and frequency $f_{AM} = 3.1$ kHz, and had a duration $t_d = 10$ ms. t was incremented along dimension 1, and ω_d was incremented along dimension 2.

W-band set-up. The detection system and probe are described in detail in Sections 3.6 and 4.1 respectively, and are summarized here. The probe was inserted into the external part of a Krymov probe, and a Krymov microwave bridge was used to generate the mw field [90]. For detection, the microwave field was amplitude-modulated by a square-wave with 50 % duty cycle and a frequency of 3.1 kHz, the resonance frequency of the detection circuit, generated by a data timing generator (DTG 5078, Tektronix, Beaverton, OR).

LOD EPR signal was detected using a 1000-turn solenoid (height 18 mm, ID 9 mm, OD 18 mm) mounted on a probe head manufactured from PCTFE. Samples were contained within a 350 μ l sample holder (height 17.5 mm, ID 5 mm), also made from PCTFE. To improve the mw field amplitude, a mirror was placed on top of the sample holder, opposite the microwave antenna.

The LOD coil is connected using a twisted pair of copper wires and a coaxial cable to a home-built pre-amplifier/filter circuit [81]. The EPR signal is amplified by 30 dB using an audio pre-amplifier (SSM2019, Analog Devices, Norwood, MA). It is equipped with a low-pass filter and a high-pass filter, both passive RC designs. The signal is digitized using an external analogue-digital/digital-analogue device (USB-6259 DAQ, National Instruments, Austin, TX).

The pulse sequence for the transient saturation experiments is shown in Figure 6.3. Transient saturation data were acquired as follows: the mw field was switched on for a time t , and the electron magnetization remaining after this time interval was measured using longitudinal detection. t was incremented along the first

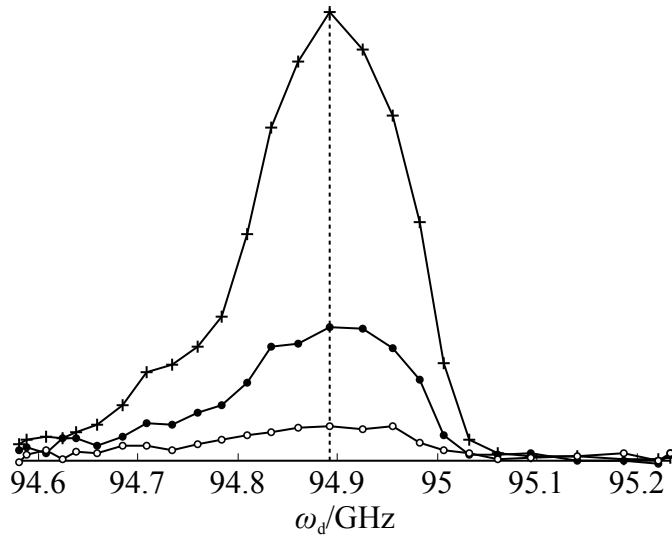


Figure 6.4: LOD EPR spectrum of 20 mM 4-Amino-TEMPO, detected using the pulse sequence in Figure 6.3, before and after continuous mw irradiation at a frequency $\omega_p = 94.89$ GHz. Crosses correspond to thermal equilibrium spectrum (mw pump time $t = 0$ s); solid and open circles correspond to mw pump times $t = 0.1$ s and $t = 5$ s, respectively. Pump frequency ω_p is indicated by dashed line. Solid lines are guides for the eye.

dimension, with data recorded at 49 nonlinearly spaced time points from 10^{-3} s to 5 s. A thermal equilibrium signal was also recorded, equivalent to a data point with $t = 0$. The mw pump frequency ω_p was fixed at a frequency 94.89 GHz, which is close to the centre of the inhomogeneously broadened EPR line, while the detection frequency ω_d was incremented along the second dimension, with 26 frequencies between 94.58 GHz and 95.23 GHz. The mw field for the detection pulses was generated by a voltage controlled oscillator (VCO) with a tunable output frequency. The output frequency of the VCO is a nonlinear function of input voltage, so the ω_d values were approximately, but not exactly, linear.

To illustrate the effect of the continuous mw field, Figure 6.4 shows the LOD EPR spectrum of 20 mM 4-Amino-TEMPO before and after a mw pump pulse. The three traces correspond to a thermal equilibrium spectrum (crosses), and spectra recorded after pump pulse durations of $t = 0.1$ s (solid circles) and $t = 5$ s (open circles).

The signal $S(t, \omega_d)$, measured at discrete sampling times t and detection frequencies ω_d , can be expressed using eq (5.1) as

$$S(t, \omega_d) = \int_0^{\infty} [e^{-t/\tau}] \mathcal{G}(\tau, \omega_d) dt + E(t, \omega_d), \quad (6.1)$$

where τ is a phenomenological time constant describing the decay of the electron magnetization during the mw irradiation; $\mathcal{G}(\tau, \omega_d)$ and $E(t, \omega_d)$ are the spectrum and experimental noise, as described in Chapter 5; and $[e^{-t/\tau}]$, relating experimental parameter t to spectral parameter τ , is the kernel \mathcal{K} . The kernel associated with ω_d , the second dimension of both the signal and the spectrum, can be represented by an identity matrix: this dimension is not inverted, but the regularization is applied to this dimension as well as to the inverted dimension. The maximum value of t was chosen to be longer than any of the observed relaxation times—this was achieved by recording data until a steady-state was reached, such that $S(t, \omega_d)$ did not change when t was increased further. A baseline-correction could then be performed on the data by subtracting $S(\max(t), \omega_d)$ from all data points $S(t, \omega_d)$ for each value of ω_d : this step often removed artifacts in the spectrum and resulted in better fits.

The data was inverted using the algorithm described in Chapter 5 and a spectrum $\hat{\mathbf{g}}$ was produced using eq (5.20). The data had an SNR of 127, calculated using $\text{SNR} = \frac{\max(S)}{\sigma(E)}$. The data was compressed using SVD of the kernel in the t dimension only, with 12 singular values retained. Standard fitting parameters were used for the regularization, calculated as described in Section 5.2.5 and reference [130].

6.3 Results and discussion

The results of the experiment measuring transient saturation as a function of detection frequency with the 20 mM 4-Amino-TEMPO sample are shown in Figure 6.5. The time-domain data is plotted in Figure 6.5a as a function of t and ω_d . The spectrum resulting from the inversion is shown in Figure 6.5c as a function of τ and ω_d . To highlight the shape of the spectrum at certain detection frequencies, three traces from the spectrum are plotted in Figure 6.5d, at positions indicated in Figure 6.5c. The residuals between the fit and the data are plotted in Figure 6.5b.

The dominant feature of the spectrum is the peak close to $\tau = 10^{-1}$ s, which has a maximum close to $\omega_d \approx \omega_p = 94.89$ GHz and is elongated in the frequency dimension, indicating a similar value of τ across all detection frequencies in the spectrum. Other significant features are the two negative peaks close to $\tau = 10^{-2}$ s, which have minima close to $\omega_d \approx 94.83$ GHz and $\omega_d \approx 94.96$ GHz, and the long

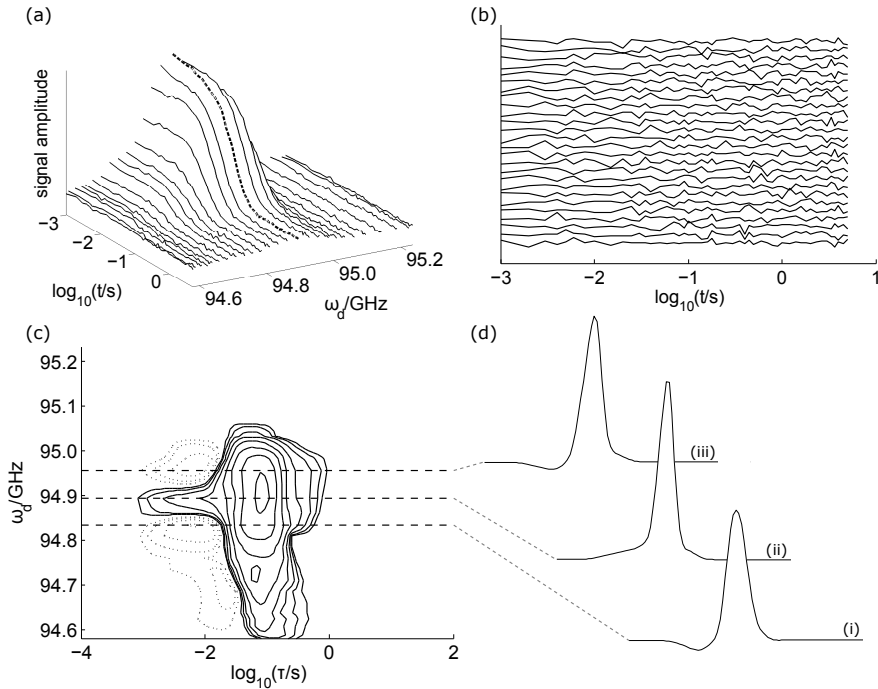


Figure 6.5: Transient saturation data for the 20 mM 4-Amino-TEMPO sample. (a) Time-domain data. The heavy dashed line represents data at $\omega_d = \omega_p$. (b) Residuals (difference between experimental data and fitted data). (c) Fitted spectrum. Contours are spaced logarithmically (amplitudes of ± 0.1 , ± 0.2 , ± 0.4 , ± 0.8 , 1.6, 3.2, 6.4, and 12.8). Solid contours represent positive values, dotted contours represent negative values. (d) Three traces from the spectrum at positions indicated in (c): (i) $\omega_d = 94.83 \text{ GHz}$, (ii) $\omega_d = \omega_p = 94.89 \text{ GHz}$, (iii) $\omega_d = 94.96 \text{ GHz}$.

tail of the peak around $\omega_d \approx \omega_p = 94.89 \text{ GHz}$, which separates the two negative peaks along the ω_d dimension and stretches as low as $\tau = 10^{-3} \text{ s}$. The long positive tail towards shorter values of τ corresponds to a quickly decaying signal at the mw pump frequency ω_p , while the negative peaks indicate a quickly increasing signal at frequencies close to ω_p . At frequencies further from ω_p , the amplitudes of the negative peaks decrease, and the position of the maximum moves to longer values of τ .

The elongated peak close to $\tau = 10^{-1} \text{ s}$ is associated with a ‘slow’ saturation of polarization, across the spectrum. This indicates that, as a hole is burned in the spectrum by the mw irradiation, the saturation spreads out across the spectrum, eventually causing the whole spectrum to be almost completely saturated (Figure 6.5a). The negative peaks and positive tail close to $\tau = 10^{-2} \text{ s}$ suggest a transfer of polarization from spins at $\omega_d \approx \omega_p = 94.89$ to ‘neighbouring’ spins in frequency-space. In other words, this appears to show an *increase* in signal due to spectral diffusion or magnetization transfer driven by the mw irradiation.

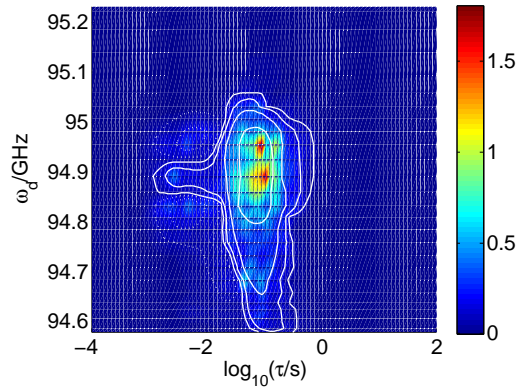


Figure 6.6: Self-consistency test: results of refitting a spectrum ten times with different random noise vectors. Standard deviation of each point (σ_{refit}) is represented by a pseudo-colour plot, and the mean of the refitted spectra ($\langle \mathbf{g}_{\text{refit}} \rangle$) is represented by logarithmically spaced contours (amplitudes of ± 0.1 , ± 0.4 , 1.6, and 6.4). Solid contours represent positive values, dotted contours represent negative values.

Although the signal close to $\omega_d \approx \omega_p = 94.89$ GHz and $\tau = 10^{-2}$ s was described as a long tail of the larger peak at this frequency, it is possible that the true underlying spectrum has two distinct peaks rather than one peak with a broad tail. However, the broadening in the spectrum means we cannot state which of these possibilities is correct. In other words, the data cannot distinguish between a single peak with a broad tail and two narrower peaks [130]. The broadening of the spectrum is due to the regularization, which is determined by the noise in the data: in this case the data does not have a sufficient SNR to support two distinct peaks, although this remains a possibility. This effect was illustrated using synthetic data in Figure 5.8a–b in Chapter 5, in which the inversion of the data with an SNR of 1000 clearly shows all four peaks, while in the inversion of the data with an SNR of 100, two of the peaks are merged into one broader peak.

Self-consistency test

To test the robustness of the fit, a self-consistency test was performed, as described in Section 5.4. The spectrum $\hat{\mathbf{g}}$ was used to calculate a fitted data set \mathbf{s}' , to which ten different noise vectors \mathbf{e}_i with unit variance were added. Each data set $\mathbf{s}' + \mathbf{e}_i$ was then inverted with identical fitting parameters to give ten refitted spectra $\hat{\mathbf{g}}_i$, which were used to calculate a mean $\langle \mathbf{g}_{\text{refit}} \rangle$ and standard deviation σ_{refit} for each point in the spectrum. The results of the self-consistency test are shown in Figure 6.6. They show that the fitted spectrum is self-consistent: the mean of the refitted

spectra is very similar to the original fitted spectrum, and all of the main features were consistently reproduced. Furthermore, σ_{refit} is close to zero at positions in the spectrum where the signal is close to zero, and much larger at positions where there is significant signal in the spectrum, as was the case for the synthetic data analysed in Chapter 5.

6.4 Conclusions

This chapter has demonstrated the inversion algorithm, presented with synthetic data in Chapter 5 and in reference [130], on experimental EPR data. The unique feature of this algorithm is the ability to fit spectra with both positive and negative peaks. This can be a crucial feature for the analysis of relaxation and transient saturation data, particularly when cross-relaxation and exchange processes are important, as was shown here. Only one dimension of the 2-dimensional data set was inverted, but the regularization was applied to both dimensions. Since the signal and spectrum vary smoothly along the non-inverted dimension, this leads to an improved SNR compared with inversions of individual 1-dimensional data subsets [131].

Song et al. performed 2-dimensional NMR relaxation experiments in porous media, and inverted the data along both dimensions to yield T_1 - T_2 correlation spectra [29]. They inverted the data with a similar algorithm to that presented here, but with a non-negativity constraint [132]. With a modified algorithm, we have shown that a non-negativity constraint is not required to achieve a robust inversion that does not show unphysical oscillations in the spectrum [130].

We used LOD to measure electron polarization. Although LOD is less sensitive than conventional EPR detection under equivalent conditions, it has two notable advantages. First, signal can be measured during high power mw irradiation. This opens up the possibility of implementing an alternative method of transient detection, in which signal is measured continuously during and after the mw pump pulse. Second, a mw resonator is not required, which is beneficial for two reasons: a broad distribution of microwave frequencies can be used for excitation and detection, and larger samples can be used, meaning NMR experiments can be performed in conjunction with EPR experiments to acquire complementary data and further investigate DNP processes. However, the absence of a mw resonator means the available mw field amplitude is significantly lower.

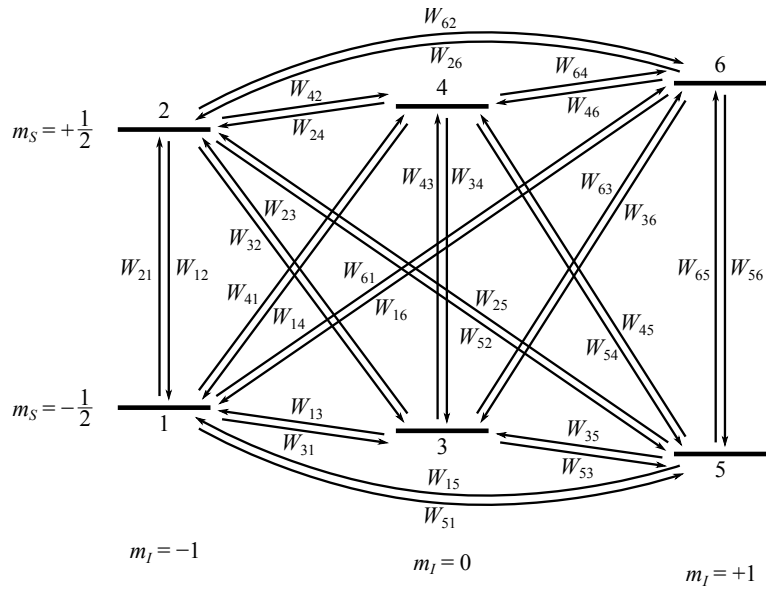


Figure 6.7: Energy level diagram and relaxation network for an electron ($S = \frac{1}{2}$) coupled to an ^{14}N nucleus ($I = 1$). W_{ab} are the transition rates for transitions from level b to level a . Diagram adapted from [43]

The transient saturation data indicates the presence of spectral diffusion or magnetization transfer with two distinguishable time constants: there is a slower decrease in signal across all frequencies, and a faster increase in signal at frequencies close to ω_p . While it is tempting to try to assign peaks in the relaxation spectrum to individual relaxation processes, given the complexity of the relaxation network, such an interpretation without further analysis would be too simplistic.

One approach to interpret the data is to model the spin system as a network of discrete energy levels. For a nitroxide radical such as 4-Amino-TEMPO, an electron ($S = \frac{1}{2}$) is strongly coupled to an ^{14}N nucleus ($I = 1$), so the network, illustrated in Figure 6.7, has six energy levels. In this model, polarization is represented by population differences, and relaxation and spectral diffusion are described by transitions between energy levels. This model can be used to derive a system of rate equations which could be used to simulate the data. In this approach, relaxation rates could, in principle, be measured by fitting the simulated data to the experimental data, with the individual relaxation rates adjusted iteratively to give the best fit [149].

An alternative approach is to use a thermodynamic model, such as that proposed by Farrar et al. [50]. In this model, the EPR spectrum is divided into a number of bins of equal frequency width, each of which is modelled as a spin bath and is characterized by a centre frequency and a spin temperature. Electron–

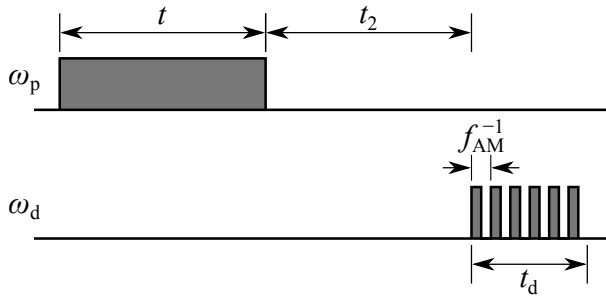


Figure 6.8: Modified pulse sequence to extend the presented method to a third dimension. Microwave pump pulse (frequency ω_p) would be switched on for a time t , off for a time t_2 , and electron magnetization remaining after $t + t_2$ would be measured using LOD. Pictured detection pulse sequence is a microwave field (frequency ω_d) amplitude-modulated by a square-wave. t , t_2 and ω_d would be incremented along dimensions 1, 2 and 3, respectively.

electron cross-relaxation is represented by transitions between adjacent bins, while electron–electron–nucleus relaxation is represented by transitions between bins separated by the nuclear Larmor frequency. This model can also be used to derive a set of rate equations to simulate the data, with the transition rates determined using the Hamiltonian describing the coupling of the baths, as discussed by Provorov [167], or by fitting the simulated and experimental data [50]. However, so far this method has only been demonstrated in the high-temperature limit, and an extension to the low temperature case is not straightforward.

Although the data has yet to be analysed in detail, the presented methodology represents a new and promising approach to investigate relaxation processes in inhomogeneously broadened EPR spectra. With further experiments at different temperatures and concentrations, together with simulations of the spin system, it should in principle be possible to interpret the data more robustly. The method presented here can, therefore, provide complementary data to other investigations into electron relaxation processes.

A straightforward extension of the presented method, similar to the approach of Song et al. [29], would be to include a delay time t_2 between the pump pulse and the detection sequence, with t_2 incremented along a third dimension. A pulse sequence for such an experiment is illustrated in Figure 6.8. Data recorded using this method could be inverted along the t_2 dimension in addition to the t dimension, yielding a 3-dimensional correlation spectrum, with pump frequency, ‘saturation time constant’ τ , and T_1 along the three spectral dimensions. Multi-dimensional correlation spectra such as this can be a useful tool to improve the

resolution and SNR of relaxation data for solids or systems with cross-relaxation and exchange. However, a drawback of the extension to three dimensions is that it is experimentally and computationally much more expensive than an inversion of 2-dimensional data.

Chapter 7

DNP Over Short Timecales

7.1 Introduction

In low temperature DNP experiments, samples are typically polarized over time-scales of minutes to hours, and the enhancement process is often characterized by a single polarization build-up rate, expressed as the build-up time constant τ_{buildup} which fits eq (2.36). However, early experimental evidence on paramagnetically doped single crystals indicates that multiple time-scales are required for a quantitative understanding of DNP processes [168]. Furthermore, when the underlying DNP mechanisms and other active processes, such as relaxation and spin diffusion, are considered, multi-exponential polarization build-up is a plausible, and perhaps even likely, possibility, particularly when many spins are involved, as discussed in Chapter 2.

When describing samples containing paramagnetic centres, such as those used for DNP experiments, a distinction is often made between two different groups of nuclei: nuclei close to the radical are called core nuclei, while nuclei further from the radical are called bulk nuclei. The boundary between these two groups of nuclei is called a diffusion barrier [53, 54], as was illustrated in Figure 2.8.

It is important to understand the mechanisms which transfer enhanced polarization to bulk nuclei, since most of the detected NMR signal is due to these spins. Several different pathways for polarization of bulk nuclei, and transport of enhanced polarization through bulk nuclei, have been proposed, and the role of core nuclei in this process is unclear [55, 56]. This was discussed in more detail in Section 2.5. If DNP data are to be compared with numerical simulations, it is useful to distinguish between the polarization of core and bulk nuclei. Depending

on orientation and distance to the radical, the resonance frequency of core nuclei can be significantly shifted, so they may be difficult to observe experimentally. For single crystals, it was shown that it is still possible to observe strongly shifted nuclear spins, and that the relaxation behaviour of such nuclei can be affected by the distance to the electron as well as by cross-relaxation with bulk nuclei [54].

Initial simulations of simple one-electron, one-nucleus model systems were performed, and these suggested that nuclear spins near the magic angle with respect to the radical and the \mathbf{B}_0 field are polarized faster than nuclear spins that experience a significant shift due to dipolar interactions with a nearby radical. The magic angle θ_m is defined as the angle at which $(3\cos^2 \theta_m - 1) = 0$: for nuclear spins at this angle with respect to the radical and the \mathbf{B}_0 field, the secular part of the dipolar part of the hyperfine interaction is zero (see eq (1.51)). The angular dependence of polarization build-up rate can be seen in the results of the simulations displayed in Figure 2.10 [15].

Low-temperature dissolution DNP is usually performed with paramagnetically doped glassy samples. This makes a quantitative description of the enhancement process and a systematic improvement of DNP performance challenging, and experimental procedures to acquire the necessary data more demanding.

The experiments presented in this chapter were designed to test the following three hypotheses: (i) core nuclei can be directly observed in an NMR experiment using a glassy sample; (ii) core and bulk nuclei are polarized at different rates, and they also relax to equilibrium with different rates; (iii) different core nuclei are polarized and relax at different rates, depending on orientation and distance to the radical.

These experiments tested the possibility of characterizing nuclear longitudinal relaxation time constants as a function of the NMR offset frequency following DNP enhancement, and whether this could be used to distinguish between core and bulk nuclei.

7.2 Experimental details and data processing

Experiments were performed at 3.39 T using a 200 μl sample of 50 mM 4-Amino-2,2,6,6-tetramethylpiperidine-1-oxyl (4-Amino-TEMPO; Sigma-Aldrich Co Ltd, Dorset, UK) in 1:1 water/glycerol at a temperature of 1.5 K. The experimental set-up, which was shown in Figure 3.16 and described in detail in Section 3.6,

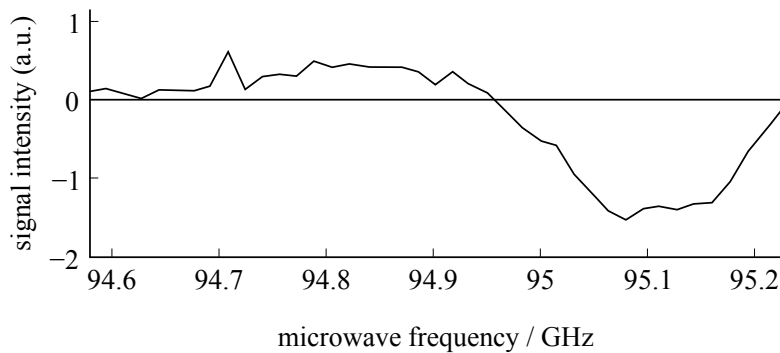


Figure 7.1: DNP enhancement spectrum of 4-Amino-TEMPO: NMR signal intensity, as a function of mw frequency, following DNP enhancement with a continuous mw field for 200 s.

is summarized here.

NMR signal was measured using a home-built DNP probe. The probe, which was described in detail in Section 4.1, was inserted into the external part of a Krymov ENDOR probe [90]. Samples were contained within a 220 μ l sample holder (height 17.5 mm, ID 4 mm). The probe is designed for EPR, NMR and DNP experiments, so EPR and NMR experiments can be measured under identical conditions, in addition to DNP NMR experiments, such as those presented here.

A Krymov microwave (mw) bridge was used as a mw source, and the wave-guide on the external part of the Krymov probe was used for transmission of the mw field to the sample [90]. The mw field is generated by a voltage controlled oscillator (VCO), with a tunable output frequency of 94.92 ± 0.34 GHz. The sample does not sit inside a resonator, but copper shielding is used to contain the mw field and increase the mw field amplitude.

NMR experiments were performed using the broadband channel of a Bruker Avance 400 console (Bruker BioSpin, Billerica, MA), and experiments were controlled using Xwin-NMR (Version 3.2, Bruker BioSpin, ibid.). NMR signal was detected using a saddle coil (1 pair of turns, height 20 mm, diameter 7 mm, angular width of loops 90°) mounted on the probe head. The saddle coil is part of a resonant circuit tuned to the ^1H Larmor frequency at 3.39 T of 144 MHz: the coil is coarsely tuned and matched using home-built variable capacitors at the probe-head, and finely tuned and matched using variable air capacitors at the top of the probe.

The mw bridge and NMR spectrometer were both triggered using a data timing generator (DTG 5078, Tektronix, Beaverton, OR), so that EPR and NMR

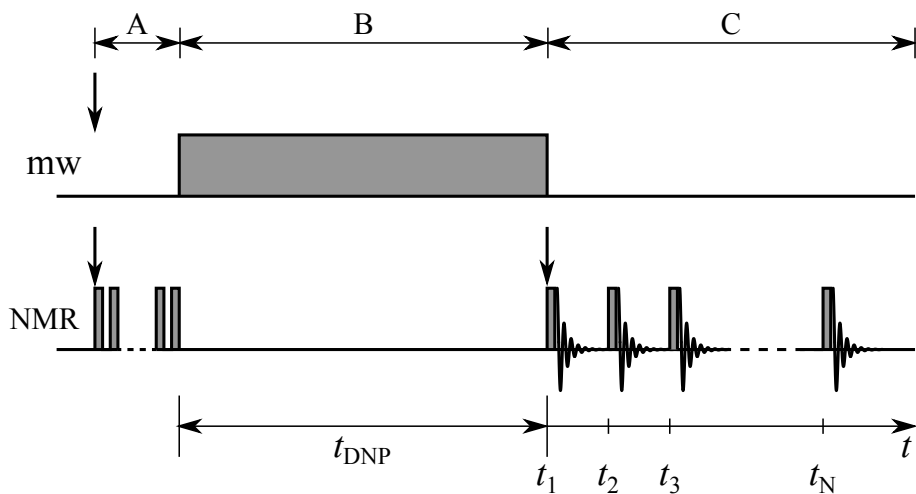


Figure 7.2: Pulse sequence used for DNP relaxation experiments. The pulse sequence can be divided into three sections: (A) NMR saturation pulse train; (B) continuous mw irradiation for a time $t_{\text{DNP}} = 100$ s; (C) series of 39 nonlinearly spaced rf pulses to record NMR spectra, each of which had a duration of 1 μ s and a nominal flip angle of 1°. Down-pointing arrows indicate positions of triggers from the DTG.

experiments could be synchronized. An analogue-digital/digital-analogue device (USB-6259 DAQ, National Instruments, Austin, TX) was used to control the mw frequency.

In a preliminary experiment, a DNP enhancement spectrum was acquired by irradiating the sample with a continuous mw field for 200 s, and measuring the integrated NMR signal intensity as a function of mw frequency. The enhancement spectrum, shown in Figure 7.1, shows that the maximum DNP enhancement was achieved with a 95.08 GHz mw field, which corresponds to a negative DNP enhancement.

The pulse sequence for the main experiment is shown in Figure 7.2. Following an rf saturation pulse train, the sample was irradiated for 100 s with a 95.08 GHz mw field, the frequency corresponding to maximum negative DNP enhancement. Immediately following the mw irradiation, NMR spectra were recorded at 39 non-linear time intervals between 5 ms and 200 s, using 1 μ s rf pulses with a nominal flip angle of 1°. A baseline was also recorded by repeating the experiment with a 94.58 GHz mw field, a frequency far outside the 4-Amino-TEMPO EPR spectrum at which DNP enhancement is negligible (see Figure 7.3).

2-dimensional NMR data, with NMR offset frequency $\Delta\nu_{\text{NMR}}$ along the first dimension and time after the end of the mw pulse along the second, was inverted using the inverse Laplace transform (ILT) algorithm described in Chapter 5. The

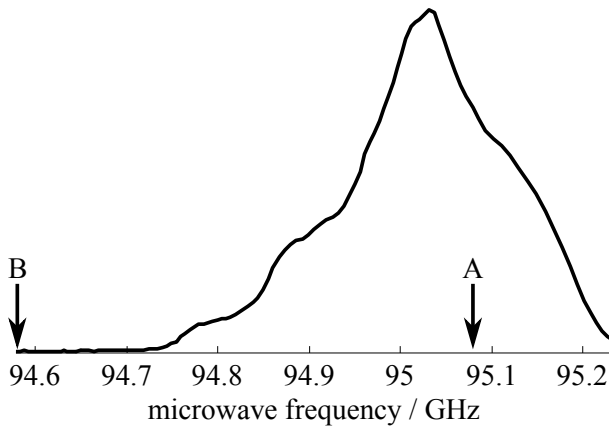


Figure 7.3: Longitudinally detected EPR spectrum of 50 mM 4-Amino-TEMPO in 1:1 water/glycerol, irradiated with a mw field, amplitude modulated by a 3.1 kHz square-wave. Microwave frequencies used for DNP experiments are indicated by arrows: (A) main irradiation pulse used a 95.08 GHz mw field, the frequency corresponding to maximum negative DNP enhancement; (B) a baseline was recorded by repeating the experiment with a 94.58 GHz mw field, a frequency at which DNP enhancement was negligible.

signal $S(\Delta\nu_{\text{NMR}}, t)$, measured at discrete NMR offset frequencies $\Delta\nu_{\text{NMR}}$ and sampling times t , can be expressed using eq (5.1) as

$$S(\Delta\nu_{\text{NMR}}, t) = \int_0^\infty [e^{-t/T_1}] \mathcal{G}(\Delta\nu_{\text{NMR}}, T_1) dT_1 + E(\Delta\nu_{\text{NMR}}, t), \quad (7.1)$$

where T_1 is the longitudinal relaxation time; $\mathcal{G}(\Delta\nu_{\text{NMR}}, T_1)$ and $E(\Delta\nu_{\text{NMR}}, t)$ are the spectrum and experimental noise, as described in Chapter 5; and $[e^{-t/T_1}]$, relating experimental parameter t to spectral parameter T_1 , is the kernel \mathcal{K} . The kernel associated with $\Delta\nu_{\text{NMR}}$, the first dimension of both the signal and the spectrum, can be represented by an identity matrix: this dimension is not inverted, but the regularization is applied to this dimension as well as to the inverted dimension.

The data was inverted using the algorithm described in Chapter 5 and a spectrum $\hat{\mathbf{g}}$ was produced using eq (5.20). Relaxation time constant distributions were extracted from the data by performing the inversion along the time dimension only. However, the full 2D data set was used for the inversion, to take advantage of the continuity of the relaxation times along the spectral dimension [132].

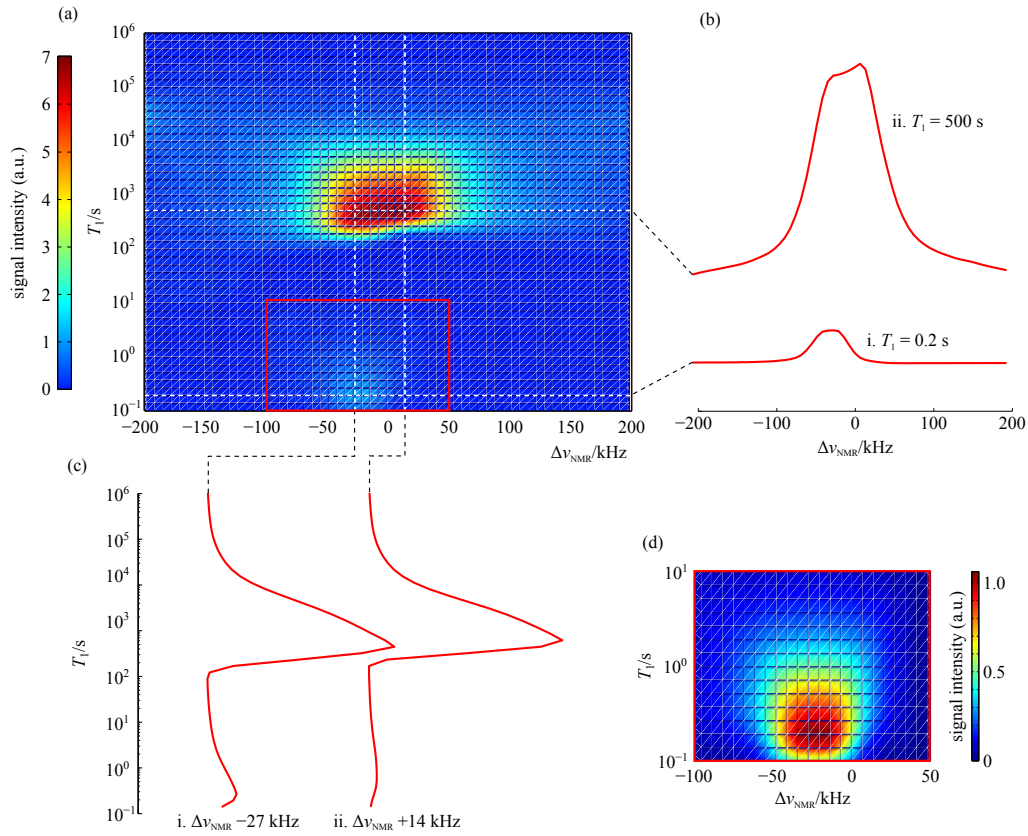


Figure 7.4: Results of inverse Laplace transform: (a) pseudocolour plot showing intensity as a function of NMR offset frequency $\Delta\nu_{\text{NMR}}$ (x -axis) and longitudinal relaxation time T_1 (y -axis); (b) traces of intensity at fixed T_1 (i. 0.2 s and ii. 500 s); (c) traces of intensity at fixed $\Delta\nu_{\text{NMR}}$ (i. -27 kHz and ii. $+14$ kHz); (d) region of pseudocolour plot indicated by red rectangle in (a), plotted with a re-scaled colour map.

7.3 Results and discussion

The results of the inverse Laplace transform are shown in Figure 7.4: the complete 2-dimensional spectrum is shown in Figure 7.4a, and 1-dimensional traces at fixed T_1 and $\Delta\nu_{\text{NMR}}$ are shown in Figures 7.4b and 7.4c, respectively. The dominant feature of this spectrum is the broad peak centred at $T_1 \sim 500$ s, $\Delta\nu_{\text{NMR}} \sim 0$ kHz, where the majority of the signal is located. This peak is significantly extended in both dimensions. There is also a peak at a much shorter value of T_1 ($T_1 \approx 0.2$ s, $\Delta\nu_{\text{NMR}} \approx -27$ kHz), which is reproduced in Figure 7.4d. The two peaks have approximate relative integrals of 19 and 1, respectively, which were estimated by summing the data points of each peak, using integration limits of -200 kHz, 200 kHz, 10^1 s and 10^6 s for the first peak, and -100 kHz, 50 kHz, 10^{-1} s and 10^1 s for the second peak. The spectrum allows us to make several observations,

which are discussed in the following paragraphs.

Close to the centre of the NMR spectral line, the majority of the signal relaxes with a longitudinal relaxation time of approximately 500 s. The distribution of relaxation times is sharper at the line centre ($|\Delta\nu_{\text{NMR}}| < 50 \text{ kHz}$), and broader at intermediate offset frequencies ($50 \text{ kHz} < |\Delta\nu_{\text{NMR}}| < 150 \text{ kHz}$).

At the wings of the NMR line, particularly the low frequency wing, the relaxation time distribution extends to distinctly shorter values ($T_1 \approx 100 \text{ s}$), compared with the relaxation time distribution at the line centre. The faster relaxation at the wings of the line indicates a stronger interaction with the electron spins, caused by spatial proximity to the nearest paramagnetic centre.

Shifted by about $\Delta\nu_{\text{NMR}} \approx -27 \text{ kHz}$ with respect to the centre of the NMR line, the signal has an additional, fast-relaxing, component, with a time constant of approximately 0.2 s. Granwehr and Köckenberger measured electron longitudinal relaxation times using samples of TEMPO, under very similar conditions to those used in the present experiment ($B_0 = 3.4 \text{ T}$, $T = 1.5 \text{ K}$), of 0.77 s (5 mM), 0.72 s (10 mM), and 0.31 s (20 mM) [43]. The time constant of this fast-relaxing component is close to these electron longitudinal relaxation times, indicating a stronger interaction with the electron spins.

One of the most notable features of the spectrum is that two separate relaxation peaks are clearly distinguishable: the peak at $T_1 \approx 0.2 \text{ s}$ (henceforth called the ‘fast peak’) is clearly an independent peak, rather than just an elongated tail of the larger peak at $T_1 \sim 500 \text{ s}$. This indicates that there exists a clear barrier within the sample that separates two regions, or two different types of nuclear spin, with different dynamics. The narrow spectral width of the fast peak suggests that there is an orientation selectivity for this region, and the negative frequency shift with respect to the line centre may indicate an equatorial position with respect to the radical centre. The frequency of the mw radiation was towards the high frequency edge of the 4-Amino-TEMPO spectrum (see Figure 7.3). This is the g_x region of the spectrum, corresponding to radicals with the x -axis of their g -matrix principal axis system aligned close to \mathbf{B}_0 . Therefore, it is conceivable that the narrow fast peak is caused by the hydrogen nuclei in the methyl groups on the 4-Amino-TEMPO molecule itself (see Figure 7.5). This could be tested by performing experiments with a deuterated solvent, with deuterated 4-Amino-TEMPO, or with different mw frequencies in the g_y and g_z regions of the spectrum.

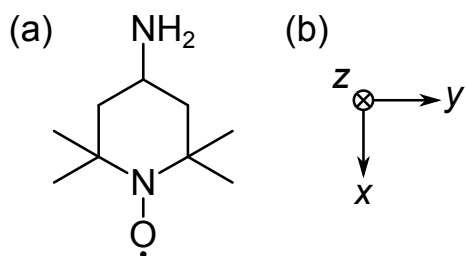


Figure 7.5: 4-Amino-TEMPO radical. (a) Molecular structure. (b) g -matrix principal axis system (PAS). Experiments were performed with a mw frequency in the g_x region of the spectrum, corresponding to radicals with the x -axis of the g -matrix PAS aligned close to \mathbf{B}_0 . Hydrogen nuclei in the methyl groups on the 4-Amino-TEMPO molecule are in equatorial positions with respect to the the x -axis of the g -matrix PAS.

7.4 Conclusions

This chapter has presented measurements of longitudinal relaxation times across an NMR spectral line in a static solid after DNP enhancement. The measurements reveal an offset dependence of the relaxation behaviour, with relatively long relaxation times ($T_1 \approx 500$ s) close to the centre of the spectral line, extending to broader distributions of relaxation times at the wings, including distinctly shorter relaxation times ($T_1 \approx 100$ s). There is also a relatively fast relaxation component ($T_1 \approx 0.2$ s) shifted by about $\Delta\nu_{\text{NMR}} \approx -27$ kHz with respect to the line centre.

The data is consistent with the following deductions: the majority of spins relax relatively slowly, with a fairly broad distribution of relaxation time constants, and are responsible for the high-amplitude signal in the spectrum close to the line centre corresponding to $T_1 \approx 500$ s; faster-relaxing signal at the wings of the line is caused by nuclei with a stronger interaction with the electron spins, due to closer spatial proximity to the nearest paramagnetic centre; the relatively narrow peak, representing the fastest observed relaxation times, may be caused by spins in the methyl groups on the 4-Amino-TEMPO molecule.

It should be noted that the assignment of the peaks is not conclusive, and these deductions may be an oversimplification of the relaxation behaviour. Although the two independent peaks indicate two distinct regions, or types of nuclei, it has not been possible to unambiguously identify signal coming from core spins or bulk spins. Nevertheless, the calculation of relaxation time constant distributions represents a promising approach to obtaining additional selectivity for the analysis of DNP enhancement in disordered samples. Comparison of the presented data with the results of simulations may allow us to draw more robust conclusions

regarding the relaxation behaviour of different groups of nuclei from the data.

Chapter 8

Conclusions and Outlook

The aim of the work presented in this thesis was to develop hardware and analysis methods to study relaxation in NMR and EPR, particularly in samples commonly used for solid-state DNP.

A low-temperature probe for NMR and longitudinally detected (LOD) EPR was built. This probe was primarily designed for relaxation studies in samples commonly used for solid-state DNP. Because state-of-the-art EPR and NMR hardware are typically not compatible at W-band frequencies, compromises had to be made to incorporate EPR and NMR detection systems into the same probe. The probe did not use a microwave (mw) resonator, but shielding was used to enhance the mw field amplitude. This probe has been used for experiments measuring transient saturation of magnetization in EPR, and relaxation experiments in DNP NMR. Potential future modifications to this probe include incorporating ^{13}C NMR detection, adding electron-nuclear double resonance (ENDOR) capabilities, and using a resonant structure with a low quality factor, to increase the mw field amplitude while retaining the ability for broadband excitation and detection. A combined NMR and EPR probe for cryoporometric studies of lignin degradation was also built. However, problems with the EPR detection system on this probe meant that, at the time of writing, no useful data has yet been recorded.

Relaxation data in EPR and NMR, including the data presented in this thesis, often exhibits multi-exponential behaviour. An algorithm for fitting multi-exponential relaxation data and producing distributions of time constants was developed. The algorithm, which is based on Tikhonov regularization, inverts the relaxation data using a numerical inverse Laplace transform (ILT). It uses a uniform penalty and a zero-crossing penalty to stabilize the solution, but does not

use a non-negativity constraint, so relaxation time spectra with both positive and negative peaks could be produced [129, 130, 132].

Finally, experiments designed to study relaxation and other dynamic processes in paramagnetically doped samples were performed. The experiments were demonstrated with samples containing 4-Amino-TEMPO, an organic radical commonly used as a polarizing agent in low-temperature solid-state DNP. In the following sections, approaches towards a more detailed interpretation of the data presented, together with possibilities for further experiments, are discussed.

8.1 Interpretation of EPR transient saturation data

The EPR transient saturation experiment presented in Chapter 6 was designed to study relaxation, saturation and spectral diffusion processes in EPR. Microwave radiation at a fixed frequency was applied to a sample, and the transient saturation of magnetization across the spectral line was recorded. Data was inverted using the ILT algorithm, and the resulting relaxation spectra exhibited both positive and negative peaks, demonstrating the importance of using an algorithm without a non-negativity constraint.

The transient saturation data indicated the presence of spectral diffusion or magnetization transfer with at least two time constants. As the transient saturation data depends on many processes, it can be difficult to interpret such data. If the data is to be used to measure time constants associated with particular physical processes, careful interpretation is necessary. One approach would be to devise a model of the spin system and perform simulations of the experiments, and compare the data with results of such simulations.

Two models which could be used for this purpose were outlined. The first approach is to model the spin system as a network of discrete energy levels. In this model, population differences represent polarization, and transitions between energy levels represent relaxation processes, saturation, and spectral diffusion [149]. The second approach is to use a thermodynamic model, in which the EPR spectrum is divided into bins of equal frequency width, each of which is characterised by a centre frequency and a spin temperature. In this model, relaxation processes are represented by transitions between bins [50]. Either of these models could be

used to derive a system of rate equations which could be used to simulate the data, and relaxation rates could, in principle, be measured by fitting the simulated data to the experimental data.

8.2 Interpretation of DNP NMR data

Chapter 7 presented measurements of longitudinal relaxation across an NMR spectral line in a static solid after DNP enhancement. The measurements revealed an offset dependence of the relaxation behaviour. One of the most significant features of the relaxation spectrum was that two separate peaks, corresponding to very different relaxation times, were clearly distinguishable. This indicated that there exists a clear barrier within the sample that separates two regions, or two different types of nuclear spin, with different dynamics. One interpretation of the data is that the faster peak is caused by the hydrogen nuclei on the 4-Amino-TEMPO molecule itself, as discussed in Chapter 7. This deduction could be tested by repeating the experiment with mw frequencies in different regions of the spectrum, with a deuterated solvent, or with deuterated 4-Amino-TEMPO.

The assignment of the peaks in the spectrum was not conclusive, and the proposed interpretation may be an oversimplification of the relaxation behaviour. However, it may be possible to draw more robust conclusions regarding the relaxation behaviour of different groups of nuclei if the data could be compared with the results of simulations of the experiment. The calculation of relaxation time constant distributions represents a promising approach to obtaining additional selectivity for the analysis of DNP enhancement in disordered samples.

8.3 Analysis of transient LOD EPR data

The longitudinally detected EPR data presented in Chapter 6 was recorded during irradiation by a train of mw pulses, with the amplitude-modulation frequency of the pulse train close to the resonance frequency of the detection circuit, ω_E . The data was analysed by calculating the Fourier transform of the transient voltage, and retaining the amplitude of the Fourier component at ω_E . This method returns a single value for each transient voltage analysed, which is assumed to be proportional to the longitudinal magnetization during the pulse train, while any transient information contained in the data is lost. More sophisticated methods

for analysing such data exist, and these methods could be used to process the data while retaining transient information.

The voltage induced in the detection coil, V_{ind} , is proportional to $\frac{dM_z}{dt}$ (eq (3.2)), so longitudinal magnetization, M_z , which is the property of interest in these experiments, is given by

$$M_z \propto \int V_{\text{ind}} dt. \quad (8.1)$$

The voltage recorded in an experiment is V_{Ξ} (Figure 3.4a). Therefore, the challenge is to use V_{Ξ} to calculate V_{ind} , which can then be integrated with respect to time to give M_z . Two methods which could be used to obtain V_{ind} from V_{Ξ} are: (a) use the equation of motion of the circuit; (b) deconvolve V_{Ξ} with the response function of the circuit. These two methods will be outlined briefly in the following paragraphs.

In Chapter 3, the LOD coil was modelled by a discrete voltage source, V_{in} , and an inductor (Figure 3.4b). This model circuit, which is a simple harmonic oscillator, has a relatively simple equation of motion, eq (3.4), which can, in principle, be solved to calculate V_{in} [20]. Since V_{in} is a function of V_{Ξ} , $\frac{dV_{\Xi}}{dt}$ and $\frac{d^2V_{\Xi}}{dt^2}$ in the equation of motion, it is algebraically very simple to calculate V_{in} from V_{Ξ} . Assuming V_{in} is equal to V_{ind} , M_z can be calculated by integrating V_{in} with respect to time.

This method is relatively straightforward. However, it has several difficulties. First, the equation of motion depends on the resonance frequency ω_{Ξ} and quality factor Q_{Ξ} of the detection circuit. These parameters must be known very accurately for a robust analysis of the data. Otherwise, the data processing is susceptible to artifacts and systematic errors. A related problem is that the model circuit may be not be an accurate representation of the actual detection circuit. For multi-turn and multi-layer coils such as the one used, it is often an over-simplification to regard the coil as a discrete inductor and voltage source. Therefore, even if ω_{Ξ} and Q_{Ξ} are known very precisely, eq (3.4) may not accurately describe the circuit. Finally, this method is particularly susceptible to noise. Numerical differentiation of noisy data amplifies the noise in the data [169]. Using eq (3.4) to calculate V_{in} involves a second derivative of V_{Ξ} . Since V_{in} is integrated to calculate M_z , the overall noise amplification is equivalent to that of a single differentiation. It is possible to use a noise-reduction method to improve the signal-to-noise ratio (SNR)

of the differentiated data, but most noise-reduction methods involve smoothing, and can reduce the information available in the data [169].

The second method models the detection circuit as a linear, time-independent system. In this method, the induced voltage V_{ind} and the detected voltage V_{Ξ} are the input and output voltages of the circuit, respectively. V_{Ξ} is written in terms of V_{ind} as

$$V_{\Xi}(t) = V_{\text{ind}}(t) * f(t), \quad (8.2)$$

where $*$ represents a convolution, and $f(t)$ is called the response function of the circuit: $f(t)$ is equal to the output ('response') voltage of the circuit when the input voltage is a Dirac delta function. $f(t)$ can be measured, and $V_{\text{ind}}(t)$ can then be calculated by deconvolving $f(t)$ out of $V_{\Xi}(t)$.

For very large data sets, numerical deconvolution can be time-consuming. An alternative is to perform the calculation in the frequency domain. Deconvolution of vectors in the time domain is equivalent to an entry-wise division of Fourier-transformed vectors in the frequency domain, so this is a straightforward calculation. However, since the Fourier transform of $f(t)$ is close to zero at frequencies far from ω_{Ξ} , noise at these frequencies can be strongly amplified. If necessary, a filter, such as the Wiener filter, can be used to reduce noise. The Wiener filter is derived by minimizing the mean square error between $V_{\text{ind}}(t)$ and the estimate of $V_{\text{ind}}(t)$ [170, 171]. Deconvolution using the Wiener filter is most effective when the power spectrum of the noise and $V_{\text{ind}}(t)$ are known. If they are not known, an estimated value of the SNR can be used instead. A disadvantage of using the Wiener filter is that it introduces a degree of smoothing, and can also lead to artifacts.

Whichever deconvolution method is used to extract $V_{\text{ind}}(t)$ from $V_{\Xi}(t)$, this method has an advantage over using the equation of motion, in that it is not necessary to know exact values of ω_{Ξ} and Q_{Ξ} . Furthermore, it is not even necessary to assume that the circuit is a simple harmonic oscillator with a single resonance frequency. The only requirement is that the response function of the circuit can be measured accurately.

Using one of these methods to estimate M_z , it would be possible to analyse the LOD EPR data in Chapter 6 more comprehensively, which may reveal more information about dynamic processes in the sample. The experiments could also be modified to record data from which even more information could be extracted. For example, data could be recorded continuously for the duration of an experi-

ment: LOD EPR signal can be recorded during high power mw irradiation, so it would be possible to record signal throughout the saturation pulse, detection pulse train, and relaxation period, until thermal equilibrium is reached. Measuring data transiently in this way could significantly reduce the duration of an experiment.

Appendix A

Spin matrices for the solid effect calculations

This section defines the spin angular momentum matrices for the spin system, comprising one electron spin S and one nuclear spin I , in which the DNP solid effect is described in Section 2.2. The spin angular momentum matrices for this spin system are 4×4 matrices, which are constructed by taking the Kronecker products of the single spin matrices. The full basis of matrices is shown in Table A.1.

$\hat{1}$	\hat{I}_x	\hat{I}_y	\hat{I}_z
\hat{S}_x	$\hat{S}_x\hat{I}_x$	$\hat{S}_x\hat{I}_y$	$\hat{S}_x\hat{I}_z$
\hat{S}_y	$\hat{S}_y\hat{I}_x$	$\hat{S}_y\hat{I}_y$	$\hat{S}_y\hat{I}_z$
\hat{S}_z	$\hat{S}_z\hat{I}_x$	$\hat{S}_z\hat{I}_y$	$\hat{S}_z\hat{I}_z$

Table A.1: Basis of spin matrices for the $\hat{I}\hat{S}$ system.

Only a subset of these matrices are needed for the derivations in Section 2.2. These are the following matrices:

$$\hat{S}_z = \hat{S}_z \otimes \hat{1} = \frac{1}{2} \begin{pmatrix} 1 & 0 & 0 & 0 \\ 0 & 1 & 0 & 0 \\ 0 & 0 & -1 & 0 \\ 0 & 0 & 0 & -1 \end{pmatrix}, \quad (\text{A.1})$$

$$\hat{I}_z = \hat{1} \otimes \hat{I}_z = \frac{1}{2} \begin{pmatrix} 1 & 0 & 0 & 0 \\ 0 & -1 & 0 & 0 \\ 0 & 0 & 1 & 0 \\ 0 & 0 & 0 & -1 \end{pmatrix}, \quad (\text{A.2})$$

$$\hat{S}_z \hat{I}_z = \hat{S}_z \otimes \hat{I}_z = \frac{1}{4} \begin{pmatrix} 1 & 0 & 0 & 0 \\ 0 & -1 & 0 & 0 \\ 0 & 0 & -1 & 0 \\ 0 & 0 & 0 & 1 \end{pmatrix}, \quad (\text{A.3})$$

$$\hat{S}_z \hat{I}_x = \hat{S}_z \otimes \hat{I}_x = \frac{1}{4} \begin{pmatrix} 0 & 1 & 0 & 0 \\ 1 & 0 & 0 & 0 \\ 0 & 0 & 0 & -1 \\ 0 & 0 & -1 & 0 \end{pmatrix}, \quad (\text{A.4})$$

$$\hat{S}_x = \hat{S}_x \otimes \hat{1} = \frac{1}{2} \begin{pmatrix} 0 & 0 & 1 & 0 \\ 0 & 0 & 0 & 1 \\ 1 & 0 & 0 & 0 \\ 0 & 1 & 0 & 0 \end{pmatrix}, \quad (\text{A.5})$$

where $\hat{1}$ is the 2×2 identity matrix.

Appendix B

Energy levels of the electron Zeeman interaction

The energy levels of the electron Zeeman interaction, stated in eq (1.42) in Section 1.4.1, are derived in this section.

The Hamiltonian for the electron Zeeman interaction is given by

$$\hat{H}_{EZ} = \frac{\mu_B}{\hbar} \mathbf{B}_0^T \mathbf{g} \mathbf{S}, \quad (\text{B.1})$$

where \mathbf{g} and \mathbf{S} are the g -matrix and spin matrix for the electron respectively, and \mathbf{B}_0 is the static magnetic field. \mathbf{g} can be expressed in its principal axis system (PAS) as

$$\mathbf{g} = \begin{pmatrix} g_x \\ & g_y \\ & & g_z \end{pmatrix}. \quad (\text{B.2})$$

The energy levels of the Zeeman interaction are the eigenvalues, or expectation values, of \hat{H}_{EZ} . They can be calculated as follows. First, the product $\mathbf{B}_0^T \mathbf{g}$ in eq (B.1) is replaced by a term representing an effective field $\mathbf{B}_{0,\text{eff}}$ multiplied by the free electron g -factor g_e . The Hamiltonian is then expressed as

$$\hat{H}_{EZ} = \frac{\mu_B}{\hbar} g_e \mathbf{B}_{0,\text{eff}}^T \mathbf{S}. \quad (\text{B.3})$$

\mathbf{S} is quantized along the effective field $\mathbf{B}_{0,\text{eff}}$, so the expectation values of $\mathbf{B}_{0,\text{eff}}^T \mathbf{S}$ are $B_{0,\text{eff}} m_S$, where $B_{0,\text{eff}} = |\mathbf{B}_{0,\text{eff}}|$ is the magnitude of $B_{0,\text{eff}}$, and $m_S = \pm \frac{1}{2}$ [78].

The energy levels are then given by

$$\left\langle \hat{H}_{EZ} \right\rangle = \frac{\mu_B}{\hbar} g_e |\mathbf{B}_{0,\text{eff}}| m_S \quad (\text{B.4})$$

where the product $g_e |\mathbf{B}_{0,\text{eff}}|$ can be calculated by recalling that $g_e \mathbf{B}_{0,\text{eff}}^T = \mathbf{B}_0^T \mathbf{g}$ and, therefore,

$$\begin{aligned} g_e |\mathbf{B}_{0,\text{eff}}| &= |\mathbf{B}_0^T \mathbf{g}| = |\mathbf{g}^T \mathbf{B}_0| \\ &= \left((\mathbf{g}^T \mathbf{B}_0)^T (\mathbf{g}^T \mathbf{B}_0) \right)^{\frac{1}{2}} \\ &= (\mathbf{B}_0^T \mathbf{g} \mathbf{g}^T \mathbf{B}_0)^{\frac{1}{2}} \\ &= (\mathbf{n}^T \mathbf{g} \mathbf{g}^T \mathbf{n})^{\frac{1}{2}} B_0 \\ &= g B_0, \end{aligned} \quad (\text{B.5})$$

where $B_0 = |\mathbf{B}_0|$ is the magnitude of \mathbf{B}_0 , $\mathbf{n} = \frac{\mathbf{B}_0}{B_0} = (n_x, n_y, n_z)^T$ is a unit vector along \mathbf{B}_0 , and

$$\begin{aligned} g &= (\mathbf{n}^T \mathbf{g} \mathbf{g}^T \mathbf{n})^{\frac{1}{2}} \\ &= (n_x^2 g_x^2 + n_y^2 g_y^2 + n_z^2 g_z^2)^{\frac{1}{2}} \end{aligned} \quad (\text{B.6})$$

is an effective g -factor [78].

Finally, the energy levels of the electron Zeeman interaction are given by

$$\left\langle \hat{H}_{EZ} \right\rangle = \frac{\mu_B}{\hbar} g B_0 m_S. \quad (\text{B.7})$$

Appendix C

Illustration of an excitation Hamiltonian

This section illustrates the effect of a mw Hamiltonian on the density matrix, as described in Section 1.4.4. Consider an ensemble of identical spins initially at thermal equilibrium. The initial density operator of such a system, $\hat{\rho}_0$, can be represented by \hat{S}_z ,

$$\hat{\rho}_0 = \hat{S}_z = \frac{1}{2} \begin{pmatrix} 1 & 0 \\ 0 & -1 \end{pmatrix}, \quad (\text{C.1})$$

and the Hamiltonian for the mw field in the rotating frame, chosen to be along the x -axis, is given by (using eq (1.66))

$$\hat{H}_{\text{mw}} = \omega_1 \hat{S}_x = \frac{\omega_1}{2} \begin{pmatrix} 0 & 1 \\ 1 & 0 \end{pmatrix}. \quad (\text{C.2})$$

Neglecting all other Hamiltonians, which are assumed to act over much longer time-scales than the mw Hamiltonian, it is straightforward to calculate the general solution to the Liouville-von Neumann equation (eq (1.35)) under the influence of the mw Hamiltonian,

$$\begin{aligned} \hat{\rho}(t) &= e^{-i\hat{H}_{\text{mw}}t} \hat{\rho}_0 e^{i\hat{H}_{\text{mw}}t} \\ &= e^{-i\omega_1 t \hat{S}_x} \hat{S}_z e^{i\omega_1 t \hat{S}_x} \\ &= \begin{pmatrix} \cos\left(\frac{\omega_1 t}{2}\right) & -i \sin\left(\frac{\omega_1 t}{2}\right) \\ -i \sin\left(\frac{\omega_1 t}{2}\right) & \cos\left(\frac{\omega_1 t}{2}\right) \end{pmatrix} \frac{1}{2} \begin{pmatrix} 1 & 0 \\ 0 & -1 \end{pmatrix} \begin{pmatrix} \cos\left(\frac{\omega_1 t}{2}\right) & i \sin\left(\frac{\omega_1 t}{2}\right) \\ i \sin\left(\frac{\omega_1 t}{2}\right) & \cos\left(\frac{\omega_1 t}{2}\right) \end{pmatrix} \end{aligned}$$

$$\begin{aligned} &= \frac{1}{2} \begin{pmatrix} \cos(\omega_1 t) & i \sin(\omega_1 t) \\ -i \sin(\omega_1 t) & -\cos(\omega_1 t) \end{pmatrix} \\ &= \hat{S}_z \cos(\omega_1 t) - \hat{S}_y \sin(\omega_1 t). \end{aligned} \quad (\text{C.3})$$

This is the result given in eq (1.67).

Bibliography

- [1] Mohr, P. J.; Taylor, B. N.; Newell, D. B. *Rev. Mod. Phys.* **2012**, *84*, 1527–1605.
- [2] Levitt, M. H. *Spin Dynamics: Basics of Nuclear Magnetic Resonance*; John Wiley & Sons: Chichester, UK, 2nd ed.; 2008.
- [3] Prisner, T. F.; Köckenberger, W. *Appl. Magn. Reson.* **2008**, *34*, 213–218.
- [4] Griffin, R. G.; Prisner, T. F. *Phys. Chem. Chem. Phys.* **2010**, *12*, 5737–5740.
- [5] Walker, T. G.; Happer, W. *Rev. Mod. Phys.* **1997**, *69*, 629–642.
- [6] Goodson, B. M. *J. Magn. Reson.* **2002**, *155*, 157–216.
- [7] Natterer, J.; Bargon, J. *Prog. Nucl. Magn. Reson. Spectrosc.* **1997**, *31*, 293–315.
- [8] Duckett, S. B.; Sleigh, C. J. *Prog. Nucl. Magn. Reson. Spectrosc.* **1999**, *34*, 71–92.
- [9] Gadian, D. G.; Panesar, K. S.; Linde, A. J. P.; Horsewill, A. J.; Köckenberger, W.; Owers-Bradley, J. R. *Phys. Chem. Chem. Phys.* **2012**, *14*, 5397–5402.
- [10] Owers-Bradley, J. R.; Horsewill, A. J.; Peat, D. T.; Goh, K. S. K.; Gadian, D. G. *Phys. Chem. Chem. Phys.* **2013**, *15*, 10413–10417.
- [11] Overhauser, A. W. *Phys. Rev.* **1953**, *92*, 411–415.
- [12] Carver, T. R.; Slichter, C. P. *Phys. Rev.* **1953**, *92*, 212–213.
- [13] Goldman, M. *Quantum Description of High-Resolution NMR in Liquids*; Oxford University Press: New York, NY, 1988.

- [14] Schweiger, A.; Jeschke, G. *Principles of Pulse Electron Paramagnetic Resonance*; Oxford University Press: New York, NY, 2001.
- [15] Van der Drift, A. *Progress in DNP Theory and Hardware*, Thesis, University of Nottingham, 2012.
- [16] Köckenberger, W. *Dynamic Nuclear Polarisation*; MPAGS Lecture Course at The University of Nottingham: 2010.
- [17] Ernst, R. R.; Bodenhausen, G.; Wokaun, A. *Principles of Nuclear Magnetic Resonance in One and Two Dimensions*; Oxford University Press: New York, NY, 1987.
- [18] Bloch, F. *Phys. Rev.* **1946**, *70*, 460–474.
- [19] Eaton, S. S.; Eaton, G. R. *Biol. Magn. Reson.* **2000**, *19*, 29–154.
- [20] Granwehr, J. *A New Approach to Longitudinally Detected Electron Paramagnetic Resonance*, Thesis, Swiss Federal Institute of Technology, Zürich, 2002.
- [21] Dzuba, S. A.; Kodera, Y.; Hara, H.; Kawamori, A. *J. Magn. Reson. A* **1993**, *102*, 257–260.
- [22] Dzuba, S. A.; Kawamori, A. *Concepts Magn. Reson.* **1996**, *8*, 49–61.
- [23] Hahn, E. L. *Phys. Rev.* **1950**, *80*, 580–594.
- [24] Zecevic, A.; Eaton, G. R.; Eaton, S. S.; Lindgren, M. *Mol. Phys.* **1998**, *95*, 1255–1263.
- [25] Romanelli, M.; Kevan, L. *Concepts Magn. Reson.* **1997**, *9*, 403–430.
- [26] Carr, H. Y.; Purcell, E. M. *Phys. Rev.* **1954**, *94*, 630–638.
- [27] Meiboom, S.; Gill, D. *Rev. Sci. Instrum.* **1958**, *29*, 688–691.
- [28] Kleinberg, R. L.; Farooqui, S. A.; Horsfield, M. A. *J. Colloid Interface Sci.* **1993**, *158*, 195–198.
- [29] Song, Y.-Q.; Venkataramanan, L.; Hürlimann, M. D.; Flaum, M.; Frulla, P.; Straley, C. *J. Magn. Reson.* **2002**, *154*, 261–268.

- [30] Kingsley, P. B. *Concepts Magn. Reson.* **1995**, *7*, 29–47, 115–136, 167–192.
- [31] Carver, T. R.; Slichter, C. P. *Phys. Rev.* **1956**, *102*, 975–980.
- [32] Abragam, A.; Proctor, W. G. *C. R. Hebd. Séances Acad. Sci.* **1958**, *246*, 2253–2256.
- [33] Jeffries, C. D. *Phys. Rev.* **1957**, *106*, 164–165.
- [34] Jeffries, C. D. *Phys. Rev.* **1960**, *117*, 1056–1069.
- [35] Hwang, C. F.; Hill, D. A. *Phys. Rev. Lett.* **1967**, *18*, 110–112.
- [36] Hwang, C. F.; Hill, D. A. *Phys. Rev. Lett.* **1967**, *19*, 1011–1014.
- [37] Goldman, M. *Spin Temperature and Nuclear Magnetic Resonance in Solids*; Oxford University Press: Oxford, 1970.
- [38] Abragam, A.; Goldman, M. *Rep. Prog. Phys.* **1978**, *41*, 395–467.
- [39] Becerra, L. R.; Gerfen, G. J.; Temkin, R. J.; Singel, D. J.; Griffin, R. G. *Phys. Rev. Lett.* **1993**, *71*, 3561–3564.
- [40] Ardenkjær-Larsen, J. H.; Fridlund, B.; Gram, A.; Hansson, G.; Hansson, L.; Lerche, M. H.; Servin, R.; Thaning, M.; Golman, K. *Proc. Natl. Acad. Sci.* **2003**, *100*, 10158–10163.
- [41] Golman, K.; Zandt, R. I.; Lerche, M.; Pehrson, R.; Ardenkjær-Larsen, J. H. *Cancer Res.* **2006**, *66*, 10855–10860.
- [42] Hu, K.-N.; Bajaj, V. S.; Rosay, M.; Griffin, R. G. *J. Chem. Phys.* **2007**, *126*, 044512.
- [43] Granwehr, J.; Köckenberger, W. *Appl. Magn. Reson.* **2008**, *34*, 355–378.
- [44] Solomon, I. *Phys. Rev.* **1955**, *99*, 559–565.
- [45] Hausser, K.; Stehlik, D. *Adv. Magn. Reson.* **1968**, *3*, 79–139.
- [46] Hovav, Y.; Feintuch, A.; Vega, S. *J. Magn. Reson.* **2010**, *207*, 176–189.
- [47] Hovav, Y.; Feintuch, A.; Vega, S. *J. Magn. Reson.* **2012**, *214*, 29–41.

- [48] Karabanov, A.; Kwiatkowski, G.; Köckenberger, W. *Appl. Magn. Reson.* **2012**, *43*, 43–58.
- [49] Serra, S. C.; Rosso, A.; Tedoldi, F. *Phys. Chem. Chem. Phys.* **2012**, *14*, 13299–13308.
- [50] Farrar, C. T.; Hall, D. A.; Gerfen, G. J.; Inati, S. J.; Griffin, R. G. *J. Chem. Phys.* **2001**, *114*, 4922–4933.
- [51] Borghini, M. *Phys. Rev. Lett.* **1968**, *20*, 419–421.
- [52] Hovav, Y.; Feintuch, A.; Vega, S. *Phys. Chem. Chem. Phys.* **2013**, *15*, 188–203.
- [53] Bloembergen, N. *Physica* **1949**, *15*, 386–426.
- [54] Wolfe, J. P. *Phys. Rev. Lett.* **1973**, *31*, 907–910.
- [55] Smith, A. A.; Corzilius, B.; Barnes, A. B.; Maly, T.; Griffin, R. G. *J. Chem. Phys.* **2012**, *136*, 015101.
- [56] Hovav, Y.; Feintuch, A.; Vega, S. *J. Chem. Phys.* **2011**, *134*, 074509.
- [57] Kwiatkowski, G. University of Nottingham, UK. Personal communication, 2013.
- [58] Dementyev, A.; Cory, D. G.; Ramanathan, C. *Phys. Rev. B* **2008**, *77*, 024413.
- [59] Boutis, G. S.; Greenbaum, D.; Cho, H.; Cory, D. G.; Ramanathan, C. *Phys. Rev. Lett.* **2004**, *92*, 137201.
- [60] Ramanathan, C. *Appl. Magn. Reson.* **2008**, *34*, 409–421.
- [61] Hovav, Y.; Levinkron, O.; Feintuch, A.; Vega, S. *Appl. Magn. Reson.* **2012**, *43*, 21–41.
- [62] Karabanov, A.; van der Drift, A.; Edwards, L. J.; Kuprov, I.; Köckenberger, W. *Phys. Chem. Chem. Phys.* **2012**, *14*, 2658–2668.
- [63] Sezer, D.; Gafurov, M.; Prandolini, M. J.; Denysenkov, V. P.; Prisner, T. F. *Phys. Chem. Chem. Phys.* **2009**, *11*, 6638–6653.

- [64] Thurber, K. R.; Tycko, R. *J. Chem. Phys.* **2012**, *137*, 084508.
- [65] Hu, K.-N.; Debelouchina, G. T.; Smith, A. A.; Griffin, R. G. *J. Chem. Phys.* **2011**, *134*, 125105.
- [66] Snipes, W.; Cupp, J.; Cohn, G.; Keith, A. *Biophys. J.* **1974**, *14*, 20–32.
- [67] Hu, J. Z.; Zhou, J.; Yang, B.; Li, L.; Qiu, J.; Ye, C.; Solum, M. S.; Wind, R. a.; Pugmire, R. J.; Grant, D. M. *Solid State Nucl. Magn. Reson.* **1997**, *8*, 129–137.
- [68] Lumata, L.; Ratnakar, S. J.; Jindal, A.; Merritt, M.; Comment, A.; Malloy, C.; Sherry, A. D.; Kovacs, Z. *Chem. Eur. J.* **2011**, *17*, 10825–10827.
- [69] Lumata, L.; Merritt, M.; Khemtong, C.; Ratnakar, S. J.; van Tol, J.; Yu, L.; Song, L.; Kovacs, Z. *RSC Adv.* **2012**, *2*, 12812–12817.
- [70] Hu, K.-N.; Yu, H.-h.; Swager, T. M.; Griffin, R. G. *J. Am. Chem. Soc.* **2004**, *126*, 10844–10845.
- [71] Song, C.; Hu, K.-N.; Joo, C.-G.; Swager, T. M.; Griffin, R. G. *J. Am. Chem. Soc.* **2006**, *128*, 11385–11390.
- [72] Matsuki, Y.; Maly, T.; Ouari, O.; Karoui, H.; Le Moigne, F.; Rizzato, E.; Lyubenova, S.; Herzfeld, J.; Prisner, T. F.; Tordo, P.; Griffin, R. G. *Angew. Chem. Int. Ed.* **2009**, *48*, 4996–5000.
- [73] Kiesewetter, M. K.; Corzilius, B.; Smith, A. A.; Griffin, R. G.; Swager, T. M. *J. Am. Chem. Soc.* **2012**, *134*, 4537–4540.
- [74] Nagarajan, V.; Hovav, Y.; Feintuch, A.; Vega, S.; Goldfarb, D. *J. Chem. Phys.* **2010**, *132*, 214504.
- [75] Corzilius, B.; Smith, A. A.; Barnes, A. B.; Luchinat, C.; Bertini, I.; Griffin, R. G. *J. Am. Chem. Soc.* **2011**, *133*, 5648–5651.
- [76] Shimon, D.; Hovav, Y.; Feintuch, A.; Goldfarb, D.; Vega, S. *Phys. Chem. Chem. Phys.* **2012**, *14*, 5729–5743.
- [77] Atherton, N. M. *Principles of Electron Spin Resonance*; Ellis Horwood: Chichester, UK, 1993.

- [78] Weil, J. A.; Bolton, J. R.; Wertz, J. E. *Electron Paramagnetic Resonance: Elementary Theory and Applications*; John Wiley & Sons: New York, NY, 1994.
- [79] Schosseler, P. M. *Electron Paramagnetic Resonance Study of the Copper(II) Complexation with Carbonate Ligands in Aqueous Solution and at Calcium Carbonate Surfaces*, Thesis, Swiss Federal Institute of Technology, Zürich, 1998.
- [80] Bloembergen, N.; Damon, R. W. *Phys. Rev.* **1952**, *85*, 699.
- [81] Granwehr, J.; Leggett, J.; Köckenberger, W. *J. Magn. Reson.* **2007**, *187*, 266–276.
- [82] Schweiger, A.; Ernst, R. R. *J. Magn. Reson.* **1988**, *77*, 512–523.
- [83] Howes, A. *NMR Hardware*; MPAGS Lecture course at The University of Warwick: 2009.
- [84] Horowitz, P.; Hill, W. *The Art of Electronics*; Cambridge University Press: Cambridge, UK, 2nd ed.; 1990.
- [85] Slichter, C. P. *Principles of Magnetic Resonance*; Springer-Verlag: Heidelberg, Germany, 3rd ed.; 1990.
- [86] Hoult, D. I.; Richards, R. E. *J. Magn. Reson.* **1976**, *24*, 71–85.
- [87] Hoult, D. I. *Concepts Magn. Reson.* **2000**, *12*, 173–187.
- [88] Bonetto, F.; Anoardo, E.; Polello, M. *Concepts Magn. Reson. B* **2006**, *29B*, 9–19.
- [89] Ginsberg, D. M.; Melchner, M. *J. Rev. Sci. Instrum.* **1970**, *41*, 122.
- [90] Gromov, I.; Krymov, V. N.; Manikandan, P.; Arieli, D.; Goldfarb, D. *J. Magn. Reson.* **1999**, *139*, 8–17.
- [91] Smith, G. M.; Lesurf, J. C. G.; Mitchell, R. H.; Riedi, P. C. *Rev. Sci. Instrum.* **1998**, *69*, 3924–3937.
- [92] Weis, V.; Bennati, M.; Rosay, M.; Bryant, J. A.; Griffin, R. G. *J. Magn. Reson.* **1999**, *140*, 293–299.

- [93] Denysenkov, V. P.; Prandolini, M. J.; Krahn, A.; Gafurov, M.; Endeward, B.; Prisner, T. F. *Appl. Magn. Reson.* **2008**, *34*, 289–299.
- [94] Bennati, M.; Farrar, C. T.; Bryant, J. A.; Inati, S. J.; Weis, V.; Gerfen, G. J.; Riggs-Gelasco, P.; Stubbe, J.; Griffin, R. G. *J. Magn. Reson.* **1999**, *138*, 232–243.
- [95] Singel, D. J.; Seidel, H.; Kendrick, R. D.; Yannoni, C. S. *J. Magn. Reson.* **1989**, *81*, 145–161.
- [96] Wind, R. A.; Hall, R. A.; Jurkiewicz, A.; Lock, H.; Maciel, G. E. *J. Magn. Reson. A* **1994**, *110*, 33–37.
- [97] Cho, H.; Baugh, J.; Ryan, C. A.; Cory, D. G.; Ramanathan, C. *J. Magn. Reson.* **2007**, *187*, 242–250.
- [98] Annino, G.; Villanueva-Garibay, J. A.; van Bentum, P. J. M.; Klaassen, A. A. K.; Kentgens, A. P. M. *Appl. Magn. Reson.* **2010**, *37*, 851–864.
- [99] van Bentum, P. J. M.; van der Heijden, G. H. A.; Villanueva-Garibay, J. A.; Kentgens, A. P. M. *Phys. Chem. Chem. Phys.* **2011**, *13*, 17831–17840.
- [100] Feintuch, A.; Shimon, D.; Hovav, Y.; Banerjee, D.; Kaminker, I.; Lipkin, Y.; Zibzener, K.; Epel, B.; Vega, S.; Goldfarb, D. *J. Magn. Reson.* **2011**, *209*, 136–41.
- [101] Granwehr, J.; Schweiger, A. *Appl. Magn. Reson.* **2001**, *20*, 137–150.
- [102] Dzuba, S.; Tsvetkov, Y. *Chemical Physics* **1988**, *120*, 291–298.
- [103] Maresch, G.; Weber, M.; Dubinskii, A.; Spiess, H. *Chem. Phys. Lett.* **1992**, *193*, 134–140.
- [104] Tkach, I.; Sicoli, G.; Höbartner, C.; Bennati, M. *J. Magn. Reson.* **2011**, *209*, 341–346.
- [105] Cruickshank, P. A. S.; Bolton, D. R.; Robertson, D. A.; Hunter, R. I.; Wylde, R. J.; Smith, G. M. *Rev. Sci. Instrum.* **2009**, *80*, 103102.
- [106] Hunter, R. I.; Cruickshank, P. A. S.; Bolton, D. R.; Riedi, P. C.; Smith, G. M. *Phys. Chem. Chem. Phys.* **2010**, *12*, 5752–5756.

- [107] Granwehr, J.; Forrer, J.; Schweiger, A. *J. Magn. Reson.* **2001**, *151*, 78–84.
- [108] Ibeh, C. C. *Thermoplastic Materials: Properties, Manufacturing Methods, and Applications*; CRC Press, Taylor & Francis Group: Boca Raton, FL, 2011.
- [109] Kim, Y. W.; Earl, W. L.; Norberg, R. E. *J. Magn. Reson. A* **1995**, *116*, 139–144.
- [110] Walton, J. H.; Conradi, M. S. *J. Magn. Reson.* **1989**, *81*, 623–627.
- [111] Kodibagkar, V. D.; Conradi, M. S. *J. Magn. Reson.* **2000**, *144*, 53–57.
- [112] Ginzburg, V. L.; Sobaynin, A. A. *Sov. Phys. Usp.* **1976**, *19*, 773–812.
- [113] Boerjan, W.; Ralph, J.; Baucher, M. *Annu. Rev. Plant Biol.* **2003**, *54*, 519–546.
- [114] Pandey, M. P.; Kim, C. S. *Chem. Eng. Technol.* **2011**, *34*, 29–41.
- [115] Martinez, A. T.; Ruiz-Duenas, F. J.; Martinez, M. J.; del Rio, J. C.; Gutierrez, A. *Curr. Opin. Biotechnol.* **2009**, *20*, 348–357.
- [116] Jackson, C. L.; McKenna, G. B. *J. Chem. Phys.* **1990**, *93*, 9002–9011.
- [117] Strange, J.; Rahman, M.; Smith, E. G. *Phys. Rev. Lett.* **1993**, *71*, 3589–3591.
- [118] Hitchcock, I.; Holt, E. M.; Lowe, J. P.; Rigby, S. P. *Chem. Eng. Sci.* **2011**, *66*, 582–592.
- [119] Petrov, O. V.; Furó, I. *Prog. NMR Spectrosc.* **2009**, *54*, 97–122.
- [120] Mitchell, J.; Webber, J. B. W.; Strange, J. H. *Phys. Rep.* **2008**, *461*, 1–36.
- [121] Flick, E. W., Ed.; *Industrial Solvents Handbook*; Noyes Data Corporation: Westwood, NJ, 5th ed.; 1998.
- [122] Chiarini, F.; Martinelli, M.; Pardi, L.; Santucci, S. *Phys. Rev. B* **1975**, *12*, 847–852.
- [123] Martinelli, M.; Pardi, L.; Pinzino, C.; Santucci, S. *Phys. Rev. B* **1977**, *16*, 164–169.

- [124] Panagiotelis, I.; Nicholson, I.; Hutchison, J. M. S. *J. Magn. Reson.* **2001**, *149*, 74–84.
- [125] Nicholson, I.; Robb, F. J. L.; McCallum, S. J.; Koptioug, A.; Lurie, D. J. *Phys. Med. Bio.* **1998**, *43*, 1851–1855.
- [126] Press, W.; Teukolsky, S.; Vetterling, W.; Flannery, B. *Numerical Recipes in C*; Cambridge University Press: Cambridge, UK, 2 ed.; 1992.
- [127] Sato, H.; Kathirvelu, V.; Spagnol, G.; Rajca, S.; Rajca, A.; Eaton, S. S.; Eaton, G. R. *J. Phys. Chem. B* **2008**, *112*, 2818–2828.
- [128] Provencher, S. W. *J. Chem. Phys.* **1976**, *64*, 2772.
- [129] Borgia, G. C.; Brown, R. J. S.; Fantazzini, P. *J. Magn. Reson.* **1998**, *132*, 65–77.
- [130] Granwehr, J.; Roberts, P. J. *J. Chem. Theory Comput.* **2012**, *8*, 3473–3482.
- [131] Levitt, M. H.; Bodenhausen, G.; Ernst, R. R. *J. Magn. Reson.* **1984**, *58*, 462–472.
- [132] Venkataraman, L.; Song, Y.-Q.; Hürlimann, M. D. *IEEE Trans. Signal Process.* **2002**, *50*, 1017–1026.
- [133] Song, Y.-Q.; Venkataraman, L.; Burcaw, L. *J. Chem. Phys.* **2005**, *122*, 104104.
- [134] Abragam, A. *The Principles of Nuclear Magnetism*; Oxford University Press: Oxford, 1961.
- [135] Mims, W. B.; Nassau, K.; McGee, J. D. *Phys. Rev.* **1961**, *123*, 2059–2069.
- [136] Eaton, G. R.; Eaton, S. S. *J. Magn. Reson.* **1999**, *136*, 63–68.
- [137] Sato, H.; Filas, B. A.; Eaton, S. S.; Eaton, G. R.; Romanyukha, A. A.; Hayes, R.; Rossi, A. M. *Radiat. Meas.* **2007**, *42*, 997–1004.
- [138] Ardenkjær-Larsen, J. H.; Laursen, I.; Leunbach, I.; Ehnholm, G.; Wisstrand, L. G.; Petersson, J. S.; Golman, K. *J. Magn. Reson.* **1998**, *133*, 1–12.

- [139] Halpern, H. J.; Peric, M.; Yu, C.; Bales, B. L. *J. Magn. Reson. A* **1993**, *103*, 13–22.
- [140] Borgia, G. C.; Brown, R. J. S.; Fantazzini, P. *J. Magn. Reson.* **2000**, *147*, 273–285.
- [141] Hansen, P. C. *Rank-Deficient and Discrete Ill-Posed Problems: Numerical Aspects of Linear Inversion*; SIAM: Philadelphia, PA, 1997.
- [142] Fordham, E. J.; Sezginer, A.; Hall, L. D. *J. Magn. Reson. A* **1995**, *113*, 139–150.
- [143] Krakauer, N. Y.; Schneider, T.; Randerson, J. T.; Olsen, S. C. *Geophys. Res. Lett.* **2004**, *31*, L19108.
- [144] Istratov, A. A.; Vyvenko, O. F. *Rev. Sci. Instrum.* **1999**, *70*, 1233–1257.
- [145] Bertini, I.; Martini, G.; Luchinat, C. Relaxation, Background and Theory. In *Handbook of Electron Spin Resonance*; Poole, C. P.; Farach, H. A., Eds.; American Institute of Physics: New York, 1994.
- [146] Bertini, I.; Martini, G.; Luchinat, C. Relaxation Data Tabulation. In *Handbook of Electron Spin Resonance*; Poole, C. P.; Farach, H. A., Eds.; American Institute of Physics: New York, 1994.
- [147] Du, J.-L.; Eaton, G. R.; Eaton, S. S. *J. Magn. Reson. A* **1995**, *115*, 213–221.
- [148] Harbridge, J. R.; Eaton, S. S.; Eaton, G. R. *J. Magn. Reson.* **2002**, *159*, 195–206.
- [149] Harbridge, J. R.; Eaton, S. S.; Eaton, G. R. *J. Phys. Chem. A* **2003**, *107*, 598–610.
- [150] Mims, W. B. *Phys. Rev.* **1968**, *168*, 370–389.
- [151] Klauder, J. R.; Anderson, P. W. *Phys. Rev.* **1962**, *125*, 912–932.
- [152] Hu, P.; Hartmann, S. R. *Phys. Rev. B* **1974**, *9*, 1–13.
- [153] Hu, P.; Walker, L. R. *Phys. Rev. B* **1978**, *18*, 1300–1305.
- [154] Romanelli, M.; Kevan, L. *Concepts Magn. Reson.* **1998**, *10*, 1–18.

- [155] Portis, A. M. *Phys. Rev.* **1956**, *104*, 584–588.
- [156] Suter, D.; Ernst, R. R. *Phys. Rev. B* **1982**, *25*, 6038–6041.
- [157] Suter, D.; Ernst, R. R. *Phys. Rev. B* **1985**, *32*, 5608–5627.
- [158] Brown, I. M. *J. Chem. Phys.* **1971**, *55*, 2377.
- [159] Brown, I. M. *J. Chem. Phys.* **1973**, *58*, 4242.
- [160] Dubinskii, A. A.; Maresch, G. G.; Spiess, H. W. *J. Chem. Phys.* **1994**, *100*, 2437–2448.
- [161] Saalmueller, J. W.; Long, H. W.; Maresch, G. G.; Spiess, H. W. *J. Magn. Reson. A* **1995**, *117*, 193–208.
- [162] Meyer, V.; Eaton, S. S.; Eaton, G. R. *Appl. Magn. Reson.* **2013**, *44*, 509–517.
- [163] Chiang, Y.-W.; Borbat, P. P.; Freed, J. H. *J. Magn. Reson.* **2005**, *172*, 279–295.
- [164] Jeschke, G.; Polyhach, Y. *Phys. Chem. Chem. Phys.* **2007**, *9*, 1895–1910.
- [165] Potapov, A.; Yagi, H.; Huber, T.; Jergic, S.; Dixon, N. E.; Otting, G.; Goldfarb, D. *J. Am. Chem. Soc.* **2010**, *132*, 9040–9048.
- [166] Stoll, S.; Schweiger, A. *J. Magn. Reson.* **2006**, *178*, 42–55.
- [167] Provotorov, B. N. *Sov. Phys. JETP* **1962**, *14*, 1126–1131.
- [168] Ramakrishna, J.; Robinson, F. N. H. *Proc. Phys. Soc.* **1966**, *87*, 945–951.
- [169] Chartrand, R. *ISRN Appl. Math.* **2011**, *2011*, 164564.
- [170] Gonzalez, R. C.; Woods, R. E. *Digital Image Processing*; Prentice Hall: Upper Saddle River, NJ, 2nd ed.; 2002.
- [171] Wiener, N. *Extrapolation, Interpolation, and Smoothing of Stationary Time Series*; The MIT Press: Cambridge, MA, 1942.